Mitigation of the Effects of High Levels of High-Frequency Noise on MEMS Gyroscopes

by

Pregassen Soobramaney

A dissertation submitted to the Graduate Faculty of Engineering
Auburn University
in partial fulfillment of the
requirements for the Degree of
Doctor of Philosophy

Auburn, Alabama
August 03, 2013

Keywords: MEMS gyroscopes, noise mitigation,
microfibrous media, modeling

Approved by

George Flowers, Co-chair, Professor of Mechanical Engineeing
Subhash Sinha,Co-chair, Professor of Mechanical Engineering
Malcolm Crocker, Professor Emeritus of Mechanical Engineering
Robert Dean, Associate Professor of Electrical and Computer Engineering

Abstract

MEMS gyroscopes are being used in a variety of applications such as camcorders, vehicle stability control and game controllers. Sometimes they are used in harsh environments such as high levels of high-frequency noise. If the frequency of the noise coincides with the natural frequency of the gyroscope, the output of the latter is corrupted. Experiments have been performed to demonstrate the effects of noise on MEMS gyroscopes. The objective of this dissertation is to suggest ways to mitigate those effects.

In the first part of this research work, a mathematical model has been developed to include the effects of an external noise signal on a MEMS gyroscope. The model is simulated to assist with understanding its dynamics and it is found that the effects of the external noise signal are superimposed on the normal gyroscope's output. This finding leads to the solution of using a non-driven gyroscope to measure the superimposed effects. Thus, a differential-measurement system consisting of two gyroscopes is implemented, and simulation of the mathematical model is performed to successfully demonstrate the mitigation of the effects of noise. Experiments were performed on five gyroscopes to confirm the simulation results, and the superposition of the effects of noise has been confirmed implying that the differential measurement is a viable solution.

The second part of this research provides a study of passive approaches to attenuate the effects of noise. In this regard, four types of nickel microfibrous material were made using three diameters of nickel fibers and a wet-lay papermaking process. The Delany-Bazley analytical

acoustical model was used to determine the optimum acoustical properties of the material. The properties were then used to calculate the absorption coefficients of the microfibrous media. Damping characterization of the media was performed using the vibration transmissibility concept. Enclosures have been designed and made from the materials to attenuate the effects of noise on MEMS gyroscopes. Acoustical tests performed in a reverberation room show up to 90% reduction in the amplitude of the effects of noise.

In conclusion, two different approaches have been suggested to mitigate the undesirable effects of noise on MEMS gyroscopes. In the first approach an active design is proposed by utilizing a pair of gyroscopes whose outputs can be manipulated to yield the desired uncorrupted results. In the second approach, a passive design is proposed using nickel microfibrous material as an acoustical enclosure. Considerable reductions in the effects of noise have been achieved, showing that the nickel microfibrous material can be used to construct an acoustical enclosure.

Acknowledgments

I thank my advisors, Dr. George T. Flowers and Dr. Subhash C. Sinha, for their guidance, support, encouragement and patience in completing this work. I wish to acknowledge Dr. Malcolm Crocker, Dr. Robert N. Dean, and Dr. John L. Evans for serving on my committee. I am thankful to Haoyue Yang, James Jantz, Fuxi Zhang, Colin Stevens, Wesley Smith, and Chong Li, for their friendship and assistance.

I thank my beautiful wife, Selvina, for her love, patience, motivation and unfailing support. I am grateful to my parents, Devarajen and Kisnamah, for giving me a great education and inculcating good values in me.

I thank God for keeping me on the right path, showing me the way and giving me the strength to complete this work.

Table of Contents

List of Tables

List of Illustrations

List of Abbreviations

HEC	hydroxethycellulose
MEMS	Microelectromechanical systems
PCB	printed circuit board
SOI	silicon on insulator
SPL	sound pressure level

CHAPTER 1

LITERATURE REVIEW

1.1 Introduction

Microelectromechanical Systems (MEMS) technology is relatively new and combines mechanical and electrical systems at the micro scale. MEMS devices are being widely used because of their small size, low cost, and low power consumption. One of the most interesting MEMS devices is the MEMS gyroscope which is replacing its traditional counterpart and is being used in applications such as image stabilization in cameras and camcorders, vehicle stability control, game controllers, and motion control of robots. MEMS gyroscopes are sometimes used in harsh environments such as high levels of high-frequency noise. If the frequency of the noise coincides with the natural frequency of the gyroscope, the proof mass is overexcited giving rise to a corrupted gyroscope output. Experiments have been performed to demonstrate the effects of noise on MEMS gyroscopes. Progress has also been made to mitigate the effects of the high levels of high-frequency noise, but there is still room for improvement.

The objective of this dissertation is to mitigate the effects of noise on MEMS gyroscopes. To meet this objective, two approaches are considered. In the first approach a mathematical model is developed to include the effects of external noise on a MEMS gyroscope and then the model is used to provide a solution to mitigate the effects of noise on the gyroscope. In the second approach the mitigation of the effects of noise is

attempted using nickel microfibrous material as an acoustical material. Nickel microfibrous materials have a porosity of above 90% making them suitable for noise attenuation. They also have interesting properties such as flame and temperature resistance. In addition they can be used in chemically-harsh and high-humidity environments.

1.2 Gyroscopes

A gyroscope is a device that measures the rotation rate of an object. The name gyroscope was coined by a French physicist, Leon Foucault, who combined the Greek words "gyros" and "skopeein" meaning rotation and to see respectively. The analysis of gyroscopic motion is one of the most fascinating problems in dynamics. As illustrated in Fig. 1.1, a conventional gyroscope consists of a flywheel which is attached to a pair of gimbal rings within the gyroscope frame. In this configuration the spinning axis of the flywheel is free to take any orientation. The flywheel has a relatively large mass and is made to spin at high speed giving it a high angular momentum. The latter counteracts externally applied torques so that the orientation of the spin axis is constant. Conventional gyroscopes are precise, robust, and are widely used in navigation. But those gyroscopes have some disadvantages, in particular, the rotation bearings wear out, they are relatively bulky, and they are expensive [1-3].

1.3 MEMS Gyroscopes

MEMS gyroscopes are micromachined sensors that are used to measure angular rates. Microfabrication techniques such as lithography, deposition and etching are used to mass-produce MEMS devices on silicon-on-insulator (SOI) wafers. Most MEMS gyro-

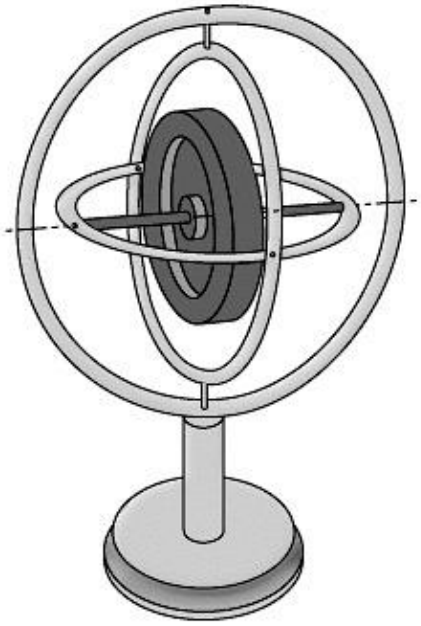

Figure 1.1 A conventional gyroscope.

scopes consist of a vibrating mass which upon rotation experiences a Coriolis force, which is proportional to the rotation rate. They do not have rotating parts and therefore they do not require bearings, and are not affected by friction and wear. Therefore MEMS gyroscopes are cheap, small, and light, have low power requirements and are maintenance free. Thus, they are finding many new applications in the automotive industry as well as consumer products such as mobile phones, games and cameras [1, 3].

1.4 Dynamics of a MEMS Gyroscope

The dynamics of the MEMS gyroscope depicted in Fig. 1.2 are governed by Eqns. (1.1) and (1.2). The proof mass m is forced into oscillation in the drive direction x by a sinusoidal force of amplitude F and rotates about the out-of-plane axis at a rotation rate Ω. A Coriolis force is therefore coupled in the sense direction, y, causing the proof mass to oscillate in that direction at the drive force frequency ω. Also, the amplitude of the sense

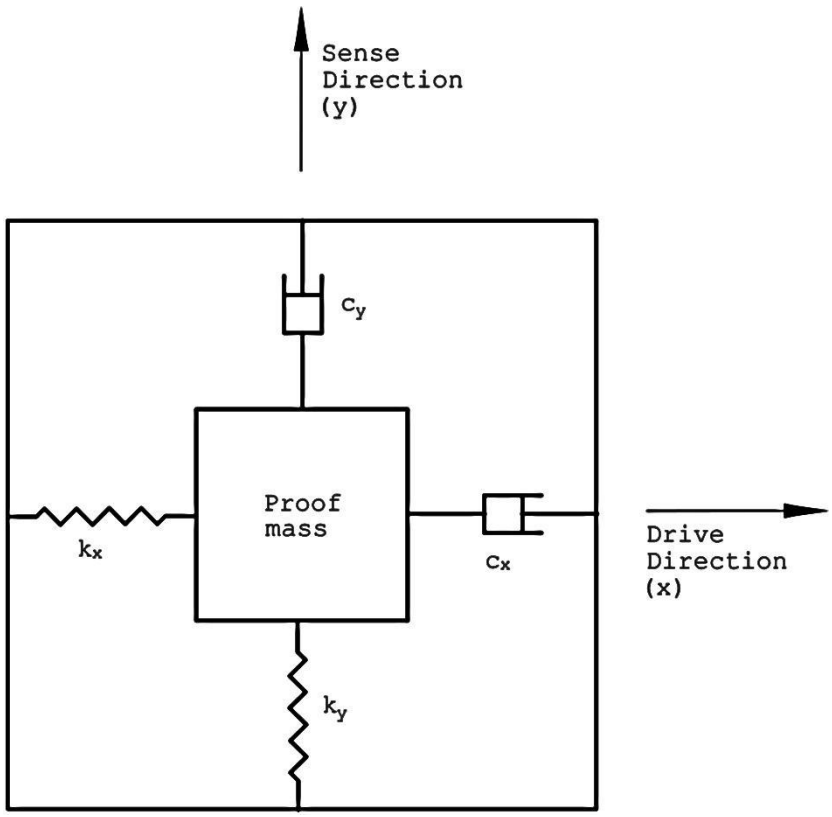

Figure 1.2 Schematic of a vibratory gyroscope.

response is proportional to the Coriolis force and therefore to the angular rate. The proof mass is held by a suspension system with stiffness k_x and damping c_x in the drive direction, and stiffness k_y and damping c_y in the sense direction [1, 4, 5].

The dynamics can be represented by [1]

$$m\ddot{x} + c_x\dot{x} + k_x x = F \sin \omega t \ , \tag{1.1}$$

and

$$m\ddot{y} + c_y\dot{y} + k_y y = -2m\Omega\dot{x} \ . \tag{1.2}$$

For maximum sense response, the proof mass is made to resonate in the sense direction, and the drive force frequency is made equal to the natural frequency of the drive mode. Therefore for high sensitivity, the natural frequencies in both directions are designed and tuned to match [1, 6]. This applies only for a constant angular rate signal,

and the detection bandwidth is zero. In practice, the sense mode frequency is separated from the drive force frequency (by approx. 100 Hz) to achieve larger bandwidth and to make the gyroscope sensitive to angular acceleration. However, this causes the gyroscope to have lower sensitivity [47].

1.5 Design Challenges for MEMS Gyroscopes

The main challenge in designing MEMS gyroscopes is that the output amplitude is very small relative to the drive force because of the small magnitude of the Coriolis force. To overcome this issue, gyroscopes are designed with high quality factor (Q) to mechanically amplify the sense amplitude. To achieve a high value of Q, high vacuum is required during packaging of a gyroscope so as to minimize damping, and also the sense mode resonance frequency is tuned to the drive force frequency by using electrostatic forces. A gyroscope with a high value of Q has a small bandwidth and is sensitive to external vibrations having frequencies at or near to the natural frequency of the gyroscope. To mitigate the effects of the vibration forces, gyroscopes are designed with high natural frequencies (10 kHz - 20 kHz). But they are still susceptible to high levels of high-frequency noise [3, 7-9].

Quadrature errors in the design of gyroscopes are due to manufacturing imperfections and consist of stiffness and damping cross-coupling between the sense and drive modes. Because of the great difference in magnitude between drive response and sense response amplitudes, a small quadrature coupling from the drive motion into the sense motion causes the Coriolis force to be corrupted. Quadrature errors are reduced by more precise and careful microfabrication, and are nullified by the control system of the gyroscope [1, 5, 9].

1.6 Effects of Noise on MEMS Gyroscopes

MEMS gyroscopes are sometimes used in harsh environments such as high levels of high-frequency noise with sound pressure levels up to 120 dB and frequencies up to and above 20 kHz. Examples of such environments are supersonic aerospace vehicles, missiles, rockets and machinery using high pressure nozzles [10, 11].

Dean *et al.* demonstrated that high levels of noise corrupt the output of MEMS gyroscopes. In the study, noise was generated by a supersonic wind tunnel and sound pressure levels up to 110 dB were generated within a frequency range of 0-24 kHz. Four commercially available gyroscopes were tested near the supersonic nozzle and in the presence of the noise, degradation of the output of the gyroscopes was observed [11]. Dean *et al.* conducted another set of experiments in a reverberation room where a speaker system was used to generate noise levels up to 130 dB within a frequency range of 0-20 kHz. Twenty four similar gyroscopes were tested using a single tone frequency sweep at the maximum output of the speakers. It was observed that in the frequency region near to and at the natural frequency of the gyroscopes, there was a large change in the output of the gyroscopes. It was concluded that the effects of the noise were frequency dependent as for frequencies of the noise away from the natural frequency, the gyroscopes were insensitive to the noise level [12]. Yunker *et al.* investigated the underwater acoustic effects on a MEMS gyroscope. The gyroscope was waterproofed and a hydrophone was used to generate a single tone sweep from 14 kHz to 20 kHz with a sound pressure level of around 140 dB. The sound pressure level was measured using a second hydrophone in a sensor configuration. Similar observations were made as when the medium was air. It

was found that the gyroscope output was corrupted near to and at its natural frequency [13].

1.7 Previous Mitigation Efforts

Castro *et al.* attempted the mitigation of the effects of noise using acoustical foam. The foam was designed to surround the gyroscope on all sides and an aluminum plate was placed on its top. Another aluminum plate was used at the bottom of the gyroscope for added mass. For testing purposes the noise was generated using a supersonic wind tunnel and considerable reductions in the effects of the noise on the MEMS gyroscopes were observed [14]. Roth performed another set of tests for the mitigation of noise in a reverberation room using several types of acoustical foams. Different attenuation levels were achieved by the use of the different foams but the effects of the noise were not completely mitigated [15]. Recently, Yunker *et al.* have used acoustical metamaterials for noise attenuation. Micro-Helmholtz resonators were designed and manufactured to have a frequency of 14.5 kHz. Microfabrication techniques were used to manufacture the sides of a cube from a 100 mm diameter silicon wafer, with each side consisting of many such resonators. Testing of the cube was done in an acoustical environment and an attenuation of the noise level of 18 dB at 14.5 kHz was achieved [16].

1.8 Acoustical Materials

Acoustical materials have the ability to absorb a considerable fraction of the total acoustic energy striking their surfaces. They are widely used in noise control and are normally placed near the noise source, near the receiver, or in the noise path. Examples of their applications are: in ships and aircraft construction, in machine enclosures, inside

earmuffs, and as the finished room surfaces in hospitals, schools and offices. Because of their wide range of application, acoustical materials are required to have other properties apart from having high sound absorptivity. They should be able to fit in the environment in which they are used and so their appearance, color, shapes, and light reflectivity are important. Also they need to be reliable, maintainable, flame resistant and durable [17, 18].

For sound absorption to take place, the exposed surface of the material should have some passages or openings for the sound waves to go through and the internal structure of the material should be able to transform the acoustic energy into heat energy. Having high porosity, which is the ratio of the void volume to the total volume, porous and fibrous materials are therefore good acoustical materials. In porous materials, the air molecules within the pores vibrates in the presence of noise and in doing so energy is lost between the molecules and the pore walls. In fibrous materials acoustic energy is converted into heat from the scattering of sound waves, the vibration of individual fibers and the rubbing of the fibers against each other [17, 18].

In acoustical applications, where high temperature resistance, flame resistance, high durability and weathering resistance are required, the use of metal foams has been investigated. Metal foams are made mostly from aluminum which is light, has good thermal conductivity and is relatively cheap. Other metals used are steel, titanium and copper. The structure of metal foams is predominantly closed cells and this has made the acoustical absorption characteristics of the material to be poor. To improve acoustical characteristics, rolling of the foams is done so as to break open the closed cells but they are still not as good as other commonly used acoustical materials [19, 17]. Alternatives to

metal foams, for high temperature applications, are aerogels which can sustain temperatures up to 1200 ^{o}C. Aerogels are nanoporous making them good acoustic absorbers. They are also claimed to be the best thermal insulators. The drawback of these materials is that they are very costly and are only used for some high-tech applications [20, 17].

1.9 Sound Absorption Coefficient (α)

The absorption coefficient of a material is defined as the ratio of the absorbed sound intensity to the total incident sound intensity. It is dependent on the frequency of the sound and the angle of incidence of the sound waves. Typical values of α vary from 1 to 100 percent. It is normally calculated using the Sabine empirical formula from the measured reverberation time (time for the sound pressure level to drop by 60 dB) with and without the presence of the material in a reverberation room [21, 22]. The absorption coefficient can also be measured using an impedance tube. The material under test is mounted at the end of the tube against a flat rigid surface and a speaker is used to generate sound waves at the other end of the tube. A two-microphone system is used for the acoustical measurements from which the absorption coefficient is derived [23].

1.10 Acoustic Models

1.10.1 Delany-Bazley Model [24, 25]

Delany and Bazley developed a model to determine the acoustical properties, the characteristic impedance Z_c and the propagation coefficient γ, of a range of fibrous materials having a porosity factor near unity. Extensive experiments were carried out to measure these properties using the impedance-tube method with plane-wave conditions.

Using the dimensional variable frequency/flow-resistance (f/σ), the measured data were normalized and empirical expressions (Eqns. (1.3) and (1.4)) were formulated in terms of power-law relationships [24, 25].

$$Z_c = \rho_o c_o \left\{ \left[1 + 0.0511 \left(\frac{f}{\sigma} \right)^{-0.75} \right] - j \left[0.0768 \left(\frac{f}{\sigma} \right)^{-0.73} \right] \right\}, \tag{1.3}$$

$$\gamma = \frac{2\pi f}{c_o} \left\{ \left[0.1749 \left(\frac{f}{\sigma} \right)^{-0.59} \right] + j \left[1 + 0.0858 \left(\frac{f}{\sigma} \right)^{-0.70} \right] \right\}, \tag{1.4}$$

where ρ_0 is the density of air, c_0 is the speed of sound in air, f is frequency of sound and σ is the airflow resistivity per unit thickness.

This model can be used with confidence when the ratio of the frequency to the air flow resistivity is between 0.01 and 1.0 m^3/kg. Extrapolation outside this range is not recommended as other power-law relationships may be required. Miki improved the Delany-Bazley model to predict the acoustical properties at low frequencies when f/σ is less than 0.01 m^3/kg [24, 21].

1.10.2 Dunn-Davern Model [26]

Using a similar approach to Delany and Bazley, Dunn and Davern developed a model for the acoustical properties of foam materials. They also developed a methodology to calculate the overall acoustical impedance of multi-layered acoustical materials, using the single layer properties [26].

1.10.3 Voronina Model [27]

The relationship between the acoustical properties and the physical structural parameters of acoustical materials was investigated by Voronina. Experimental measurements of the characteristic impedance and the propagation constant were carried out for several materials with different fiber diameters and values of porosity. Empirical

formulae were developed as a function of the material properties. Unlike the Delany-Bazley model, the Voronina model does not consider the ratio of frequency to air flow resistivity as the latter is already a function of the fiber size and porosity. Voronina compared her model with experimental values and showed that her model is accurate for materials made of relatively thick fibers [27].

1.11 Vibration Isolation and Damping

Vibration isolation can be either passive or active depending on whether external power is required or not for the isolator to work. A passive vibration isolation system consists of three main parts; the payload which requires isolation, the vibration isolators and the supporting surface or foundation. This is illustrated in Fig. 1.3 where the supporting surface, the base, is subjected to a motion *y(t)*, the payload, represented by a rigid mass *m*, and the isolator, a linear spring/damper pair [28, 29]. The equation of motion for this system is

$$m\ddot{x} + c(\dot{x} - \dot{y}) + k(x - y) = 0 \,. \tag{1.5}$$

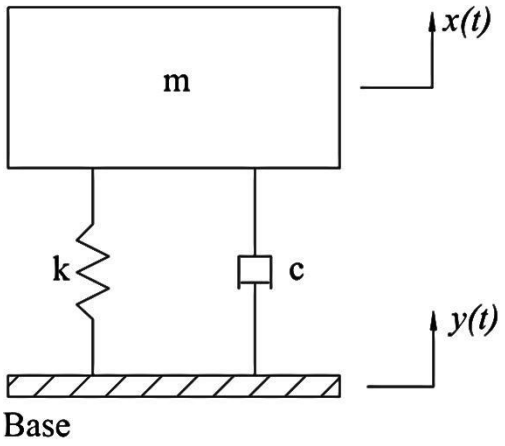

Figure 1.3 Vibration isolation system.

Eqn. (1.5) can be rewritten as

$$\ddot{x} + 2\zeta\omega_n(\dot{x} - \dot{y}) + \omega_n{}^2(x - y) = 0, \tag{1.6}$$

where ζ is the damping ratio, and ω_n is the angular natural frequency.

The displacement transmissibility T_d is the ratio of the displacement amplitude of object (X) to that of the base motion (Y), and is given by

$$T_d = \left|\frac{X}{Y}\right| = \left[\frac{1+(2\zeta r)^2}{(1-r^2)^2+(2\zeta r)^2}\right]^{1/2}, \tag{1.7}$$

where r is the frequency ratio [29].

The maximum displacement transmissibility occurs at a frequency ratio [29, 30]

$$r_m = \frac{\omega_m}{\omega_n} = \frac{1}{2\zeta}\sqrt{\left(\sqrt{1+8\zeta^2}-1\right)}, \tag{1.8}$$

where ω_m is the frequency at which there is maximum transmissibility.

Also at maximum transmissibility, the amplitude ratio (see Appendix A) is

$$\left|\frac{X}{Y}\right|_m = \left[\frac{8\zeta^4}{8\zeta^4-4\zeta^2+\sqrt{1+8\zeta^2}-1}\right]^{1/2}, \tag{1.9}$$

which is a function of the damping ratio only.

The system showed in Fig. 1.3 is for the case when vibration is transmitted from the foundation to the equipment. Another common type of vibration isolation is when the equipment itself generates the vibration and the isolation prevents the generated vibration to be transmitted to the foundation. Examples of machine generated vibrations are unbalanced forces in rotating machinery, impact forces in forging or stamping and vibration shakers [28, 29].

Vibration isolators are chosen so that the natural frequency of the system is much lower than the operating frequency of the equipment, therefore reducing the magnitude of

the force transmitted. For frequency ratios greater than $\sqrt{2}$, a smaller damping ratio leads to a smaller magnitude of transmitted vibration. Therefore, the damping ratio should be as small as possible. But some damping is required in the system because the machine has to go through resonance during start-up and stopping. In the case when the system is exposed several excitation frequencies and harmonics, it is not easy to isolate all those frequencies and it is better to use a high damping ratio [28, 29].

Damping is the dissipation of energy by the conversion of mechanical (vibration) energy into heat energy. Damping can be modeled as viscous damping, Coulomb damping (dry friction) or hysteretic damping. Viscous damping occurs when a system vibrates in a viscous medium such as oil or air and the resistance of the medium to the vibrating body causes the dissipation of energy. Viscous damping is proportional to the velocity of the vibrating body. Coulomb or sliding-friction damping happens due to the relative motion of surfaces. It is of constant amplitude and opposite to the direction of motion of the vibrating body. Hysteretic or material damping occurs within a material as it is deformed and the internal planes slide or slip losing energy by friction. The stress-strain diagram of material damping forms a hysteresis loop and the area of the loop is indicative of the amount of energy lost. [29, 31]

1.12 Elasto-Damping Materials

An elasto-damping material (EDM) is one that has a relatively small value of elastic modulus and therefore has relatively large deformations when subjected to small stresses. Because of this property, an EDM dissipates a lot of energy which is of hysteric nature when subjected to vibration. The use of an EDM as a vibration isolator has the

advantage of providing good damping not requiring additional dampers. Types of EDMs are elastomers and meshed fibrous materials [28].

1.12.1 Elastomers (Rubbers)

Elastomers have a small value of elastic modulus and some of them can be stretched to ten times their original length without failure. Because they can experience large deformations, rubbers dissipate a lot of energy. The properties of an elastomer can be tailored by blending a base elastomer with some additives allowing elastomers to be made in many shapes [28].

1.12.2 Wire-mesh Materials

Wire-mesh materials consist of relatively thick wires (0.1-0.6 mm diameter) which are interwoven, then rolled into small balls followed by compression to the desired shape. The amount of compression determines the stiffness and damping properties of the final product. Under a dynamic load, the wires slip against each other dissipating energy. The energy dissipation and the material stiffness are vibration-amplitude dependent. An increase in vibration amplitude leads to greater energy dissipation and a reduction in stiffness [28].

1.12.3 Felt

"Felt is a fabric produced by meshing natural or synthetic fibers by a combination of mechanical movements, chemical actions, and application of moisture and heat, but without using looms or knitting operation" [28]. The internal structure of felts is very similar to wire-mesh materials and therefore they exhibit similar dynamic characteristics.

1.13 Microfibrous Metallic Cloth

Microfibrous metallic cloth is made by intermingling and fusing micro metal fibers together. The preparation consists of making an aqueous suspension of the metal fibers and cellulose, which acts as a binding agent both in the liquid and dried state. Using a wet-lay papermaking technique the mixture is then cast into a preform sheet followed by drying to remove moisture. The dried sheet is sintered in a continuous hydrogen furnace at 1000 ^{o}C, which removes the cellulose and causes the metallic fibers to sinter-bond at their junctures. A felt-like cloth with a high void volume of more than 90% is obtained. The manufacturing process of microfibrous cloth can be tailored to produce varying surface areas, void volumes and pore sizes [32-34]. Damping is achieved in this type of material because of the sliding contact between the fibers as they are compressed causing dissipation of energy. Microfibrous materials are notably insensitive to temperature variations and have demonstrated resistance to harsh environments, including extreme temperature and humidity [35].

The high-speed papermaking process used in the manufacture of microfibrous materials is a low cost one compared to other traditional ways of making metal fibrous materials. This has made the microfibrous materials more affordable for use as filters. Also the wet-lay process permits the use of different fiber size in a single sheet. This gives rise to asymmetric porosity leading to better filtration as entrapment of finer particles is achieved [37].

The use of microfibrous cloth has been experimentally investigated for vibration isolation and noise attenuation. Layers of nickel microfibrous cloth were sandwiched between a fixture and a printed circuit board which was subjected to vibration. Effective

vibration damping was achieved. A similar set up was used for the acoustic tests except that a gyroscope was mounted on the printed circuit board. The effects of the noise on the gyroscope were considerably reduced [36, 38, 39]. Sintered fibrous metals have also been utilized in muffler designs of internal combustion engines and successful noise attenuation was achieved which was comparable to commercially available perforated duct silencers [40].

1.14 Dissertation Organization

In Chapter 2 the dynamics of a vibratory gyroscope are analyzed and the equations of motion have been derived. The model is then modified to include the effects of noise on the gyroscope and corresponding governing equations are developed.

In Chapter 3 the mitigation of the effects of noise on a MEMS gyroscope was investigated using a differential measurement system. Two types of noise signals are considered: pure tones and random noise.

Chapter 4 describes the mounting of gyroscopes on printed circuit boards. The gyroscopes are used to experimentally verify the model and the mitigation presented in Chapters 2 and 3, respectively.

Chapter 5 describes the fabrication of nickel microfibrous sheets. A wet-lay papermaking process is used to make a preform of nickel and cellulose fibers. The preform is then dried and sintered to give a highly porous microfibrous media

In Chapter 6 the airflow resistivity of nickel microfibrous materials (media) was experimentally determined. The Delany-Bazley model was then used to obtain the acoustical properties of the media using the airflow resistivity.

In Chapter 7 the damping characterization of nickel microfibrous materials was performed using the displacement transmissibility concept. A fixture was designed for attachment to the shaker head and to hold the material during testing.

In Chapter 8 nickel microfibrous enclosures were designed and fabricated by sintering together layers of the microfibrous material. Experiments were then done in a reverberation room to validate the effectiveness of the enclosures for noise attenuation.

CHAPTER 2

MATHEMATICAL MODEL FOR NOISE SIMULATION

In this chapter, the dynamics of a vibratory MEMS gyroscope are analyzed, and the equations of motion are derived. The model is then modified to include external noise affecting a gyroscope, and the corresponding governing equations are developed.

2.1 Dynamics of a Vibratory Gyroscope

A vibratory gyroscope (illustrated in Fig. 2.1) consists of a proof mass which is attached to the gyroscope frame by a suspension system with stiffness k_x in the drive direction x and k_y in the sense direction y. During operation, the proof mass is made to oscillate in the drive direction by a sinusoidal electrostatic drive force (F_D) generated by a pair of comb drive actuators, one on each side of the proof mass. When the gyroscope rotates about the out-of-plane axis at a rate $\boldsymbol{\Omega}$ rad/s, a sinusoidal orthogonal force, the Coriolis force, is induced in the sense direction. The sense motion is measured using capacitive sensors and is proportional to the rotation rate. The suspension system is such that the proof mass does not rotate with respect to the frame.

2.1.1 Equations of Motion

Lagrange's equations (Eqn. (2.1)) are used to derive the equations of motion for the vibratory gyroscope.

$$\frac{d}{dt}\left(\frac{\partial T}{\partial \dot{q}_j}\right) - \frac{\partial T}{\partial q_j} + \frac{\partial V}{\partial q_j} + \frac{\partial R}{\partial \dot{q}_j} = Q_j, \quad j = 1,2 \ldots, N, \tag{2.1}$$

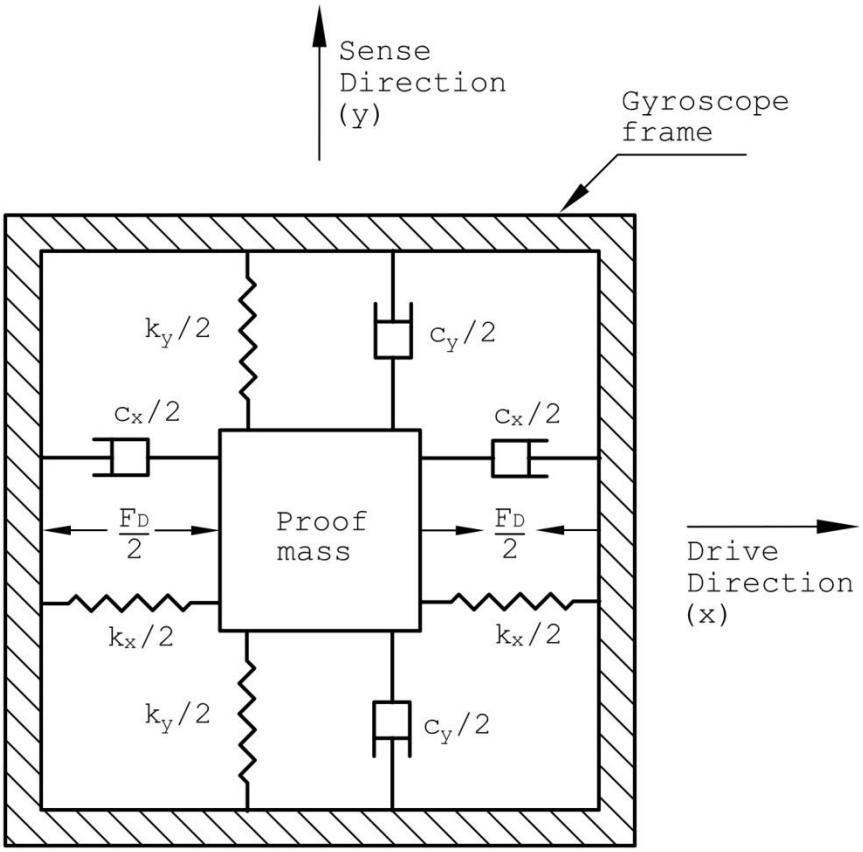

Figure 2.1 Schematic of a MEMS Gyroscope

where T is the kinetic energy, V is the potential energy, R is the Rayleigh dissipation function, Q_j are the generalized forces and q_j are the generalized coordinates.

Kinetic energy

The total kinetic energy is given by

$$T = \frac{1}{2}m(\bar{v}.\bar{v}) + \frac{1}{2}I\Omega^2, \tag{2.2}$$

where m is the mass, $\bar{v}$ is the velocity and I is the second moment of inertia of the proof mass.

The velocity of the proof mass is

$$\bar{v} = \dot{x}\hat{i} + \dot{y}\hat{j} + \Omega\hat{k} \times (x\hat{i} + y\hat{j})$$

$$= (\dot{x} - \Omega y)\hat{i} + (\dot{y} + \Omega x)\hat{j}. \tag{2.3}$$

Substituting the velocity in Eqn. (2.2) gives

$$T = \frac{1}{2}m\dot{x}^2 + \frac{1}{2}m\dot{y}^2 + \frac{1}{2}m\Omega^2(x^2 + y^2) - m\Omega\dot{x}y + m\Omega x\dot{y} + \frac{1}{2}I\Omega^2. \tag{2.4}$$

Potential Energy

The potential energy *V* of the gyroscope is given by

$$V = \frac{k_x}{2}(x)^2 + \frac{k_y}{2}(y)^2. \tag{2.5}$$

Rayleigh Dissipation Function

The Rayleigh dissipation function for the vibratory gyroscope is

$$R = \frac{1}{2}c_x(\dot{x})^2 + \frac{1}{2}c_y(\dot{y})^2. \tag{2.6}$$

Virtual work

The virtual work and the generalized forces are related by

$$\delta W = \sum_{j=1}^{N} Q_j \, \delta q_j \, . \tag{2.7}$$

Equations of motion

Applying the Lagrange equations for the generalized coordinate x gives

$$\frac{d}{dt}\left(\frac{\partial T}{\partial \dot{x}}\right) = \frac{d}{dt}(m\dot{x} - m\Omega y) = m\ddot{x} - m\Omega\dot{y}, \tag{2.8}$$

$$\frac{\partial T}{\partial x} = m\Omega^2 x + m\Omega\dot{y}, \tag{2.9}$$

$$\frac{\partial V}{\partial x} = k_x x, \tag{2.10}$$

$$\frac{\partial R}{\partial \dot{x}} = c_x\dot{x}, \tag{2.11}$$

and

$$Q_x = F_D \sin \omega t. \tag{2.12}$$

Therefore, the equation of motion in the *x*-direction is

$$m\ddot{x} + c_x\dot{x} + k_x x - 2m\Omega\dot{y} - m\Omega^2 x = F_D \sin \omega t \,. \tag{2.13}$$

Similarly the equation of motion for the sense motion was derived:

$$m\ddot{y} + c_y\dot{y} + k_y y + 2m\Omega\dot{x} - m\Omega^2 y = 0. \tag{2.14}$$

Dividing Eqns. (2.13) and (2.14) by *m* and rearranging give

$$\ddot{x} + \frac{c_x}{m}\dot{x} + \left(\frac{k_x}{m} - \Omega^2\right)x - 2\Omega\dot{y} = \frac{F_D}{m}\sin \omega t \,, \tag{2.15}$$

and

$$\ddot{y} + \frac{c_y}{m}\dot{y} + \left(\frac{k_y}{m} - \Omega^2\right)y + 2\Omega\dot{x} = 0. \tag{2.16}$$

The natural frequencies of the gyroscope are much greater than the rotation rate, and therefore, the $\Omega^2 x$ and $\Omega^2 y$ terms are negligible. Also the amplitude of the sense motion is small compared to that of the amplitude of the drive motion causing the Coriolis component $2\Omega\dot{y}$ to be negligible. To maximize sensitivity and response gain, the natural frequencies of the drive and sense modes are made equal, and resonance is used in both modes (by making drive force frequency equal to the natural frequency). Similar results have been obtained in previous studies where Newtonian Mechanics were used to derive the equations of motion [1].

The equations of motion can therefore be simplified to:

$$m\ddot{x} + c\dot{x} + kx = F_D \sin \omega_n t \,, \tag{2.17}$$

and

$$m\ddot{y} + c\dot{y} + ky + 2m\Omega\dot{x} = 0 \,. \tag{2.18}$$

The solutions (Appendix B) to the above Eqns. (2.17) and (2.18) are

$$x = \frac{F_D}{c\omega}\cos \omega_n t \,, \tag{2.19}$$

and

$$y = \frac{2m\Omega F_D}{c^2\omega_n}\sin\left(\omega_n t - \frac{\pi}{2}\right) = -\frac{2m\Omega F_D}{c^2\omega_n}\cos\omega_n t\,. \tag{2.20}$$

Eqn. (2.20) shows that the amplitude of the sense response is directly proportional to the rotation rate Ω. The phase angle between the two displacements is used to determine the direction of rotation. For a positive rotation rate (counterclockwise rotation), the displacements are out of phase, and for a clockwise rotation, the displacements are in phase. The mathematical model, represented by Eqns. (2.13) and (2.14), was integrated using the Matlab solver ODE45 (Appendix C), and comparison plots for counterclockwise and clockwise rotation were produced as shown in Figs. 2.2 and 2.3 respectively. Both of the natural frequencies of the gyroscope were designed to be 14 kHz (Appendix B), and the rotation rate was set at 1 rad/s.

The Matlab model was also used to show that the amplitude of the sense motion was directly proportional to the angular rate (Fig. 2.4). The effect of the frequency of the drive force on the sense response amplitude was then investigated (Fig. 2.5), and as expected, the displacement was found to be maximum when the drive force frequency was equal to the natural frequency of the system.

2.2 Gyroscope Model for Noise Simulation

To simulate the effects of noise on a gyroscope, the basic model of Fig. 2.1 was modified as shown in Fig. 2.6. The new model consists of two masses, the proof mass (m_p) and the mass of the gyroscope frame and packaging (m_f), each with two degrees of freedom so that the model is a four-degree-of-freedom system. Because the electrostatic drive force is generated by two pairs of comb drive actuators with half of each interdigitating comb attached to the proof mass and the other half attached to the frame, both masses are affected by the generated drive force but in opposite directions. The

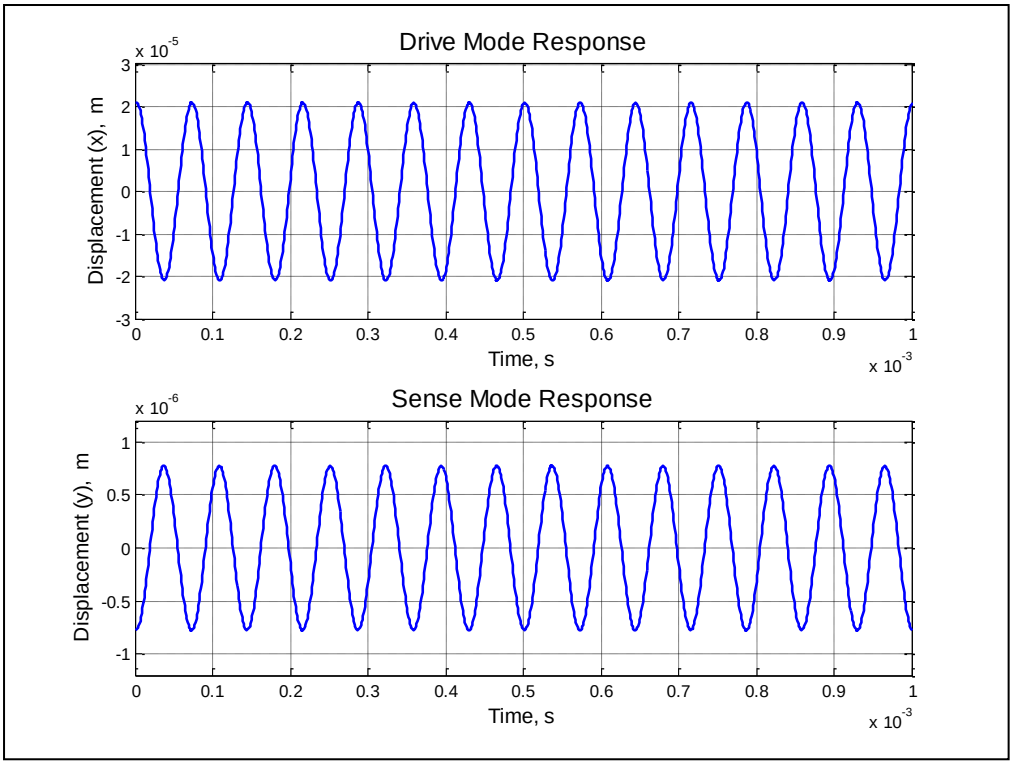

Figure 2.2 Counterclockwise rotation.

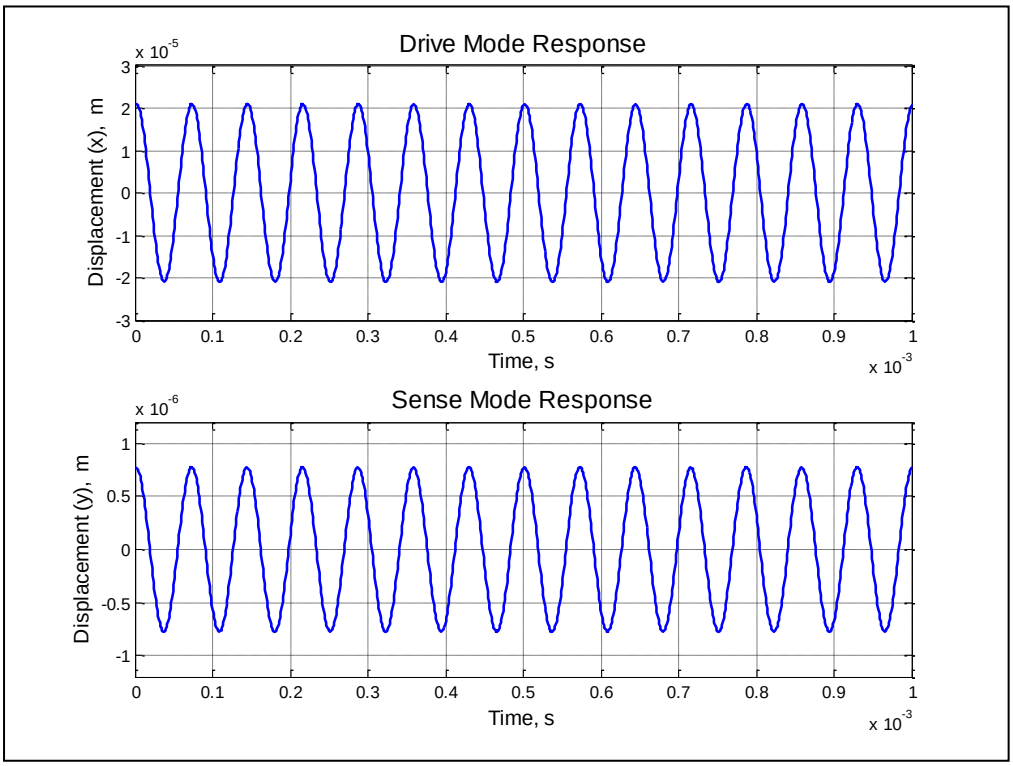

Figure 2.3 Clockwise rotation

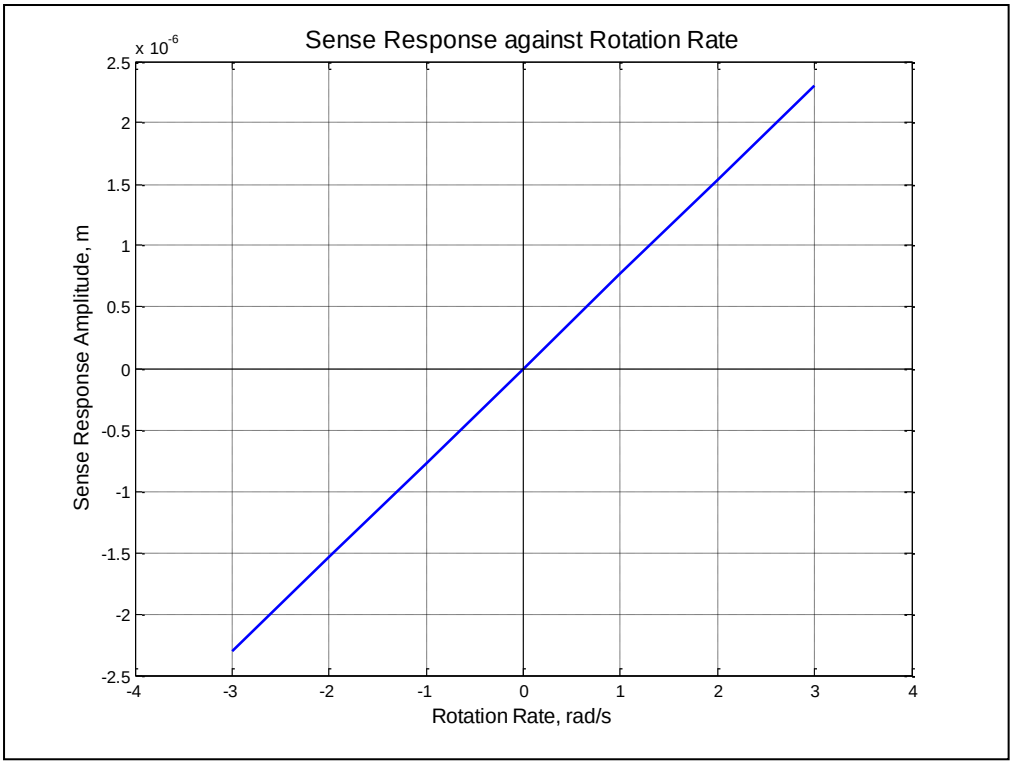

Figure 2.4 Relation between sense response and rotation rate.

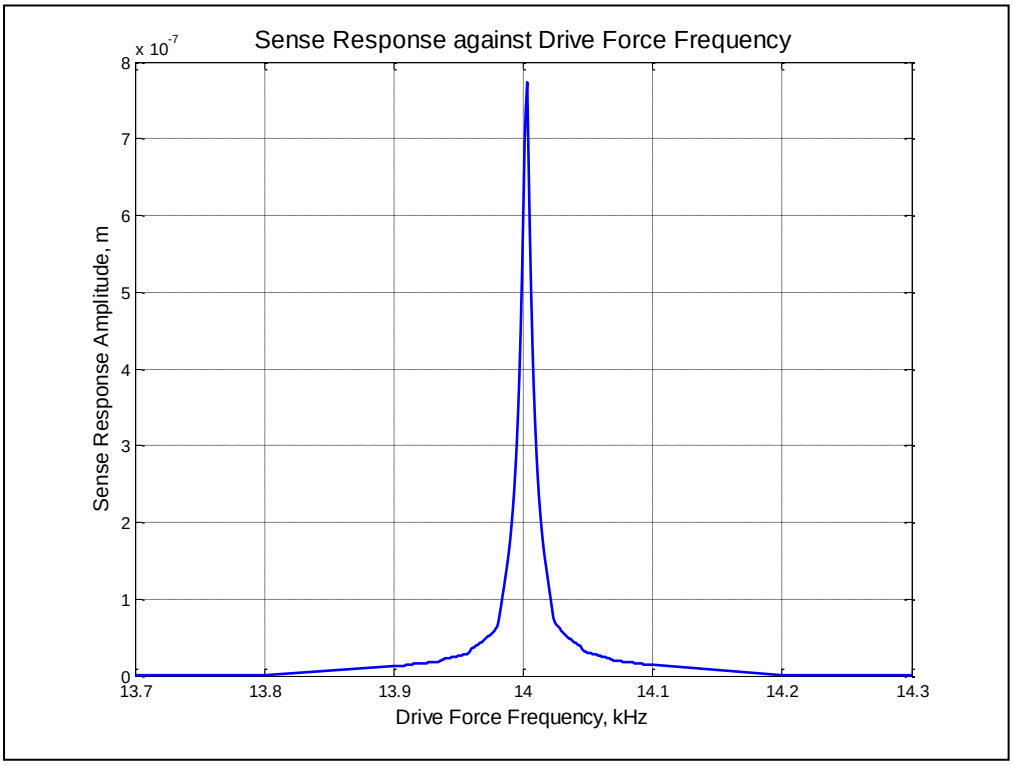

Figure 2.5 Effects of drive force frequency on sense response.

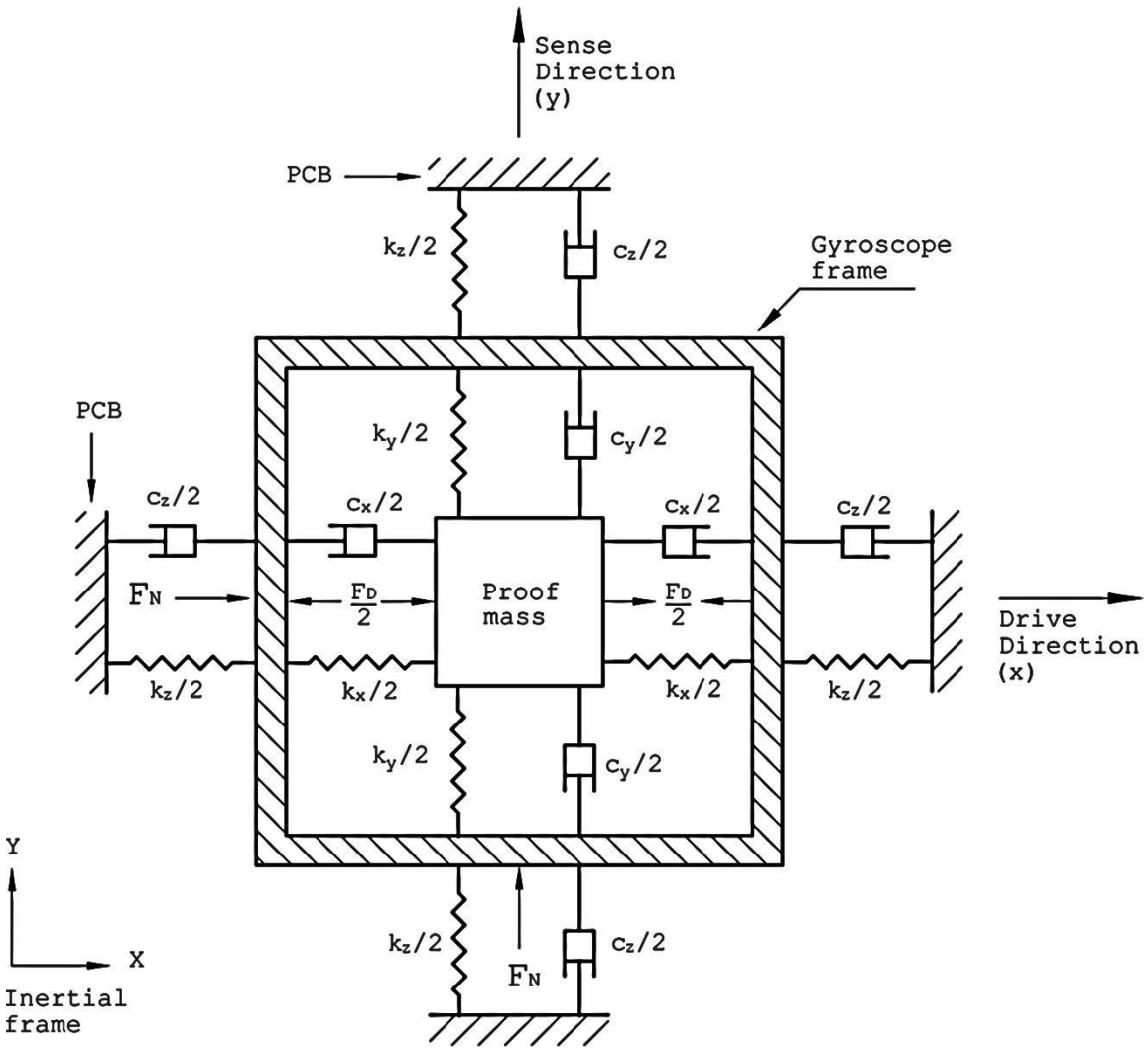

Figure 2.6 Gyroscope model with external noise.

damping and stiffness between the proof mass and the frame are the same as in the basic model. The suspension system is such that the proof mass does not rotate with respect to the frame.

The packaging of the gyroscope is fixed onto a printed circuit board (PCB) which rotates at a constant angular rate Ω. The stiffness and damping between the packaging and the PCB are k_z and c_z, respectively. For modeling purposes, the packaging is subjected to high levels of noise, F_N, as shown in Fig. 2.6.

2.2.1 Equations of motion

The displacements and velocities of the proof mass and the gyroscope frame with reference to the inertial frame are summarized in Table 2.1.

	Mass	Displacement in *x* direction	Displacement in *y* direction	Velocity in *x* direction	Velocity in *y* direction
Gyro frame	m_f	x_f	y_f	$\dot{x}_f$	$\dot{y}_f$
Proof mass	m_p	x_p	y_p	$\dot{x}_p$	$\dot{y}_p$

Table 2.1 Displacements and velocities of the proof mass and the gyroscope frame.

Lagrange's equations were used to derive the equations of motion.

Kinetic energy

The total kinetic energy T is given by

$$T = T_F + T_P, \tag{2.21}$$

where T_F and T_P are the kinetic energy of the frame and the proof mass respectively.

$$T_F = \frac{1}{2} m_f \left(\bar{v}_f . \bar{v}_f\right) + \frac{1}{2} I_f \Omega^2 , \tag{2.22}$$

and

$$T_p = \frac{1}{2} m_p \left(\bar{v}_p . \bar{v}_p\right) + \frac{1}{2} I_p \Omega^2 , \tag{2.23}$$

where I_f and I_p are the second moments of inertia of the frame and the proof mass respectively.

The velocity of the frame is

$$\begin{aligned} \bar{v}_f = & \ \dot{x}_f \hat{i} + \dot{y}_f \hat{j} + \Omega \hat{k} \times (x_f \hat{i} + y_f \hat{j}) \\ = & \ (\dot{x}_f - \Omega y_f)\hat{i} + (\dot{y}_f + \Omega x_f)\hat{j} . \end{aligned} \tag{2.24}$$

The velocity of the proof mass is

$$\bar{v}_p = \dot{x}_p\hat{i} + \dot{y}_p\hat{j} + \Omega\hat{k} \times (x_p\hat{i} + y_p\hat{j})$$

$$= (\dot{x}_p - \Omega y_p)\hat{i} + (\dot{y}_p + \Omega x_p)\hat{j}\,. \qquad (2.25)$$

Substituting Eqn. (2.24) in Eqn. (2.22) gives

$$T_F = \frac{1}{2}m_f\,\dot{x}_f{}^2 + \frac{1}{2}m_f\,\dot{y}_f{}^2 + \frac{1}{2}m_f\,\Omega^2\left(x_f{}^2 + y_f{}^2\right) - m_f\,\Omega\dot{x}_f y_f + m_f\,\Omega x_f\dot{y}_f + \frac{1}{2}I_f\Omega^2. \quad (2.26)$$

Substituting Eqn. (2.25) in Eqn. (2.23) gives

$$T_P = \frac{1}{2}m_p\,\dot{x}_p{}^2 + \frac{1}{2}m_p\,\dot{y}_p{}^2 + \frac{1}{2}m_p\,\Omega^2\left(x_p{}^2 + y_p{}^2\right) - m_p\,\Omega\dot{x}_p y_p + m_p\,\Omega x_p\dot{y}_p + \frac{1}{2}I_p\Omega^2. \quad (2.27)$$

Therefore the total kinetic energy is

$$T = \frac{1}{2}m_f\,\dot{x}_f{}^2 + \frac{1}{2}m_f\,\dot{y}_f{}^2 + \frac{1}{2}m_f\,\Omega^2\left(x_f{}^2 + y_f{}^2\right) - m_f\,\Omega\dot{x}_f y_f + m_f\,\Omega x_f\dot{y}_f + \frac{1}{2}I_f\Omega^2 +$$

$$\frac{1}{2}m_p\,\dot{x}_p{}^2 + \frac{1}{2}m_p\,\dot{y}_p{}^2 + \frac{1}{2}m_p\,\Omega^2\left(x_p{}^2 + y_p{}^2\right) - m_f\,\Omega\dot{x}_p y_p + m_p\,\Omega x_p\dot{y}_p + \frac{1}{2}I_p\Omega^2. \qquad (2.28)$$

Potential Energy

The total potential energy for the gyroscope is

$$V = \frac{k_x}{2}\left(x_p - x_f\right)^2 + \frac{k_y}{2}\left(y_p - y_f\right)^2 + \frac{k_z}{2}\left(x_f\right)^2 + \frac{k_z}{2}\left(y_f\right)^2. \qquad (2.29)$$

Rayleigh Dissipation Function

The total Rayleigh dissipation function for the gyroscope is

$$R = \frac{1}{2}c_z\dot{x}_f{}^2 + \frac{1}{2}c_x\left(\dot{x}_p - \dot{x}_f\right)^2 + \frac{1}{2}c_z\dot{y}_f{}^2 + \frac{1}{2}c_y\left(\dot{y}_p - \dot{y}_f\right)^2. \qquad (2.30)$$

Virtual work

To obtain the generalized forces, the virtual work δW was determined.

$$\delta W = (F_N \sin\omega t - F_D \sin\omega_n t)\delta x_f + F_D \sin\omega_n t\,\delta x_p + F_N \sin\omega t\,\delta y_f\,. \qquad (2.31)$$

The virtual work and generalized forces are related by

$$\delta W = \sum_{j=1}^{4} Q_j\,\delta q_j\,. \qquad (2.32)$$

Equations of motion

For the generalized coordinate x_f,

$$\frac{d}{dt}\left(\frac{\partial T}{\partial \dot{x}_f}\right) = \frac{d}{dt}\left(m_f\dot{x}_f - m_f\omega y_f\right) = m_f\ddot{x}_f - m_f\Omega\dot{y}_f\ , \tag{2.33}$$

$$\frac{\partial T}{\partial x_f} = m_f\Omega^2 x_f + m_f\Omega\dot{y}_f\ , \tag{2.34}$$

$$\frac{\partial V}{\partial x_f} = k_x\left(x_f - x_p\right) + k_z x_f\ , \tag{2.35}$$

$$\frac{\partial R}{\partial \dot{x}_f} = c_x\left(\dot{x}_f - \dot{x}_p\right) + c_z\dot{x}_f\ , \tag{2.36}$$

and

$$Q_{x_f} = F_N \sin\omega t - F_D \sin\omega_n t. \tag{2.37}$$

Therefore, the equation of motion for the generalized coordinate x_f is

$$m_f\ddot{x}_f + c_x\left(\dot{x}_f - \dot{x}_p\right) + c_z\dot{x}_f + k_x\left(x_f - x_p\right) + k_z x_f - 2m_f\Omega\dot{y}_f - m_f\Omega^2 x_f = F_N \sin\omega t - F_D \sin\omega_n t. \tag{2.38}$$

Similarly the equations of motion for the other three generalized coordinates x_p, y_f and y_p are obtained as:

$$m_p\ddot{x}_p + c_x\left(\dot{x}_p - \dot{x}_f\right) + k_x\left(x_p - x_f\right) - 2m_p\Omega\dot{y}_p - m_p\Omega^2 x_p = F_D \sin\omega_n t\ , \tag{2.39}$$

$$m_f\ddot{y}_f + c_y\left(\dot{y}_f - \dot{y}_p\right) + c_z\dot{y}_f + k_y\left(y_f - y_p\right) + k_z y_f + 2m_f\Omega\dot{x}_f - m_f\Omega^2 y_f = F_N \sin\omega t\ , \tag{2.40}$$

and

$$m_p\ddot{y}_p + c_y\left(\dot{y}_p - \dot{y}_f\right) + k_y\left(y_p - y_f\right) + 2m_p\Omega\dot{x}_p - m_p\Omega^2 y_p = 0\ . \tag{2.41}$$

2.2.2 Model Simulation

The four equations were integrated using Matlab solver ODE45 (Appendix C). To simulate the model, the following parameters were considered:

1. Stiffness, $k_x = k_y = 77.38$ N/m.

2. Damping, $c_x = c_y = 5 \times 10^{-7}$ Ns/m.
3. Stiffness, $k_z = 200$ N/m.
4. Damping, $c_z = 5 \times 10^{-3}$ Ns/m.
5. Proof mass, $m_p = 1 \times 10^{-8}$ kg.
6. Mass of frame and packaging, $m_f = 3.8 \times 10^{-4}$ kg.
7. Drive force amplitude, $F_D = 1 \times 10^{-6}$ N.
8. Noise amplitude, $F_N = 1.26 \times 10^{-3}$ N.

The computed natural frequencies using the above parameters (Appendix B) were 14,001 Hz, 14,000 Hz, 115.3 Hz and 115.62 Hz.

The first simulation was carried out to show the effects of the frequency of the external noise on the gyroscope output. The rotation rate was set at 1 rad/s, the frequency of the drive force was fixed at the natural frequency of the proof mass, 14, 000 Hz, and the frequency of the noise varied from 13,000 Hz to 15,000 Hz. As expected, it was observed that the output was maximum when the frequency of the noise was equal to the natural frequency of the gyroscope (Fig. 2.7). Also, when the frequency of the noise did not coincide with the natural frequency, no effects on the output of the gyroscope were observed.

The effects of the amplitude of the noise on the gyroscope's output were then investigated. To maximize the effects of the noise, its frequency was kept constant at the natural frequency of the gyroscope. The rotation rate was also kept constant at 1 rad/s and the noise level amplitude was varied from 0 to 126 dB. For simulation purposes, the noise level was approximated to a force as shown in Appendix B. The simulation results (Fig. 2.8) showed a linear increase in sense response with an increase in noise amplitude.

The model was then run at different rotation rates in the presence of external noise having fixed amplitude and frequency. The rotation rate was varied from -3 to +3 rad/s in

steps of 1 rad/s. The simulation results (dashed line) were plotted in Fig. 2.9. It was observed that at zero rotation rate the gyroscope had a positive amplitude but a zero output amplitude at a rotation rate of – 0.92 rad/s. The sense response amplitude also increased with increasing rotation rates. To explain these observations, the model was run at the same rotation rates but without external noise, that is F_N = 0, and the results were compared in Fig. 2.9. The comparison showed that the presence of the noise caused an upward shift in the sense response amplitude. Also the shift was greater when the rotation was negative. This was due to the Coriolis component (Refer to Eqn. (2.41).) which caused an increase in amplitude when the rotation was negative and a decrease in amplitude when the rotation rate was positive. It was therefore concluded that the effects of the noise were superimposed on the normal gyroscope's output.

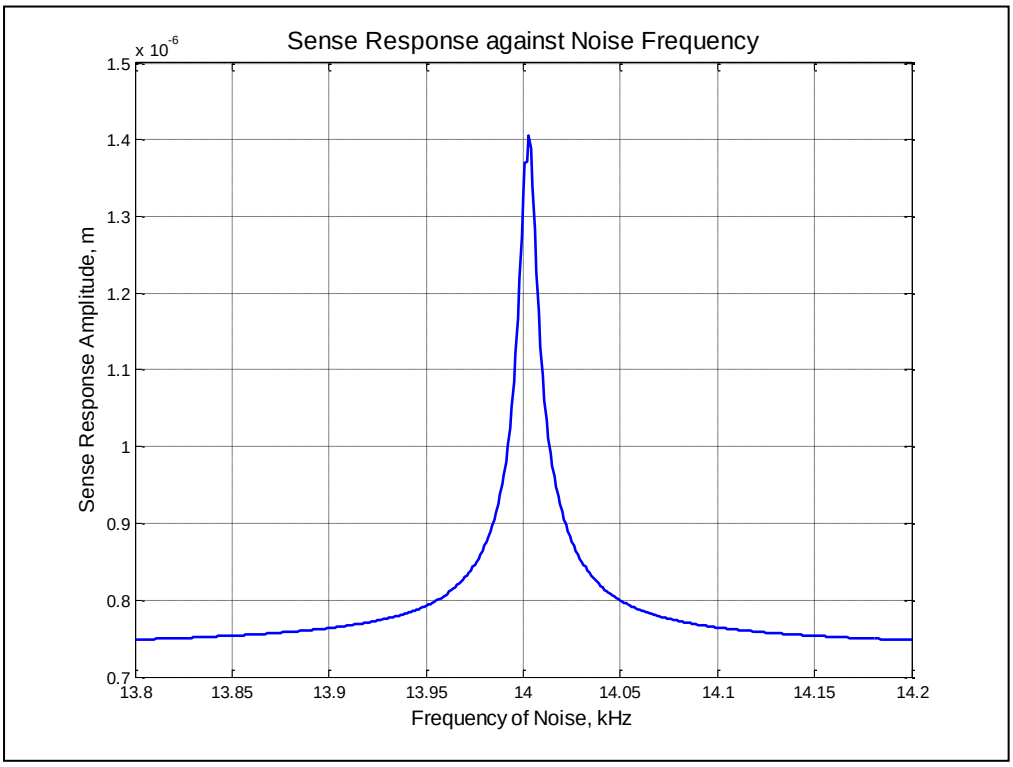

Figure 2.7 Effects of noise frequency on sense response.

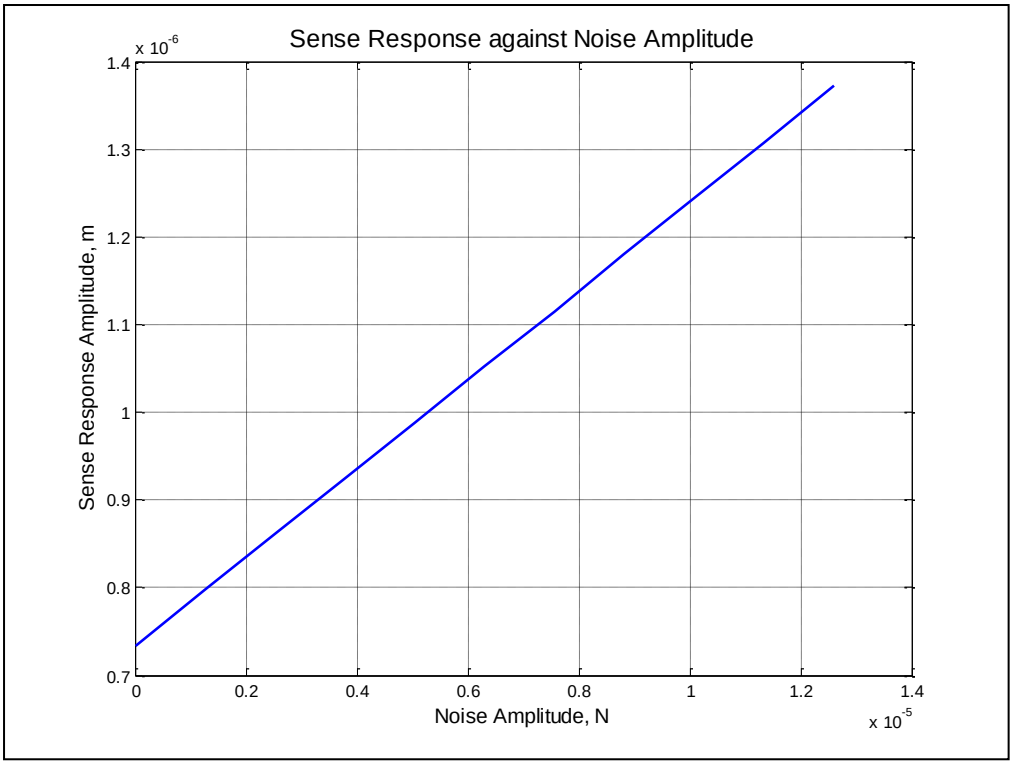

Figure 2.8 Effects of noise amplitude on sense response.

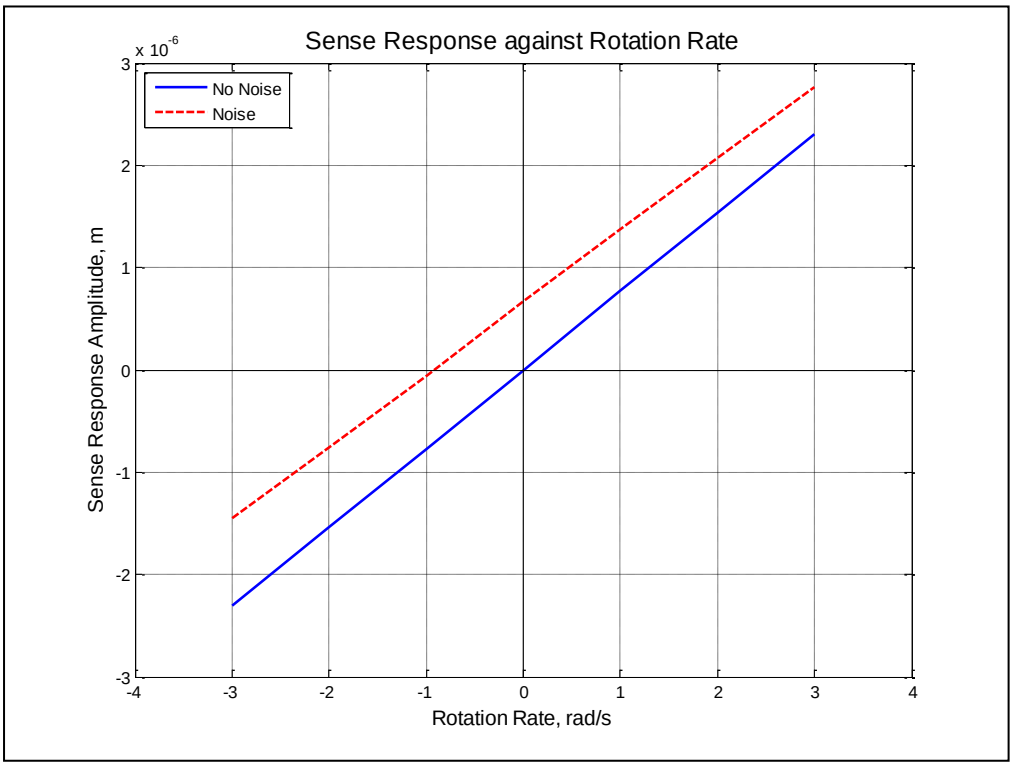

Figure 2.9 Effects of noise on sense response at different rotation rates.

CHAPTER 3

MITIGATION OF THE EFFECTS OF NOISE

In this chapter the effects of noise on a MEMS gyroscope are quantified and a differential-measurement system is used to mitigate the effects of the noise. Two types of noise signals are considered: a pure tone and random noise.

3.1 The Mitigation Procedure

The simulation of the MEMS gyroscope model (section 2.2.2) showed that in the presence of an external noise signal, the output of the gyroscope was augmented by almost a constant value. It was concluded that the effects of the noise were superimposed on the normal gyroscope's output.

In order to measure the superimposed effects of noise, a non-driven gyroscope was used as shown in Fig. 3.1. Being affected by the external noise signal only, its output is assumed to be equal to the superimposed effects of noise that needed to be determined.

Therefore, if the superimposed effects of noise can be quantified, a differential-measurement system can be proposed to consist of a pair of similar gyroscopes to mitigate the effects of the noise. In this system, the first gyroscope (Gyro 1) will be a normal gyroscope affected by noise, and the second gyroscope (Gyro 2) will measure the effects of noise only (no drive force). Subtracting the output of Gyro 2 from the output of Gyro 1 will give an uncorrupted output.

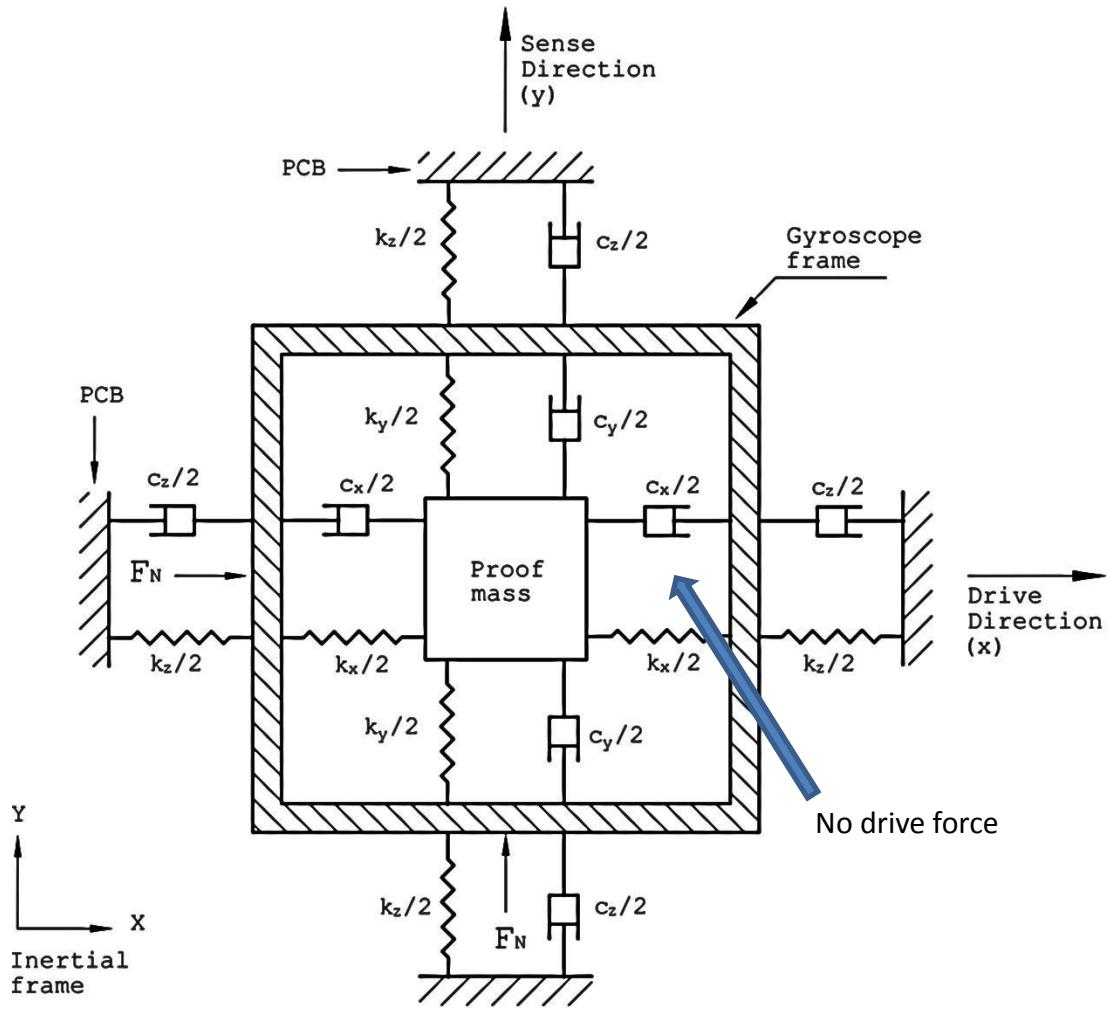

Figure 3.1 Gyroscope model without drive force F_D.

3.2 Quantifying the Effects of an External Noise Signal

The approach used to show that the superposition of the effects of an external noise signal on the normal output of a gyroscope could be quantified was to simulate Gyro 1 in the presence of the noise signal and in the absence of the noise signal. Then the difference between the two measured outputs of Gyro 1 can be compared to the output of Gyro 2 in the presence of the same noise signal.

3.2.1 Pure Tone Case

A pure tone was first considered as the external noise signal. Since the simulations of section 2.2.2 used a pure tone of constant amplitude as the noise signal, the results were used in this section and are reproduced in Fig. 3.2 as *'Gyro 1 + noise'* and *'Gyro 1 without noise'*. The difference between the outputs is represented by a nearly horizontal line showing that the effects of the pure tone caused the amplitude of the gyroscope to be augmented by almost a constant amplitude. The model of section 2.2.2 was then simulated as Gyro 2 by making F_D equal to zero. The same noise signal was used, and the results are plotted in Fig. 3.2. It is observed that the output of Gyro 2 is exactly the same as the difference between the outputs of Gyro 1, implying that the effects of the noise signal have been quantified.

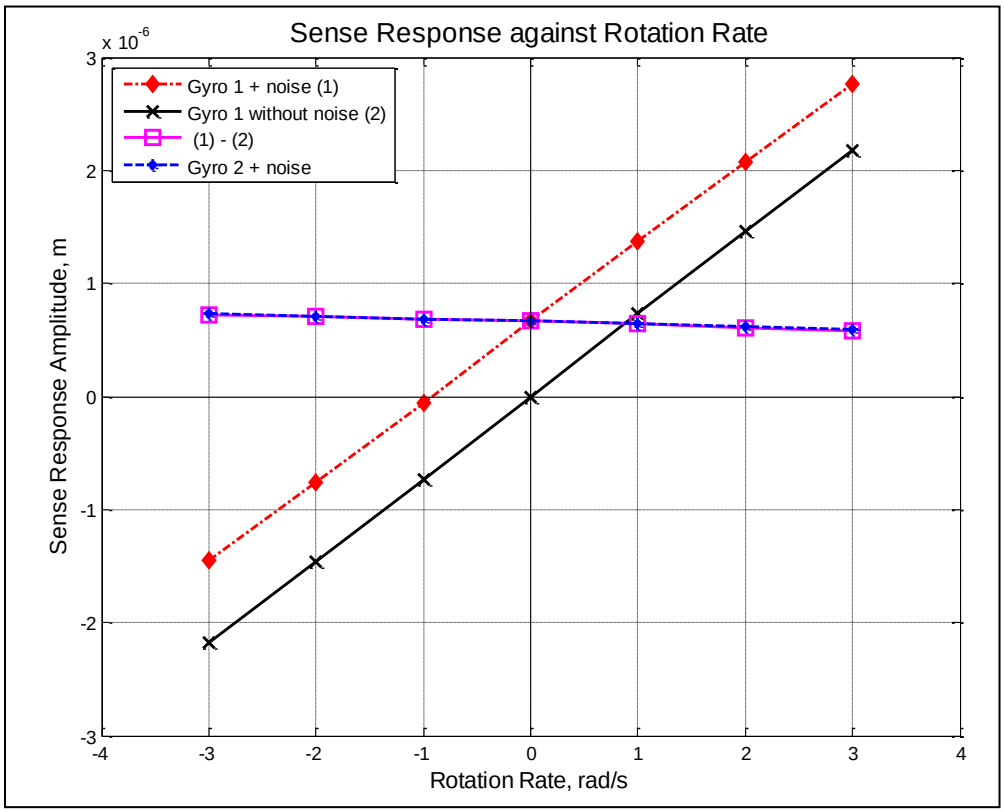

Figure 3.2 Difference between Gyro 1 outputs compared to the output of Gyro 2.

3.2.2 Random Noise Case

Since real life situations consist mostly of random noise, another set of simulations was performed using a random noise signal. Since the latter could be generated in 'Simulink', a graphical modeling tool in Matlab, the governing equations of the gyroscope were modeled using the software shown in Fig. 3.3. Basic modeling blocks such as addition, integration and gain were used along with the two specific blocks, band-limited white noise block and peak-notch filter. The band-limited white noise block generates normally distributed random numbers at a specific sample rate which is related to the correlation time of the noise. Based on the bandwidth of the system, the correlation time t_c is given by

$$t_c \approx \frac{1}{100} \times \frac{2\pi}{f_{max}} \ , \tag{3.1}$$

where f_{max} is the bandwidth of the system in rad/sec [44].

Since the natural frequency of the gyroscope's model was designed to be 14 kHz, the bandwidth was set at 20 kHz, and therefore t_c was set at 5 x 10^{-7} s. Also because the output component at the natural frequency of the gyroscope was needed, a peak filter was used for filtering out all the remaining frequency components affecting the gyroscope's output and was implemented in the Simulink model by the peak-notch filter block.

Using the same parameters as in section 2.2.2, the Simulink model was simulated, and the results are plotted in Figs. 3.11 and 3.12 for the unfiltered and filtered gyroscope outputs, respectively. As expected the unfiltered signal is noisy showing the random nature of the noise signal. The filtered signal on the other hand is smooth showing that successful filtration was achieved.

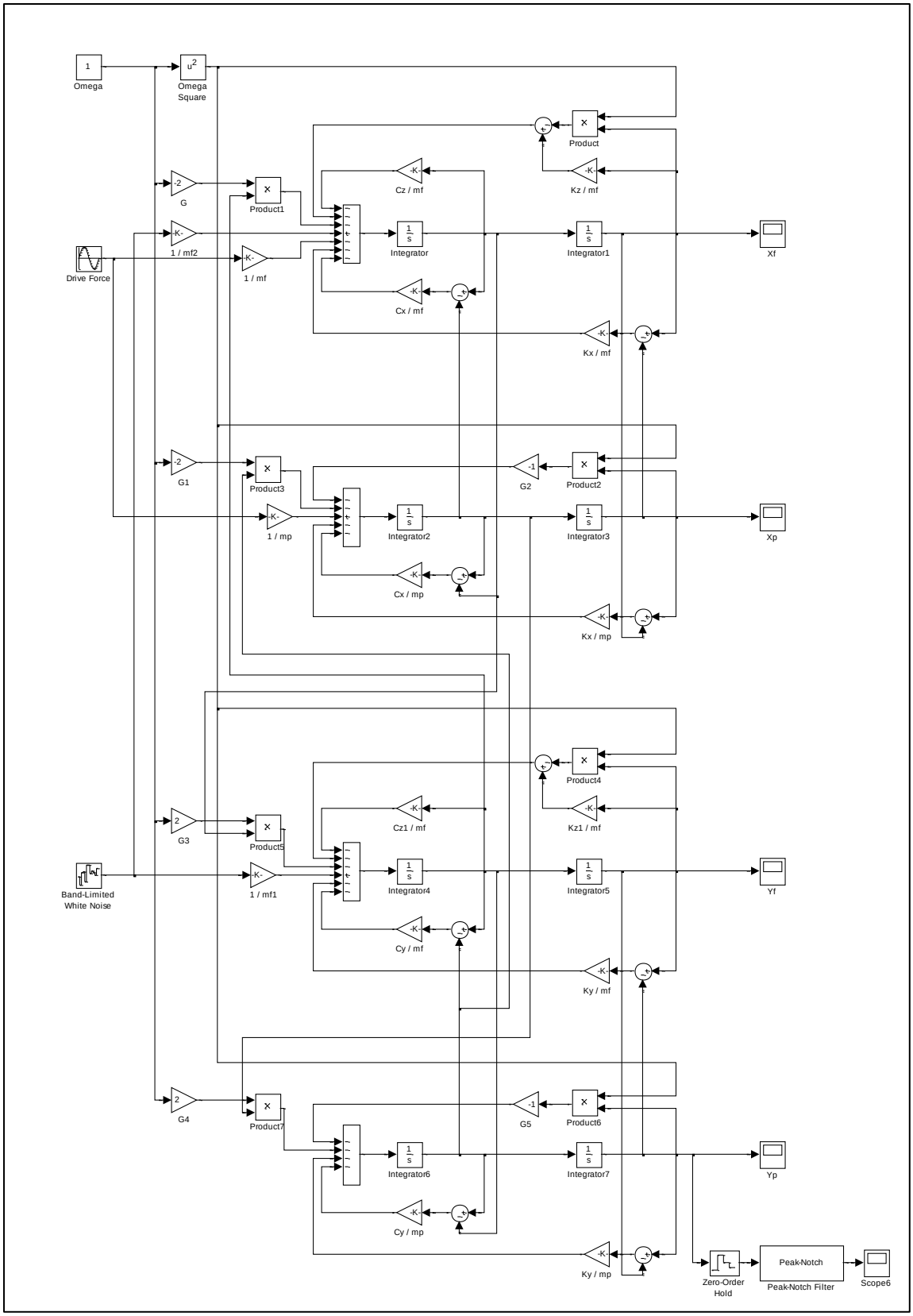

Figure 3.3 Simulink model of gyroscope.

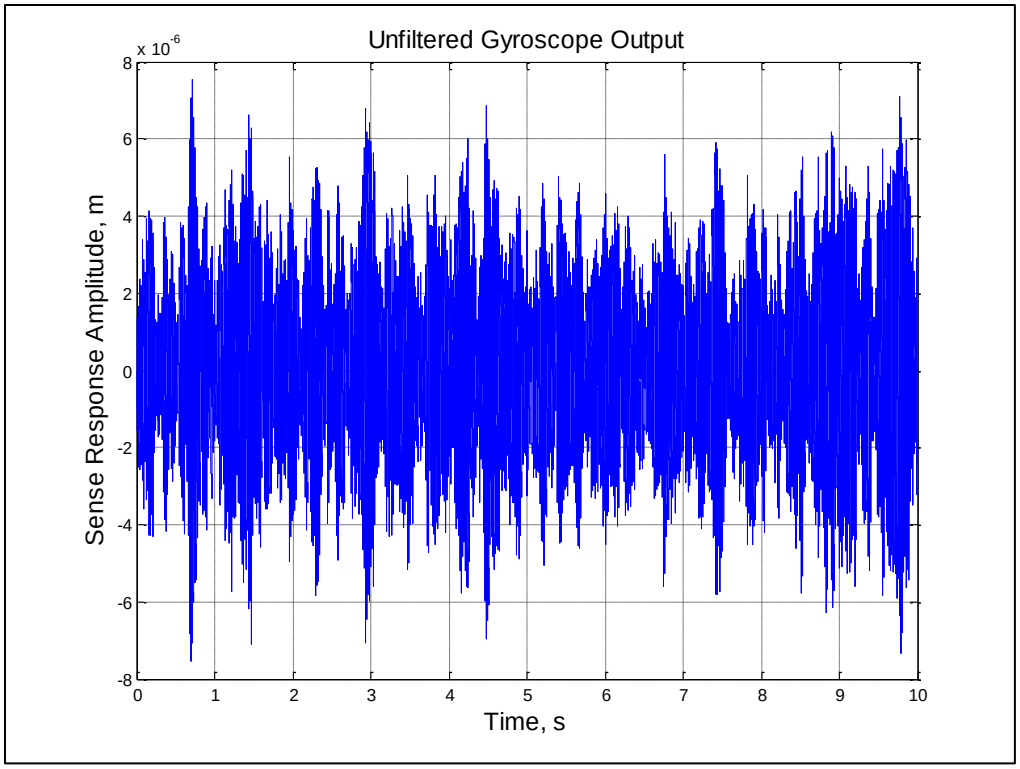

Figure 3.4 Unfiltered output of gyroscope in presence of a random noise signal.

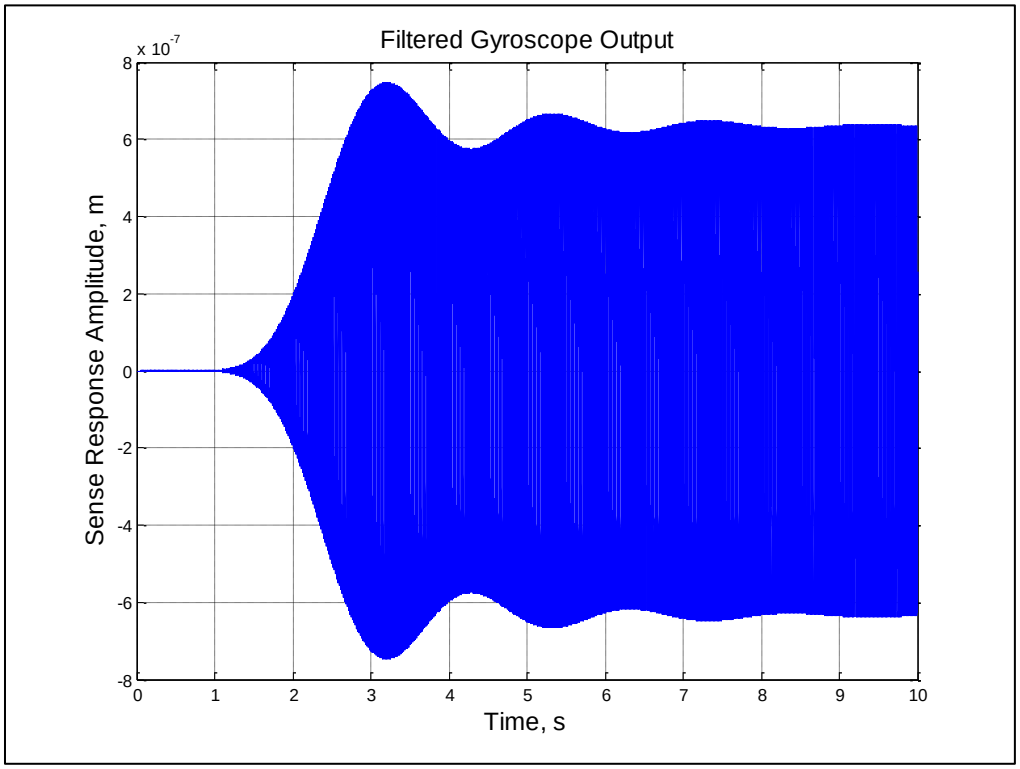

Figure 3.5 Filtered output of gyroscope in presence of a random noise signal.

For the pure tone case, Gyro 1 and Gyro 2 were run independently, since the noise signal could be reproduced. But in the case of a random noise signal, for the gyroscopes to be affected by the same noise signal, it should be applied to both gyroscopes simultaneously. Therefore for quantifying the effects of noise, a new Simulink model was made (Fig. 3.6) consisting of three subsystems: Gyro 1 affected by a random noise signal, Gyro 1 not affected by the noise signal and Gyro 2 (no drive force) affected by the same noise signal as Gyro 1. Each of the subsystems had the same internal structure as that of the gyroscope of Fig. 3.3. The model was also designed to take the difference between the outputs of Gyro 1 subsystems (to determine the superimposed effects of noise on the gyroscope output), and compare it to the output of Gyro 2.

The model was simulated, and the results, the difference between the outputs of Gyro 1 subsystems and the output of Gyro 2, are shown in Figs. 3.7 and 3.8, respectively. The data of both figures are exactly the same from which it was concluded that Gyro 2 was able to measure the superimposed effects of noise due to a random noise signal on Gyro 1.

3.3 Conclusions

The model simulations described in this Chapter have shown that Gyro 2 is able to quantify the superimposed effects of a pure tone and random noise signals on Gyro 1. Therefore a differential-measurement system consisting of two gyroscopes, Gyro 1 and Gyro 2, can be used to provide an uncorrupted output of a gyroscope in the presence of noise signal by subtracting the output of Gyro 2 from the output of Gyro 1.

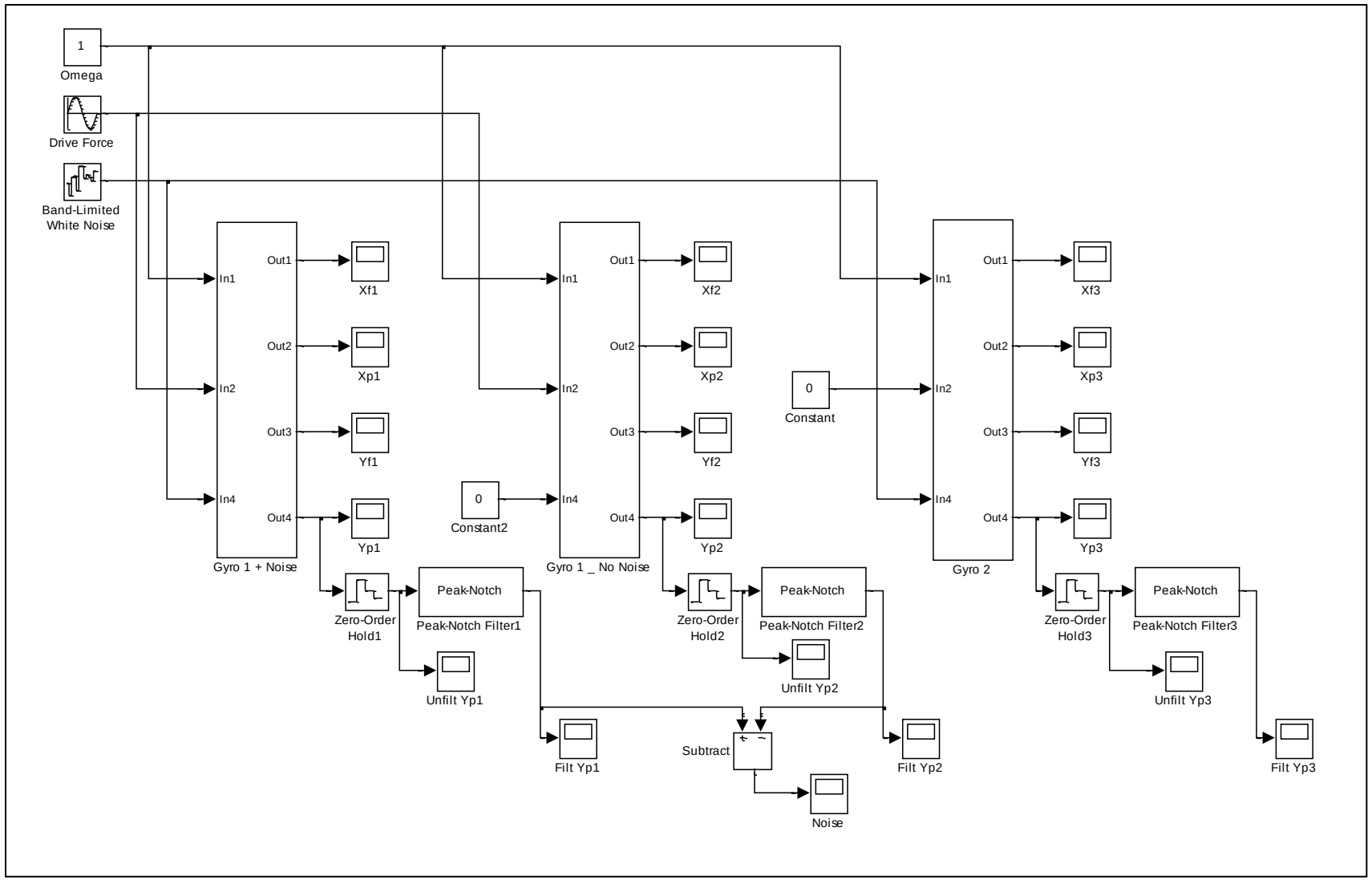

Figure 3.6 Simulink model of three subsystems.

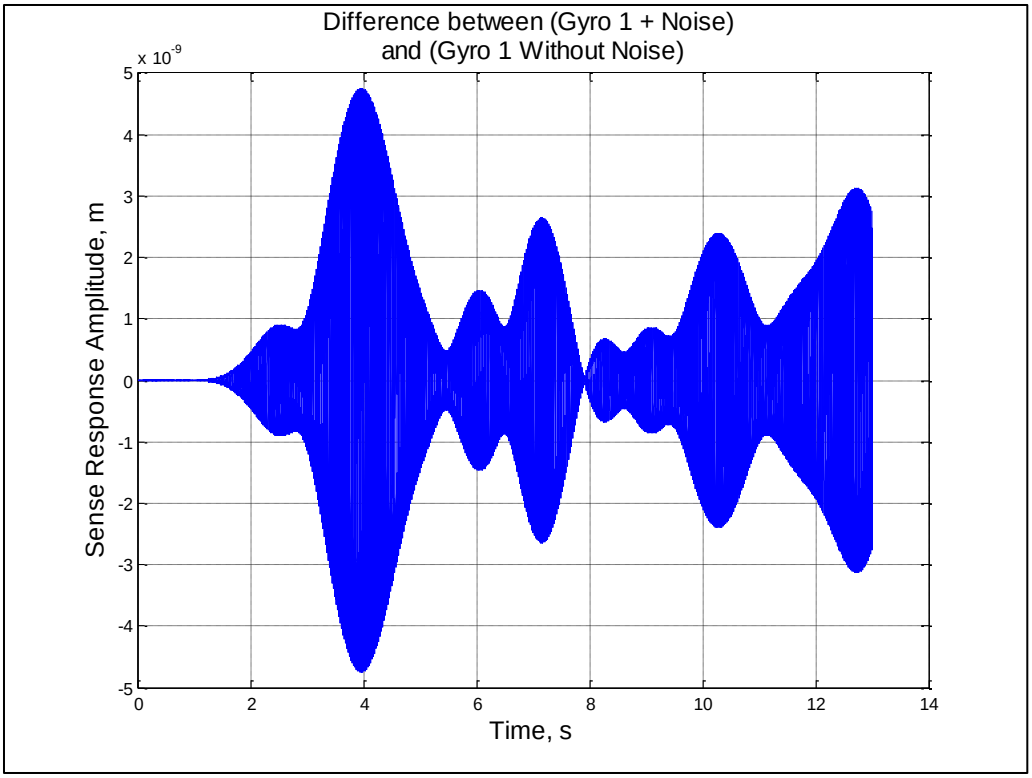

Figure 3.7 Difference between the outputs of Gyro 1 subsystems.

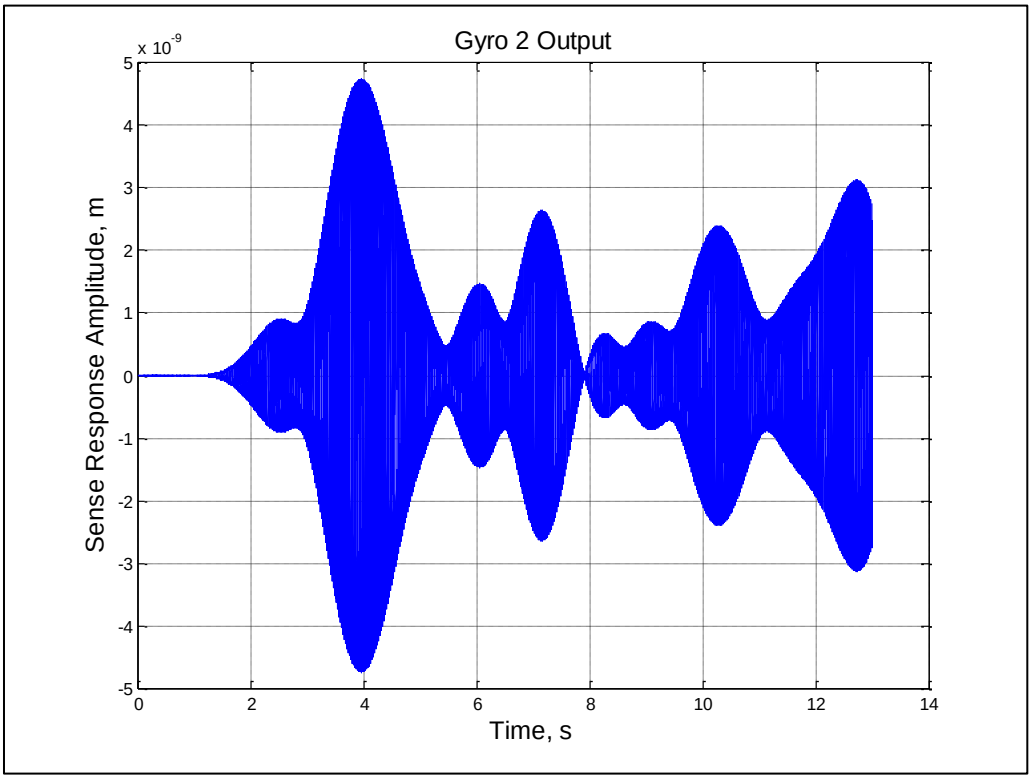

Figure 3.8 Output of Gyro 2.

CHAPTER 4

EXPERIMENTAL VERIFICATION OF GYROSCOPE MODEL AND MITIGATION OF THE EFFECTS OF NOISE

In this chapter the assembly of gyroscopes on printed circuit boards is described. The gyroscopes are used to experimentally verify the model and the mitigation solutions presented in Chapters 2 and 3, respectively.

4.1 Gyroscope Assembly

The MEMS gyroscope selected for the experimental verification was an automotive grade one from Analog Devices, model ADXRS652. For it to be functional it had to be mounted on a printed circuit board (PCB) so that the unit could be supplied with power and the output signal could be read.

4.1.1 ADXRS652 Gyroscope

The ADXRS652 gyroscope comes as ball grid array (BGA) chip-scale package with dimensions 7 mm x 7 mm x 3 mm and produces an output voltage which is proportional to the angular rate about the Z-axis, which is perpendicular to the top surface of the package. The sensor as well as all the required electronics are integrated on a single chip. Seven external capacitors are required for the operation of the gyroscope as illustrated in Fig. 4.1. The typical natural frequency and measurement range of the gyroscope are 14.5 kHz and ± 300 ^{o}/sec respectively [41].

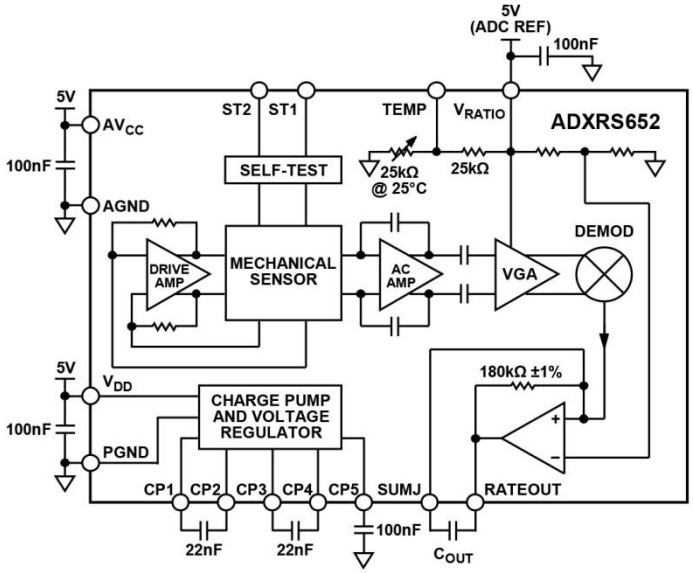

Figure 4.1 ADXRS652 Functional Block Diagram [41].

Being a vibratory gyroscope, the proof mass is driven into resonance electrostatically yielding the velocity required to produce a Coriolis force, which is sensed by a capacitive pickoff structure, during rotation. The voltage required to drive the proof mass is 18 to 20 V. Since 5 V is normally available in most applications, a charge pump is built in the chip which requires two external capacitors for operation. The gyroscope is designed to reject external vibration. Experiments performed by the manufacturer using a sinusoidal vibration (with amplitude 100 $m.s^{-2}$) from 100 Hz to 3000 Hz showed little effect on the gyroscope output [41]. The frequency range used in the experiments was much below the natural frequency of the sensor.

4.1.2 PCB Design

A PCB was designed to mount the gyroscope and the capacitors using Surface Mount Technology (SMT). FreePcb which is a free software for designing circuit boards was used. Fig. 4.2 shows the software interface along with the design which consists of the gyroscope land patterns at the center, all the wiring land patterns on the right, and

those for the capacitors around the board at a distance of 13 mm from the gyroscope. The space between the gyroscope and the capacitors was provided so as to fit in an acoustical enclosure made of nickel microfibrous material (the second approach of this dissertation to mitigate the effects of noise on a MEMS gyroscope).

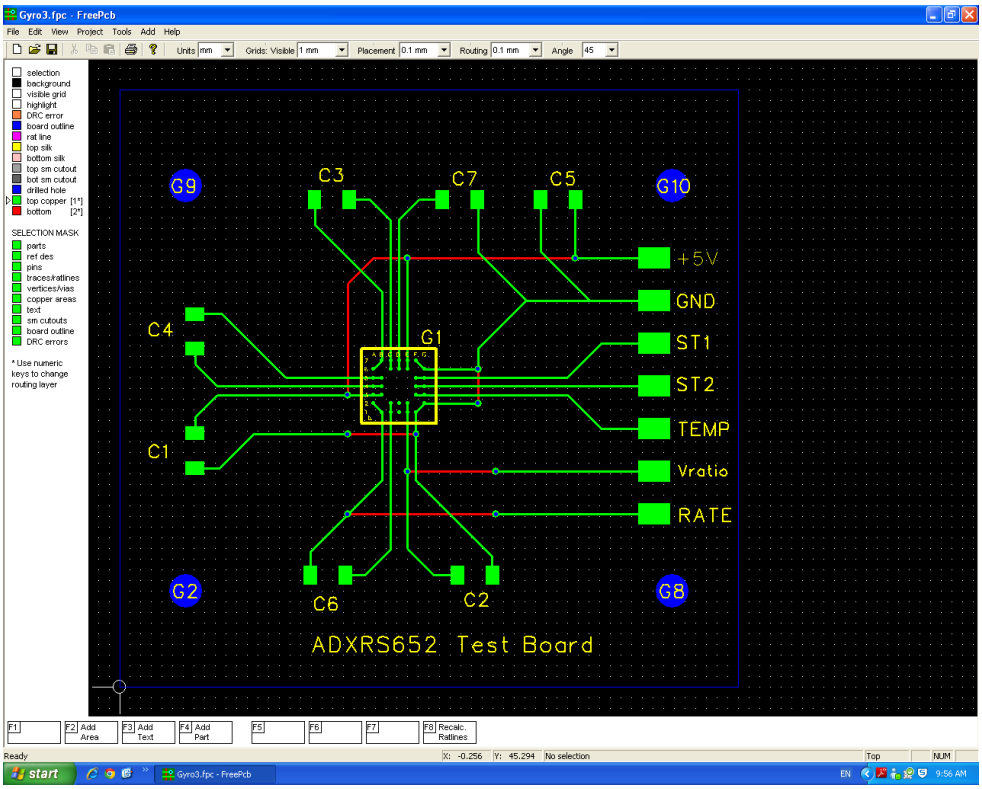

Figure 4.2 FreePcb interface showing the designed PCB.

The landing pattern geometry is a very important factor in SMT. The proper geometry promotes self-alignment of components during the reflow-solder process and provides good soldering of the component. Therefore specific design guidelines were used to determine the landing pattern size and spacing [42]. For the ceramic capacitors which had dimensions 1.6 mm x 3.2 mm, the landing pattern consisted of two pads 1.8 mm x 1.27 mm with 2 mm separation between the pads. The landing pattern of the gyroscope was governed by its BGA arrangement. Design rules were also followed for

the proper conductor routing [43]. Two layers of copper were needed for the conductor network and the layers were connected by through-hole vias.

After designing the PCB, the software (FreePcb) was used to generate Computer Aided Manufacturing (CAM) files that are needed for the manufacturing of the PCBs. Six files were generated; top copper, top mask, top silk, bottom copper, bottom mask and drill file. Those files are also known as "Gerber" files and can only be viewed using a "Gerber" viewer. Fig. 4.3 illustrates some of the "Gerber" files. The fabrication of the board was contracted out to a commercial PCB manufacturer, "Advance Circuits".

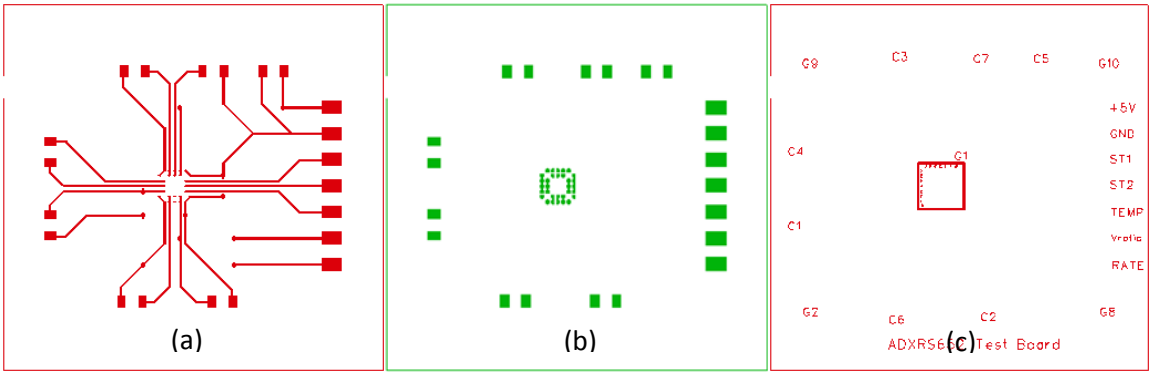

Figure 4.3 Gerber files: (a) Top copper, (b) Top mask, and (c) Top silk.

4.1.3 Surface Mounting of Capacitors and Gyroscopes

Ten gyroscopes were mounted on boards. The first step was to populate the boards with capacitors. This was done by first applying a small quantity of solder paste on each capacitor landing pad by using a pneumatic syringe and then carefully placing the capacitors on their respective pads. A tray was used to hold all the ten boards which were passed through a reflow oven in one go as shown in Fig. 4.4.

Then the gyroscopes were mounted one at a time on the boards. Flux was applied to the array of landing pads so as to facilitate the placement of the gyroscope on the board

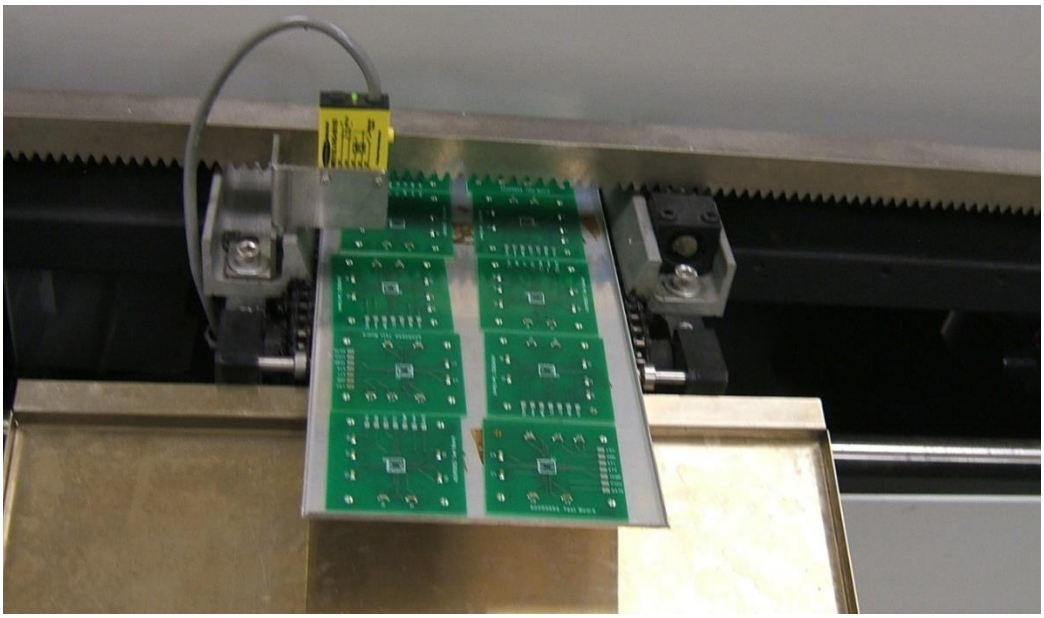

Figure 4.4 Picture of boards coming out of the oven with mounted capacitors.

and for good soldering. No additional solder material was applied onto those pads. A flip chip bonder with a split alignment system was used to carefully align the gyroscopes to the landing pads. Fig. 4.5(a) illustrates the alignment. Once a good position was obtained the gyroscope was carefully lowered into place. Before the reflow process, an x-ray (Fig. 4.5(b)) was done to confirm the positioning of the gyroscope.

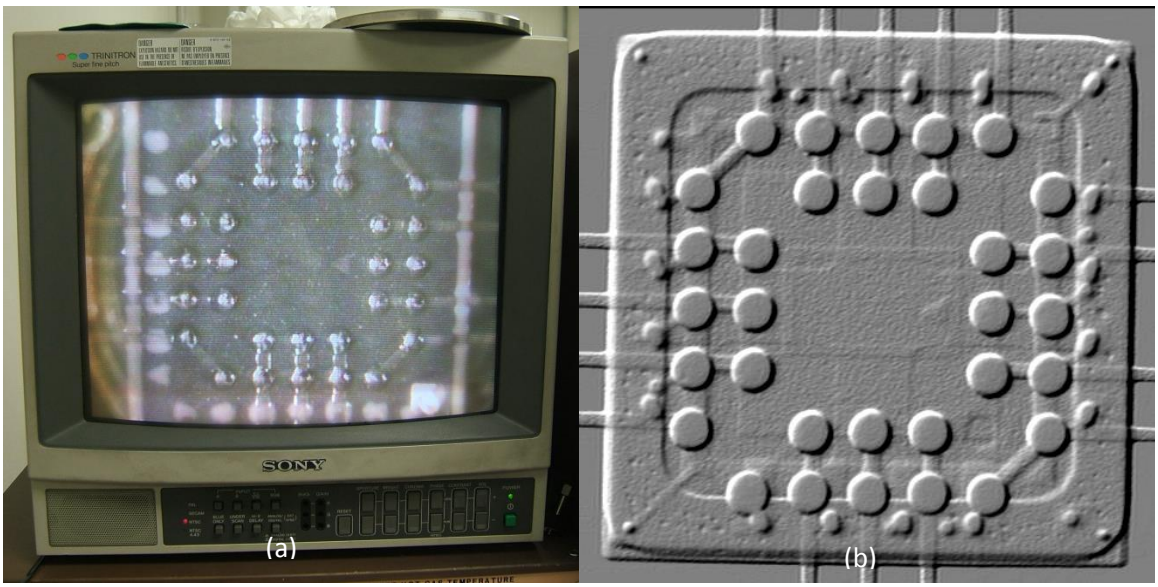

Figure 4.5 (a) Alignment using flip-chip bonder, and (b) X-ray of alignment.

The PCB was then sent through the reflow oven to solder the gyroscope onto the board. Another x-ray of the mounted gyroscope was taken to check the correctness of the soldering process. During the reflow process, based on the design of the PCB, self-alignment of the gyroscope should have taken place but the second x-ray revealed that it did not happen. Further investigations revealed that the mask layer overlapped slightly on the pads preventing the perfect alignment. Since no contacts were made between adjacent balls and all balls were soldered to their respective pads, the alignment obtained was considered as satisfactory. Wires were then manually soldered to the boards using a heating iron and the boards were tested using a power supply, Agilent E3631A, and an oscilloscope, Agilent DSO1004A. The testing is illustrated in Fig. 4.6 where 5 V is supplied to the gyroscope and the oscilloscope displays the output signal.

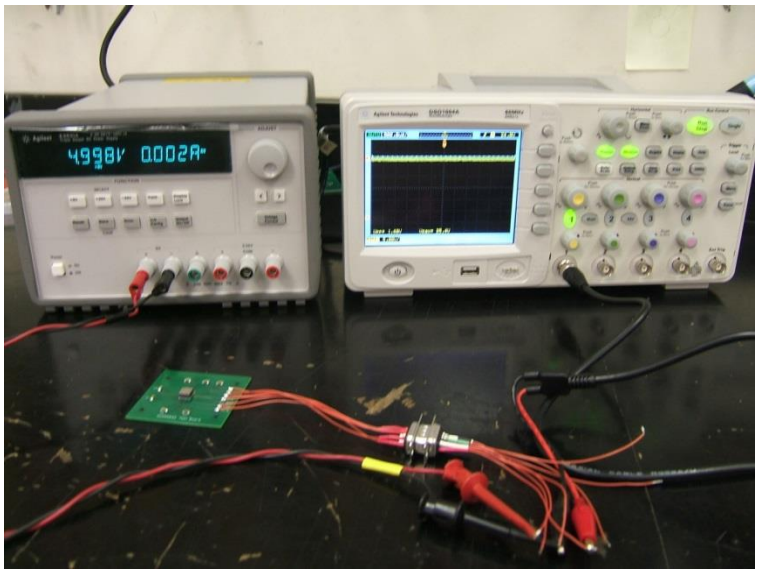

Figure 4.6 Testing of gyroscope after assembly.

4.2 Experimental Verification

Five gyroscopes, labeled G1-G5, were used for verifying the superposition of the effects of noise and therefore the mitigation of these effects.

4.2.1 Equipment Setup

The setup used for the experimental tests on the gyroscopes consisted of four main parts: the sound generation system, the rate table system, the acquisition of the gyroscopes' output and the measurement of the sound pressure level. The setup is illustrated in Fig. 4.7.

A software package, NCH Tone Generator, was used to generate sound source types such as a pure tone, a tone sweep and random noise. A converter (model TX-AFC 1 M) was used to change the connector type from the computer output connector to the amplifier (model Crown XTi 1000) connector. The sound was amplified and fed to the two speakers, model VHF100.

The top surface of the rate table, model Aerotech ADR 160-MA-RTAS-HM, was used to mount the gyroscopes. A controller, model Aerotech A3200, was used to control the rate table and a computer software was used to communicate with the controller. The latter precisely controlled the rotation rate and direction of the rate table.

A power supply was used to provide power to the gyroscopes. A total of five gyroscopes could be tested at a time and a data acquisition box, model TEXAS BNC 2110, was used to collect the gyroscopes' output. A Labview program was used to read and display all measured data.

A quarter inch free-field microphone, model Bruel and Kjaer (B&K) Type 4939, was placed near the gyroscopes to measure the sound pressure level. A B & K system, the PULSE LabShop, was used to acquire and display the microphone's output.

The rate table as well as the speakers were in a reverberation room while the data acquisition systems and computers were outside the room (Figs. 4.8 and 4.9).

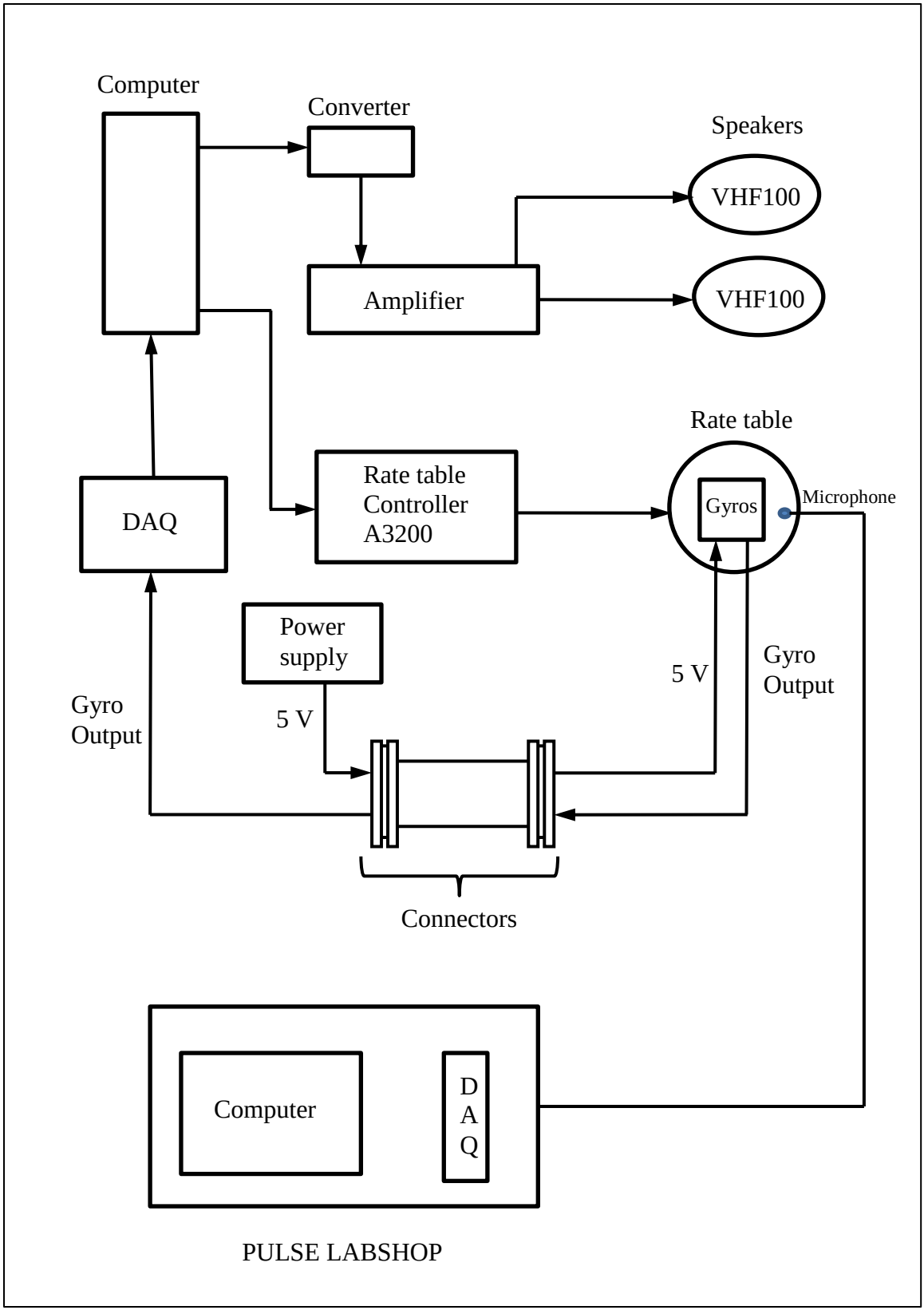

Figure 4.7 Schematic of rate table and acoustical test setup.

Figure 4.8 Picture of rate table and speakers.

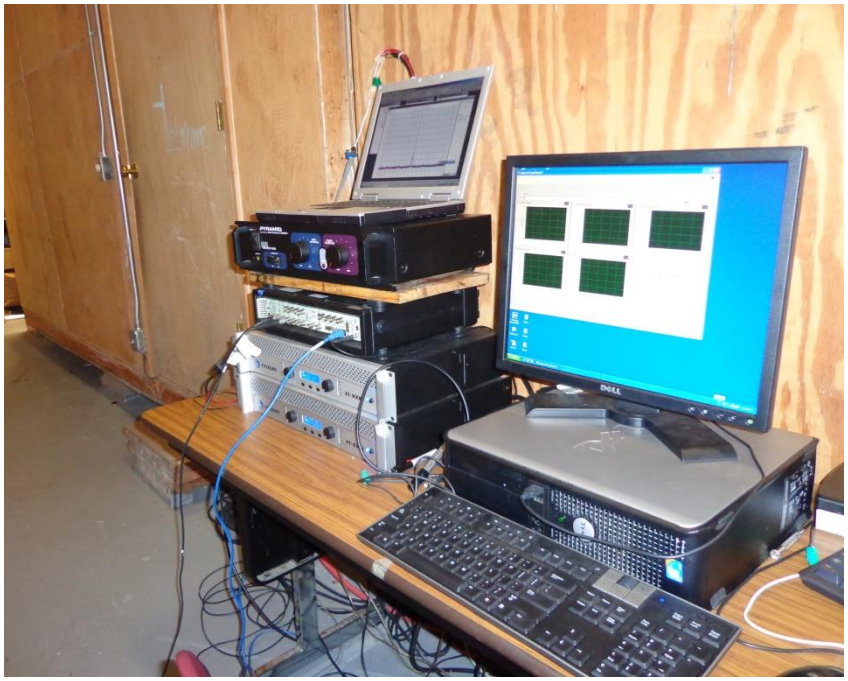

Figure 4.9 Picture of control and data acquisition systems.

4.2.2 Testing

The testing procedure consisted of running the gyroscopes at different rotation rates in the presence and the absence of a noise field. Then the superimposed effects of noise on the gyroscope's output was determined by taking the difference of the measured outputs in the presence and the absence of the noise field. Since the maximum effects of the noise field is experienced when the noise frequency is equal to the natural frequency of the gyroscope, a pure tone at the natural frequency of the gyroscope was used as the noise field.

The first step was to find the natural frequency of the gyroscope which was determined by sweeping a pure tone from 13000 to 16000 Hz. The output of gyroscope G1 is shown in Fig. 4.10, where the big change in the output slightly above 15 kHz indicates the natural frequency. The sweep was repeated few more times with a smaller bandwidth to narrow down the exact natural frequency, which was 15031 Hz.

Gyroscope G1 was then run at different rotation rates (without any noise field) from -30 deg/s to +30 deg/s in steps of 10 deg/s and the gyroscope output amplitude recorded. A pure tone at 15301 Hz was generated at the maximum power of the amplifier which gave a recorded sound pressure level of 115 dB (Fig. 4.11). The gyroscope was run in the presence of the noise field at the same rotation rates and the maximum output amplitude recorded. The plot of the gyroscope's outputs is shown in Fig. 4.12 and the difference between the outputs is shown as the near horizontal line.

The same procedures were repeated for gyroscopes G2-G5. Table 4.1 summarizes the natural frequencies and the recorded sound pressure levels for the gyroscopes and Figs. 4.13-4.16 illustrate the results.

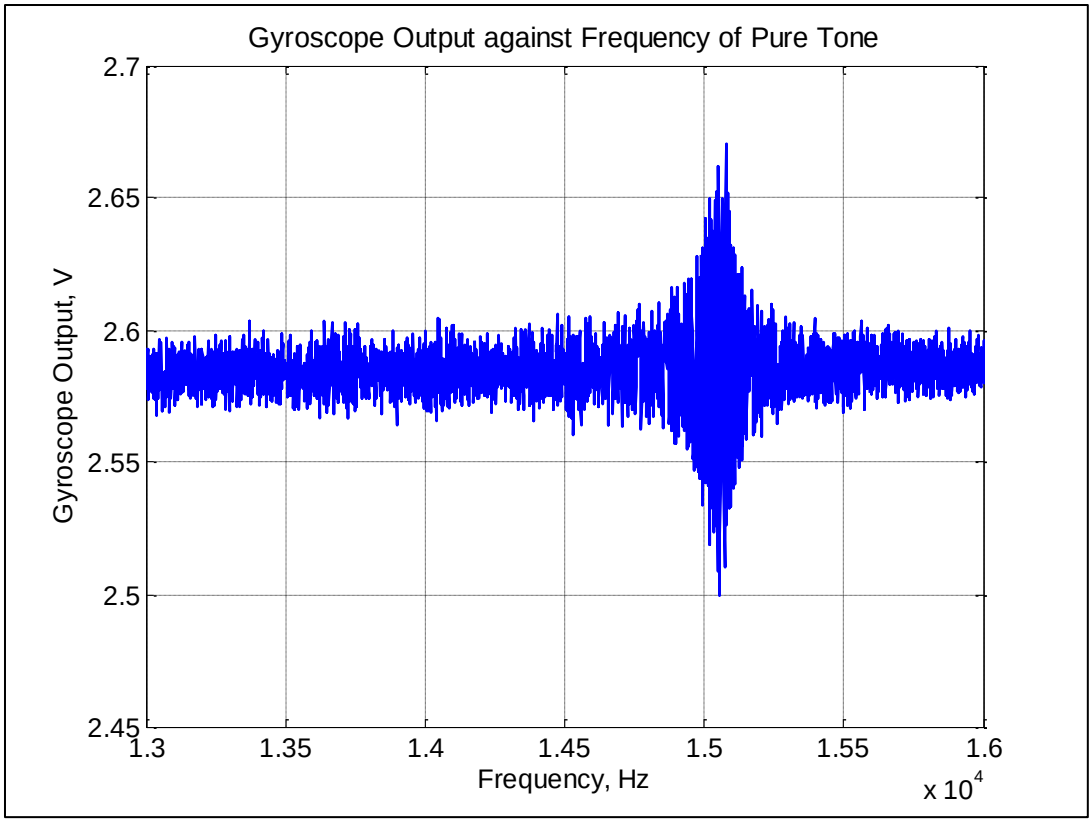

Figure 4.10 Finding the natural frequency of gyroscope G1.

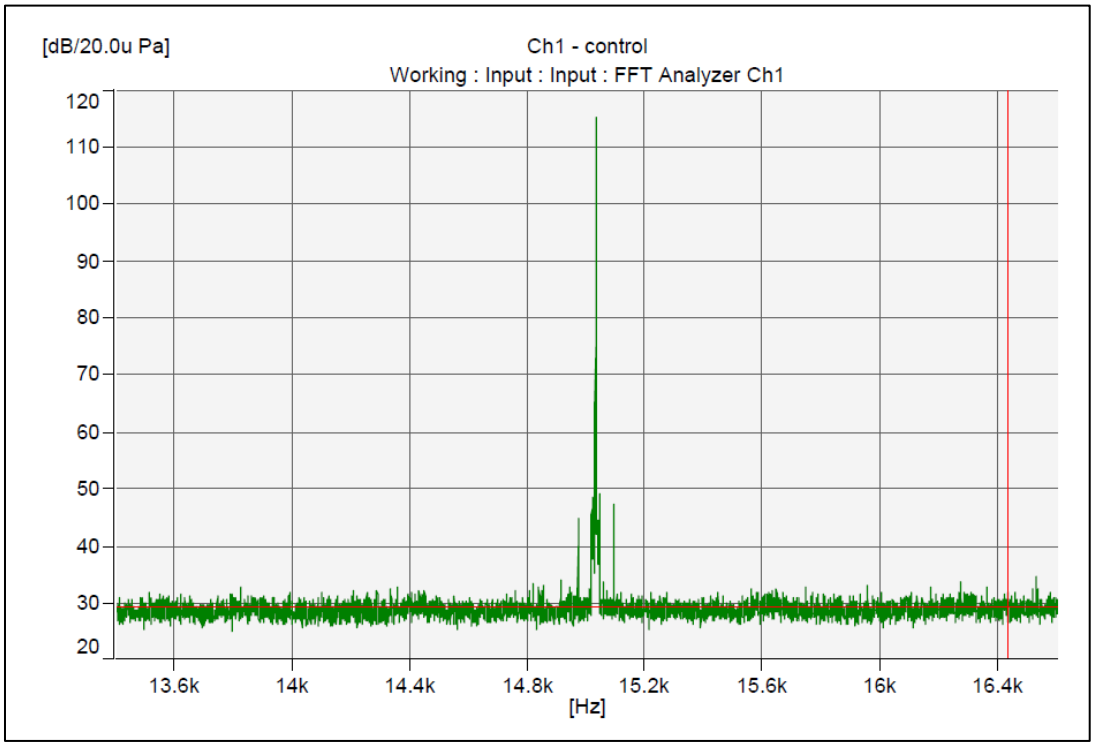

Figure 4.11 Amplitude of pure tone at the natural frequency of Gyroscope G1.

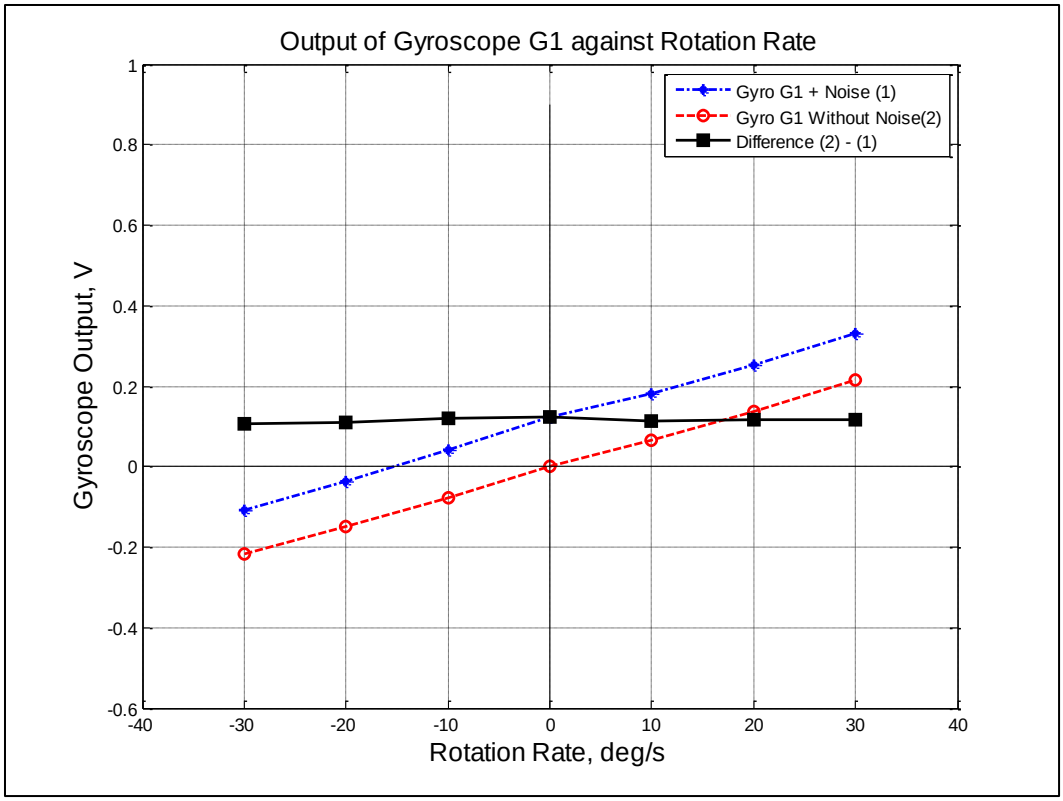

Figure 4.12 Experimental results for gyroscope G1.

Gyroscope	Natural Frequency, Hz	Sound Pressure Level, dB
G1	15031	115
G2	15114	117
G3	14492	116
G4	15105	118
G5	15227	115

Table 4.1 Natural frequencies and sound pressure levels of the gyroscopes.

4.2.3 Statistical Analysis of Results

A statistical analysis was also performed to show the accuracy of the experimental results and is summarized in Table 4.2. It was concluded that the measurements were accurate as the standard deviation was within 5 % of the mean for 4 out the 5 gyroscopes.

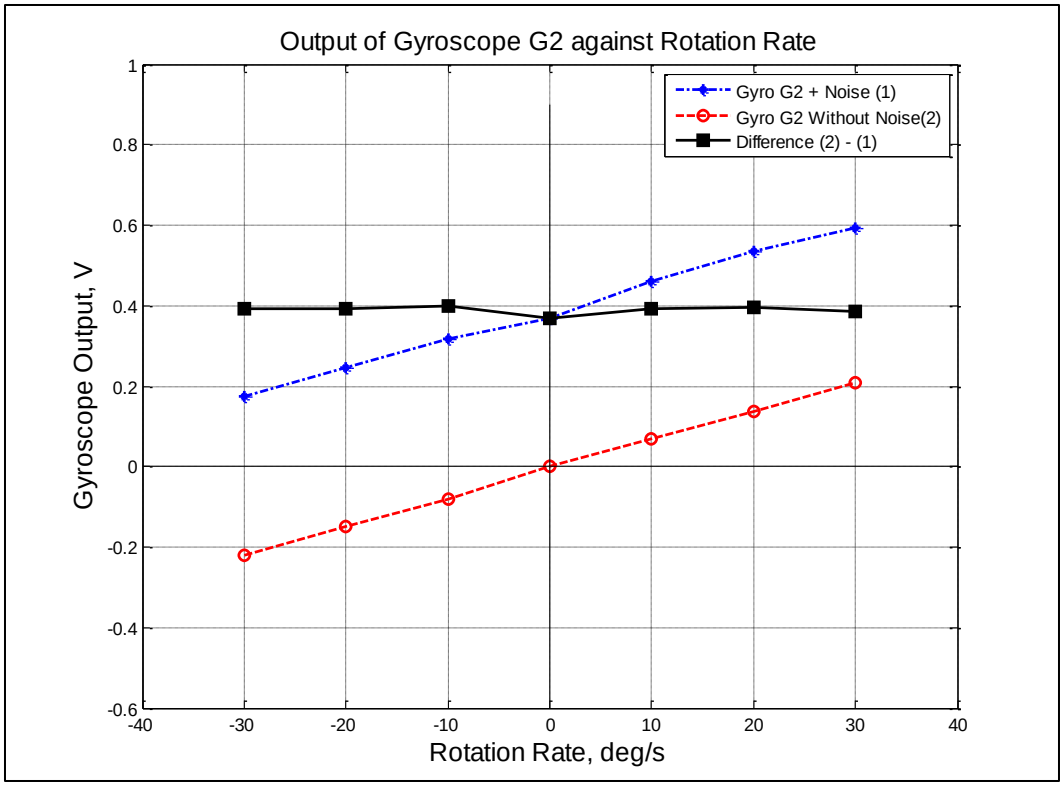

Figure 4.13 Experimental results for gyroscope G2.

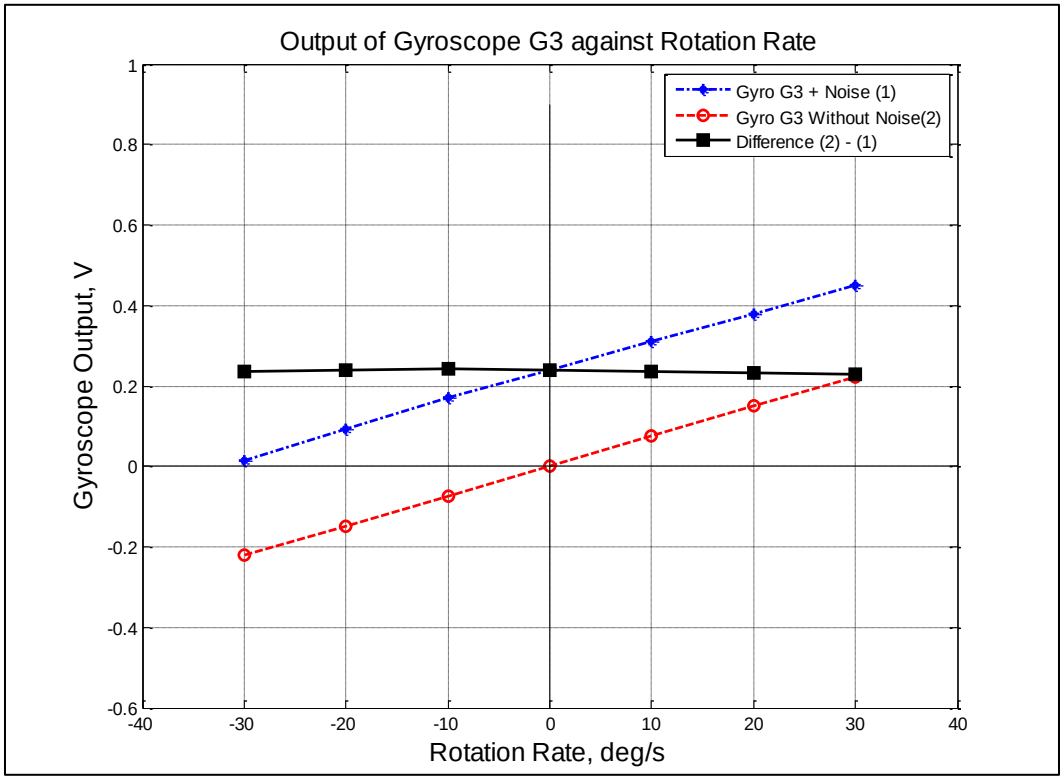

Figure 4.14 Experimental results for gyroscope G3.

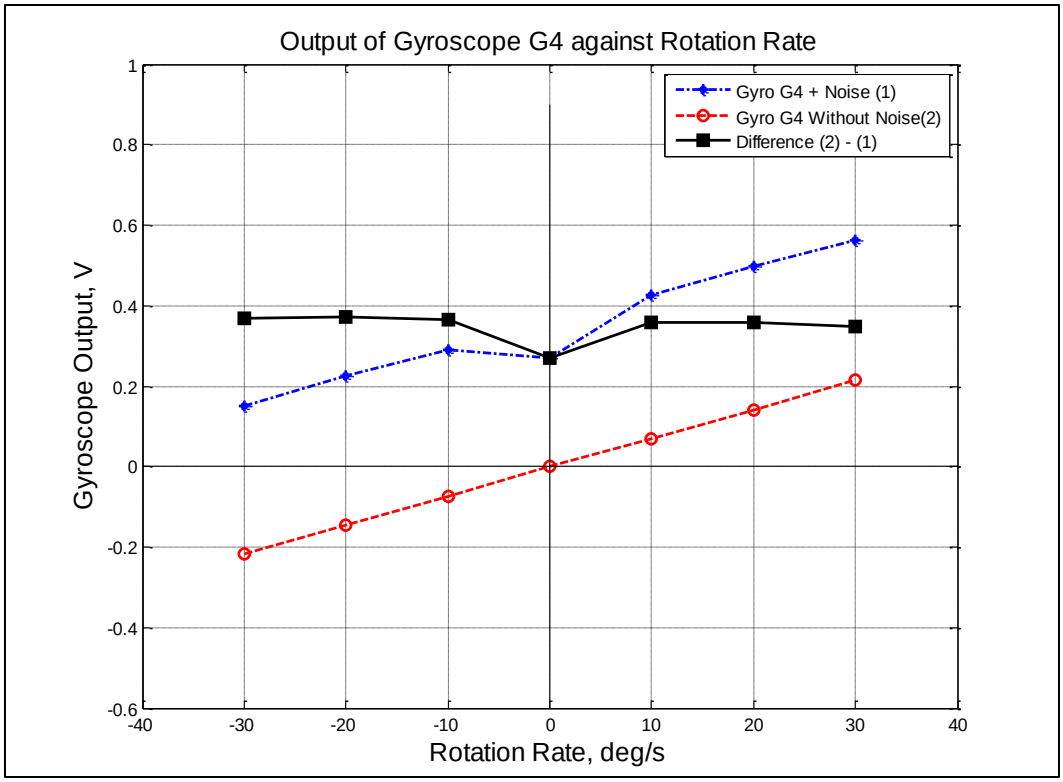

Figure 4.15 Experimental results for gyroscope G4.

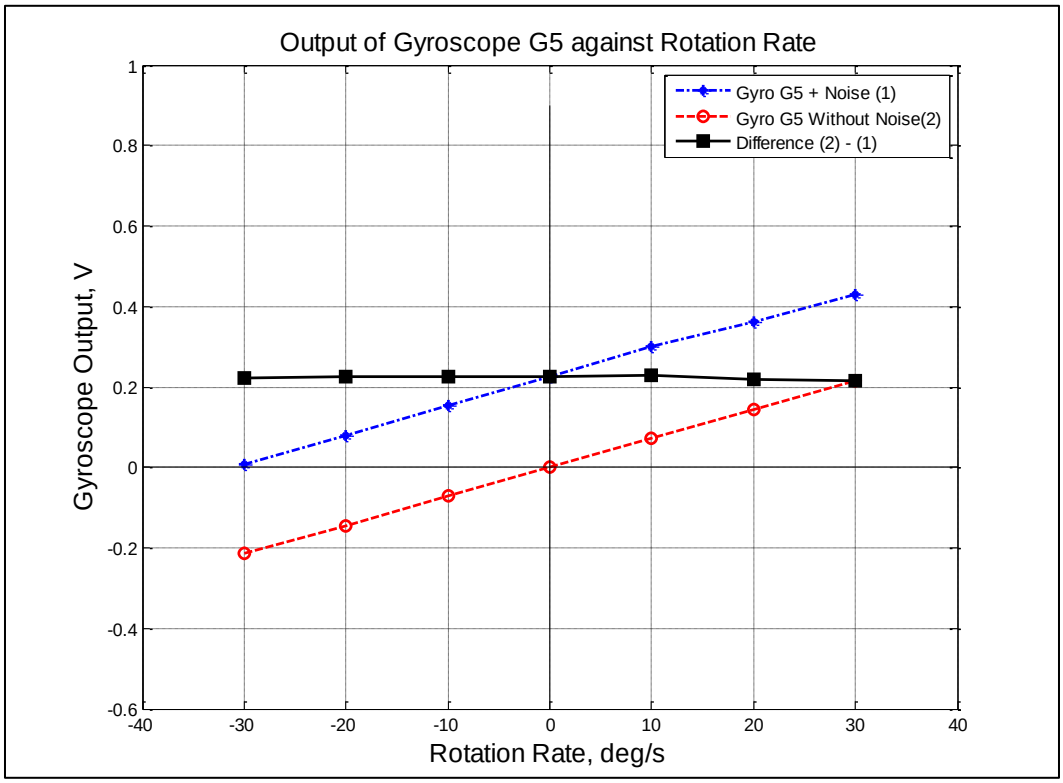

Figure 4.16 Experimental results for gyroscope G5.

Gyroscope	Amplitude of Effects of noise		
	Mean, V	**Standard deviation**	**Standard deviation as a percentage of the mean**
G1	0.1156	0.0058	5.01 %
G2	0.3894	0.0105	2.70 %
G3	0.2363	0.0052	2.21 %
G4	0.3480	0.0357	10.25 %
G5	0.2229	0.0045	2.01 %

Table 4.2 Statistical analysis of results.

4.3 Conclusions

The results of the experiments for each of the five gyroscopes show that the difference between the outputs in the presence and absence of the external sound field has little variance. This shows that the effects of the noise are superimposed on the normal output of the gyroscope and therefore confirming the simulation results of Chapter 3. Also, because the superposition of the effects of noise has been proven experimentally, a MEMS gyroscope not driven into oscillation will be affected by the noise field only and will measure the amplitude of the effects of noise. Therefore mitigation of the effects of noise can be achieved using the proposed differential measurement of two similar gyroscopes discussed in Chapter 3. Also, it is observed that for gyroscopes G2 and G4, the amplitude of the effects of noise on the gyroscope output at zero rotation rate is slightly smaller than when the gyroscope is rotating.

CHAPTER 5

MICROFIBROUS MATERIAL FABRICATION

This chapter describes the fabrication of nickel microfibrous sheets. A wet-lay papermaking process was used to make a preform of nickel and cellulose fibers. The preform was then dried and sintered to give a highly porous microfibrous media.

5.1 Introduction

Nickel microfibrous sheets were made using nickel fibers and cellulose, which acts as binding agent both in the liquid and dried states. The diameters of fibers used were: 4, 8 and 12 microns. Forty square sheets of 20 cm were made; ten for each fiber diameter, and ten for a mixture of 8 and 12 microns fibers in a ratio of 1:1 by mass.

5.2 Fabrication Procedure

A domestic blender was used to agitate 800 ml of water at low speed to remove air from it. The blender was controlled by a variable speed controller and the agitation was done at low speed to prevent turbulence, which would add more air to the water. When air bubbles were no longer perceived in the water, 7.5 g of hydroxyethyl cellulose (HEC) were added as a dispersion agent to breakdown cellulose into fibers. A fine sieve was used to ensure that the added HEC was in the powdered state. 3-5 ml of a 10% sodium hydroxide (NaOH) solution, made from 100 ml of water and 0.4 g of NaOH, were then progressively added to the blender until a weakly alkaline solution mixture was obtained (determined by a litmus test). The NaOH was a catalyst for breaking down

cellulose, and made the solution more viscous and turbid, requiring an increase in the mixing speed. The above steps are illustrated in Fig. 5.1.

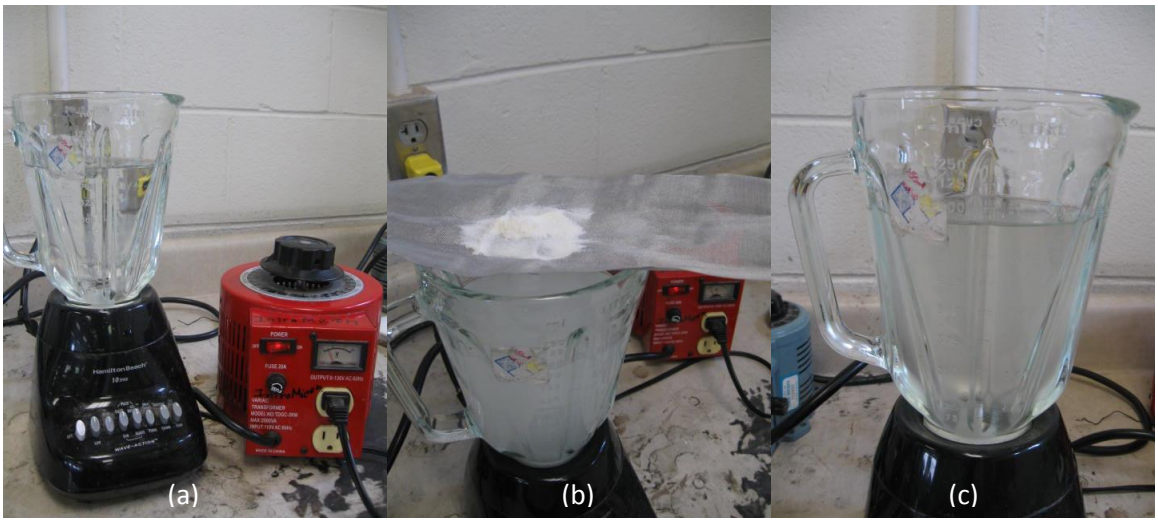

Figure 5.1 (a) Blender and speed controller, (b) HEC sieved into water, and (c) Turbid mixture.

The turbid mixture was agitated vigorously, causing the viscosity to increase continuously, until it turned into a clear solution. At this point 1.58 g of damped cellulose cut into small strips were added to the blender. The speed of the latter had to be further increased so as to break down the cellulose into fibers. When a homogeneous cellulose mixture was obtained, 7 g of nickel fibers, broken down into small lumps, were added. An aqueous suspension of nickel fibers was eventually obtained. Furthermore, it was ensured that fiber lumps did not cling to the blades of the blender. These steps are illustrated in Fig. 5.2.

A conventional papermaker was used to make a preform sheet from the aqueous suspension of nickel fibers. The paper maker was lined at the bottom with a very fine screen to filter out the nickel and cellulose fibers from the mixture. A water test was done to make sure that the papermaker was leak proof, and that there was no air trapped within

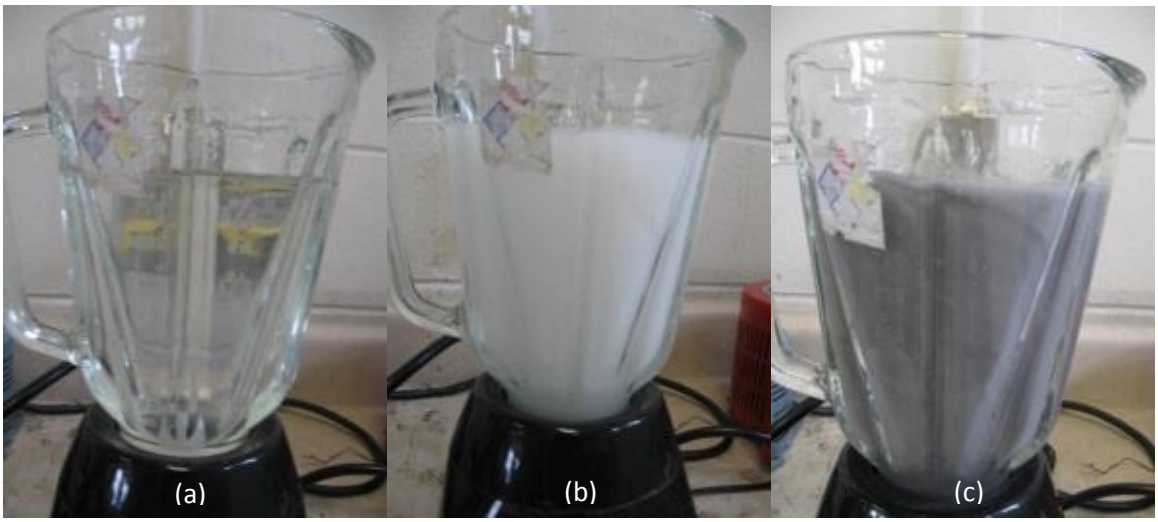

Figure 5.2 (a) Turbid mixture turns clear, (b) Cellulose mixture, and (c) Aqueous suspension of nickel fibers.

its piping system. For this purpose 2 cm of water was left at the bottom of the papermaker and the prepared mixture was added to it. Additional water was used to ensure that all the fibers were removed from the blender. A paddle was used to agitate the mixture and to press the fibers together (Fig. 5.3(a)), before the system valve was opened to release all the fluid leaving a square preform of fibers behind (Fig. 5.3(b)). A rolling pin was used to press the excess of water out of the sheet, and the latter was then dried overnight in an oven at 70 ^{o}C so as to remove all moisture from it. The drying process was done to prevent the tearing of the sheet during the sintering process. The forty sheets, that were made, were then sintered in a continuous hydrogen furnace at 1000 ^{o}C at a speed of 10 cm/min for a total sintering time of 30 minutes. The sintering is done in the middle of the furnace, allowing time for the sheets to warm after they are introduced and to cool down after the sintering. Therefore it took a total of one hour from the time the sheets were inserted on the conveyor belt of the furnace to the time they came out of it. Also the furnace required 6 hours to warm up and 6 hours to cool down.

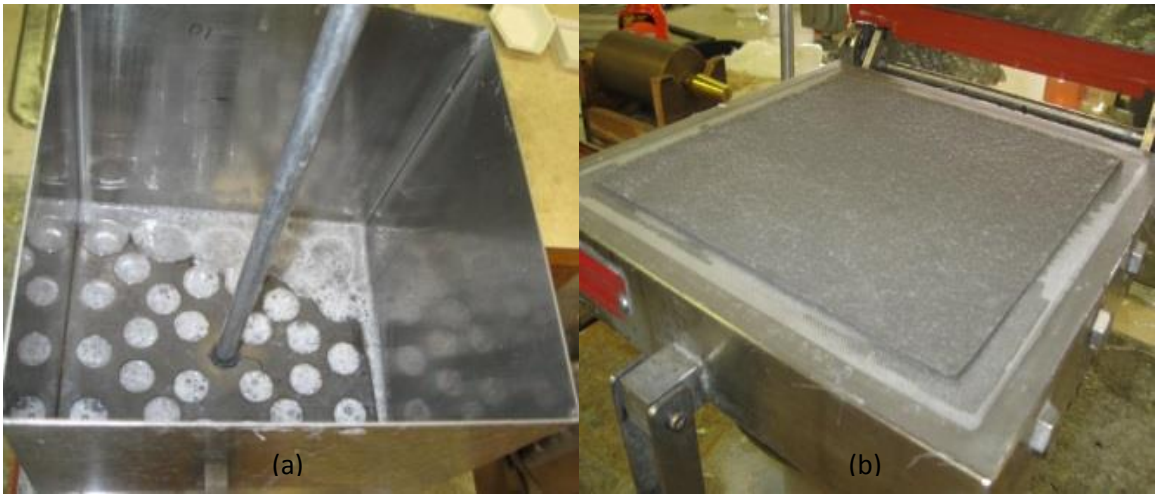

Figure 5.3 (a) Paddle agitating the mixture and (b) Perform after water is drained.

5.3 Optical Microscopy of Microfibrous Sheets

The different types of microfibrous sheets produced were observed under an optical microscope study their fibrous structure. For each type, four magnification factors were used; 100X, 300X, 500X and 1000X. The optical microscopic pictures are shown in Figs. 5.4-5.7. At 100X, a general view of the fiber network is obtained where the randomness in the layout of the fibers can be observed. The 4 microns material has a compact structure and with an increase in fiber size, it is observed that the microfibrous structure is looser as the spaces between the fibers become larger. Another way to visualize the space between the fibers is to look at a light source through the material. The 4 microns material is so compact that it is opaque, but the 12 microns material allows a lot of light to pass through so that the spaces between the fibers are seen as minute pores. At 500 X and 1000X, the sintering (the fusion) of the fibers ends can be seen. It is also clear from Fig. 5.7 that the sheet consists of two fiber diameters.

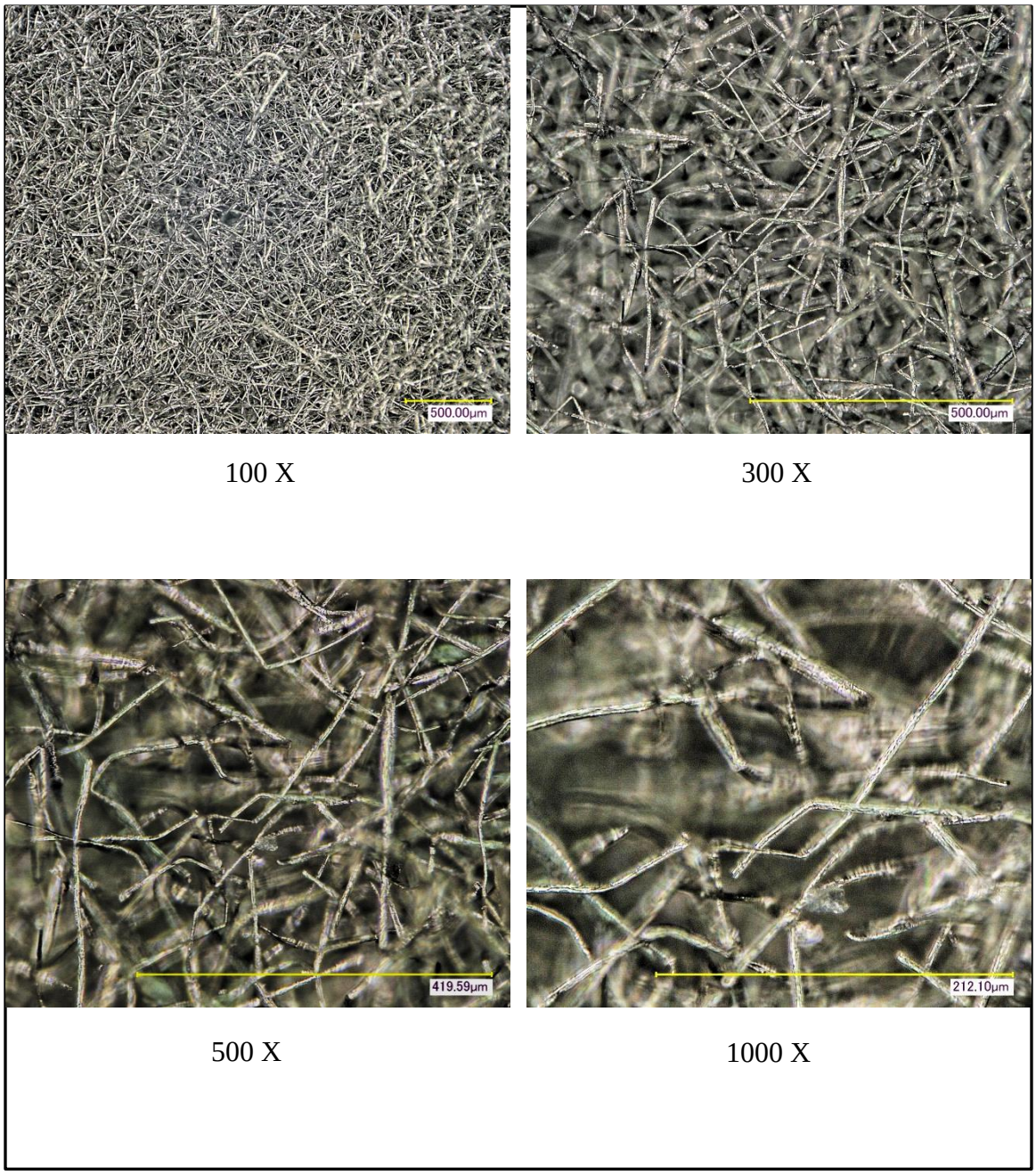

Figure 5.4 Optical microscopic images of 4 microns diameter material at magnification factors 100 X, 300 X, 500 X and 1000 X.

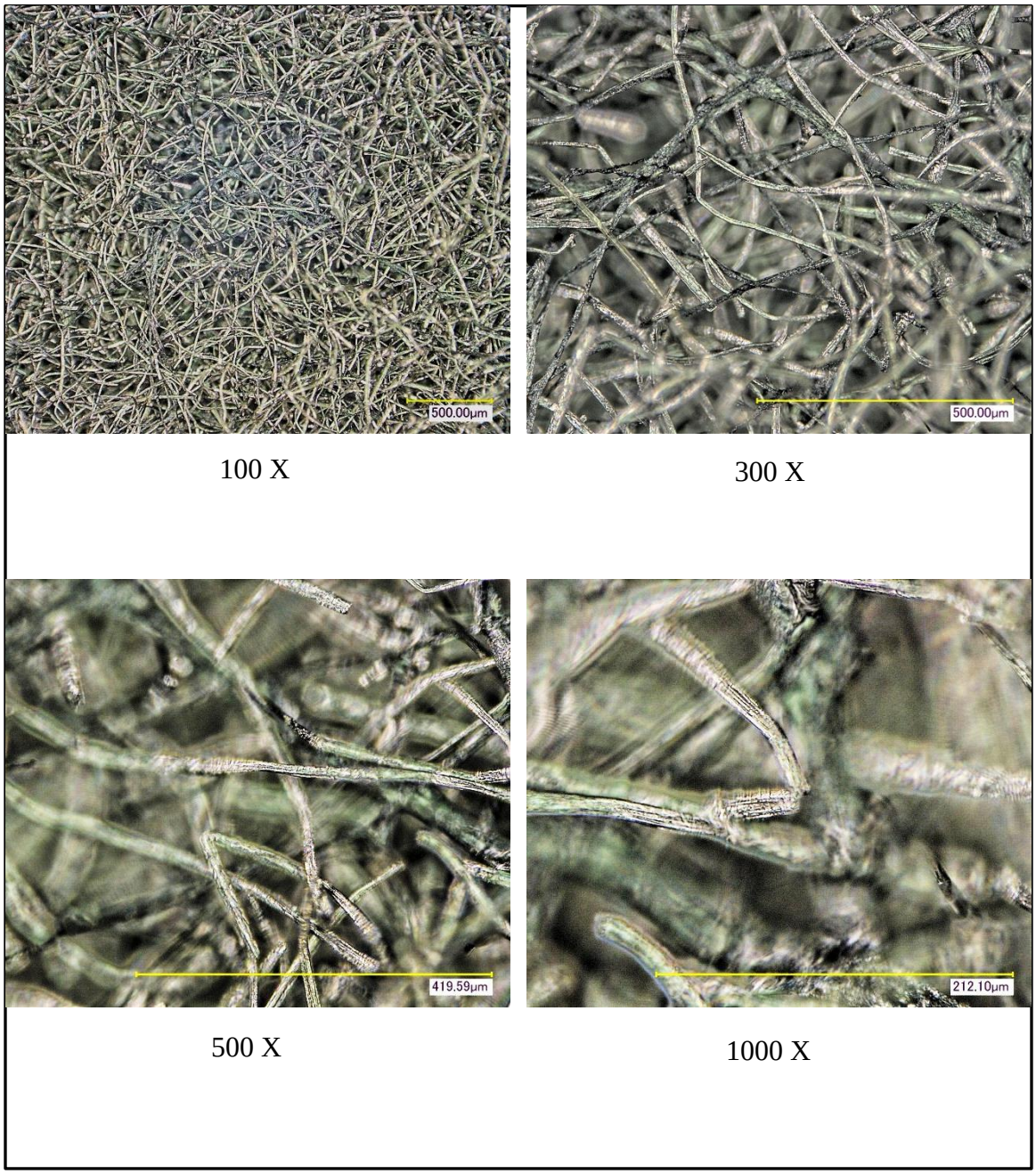

Figure 5.5 Optical microscopic images of 8 microns diameter material at magnification factors 100 X, 300 X, 500 X and 1000 X.

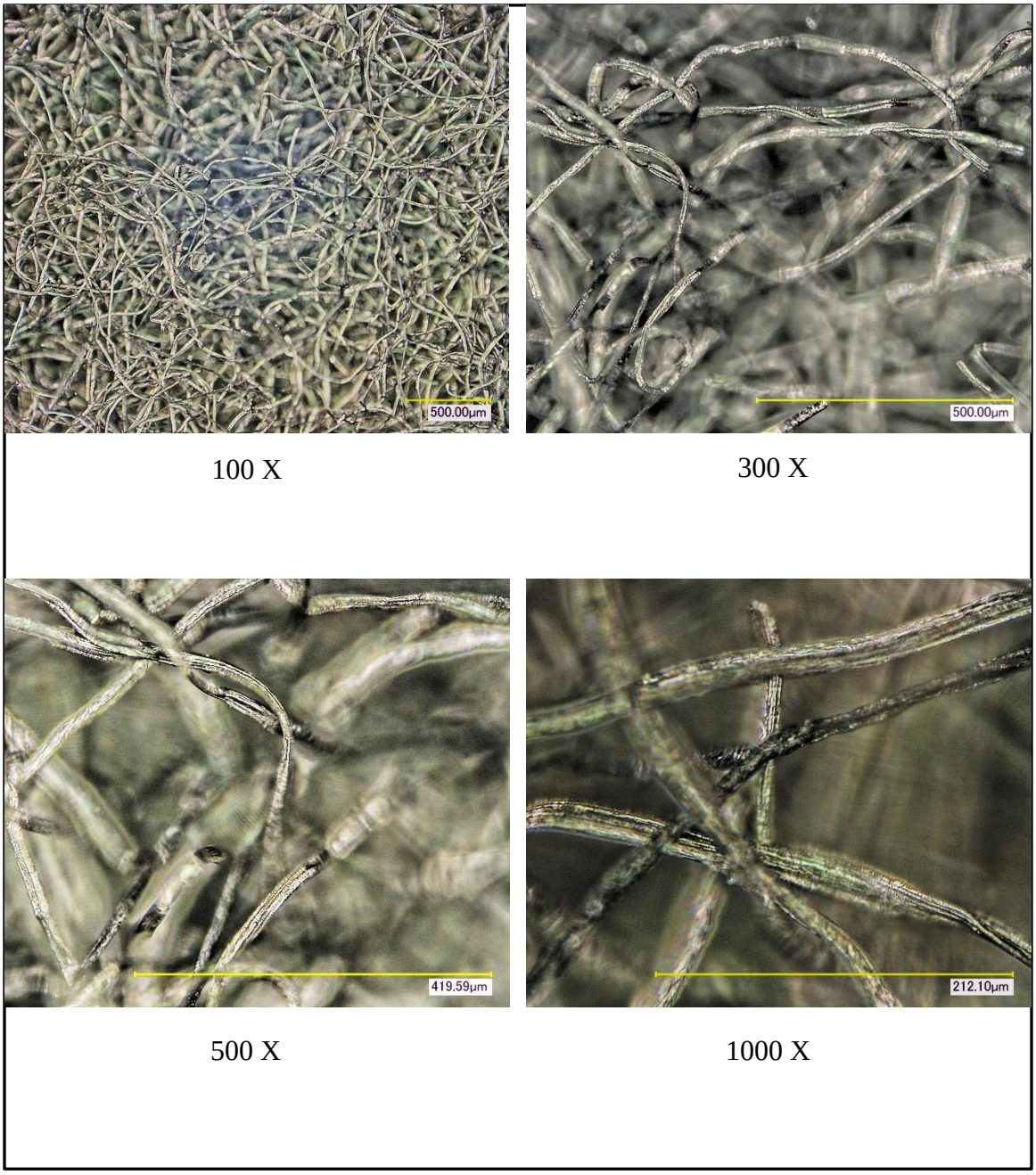

Figure 5.6 Optical microscopic images of 12 microns diameter material at magnification factors 100 X, 300 X, 500 X and 1000 X.

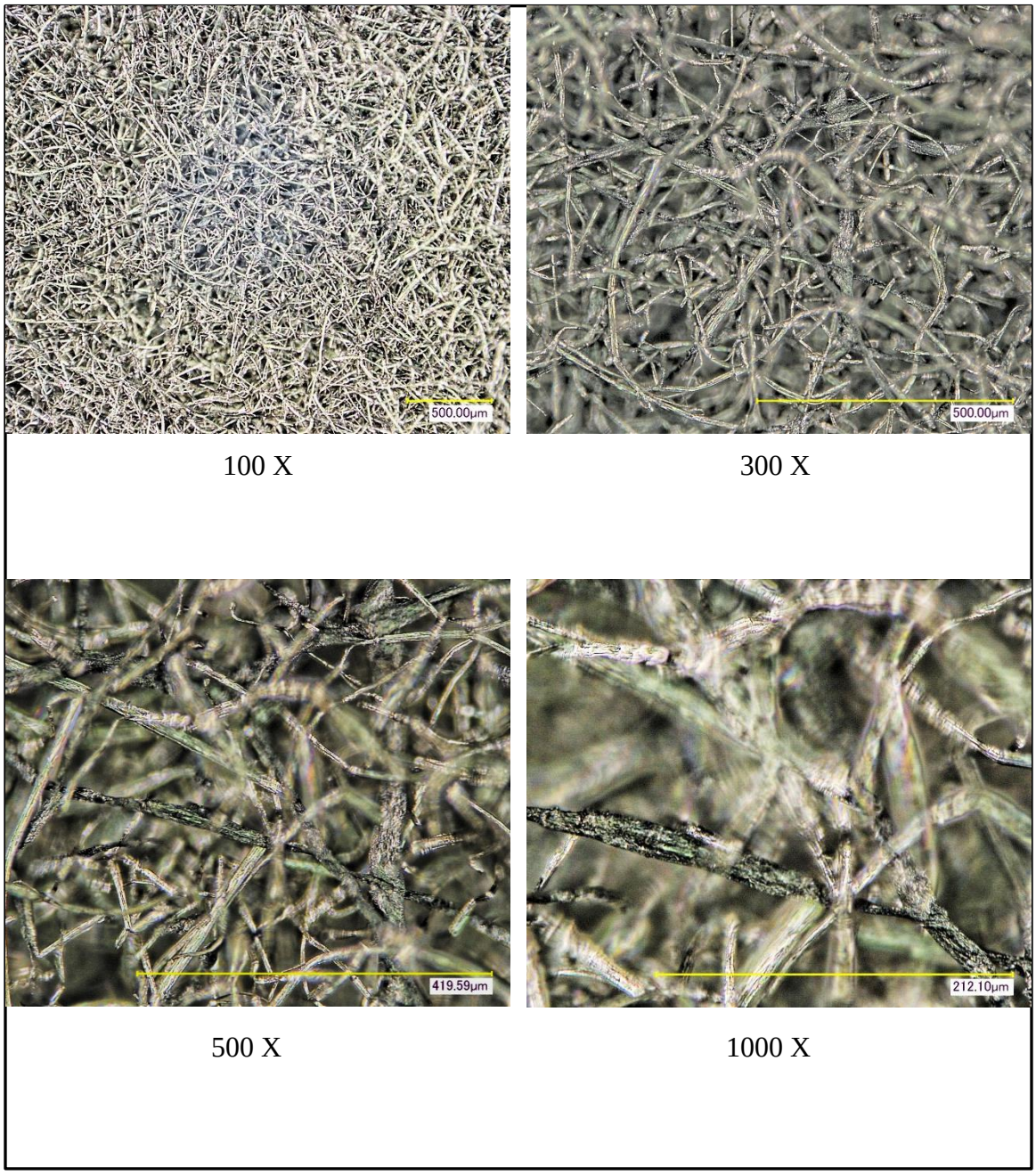

Figure 5.7 Optical microscopic images of 4 and 8 microns diameters material (mixed in a ratio of 1:1) at magnification factors 100 X, 300 X, 500 X and 1000 X.

CHAPTER 6

DETERMINATION OF ACOUSTICAL PROPERTIES

In this chapter the airflow resistivity of nickel microfibrous materials (media) is experimentally determined. The Delany-Bazley model is then used to obtain the acoustical properties of the media using the airflow resistivity.

6.1 Material Porosity

The porosity of the materials was determined using the bulk volume of a sheet and the mass of nickel fibers used for making the sheet. The bulk volume was calculated from the surface area and the thickness of the sheet. The latter was obtained by taking the average of nine measurements at different places on the sheet, as the thickness of the sheet was not uniform. The equipment used for thickness measurement is shown in Fig. 6.1. Since a known mass of nickel (7g) was used in a sheet, its volume was computed, and therefore, the porosity was calculated as the percentage of the void volume to the bulk volume. The calculations for the four media types were summarized in Table 6.1.

6.2 Delany-Bazley Model

Delany and Bazley developed a model to predict the acoustical properties; the characteristic impedance Z_c and the propagation constant γ, for fibrous materials having porosity factors near unity [24, 25]. Since the calculated porosity of the media in this study was at least 98%, the Delany-Bazley model, Eqns. (6.1) and (6.2), were expected to be accurate.

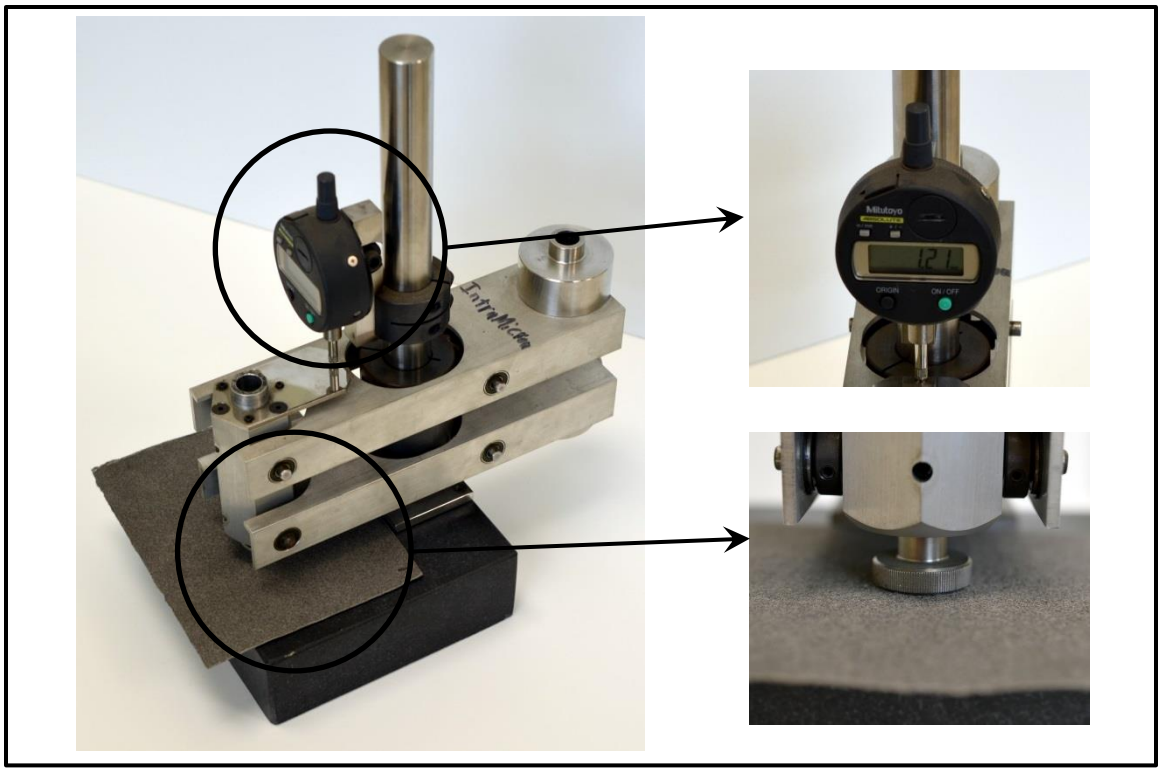

Figure 6.1 Equipment for measuring media thickness.

$$Z_c = \rho_o c_o \left\{ \left[1 + 0.0511 \left(\frac{f}{\sigma} \right)^{-0.75} \right] - j \left[0.0768 \left(\frac{f}{\sigma} \right)^{-0.73} \right] \right\}, \tag{6.1}$$

$$\gamma = \frac{2\pi f}{c_o} \left\{ \left[0.1749 \left(\frac{f}{\sigma} \right)^{-0.59} \right] + j \left[1 + 0.0858 \left(\frac{f}{\sigma} \right)^{-0.70} \right] \right\}, \tag{6.2}$$

where ρ_0 is the density of air, c_0 is the speed of sound in air, f is the frequency of sound and σ is the airflow resistivity.

Therefore, to obtain the acoustical properties, the airflow resistivity of the media was required and was sufficient.

6.3 Flow Resistance Measurement

The flow resistance for each of the four media types was determined experimentally. For each type, 5 samples of 50 mm diameter were cut from a sheet using a circular leather punch. The experimental set up is illustrated in Fig. 6.2.

Fiber Size (μm)	Sheet No.	Thickness Measurement (mm)										Sheet dim. (mm)		Bulk Volume (mm^3)	Vol. of Nickel Fibers (mm^3)	Porosity (%)
		1	2	3	4	5	6	7	8	9	Ave.	Length	Width			
4	1	1.85	1.87	1.89	1.80	1.66	1.75	2.05	1.92	1.90	1.85	180	178	59416.40	786.3	98.68
4	2	2.18	1.91	1.83	2.13	1.91	1.92	1.94	1.99	1.92	1.97	171	175	58952.25	786.3	98.67
4	3	2.25	2.01	2.12	2.10	1.93	1.90	2.15	1.90	2.12	2.05	178	176	64326.83	786.3	98.78
4	4	2.09	1.93	1.95	2.01	1.83	1.86	2.05	1.94	1.98	1.96	178	176	61402.88	787.3	98.72
4/8	1	1.44	1.46	1.52	1.40	1.37	1.54	1.71	1.48	1.43	1.48	170	175	44129.17	786.3	98.22
4/8	2	1.74	1.72	1.82	1.70	1.65	1.62	1.99	1.89	1.80	1.77	170	173	52055.70	786.3	98.49
4/8	3	1.77	1.72	1.79	1.49	1.56	1.56	1.78	1.53	1.52	1.64	175	175	50088.89	786.3	98.43
4/8	4	1.72	1.53	1.69	1.46	1.47	1.60	1.57	1.53	1.52	1.57	170	175	46575.28	786.3	98.31
4/8	5	1.55	1.70	1.87	1.59	1.53	1.50	1.63	1.57	1.65	1.62	165	174	46542.10	786.3	98.31
8	1	1.40	1.37	1.32	1.37	1.32	1.30	1.26	1.25	1.47	1.34	170	170	38726.00	786.3	97.97
8	2	1.49	1.42	1.53	1.35	1.29	1.35	1.64	1.62	1.46	1.46	165	170	40984.17	786.3	98.08
8	3	1.72	1.62	1.86	1.70	1.57	1.71	1.87	1.78	1.75	1.73	177	175	53548.03	786.3	98.53
8	4	1.82	1.53	1.96	1.66	1.54	1.87	1.82	1.61	1.65	1.72	180	180	55656.00	786.3	98.59
8	5	1.66	1.65	1.62	1.47	1.45	1.44	1.42	1.26	1.59	1.51	170	166	42518.13	786.3	98.15
12	1	1.31	1.24	1.42	1.42	1.42	1.28	1.39	1.31	1.41	1.36	170	172	39636.44	786.3	98.02
12	2	1.52	1.44	1.58	1.29	1.45	1.43	1.42	1.24	1.35	1.41	172	171	41568.96	786.3	98.11
12	3	1.42	1.35	1.21	1.39	1.44	1.30	1.41	1.32	1.29	1.35	175	175	41275.69	786.3	98.10
12	4	1.21	1.28	1.39	1.28	1.30	1.30	1.19	1.22	1.27	1.27	175	175	38927.78	786.3	97.98
12	5	1.07	1.22	1.24	1.15	1.12	1.17	1.18	1.33	1.27	1.19	172	171	35131.00	786.3	97.76

Table 6.1 Media thickness measurements and porosity calculations.

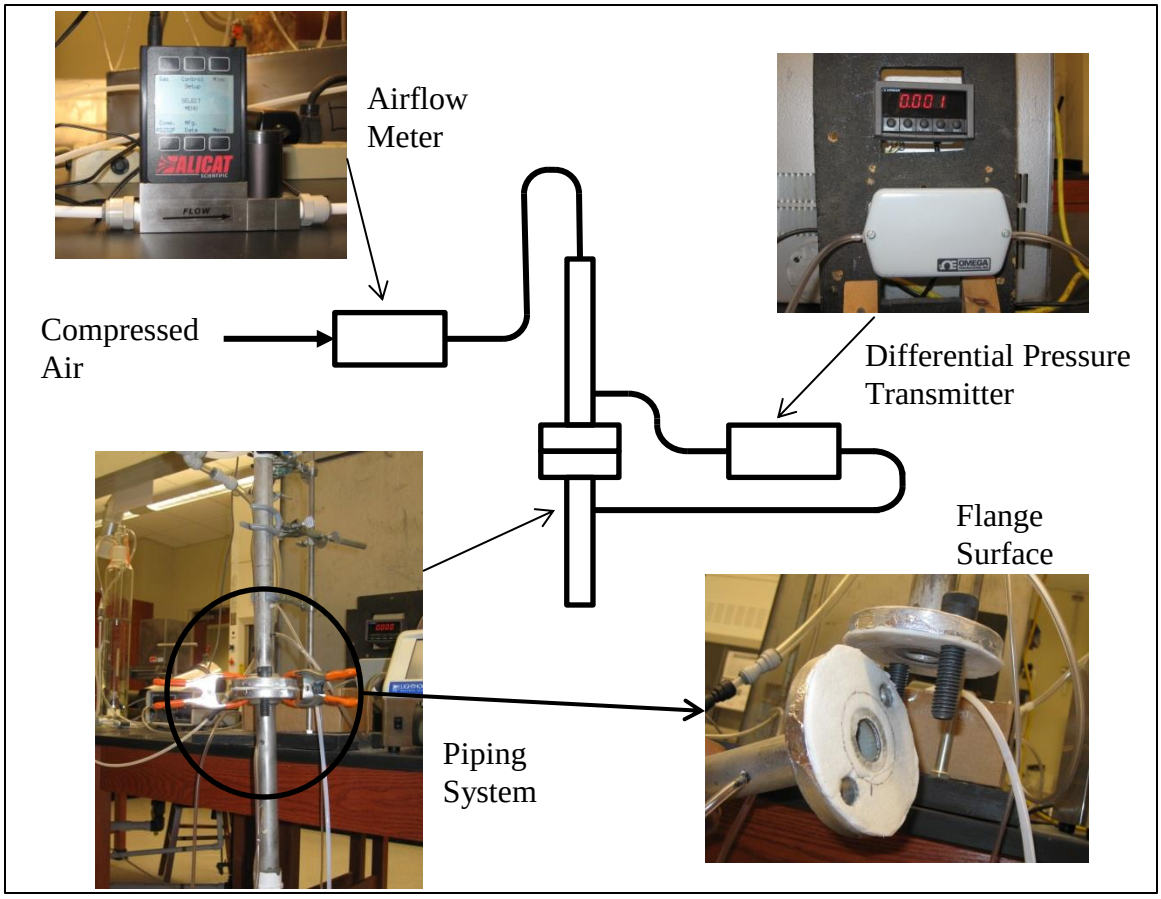

Figure 6.2 Schematic of equipment setup for airflow resistivity measurement.

One sample was clamped between the two sections of a 25.4 mm diameter pipe system, where the contact surfaces of the flanges had a layer of foam to prevent air leakage when the system was pressurized. Airflow through the pipe was precisely controlled by a mass airflow meter, ALICAT MC-5SLPM-D/5M. According to ASTM C522 [45], which is the standard for airflow resistivity measurement of porous acoustical materials, the airflow velocity should be between 0.5 to 50 mm/s, and the pressure drop across the media should be between 0.1 to 250 Pa. If higher airflow velocity is used, the flow characteristic will shift from laminar to turbulent. For a desired airflow velocity, the corresponding volumetric airflow rate was obtained by multiplying the velocity by the effective area of the media, and therefore, the airflow meter was programmed accordingly

in standard liters per minute. The two sections of central piping system were connected to a low differential pressure transmitter, OMEGA PX154-010DI, which measured the pressure drop across the media in inches of water (which was then converted to Pascals). The results of the experiments were recorded in Tables 6.2-6.5.

Using the experimental results, a graph of pressure drop against the airflow velocity was plotted (Fig. 6.3) for each media type. It is observed that there is a linear relation between pressure drop and velocity. Also for bigger fiber diameters, the pressure drop is smaller as the resistance to the airflow is less. The gradient of the plotted lines of Fig. 6.3 gives the airflow resistivity of the material, which is ratio of the pressure drop per unit thickness to the airflow velocity. The airflow resistivity values obtained are 138 844, 109 499, 54 814 and 32 732 Pa.s/m^2 for fiber diameters 4, 4/8, 8 and 12 microns, respectively.

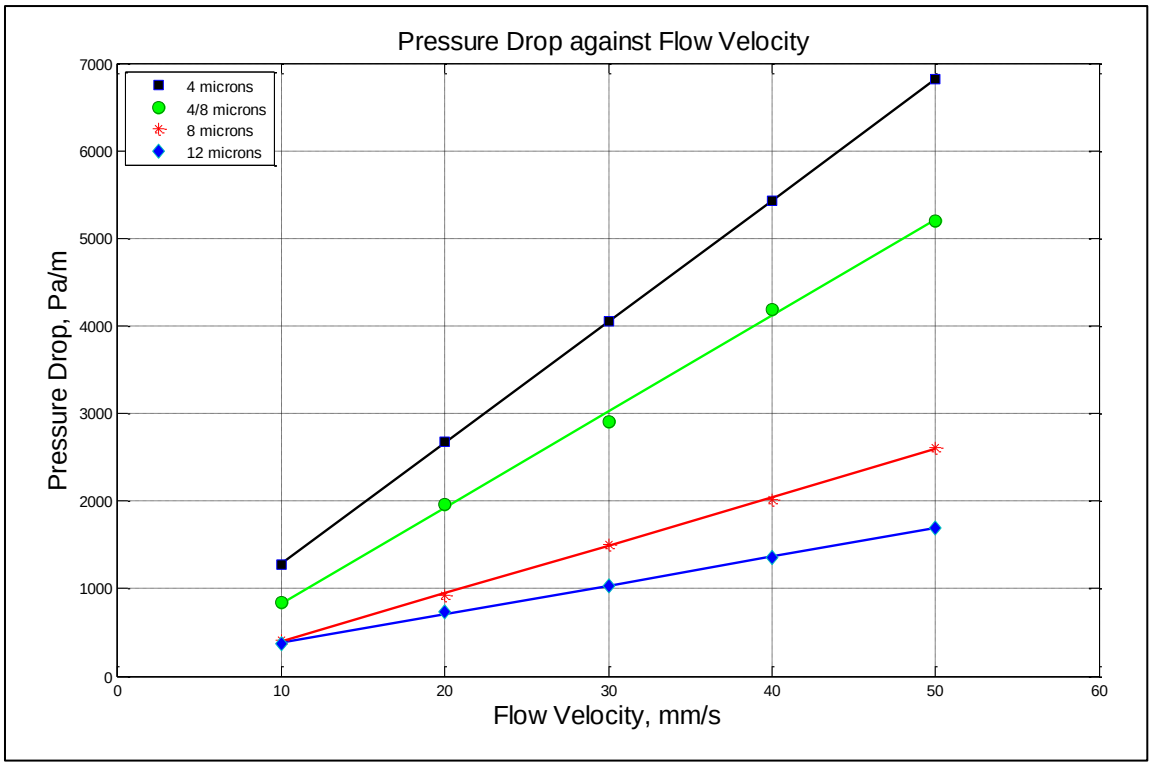

Figure 6.3 Plot of pressure drop as a function of flow velocity.

Fiber dia. (µm)	Material Thickness (mm)	Flow Rate (L/min)	Face Vel. (mm/s)	Pressure drop (inch of water)						Mean Press. drop (Pa)	Press. drop per unit thickness (Pa/m)
				Sample 1	Sample 2	Sample 3	Sample 4	Sample 5	Mean		
4	1.85	0.304	10.0	0.010	0.010	0.007	0.009	0.011	0.009	2.35	1270.73
4	1.85	0.608	20.0	0.020	0.021	0.017	0.019	0.022	0.020	4.95	2676.64
4	1.85	0.912	30.0	0.031	0.030	0.026	0.030	0.033	0.030	7.50	4055.51
4	1.85	1.216	40.0	0.042	0.040	0.036	0.040	0.043	0.040	10.05	5434.39
4	1.85	1.52	50.0	0.053	0.051	0.044	0.050	0.054	0.050	12.60	6813.26

Table 6.2 Pressure drop measurements for 4 microns media.

Fiber dia. (µm)	Material Thickness (mm)	Flow Rate (L/min)	Face Vel. (mm/s)	Pressure drop (inch of water)						Mean Press. drop (Pa)	Press. drop per unit thickness (Pa/m)
				Sample 1	Sample 2	Sample 3	Sample 4	Sample 5	Mean		
4/8	1.48	0.304	10.0	0.004	0.004	0.006	0.006	0.005	0.005	1.25	844.90
4/8	1.48	0.608	20.0	0.010	0.010	0.013	0.013	0.012	0.012	2.90	1960.16
4/8	1.48	0.912	30.0	0.015	0.016	0.019	0.018	0.018	0.017	4.30	2906.45
4/8	1.48	1.216	40.0	0.022	0.023	0.028	0.026	0.025	0.025	6.20	4190.70
4/8	1.48	1.52	50.0	0.028	0.029	0.034	0.033	0.030	0.031	7.70	5204.58

Table 6.3 Pressure drop measurements for 4/8 microns media.

Fiber dia. (µm)	Material Thickness (mm)	Flow Rate (L/min)	Face Vel. (mm/s)	Pressure drop (inch of water)						Mean Press. drop (Pa)	Press. drop per unit thickness (Pa/m)
				Sample 1	Sample 2	Sample 3	Sample 4	Sample 5	Mean		
8	1.46	0.304	10.0	0.004	0.002	0.002	0.002	0.002	0.002	0.60	411.11
8	1.46	0.608	20.0	0.007	0.005	0.005	0.005	0.005	0.005	1.35	924.99
8	1.46	0.912	30.0	0.011	0.009	0.008	0.008	0.008	0.009	2.20	1507.39
8	1.46	1.216	40.0	0.015	0.012	0.010	0.011	0.011	0.012	2.95	2021.28
8	1.46	1.52	50.0	0.018	0.016	0.014	0.014	0.014	0.015	3.80	2603.68

Table 6.4 Pressure drop measurements for 8 microns media.

Fiber dia. (µm)	Material Thickness (mm)	Flow Rate (L/min)	Face Vel. (mm/s)	Pressure drop (inch of water)						Mean Press. drop (Pa)	Press. drop per unit thickness (Pa/m)
				Sample 1	Sample 2	Sample 3	Sample 4	Sample 5	Mean		
12	1.36	0.304	10.0	0.002	0.003	0.002	0.001	0.002	0.002	0.50	367.78
12	1.36	0.608	20.0	0.005	0.005	0.003	0.003	0.004	0.004	1.00	735.56
12	1.36	0.912	30.0	0.007	0.006	0.005	0.005	0.005	0.006	1.40	1029.78
12	1.36	1.216	40.0	0.009	0.008	0.007	0.006	0.007	0.007	1.85	1360.78
12	1.36	1.52	50.0	0.011	0.010	0.009	0.008	0.008	0.009	2.30	1691.79

Table 6.5 Pressure drop measurements for 12 microns media.

6.4 Absorption Coefficient

At a particular sound frequency, the characteristic impedance Z_c and the propagation constant γ were computed by using the measured air flow resistivity in Eqns. (6.1) and (6.2). The impedance Z_l of a rigidly-backed layer of thickness l was then calculated using [24]

$$Z_l = Z_c \coth \gamma l \,. \tag{6.3}$$

The normal-incidence energy absorption coefficient α_n was obtained by

$$\alpha_n = 1 - \left|\frac{Z_l - \rho_0 c_0}{Z_l + \rho_0 c_0}\right|^2. \tag{6.4}$$

α_n was computed as a function of frequency for material thicknesses 0.5, 1, 2 and 5 cm. As a requirement of the Delany-Bazley model the ratio of frequency to the airflow resistivity was kept between 0.01 and 1 m^3/kg. The graphs for each media type were plotted in Figs. 6.4 – 6.7. The graphs show that the absorption coefficient increases with frequency and material thickness which are typical of acoustical materials. With an increase in fiber size, an increase in the absorption coefficient especially in the low frequency range is observed (for thicknesses 2 and 5 cm). Also, it is observed that for a thin layer of the media (0.5 cm), the absorption coefficient decreased with an increase in fiber diameter. For a material thickness of 1 cm and for frequencies above 6 kHz, all the media types have good absorption coefficients between 0.9 and 1.0.

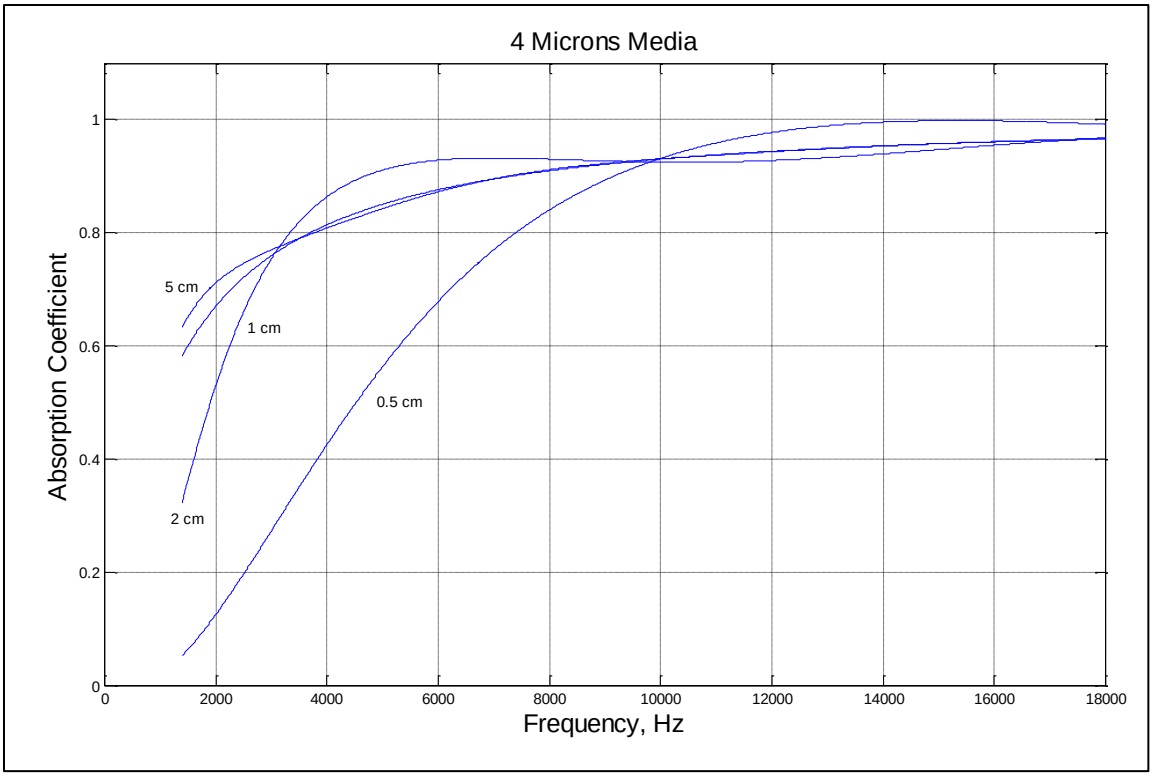

Figure 6.4 Absorption coefficients of 4 microns media.

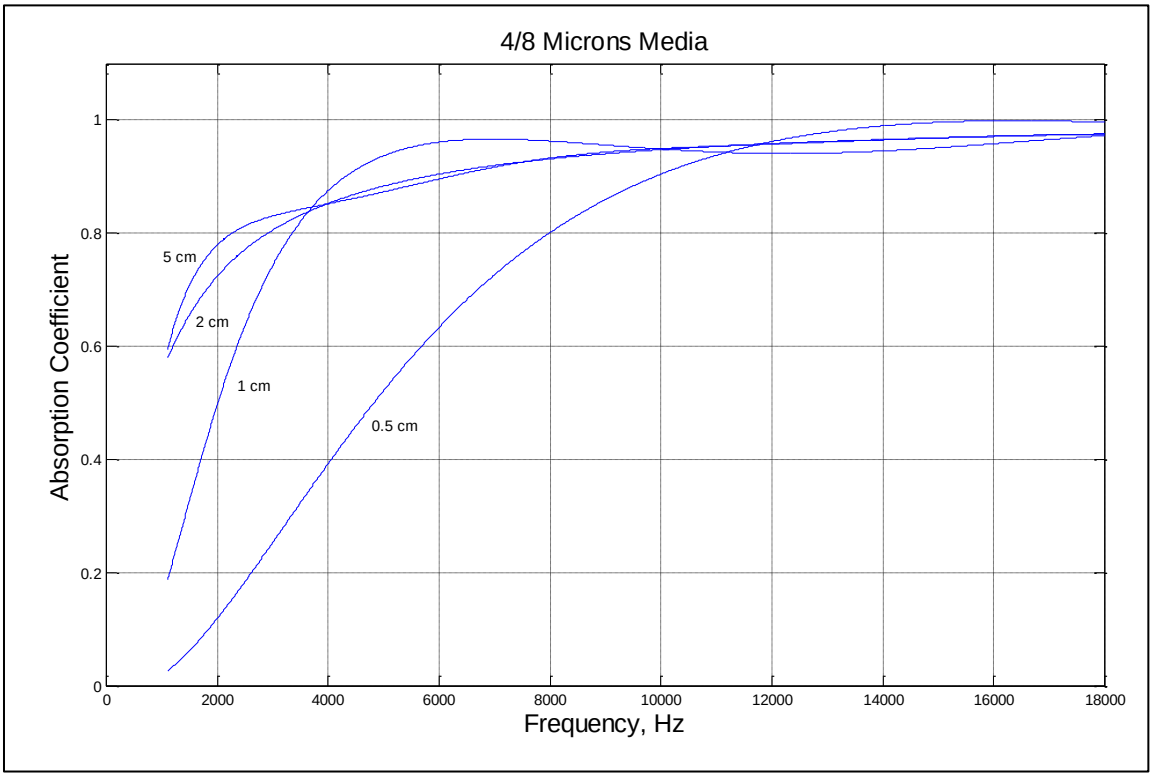

Figure 6.5 Absorption coefficients of 4/8 microns media.

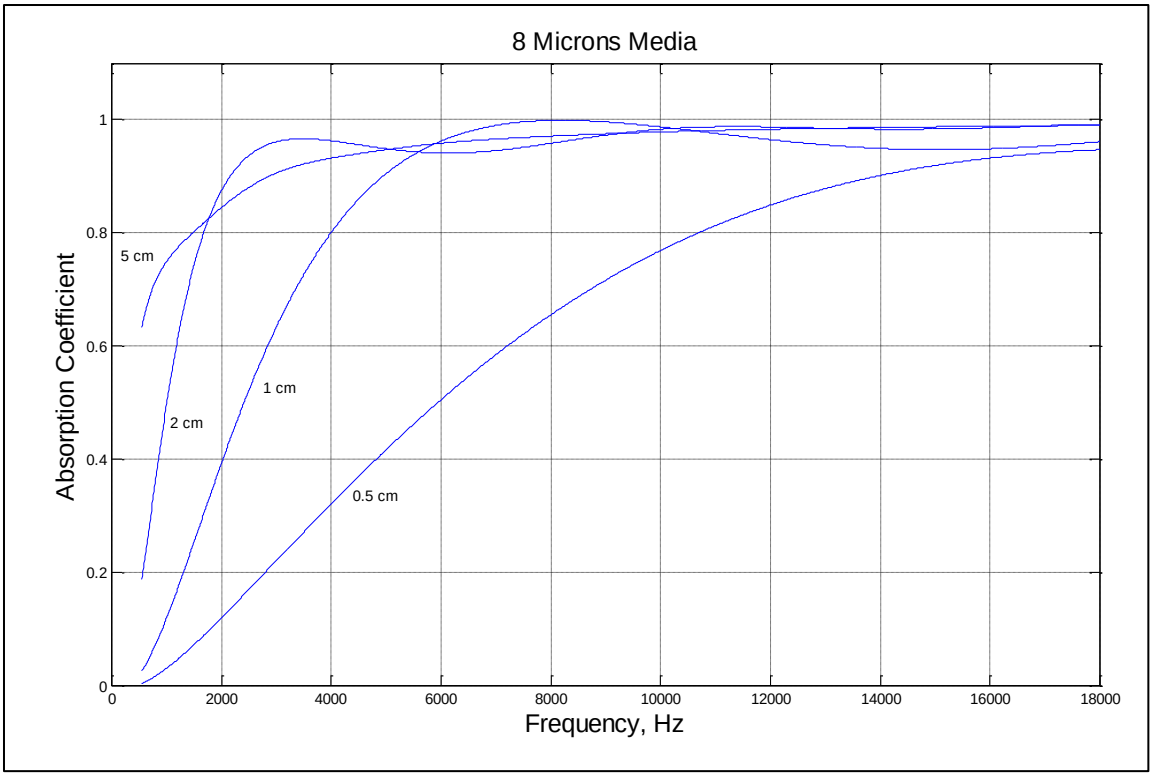

Figure 6.6 Absorption coefficients of 8 microns media.

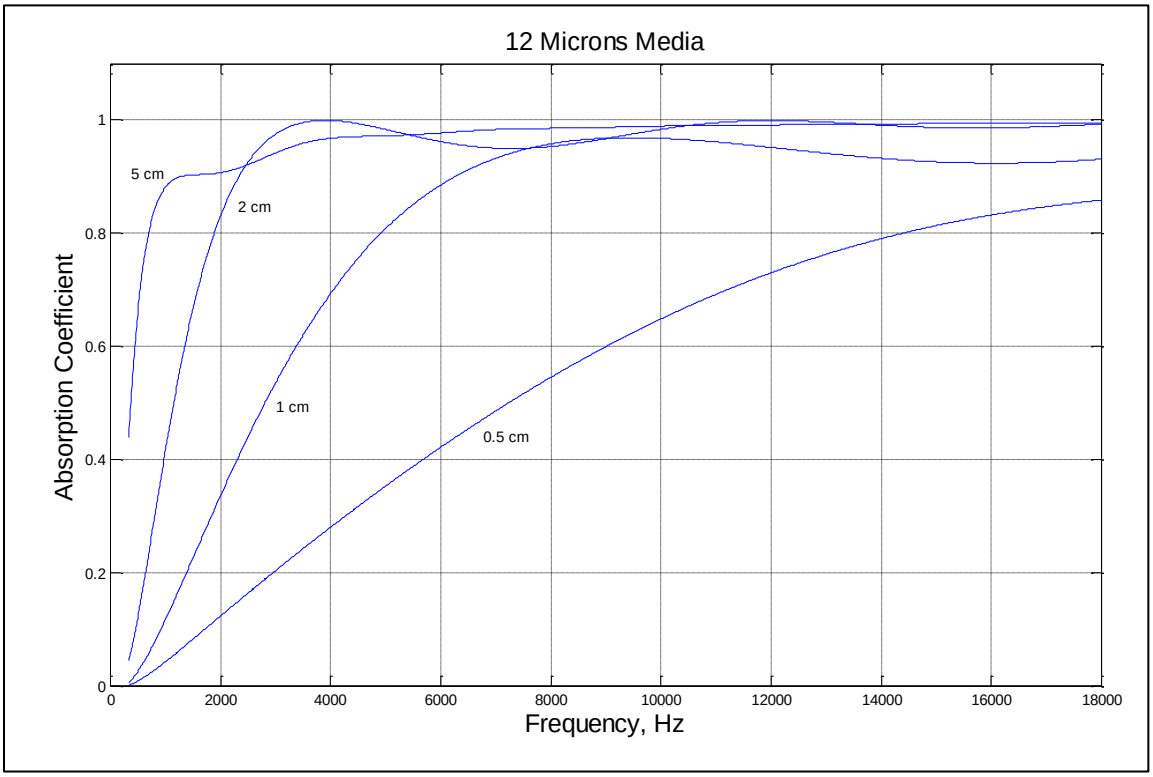

Figure 6.7 Absorption coefficients of 12 microns media.

CHAPTER 7

DAMPING CHARACTERIZATION

In this chapter, the damping characterization of nickel microfibrous materials was performed using the displacement transmissibility concept. A fixture was designed for attachment to the shaker head and to hold the material during testing.

7.1 Test Design

In a displacement transmissibility plot, the natural frequency is related to the frequency ratio at the maximum transmissibility while the damping ratio is related to the amplitude of the maximum transmissibility. Therefore displacement transmissibility was used to characterize the damping in the microfibrous media. The experiment was designed to emulate the simple vibration isolation system illustrated in Fig. 7.1. The material under test, of stiffness k and damping c, is sandwiched between a known mass and vibrating base. The displacement of the mass is measured and compared to the measured displacement of the base so as to obtain the displacement transmissibility.

7.2 Test Fixture

A test fixture was required to hold the material under test, for positioning the mass on top of material, and for attachment to the shaker head. Therefore the fixture (Fig. 7.2) was designed with three main parts; an aluminum bracket, a sliding mass and a Teflon top. A cap screw was used to attach the aluminum bracket to the shaker head. Also the flat interior surface of the bracket had two dowels press fitted near the corners to

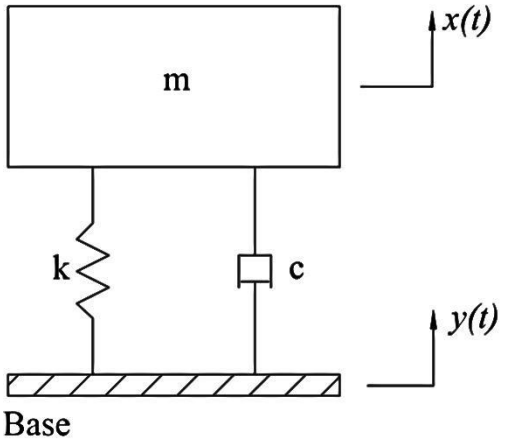

Figure 7.1 Vibration transmitted through base motion.

hold the test material, preventing any side movement of the latter during vibration. The sliding mass was designed with a flat bottom surface to sit squarely on top of the test material. The mass could be altered by using thick washers, and the aluminum slider part was highly polished to reduce friction during motion within the Teflon top part. The latter was made of Teflon for minimum friction and was attached to the aluminum brackets by four cap screws. Mechanical drawings of the fixture are shown in Appendix D.

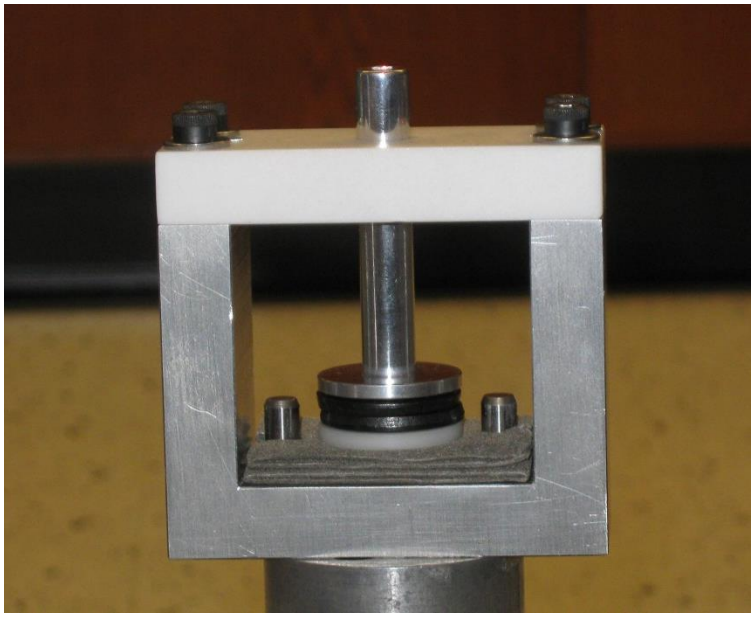

Figure 7.2 Photograph of test fixture.

7.3 Equipment Setup

A schematic of the equipment setup is shown in Fig. 7.3. The test fixture is attached to the electromagnetic shaker, model LDS 408, which vibrates vertically based on the input from the amplifier, model LDS PA500L. The input to the amplifier is the source signal generated by the analyzer, model HP 35665A. Two laser vibrometers are used; one for measuring the input (the displacement of the shaker head), and one for measuring the output (the displacement of the mass). Each of the vibrometers consists of a sensor head, model Polytec OFV 353, and a controller, model Polytec OFV 2610. The controller provides power to the sensor head and decodes the measured signal from the sensor head. The sensor head emits a laser beam, which is reflected from a small reflective sticker placed on the surface being measured. The input and output vibrometers' signals are respectively fed to channels 1 and 2 of the analyzer, and the transfer function of the output/input is displayed on the analyzer. To improve signal to noise ratio, the laser is focused at the center of the reflective material for maximum reflection. The test set up is illustrated in Fig. 7.4.

7.4 Experimental Procedure

For each of the four media types, a series of experiments was conducted using different vibration amplitudes and different number of layers of the material. The generated source signal was a random noise and its amplitude and bandwidth were specified in the analyzer. The vibration amplitude was varied by increasing the source amplitude from 20 mV_{rms} to 60 mV_{rms} in steps of 10 mV_{rms} while keeping the gain of the amplifier constant. An accelerometer was used to measure the acceleration corresponding to the source amplitudes and the respective values were 0.694 m/s^2, 1.103 m/s^2, 1.468 m/s^2,

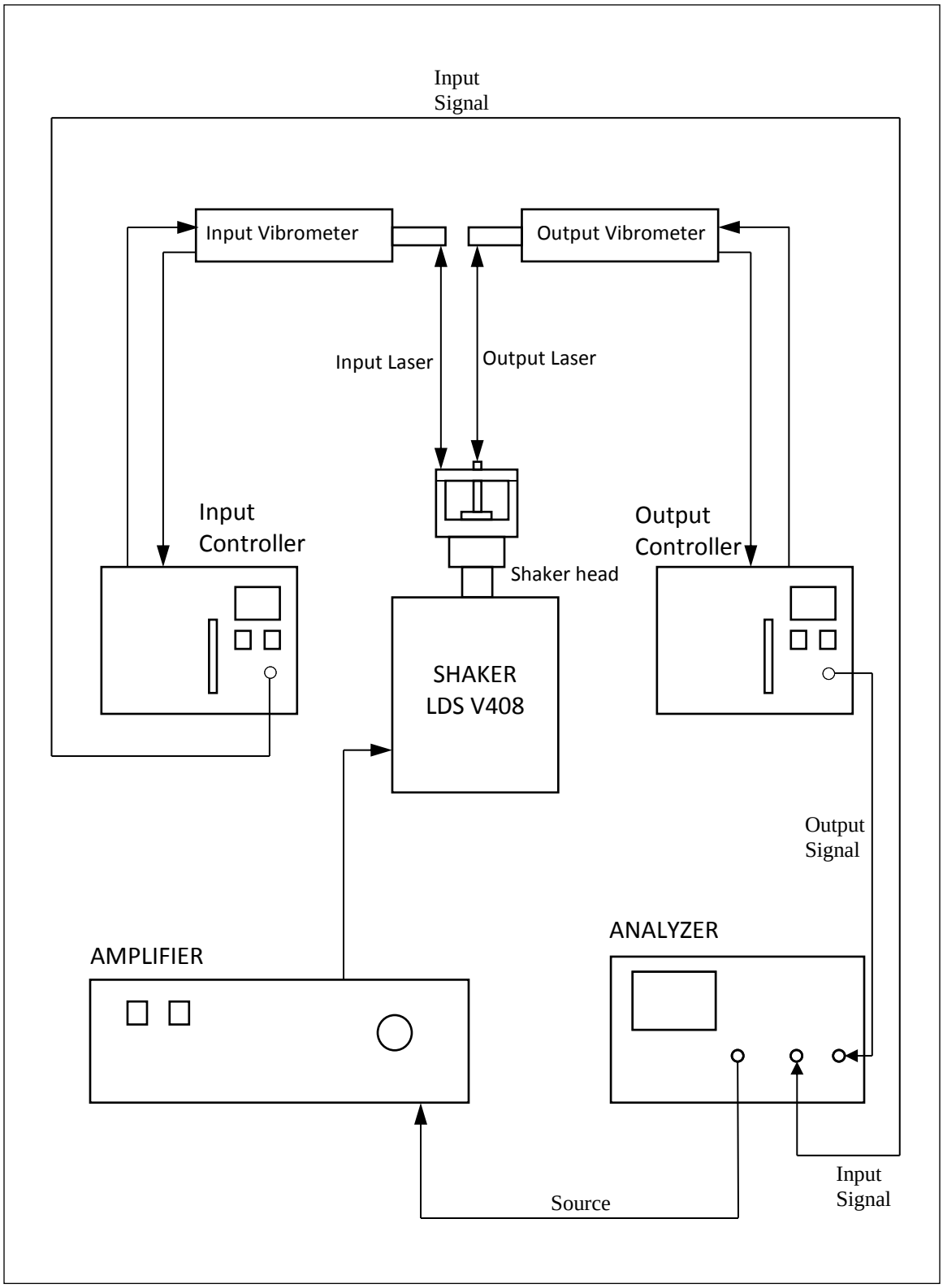

Figure 7.3 Schematic of vibration test equipment setup.

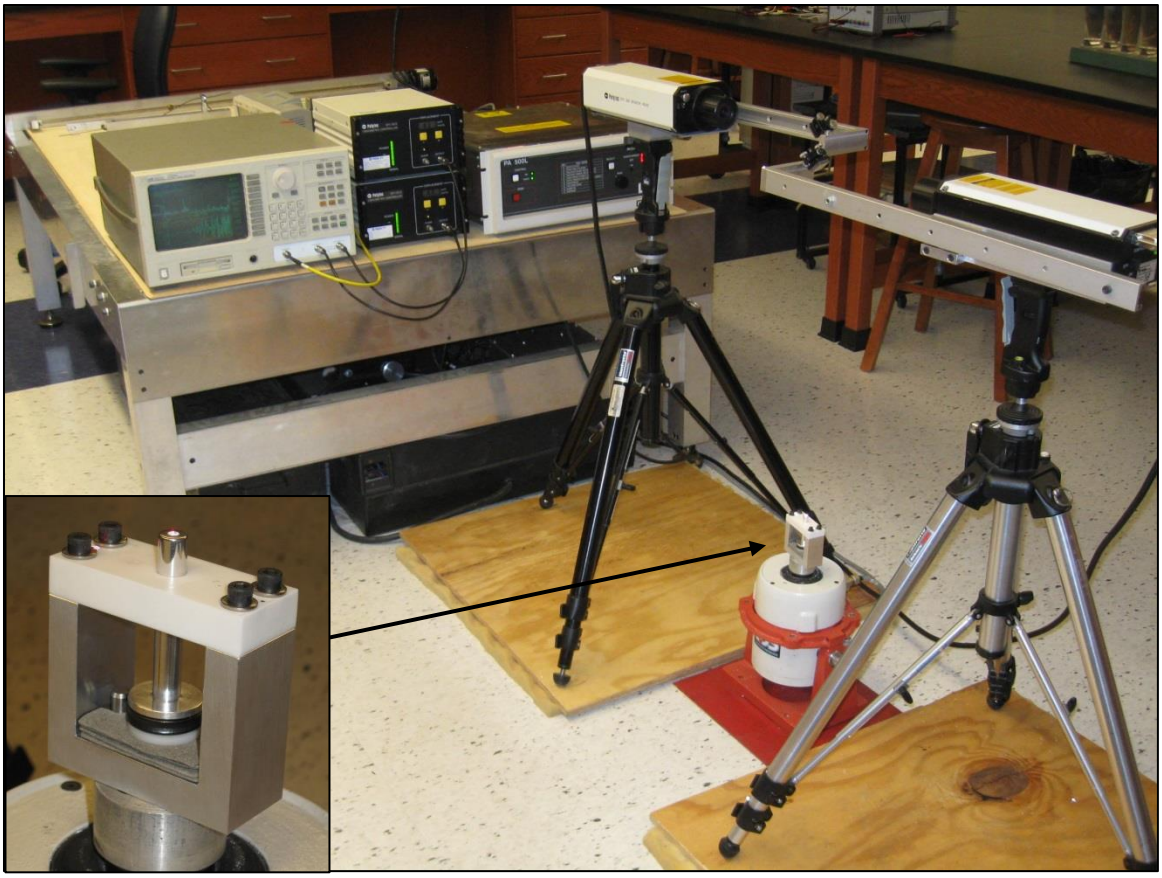

Figure 7.4 Photograph of test setup.

1.831 m/s^2 and 2.202 m/s^2. The number of layers was varied from 1 to 5.

The 20 cm x 20 cm microfibrous sheets were cut according to the dimensions and shape of the fixture. As such, 15 samples were obtained from one sheet and were labeled 1-15. The samples were first tested individually at the different vibration amplitudes and their transfer functions saved on the analyzer. Averaging of the transfer function was done for noise rejection. A typical transfer function is illustrated in Fig. 7.5, where a phase shift of 90^o is clearly observed at the natural frequency. An example of the transfer functions at the different vibration amplitudes is illustrated in Fig. 7.6 for sample number 9 made of 4 micron diameter fibers. It is observed that the amplitude of the transfer function increases, and the natural frequency decreases, with increasing vibration

amplitude. For each test performed, the frequency and amplitude of the maximum of the transfer function were recorded and the average computed for the 15 samples. The number of layers was then incremented and the same process repeated until all the tests were completed. The transfer functions for the different material types and the different number of layers used are shown in Appendix D. A series of tables were then made (Appendix D) for recording the frequency and amplitude of the transfer functions.

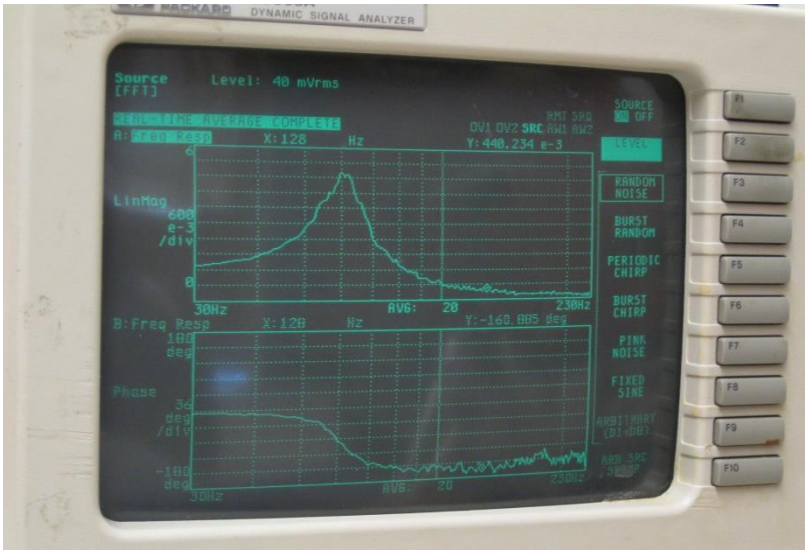

Figure 7.5 Picture of analyzer screen showing a Bode plot.

7.5 Stiffness and Damping Ratio

The average values of the frequency and amplitude of the transfer functions were used to determine the stiffness and damping ratio of the materials. The relation between the frequency ratio at maximum amplitude r_m and the damping ratio ζ is given by Eqn. (7.1), and the relation between the maximum amplitude A_m and the damping ratio is given by Eqn. (7.2). The equations were derived from the displacement transmissibility as shown in Appendix A.

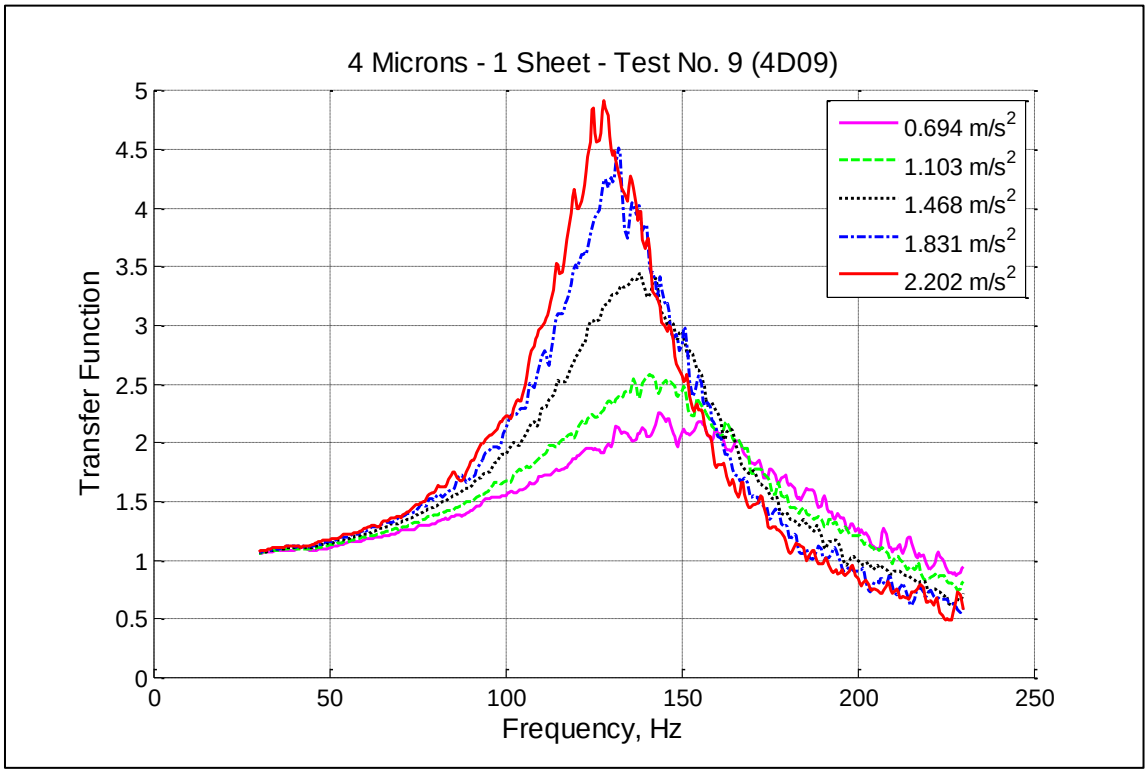

Figure 7.6 Transfer function at different vibration amplitudes.

$$r_m = \frac{1}{2\zeta}\sqrt{\sqrt{1+8\zeta^2}-1}\ . \tag{7.1}$$

$$A_m = \left[\frac{8\zeta^4}{8\zeta^4-4\zeta^2+\sqrt{1+8\zeta^2}-1}\right]^{1/2}. \tag{7.2}$$

Using the maximum amplitude, iteration of Eqn. (7.2) was done to obtain the damping ratio. Subsequently the frequency ratio at resonance was obtained using Eqn. (7.1). The frequency ratio at resonance is also given by

$$r_m = \frac{\omega_m}{\omega_n}\ , \tag{7.3}$$

where ω_m is the frequency of maximum amplitude, obtained from the transfer function, in rad/s and ω_n is the natural frequency.

Therefore from Eqn. (7.3), the natural frequency of the system was determined. Using the mass of the slider *m* and the natural frequency, the stiffness *k* was determined using Eqn. (7.4).

$$k = \omega_n{}^2 m \ . \tag{7.4}$$

For all the tests performed, the damping ratio and stiffness were computed and plotted in Figs. 7.7 – 7.14 as a function of the number of layers and vibration amplitude.

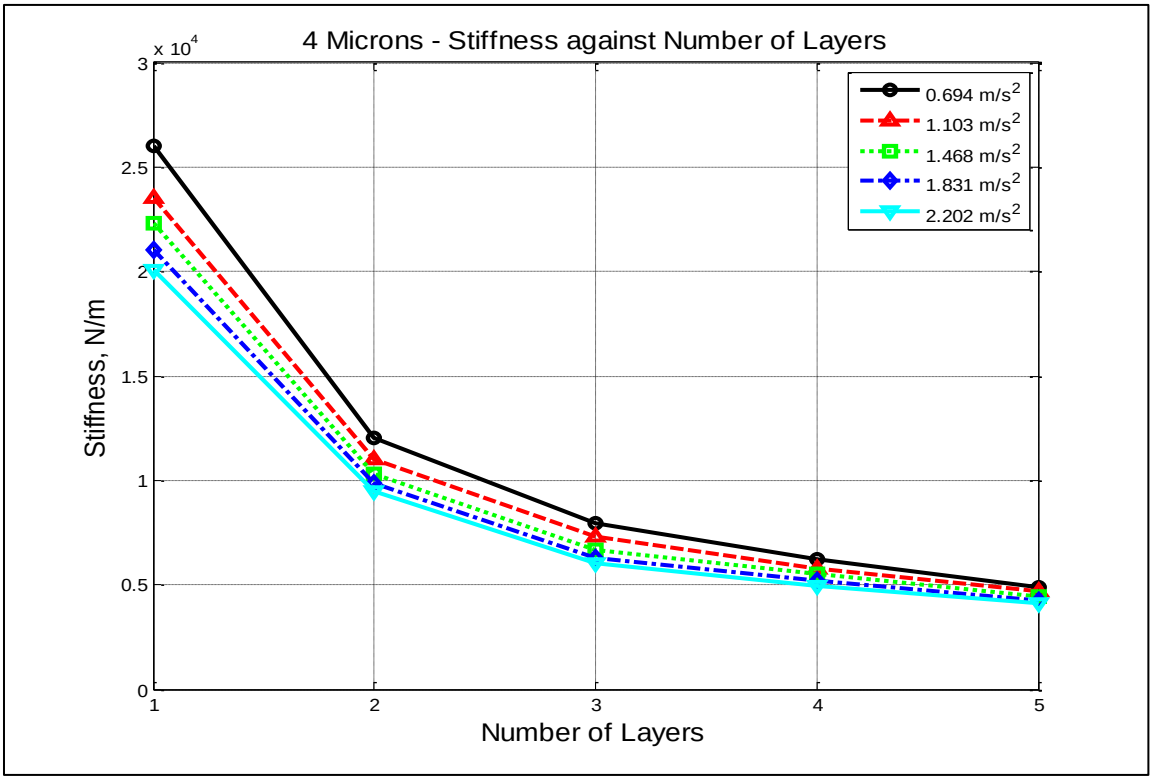

Figure 7.7 Stiffness of 4 microns media

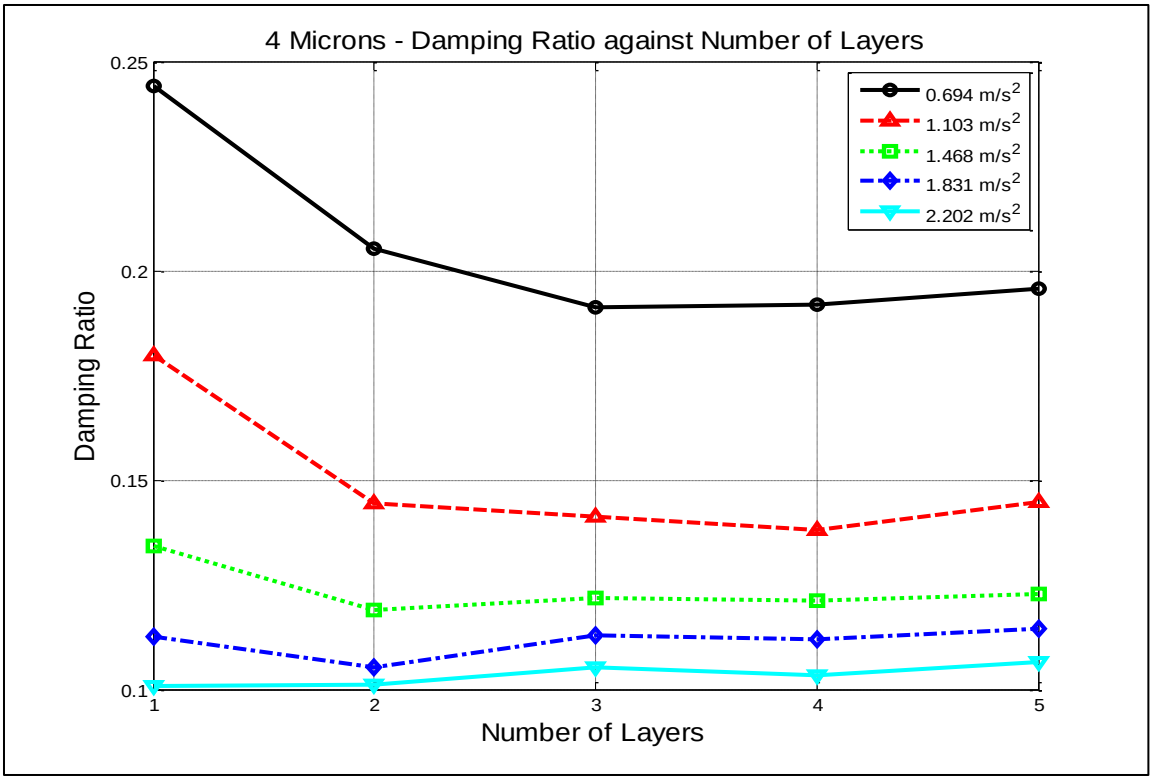

Figure 7.8 Damping ratio of 4 microns media.

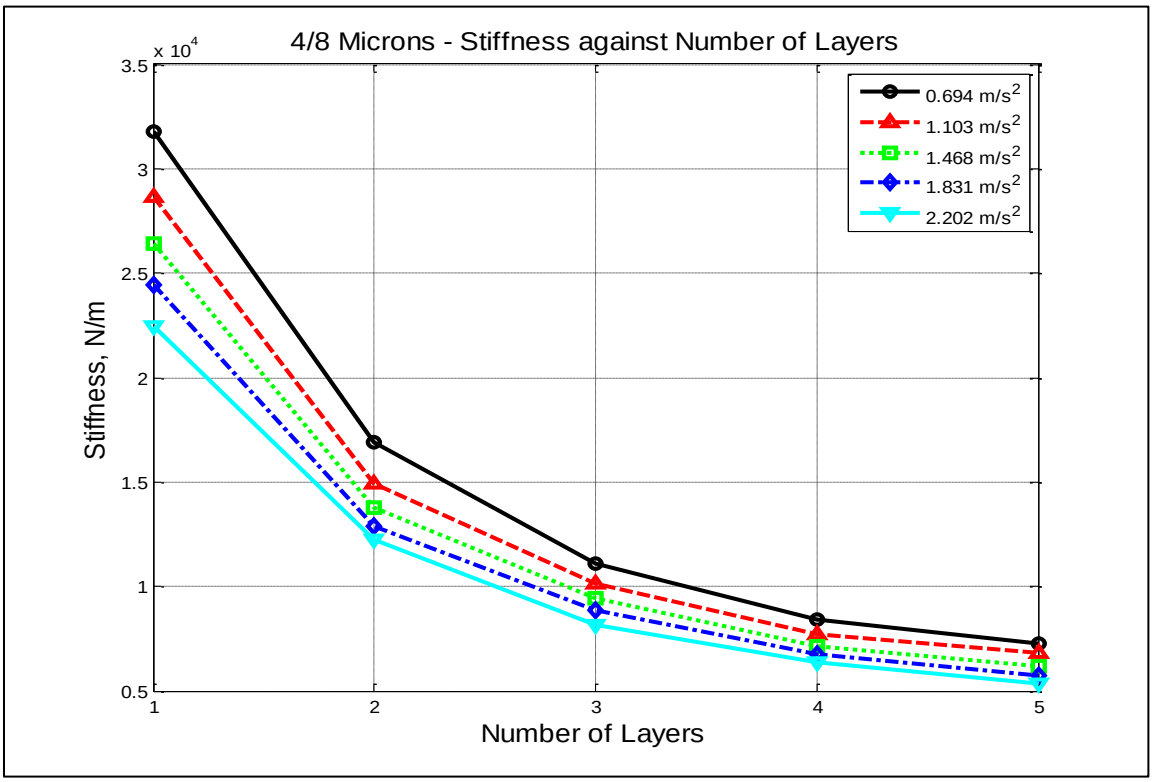

Figure 7.9 Stiffness of 4/8 microns media

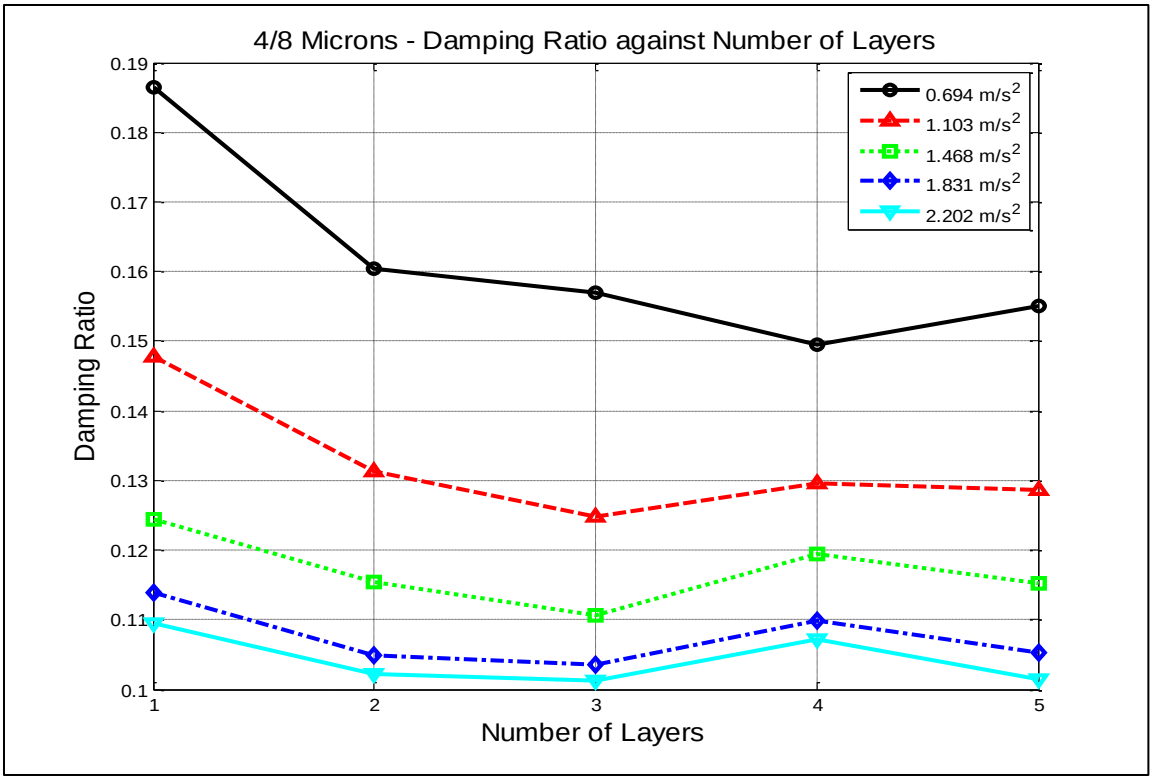

Figure 7.10 Damping ratio of 4/8 microns media.

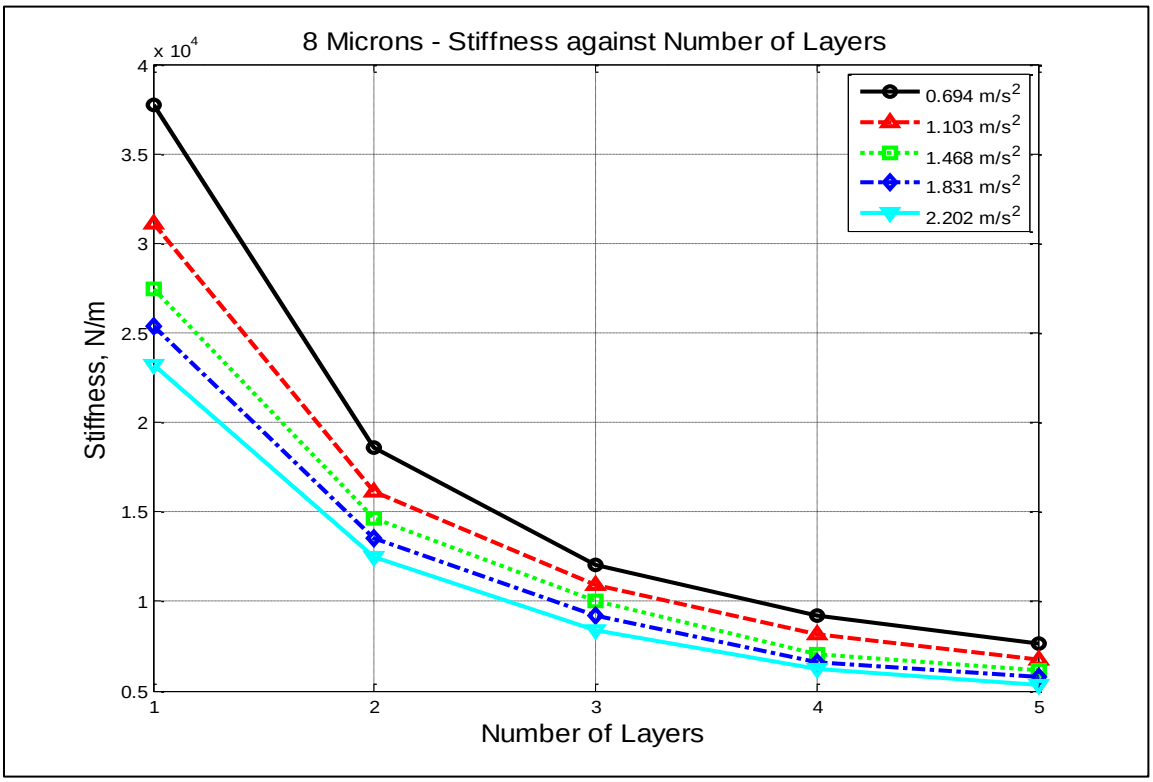

Figure 7.11 Stiffness of 8 microns media.

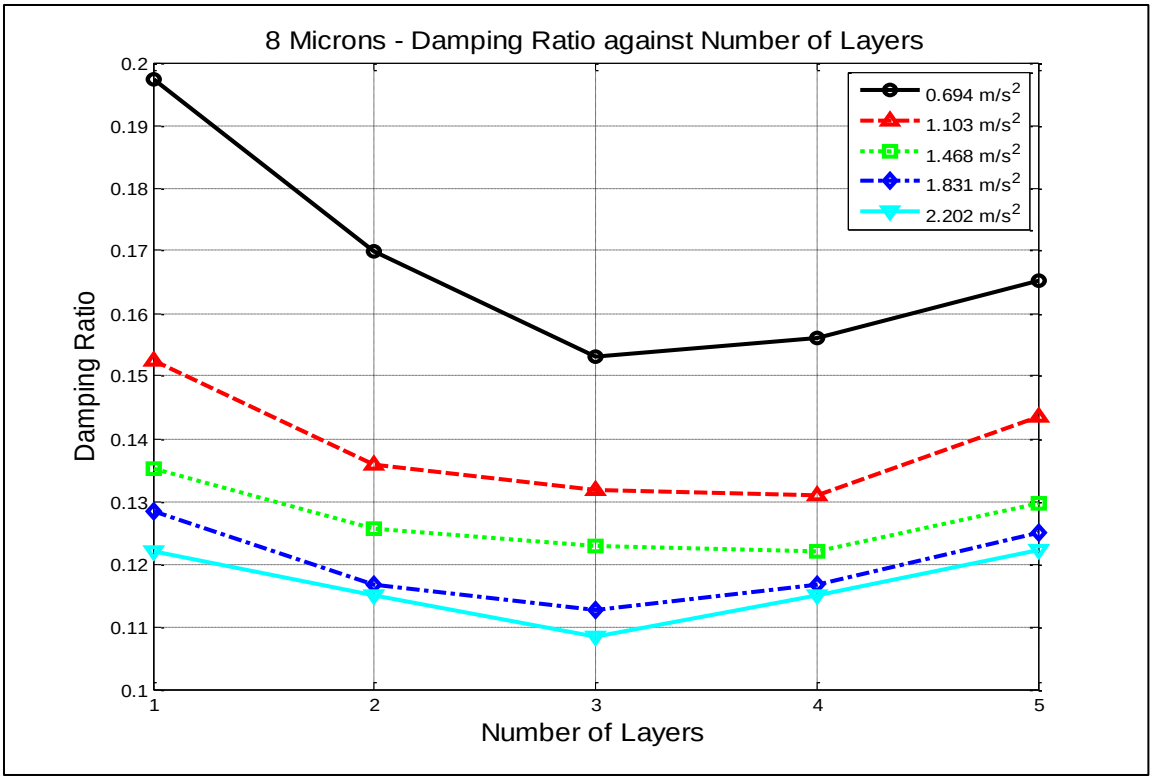

Figure 7.12 Damping ratio of 8 microns media.

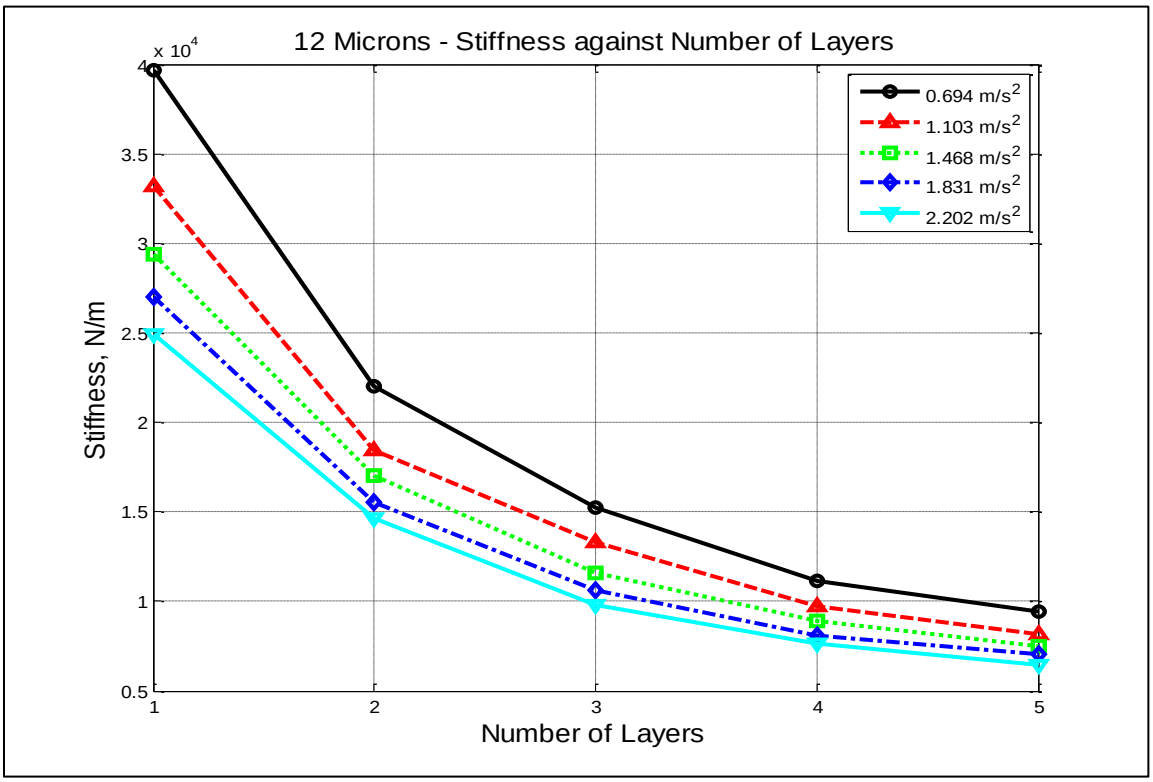

Figure 7.13 Stiffness of 12 microns media.

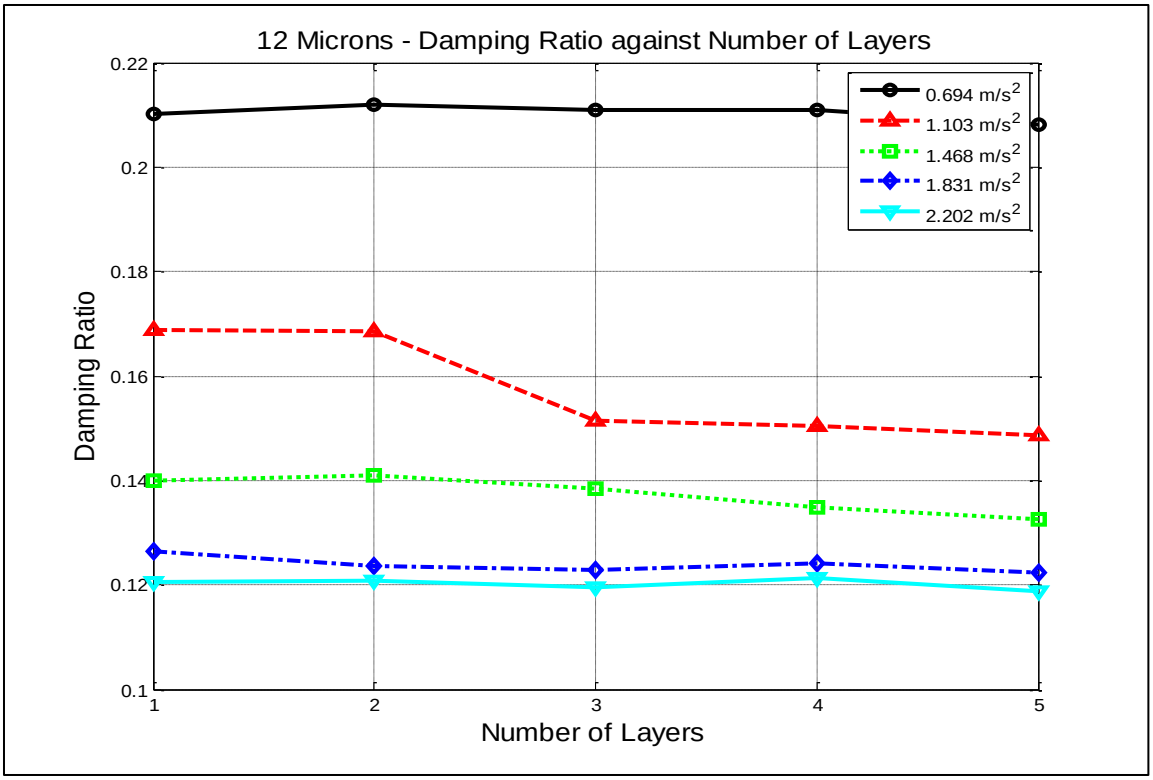

Figure 7.14 Damping ratio of 12 microns media.

7.6 Analysis of Results

With an increase in the number of layers, a decrease in the stiffness was observed. This is similar to adding springs in series causing the overall stiffness to decrease. The stiffness also decreased with an increase in vibration amplitude. This shows that the stiffness of the materials is nonlinear and that they behave a soft springs.

The damping ratio was found to be almost constant with an increase in the number of layers. The damping ratio is a property of the material, and therefore is not affected by the number of layers. The magnitude of the damping ratio is found to decrease with an increase in the vibration amplitude. This can be explained by the fact that damping in the system is proportional to the material damping and friction between

the slider and top frame. An increase in the vibration amplitude causes the friction to be less, reducing the total damping in the system.

CHAPTER 8

MITIGATION OF THE EFFECTS OF NOISE USING NICKEL MICROFIBROUS MATERIALS

In this chapter nickel microfibrous enclosures are designed and fabricated by sintering together layers of the microfibrous material. Experiments are then done in a reverberation room to validate the effectiveness of the enclosures for noise attenuation.

8.1 Enclosure Design and Fabrication

Based on the results obtained using the Delany-Bazley model (section 6.4), the absorption coefficient of a 10 mm thick microfibrous media at a sound frequency of 15 kHz was between 0.9 and 1.0. Therefore to obtain good noise attenuation, the enclosures were designed so that the gyroscope could be surrounded by 12 mm of the media on all sides. Since the media was fabricated in sheets, the enclosure was obtained by cutting the sheets into the desired dimension and stacking them as illustrated in Fig. 8.1(a). A wire mesh was then bent and shaped so as to hold all the stacked sheets (Fig. 8.1(b)), which were then sintered to give the final enclosure.

The sintering was done in a small continuous hydrogen furnace at 950 ^{o}C for 40 minutes. The wire mesh was placed at the bottom of a sintering tube which was then positioned inside the furnace (Fig. 8.2). Alumina fibers which can sustain a temperature of 1700 ^{o}C were placed on top of the furnace to prevent heat loss. The four enclosures made (one for each media type) are illustrated in Fig. 8.3.

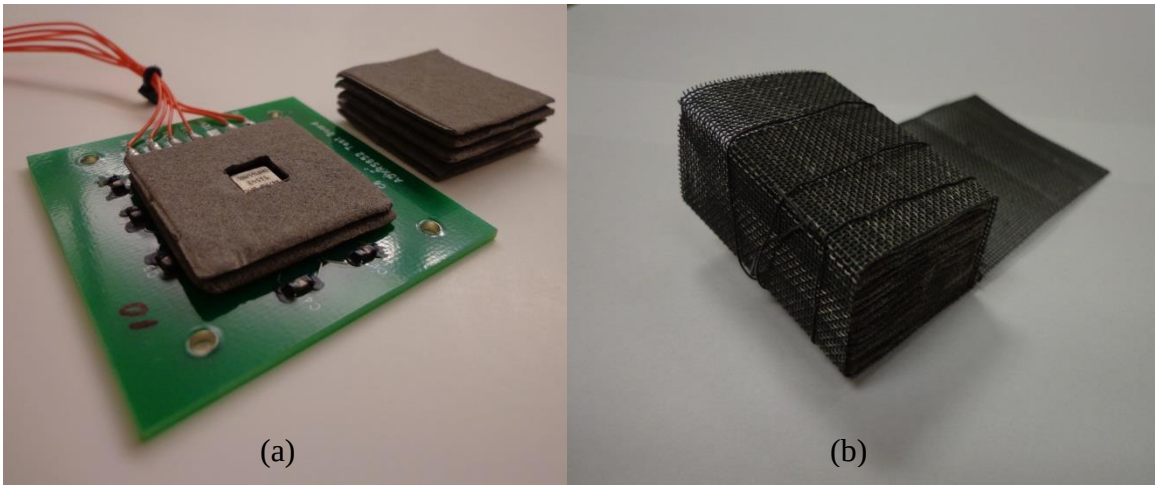

Figure 8.1 (a) Stacked sheets, and (b) Wire mesh frame.

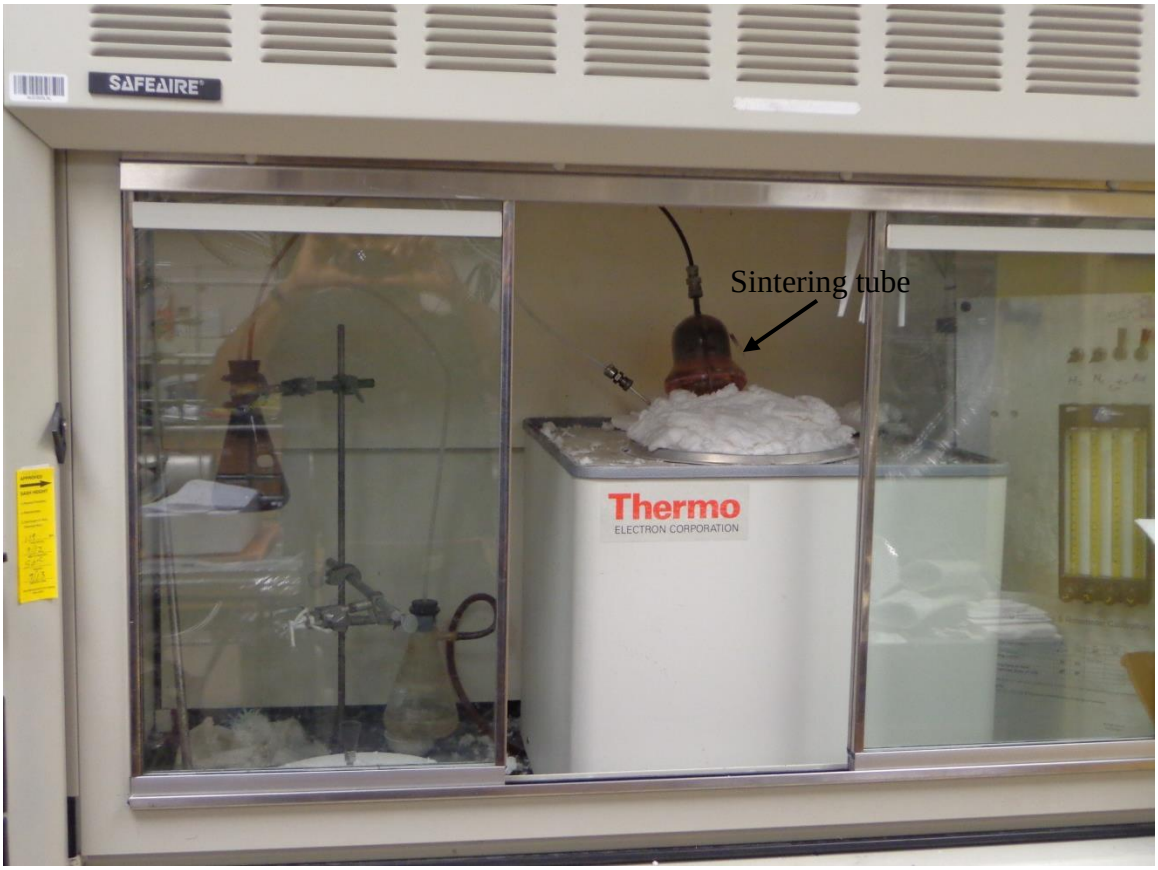

Figure 8.2 Photograph of furnace.

Figure 8.3 Photograph of enclosures showing top and bottom surfaces.

8.2 Experimental Validation of Enclosures

The equipment setup for the acoustical tests of section 4.2 was used for validating the effectiveness of the microfibrous enclosures. Seven gyroscopes, labeled G1-G7, were tested. For each gyroscope, a reference signal (without noise) was recorded. A pure tone was then generated at the natural frequency of the gyroscope, and at the maximum power of the amplifier. The effects of the noise on the gyroscope's output were recorded. Then one enclosure was placed on the gyroscope to attenuate the effects of the noise, but no reduction in the effects of noise was achieved. Investigations showed that the bottom surface of the enclosure was not perfectly flat and was not making full contact with the PCB, allowing noise to leak through. To solve this issue, a mass was placed on top of the enclosure as depicted in Fig. 8.4. With the mass on, considerable attenuation in the effects of noise was observed. The test was then repeated using the other enclosures and the other gyroscopes. Another problem that was encountered during testing was that the enclosure, being made of metal, was short-circuiting the surface mounted capacitors required for the gyroscope operation. Therefore liquid tape was used to electrically isolate the capacitors.

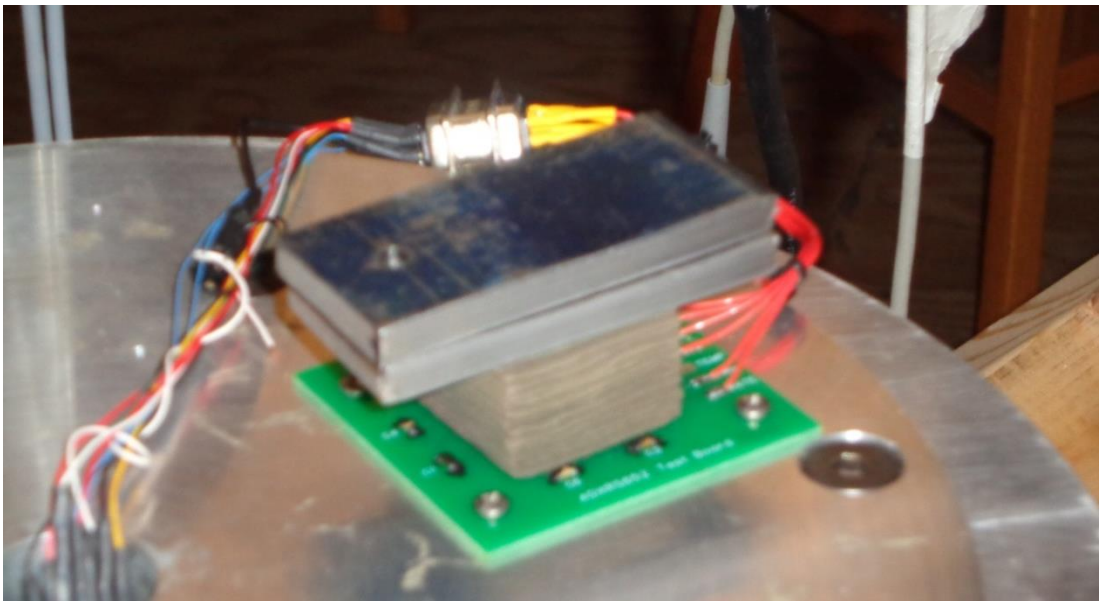

Figure 8.4 Photograph of mass sitting on top of enclosure.

The results of the acoustical tests performed on gyroscopes G1 and G2 are shown in Figs. 8.5 - 8.12, where each figure illustrates the gyroscope's outputs, namely, the reference signal, the output in the presence of noise, and the output with the enclosure on. Considerable reduction in the effects of noise on the gyroscopes is observed. The results for gyroscopes G3-G7 are found in Appendix F. Table 8.1 is a summary of all test results, in which the amplitudes of the effects of noise are compared to the attenuated amplitudes, and the attenuation as a percentage of the amplitude of the effects of noise computed.

8.3 Conclusions

The experimental results show that the enclosures have been effective in attenuating the effects of noise on the MEMS gyroscopes. Though the effects are not completely mitigated, up to 90% reduction in the amplitude of the effects of noise has been observed. On the average, 65% reduction in the effects of noise can be easily obtained. No major difference in attenuation was observed between the different

enclosures. This is due to the fact that they all have similar absorption coefficient at around 15 kHz.

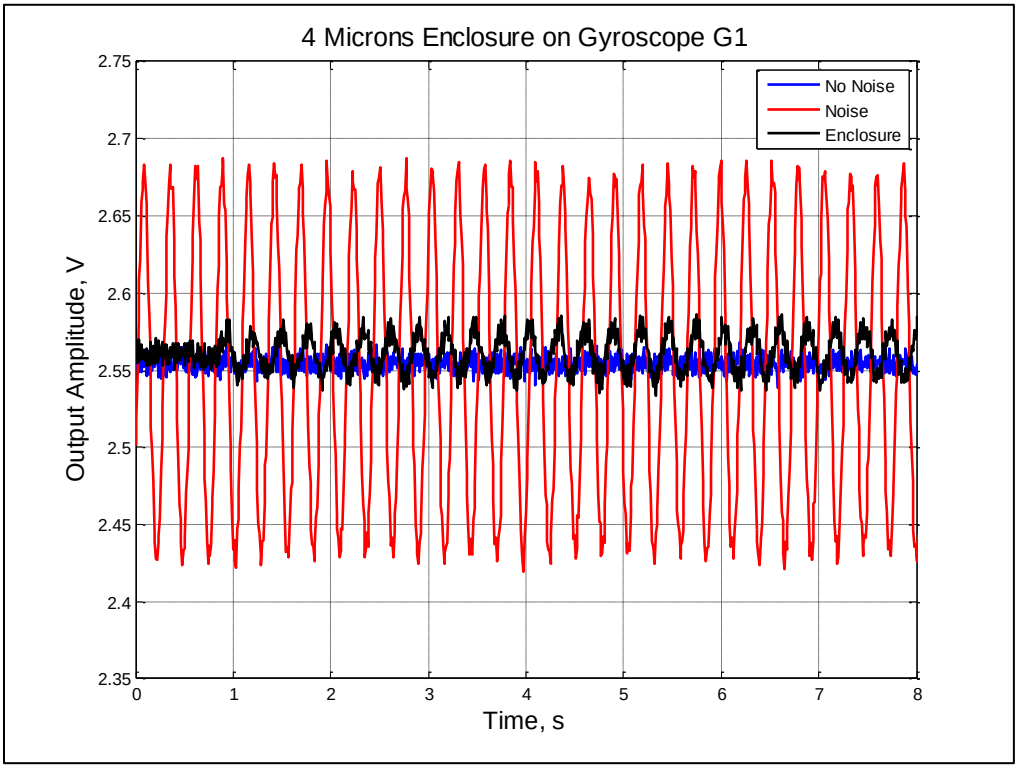

Figure 8.5 Experimental results of the 4 microns enclosure on gyroscope G1.

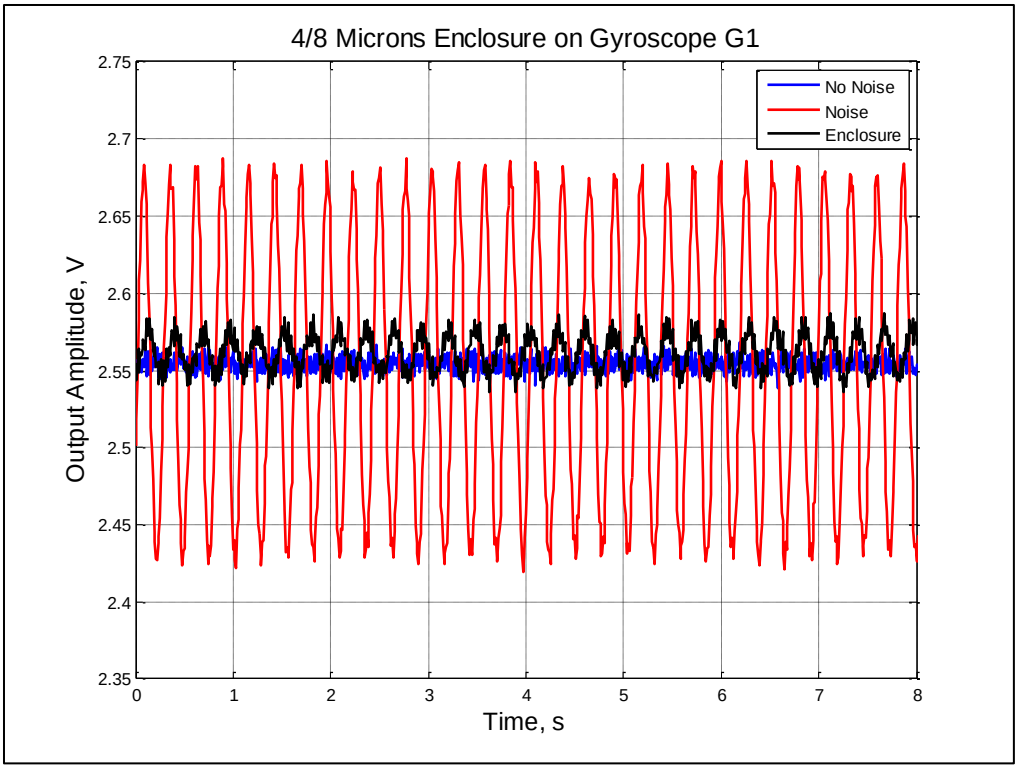

Figure 8.6 Experimental results of the 4/8 microns enclosure on gyroscope G1.

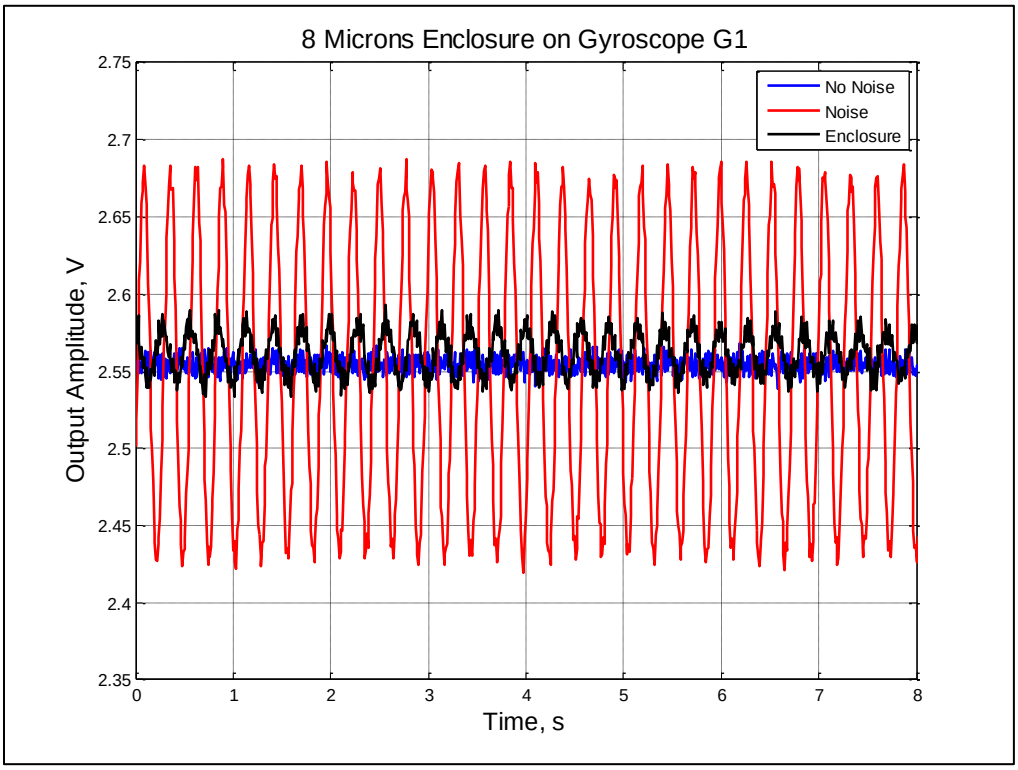

Figure 8.7 Experimental results of the 8 microns enclosure on gyroscope G1.

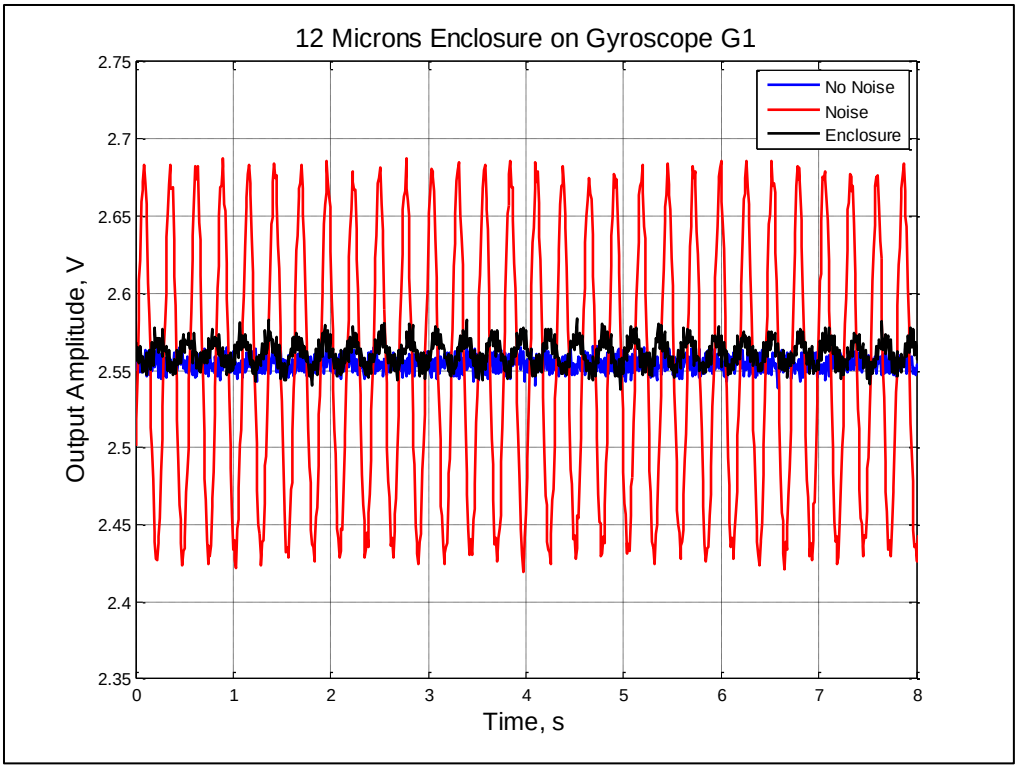

Figure 8.8 Experimental results of the 12 microns enclosure on gyroscope G1.

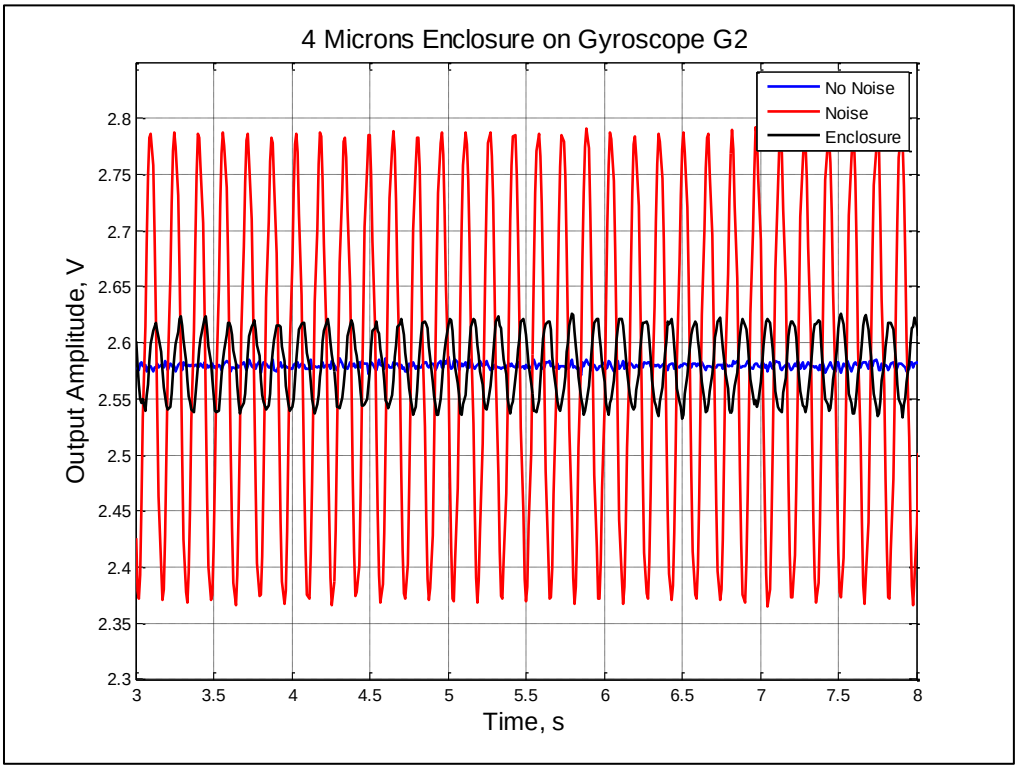

Figure 8.9 Experimental results of the 4 microns enclosure on gyroscope G2.

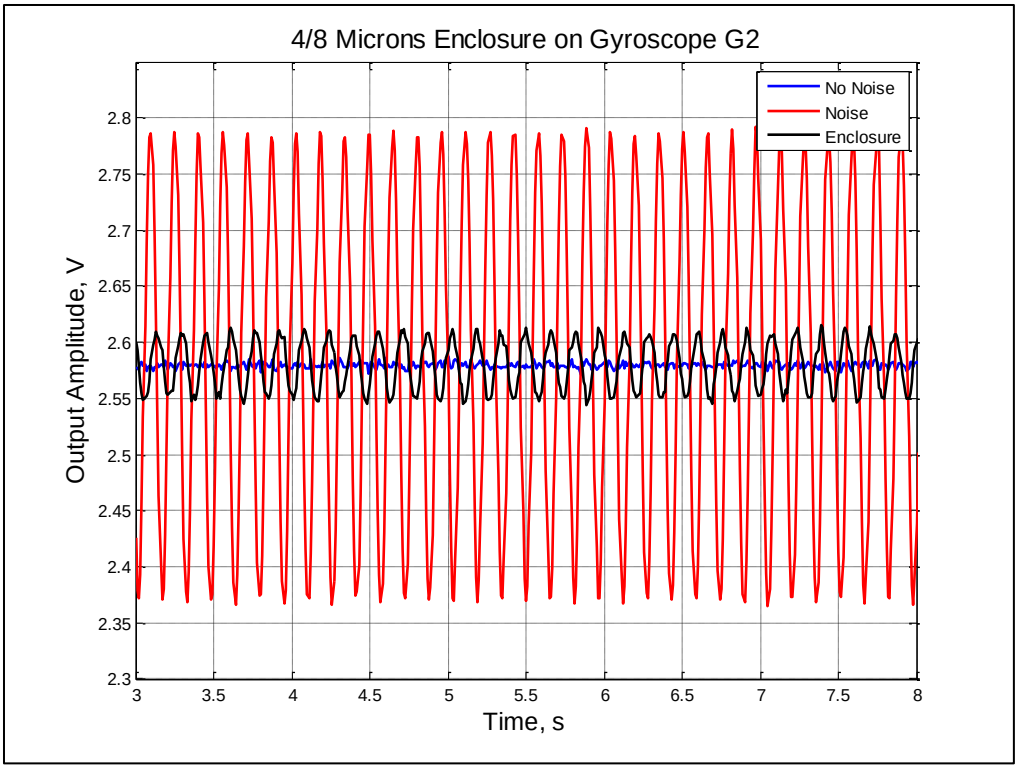

Figure 8.10 Experimental results of the 4/8 microns enclosure on gyroscope G2.

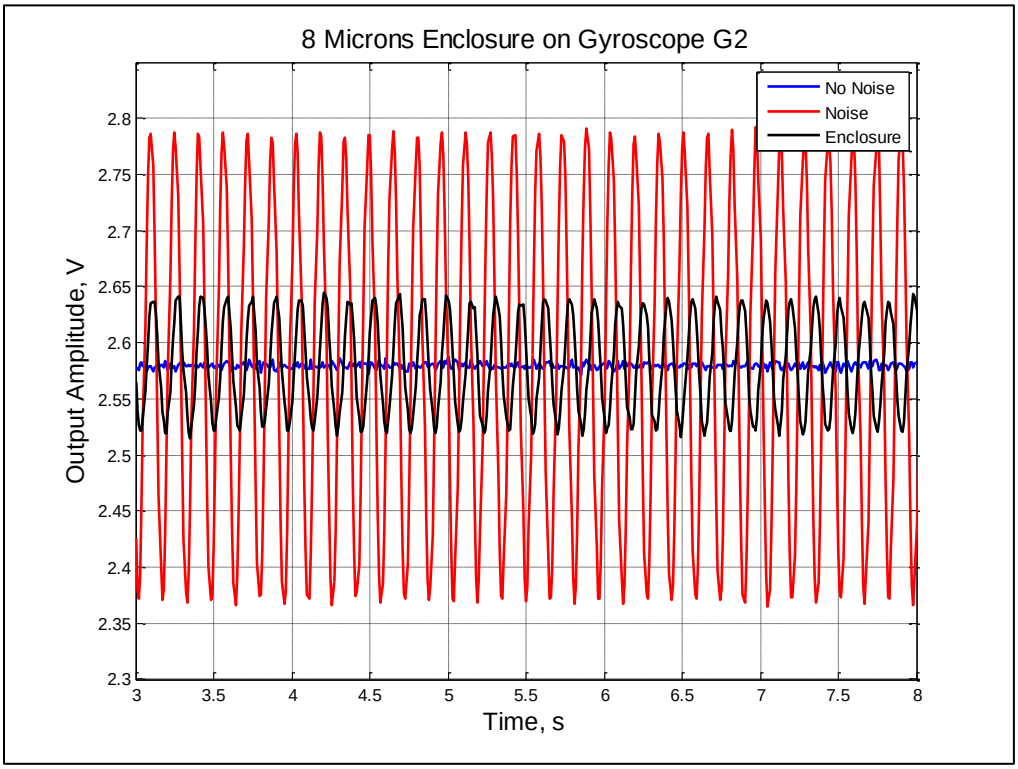

Figure 8.11 Experimental results of the 8 microns enclosure on gyroscope G2.

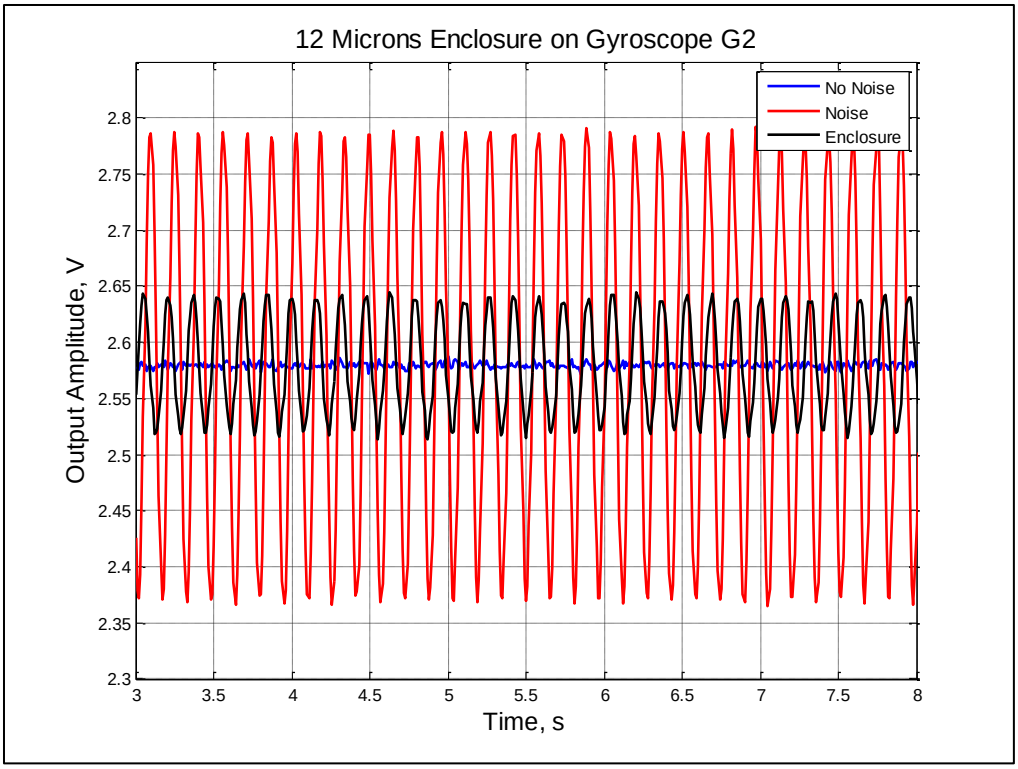

Figure 8.12 Experimental results of the 12 microns enclosure on gyroscope G2.

Gyro	Natural Frequency (Hz)	SPL (dB)	Amplitude of Noise Effects (mV)	Amplitude of Noise Effects with Enclosure (mV)				Percentage Reduction in the Amplitude of Noise Effects due to Enclosure (%)			
				4 microns	4/8 microns	8 microns	12 microns	4 microns	4/8 microns	8 microns	12 microns
G1	15031	119	128.5	20.5	22.0	24.0	18.0	84.0	82.9	81.3	86.0
G2	15114	118	207.5	42.5	32.0	60.0	48.0	79.5	84.6	71.1	76.9
G3	14492	115	93.5	43.0	24.0	53.0	42.0	54.0	74.3	43.3	55.1
G4	15105	118	136.0	32.5	13.0	25.5	30.0	76.1	90.4	81.3	77.9
G5	15227	119	201.5	118.5	103.5	150.5	105.0	41.2	48.6	25.3	47.9
G6	14883	123	123.0	51.0	34.0	34.5	46.0	58.5	72.4	72.0	62.6
G7	15066	119	137.0	62.5	72.0	73.0	73.0	54.4	47.5	46.7	46.7

Table 8.1 Summary of experimental results.

CHAPTER 9

CONCLUSIONS AND SCOPE FOR FURTHER WORK

In this dissertation, ways to mitigate the effects of noise on MEMS gyroscopes have been suggested using two approaches. In the first approach, a mathematical model has been developed that includes an external noise signal affecting the gyroscopes. The simulations of the model show that the magnitude of the effects of noise on the gyroscope's output depends on the frequency contents of the noise signal. As expected, the maximum effect occurs when the frequency is equal to the natural frequency of the gyroscope. Also, when the frequency of noise is not near the natural frequency, no effect on the output of the gyroscope is observed. This concurs with the results of previous experimental tests performed on MEMS gyroscopes.

The simulations at different rotation rates in the presence of external noise show that at a zero rotation rate the gyroscope has a positive output amplitude but a zero output amplitude at a rotation rate of -0.92 rad/s. Further, an increase in rotation rate causes the sense response to increase. To explain these observations, the model was run at the same rotation rates but without the external noise. A comparison of the two cases shows that the presence of the noise causes an increase in the sense response amplitude. Also, the shift is greater when the rotation is negative. This effect is due to the Coriolis component of acceleration, which causes an increase in the amplitude when the rotation is negative (clockwise rotation) and a decrease in the amplitude when the rotation rate is positive

(counterclockwise). It is therefore concluded that the effects of the noise is superimposed on the normal output of the gyroscope.

To mitigate the superimposed effects of noise, a differential- measurement system consisting of two gyroscopes is suggested. The first gyroscope (Gyro 1) is a regular MEMS gyroscope, while the second gyroscope (Gyro 2) is a non-driven gyroscope and thus affected by the noise field only. In this configuration, the Gyro 2 is able to quantify the superimposed effects and subtracting its output from the output of Gyro 1 yields an uncorrupted output. Simulations were performed for two types of noise signals: a pure tone and band-limited white noise. In both cases, Gyro 2 was able to quantify the effects of noise and the differential-measurement system mitigated these effects on a MEMS gyroscope.

Experiments were performed on five gyroscopes to verify the simulations. The experimental results show that the difference between the outputs of the gyroscopes in the presence and absence of the external noise is almost constant. Since the amplitude of the supplied noise was made constant, it is concluded that the effects of noise were superimposed on the normal output of the gyroscope as indicated by the simulations. Further, because the superposition of the effects of noise was experimentally shown, a MEMS gyroscope not driven into oscillation is affected by the noise field only, and quantifies the amplitude of the effects of noise. Therefore, the experimental results confirm that mitigation of effects of noise can be achieved using the proposed differential measurement.

The second approach to mitigate the effects of noise was to use a nickel microfibrous material for noise attenuation. Four types of the material were made using

three diameters of fibers and a wet-lay papermaking process. The sheets had a porosity of at least 98%. The Delany-Bazley analytical model was used to determine the optimum acoustical properties of the media and the absorption coefficients were then computed. The results show that the four types of media have an absorption coefficient between 0.9 and 1.0 in the region of interest, which is 15 kHz.

The damping characterization of the materials was carried out using the displacement transmissibility concept. Different vibration amplitudes were used to test five stacked layers of the material. With an increase in the number of layers, a decrease in the stiffness was observed. This is similar to adding springs in series causing the overall stiffness to decrease. The stiffness also decreased with an increase in vibration amplitude. This shows that the stiffness of the materials is nonlinear and they behave as a soft spring. Being a property of the material, the damping ratio is not affected by the number of layers. The magnitude of the damping ratio is found to decrease with an increase in the vibration amplitude. This can be explained by the fact that damping in the system is proportional to the material damping and friction between the slider and the top frame of the fixture. An increase in the vibration amplitude causes the friction to decrease, reducing the total of the damping in the system.

Microfibrous enclosures were designed so that the gyroscope could be surrounded by 12 mm of the material on all sides. Four enclosures, one for each material type, were made by sintering together layers of the material. The experimental results show that the enclosures have been effective in attenuating the effects of noise on the MEMS gyroscopes. Though the effects are not completely mitigated, up to 90% reduction in the amplitude of the effects of noise has been observed. On average, 65% reduction in the

amplitude of the effects of noise can be easily obtained. No major difference in attenuation was observed between the different enclosures. This is due to the fact that they all have similar absorption coefficients at around 15 kHz.

In summary this research describes two different approaches that have been studied to mitigate the undesirable effects of noise fields on MEMS gyroscopes. In the first approach an active design is proposed by utilizing a pair of gyroscopes whose outputs can be manipulated to yield the desired uncorrupted results. In the second approach, a passive design is proposed using nickel microfibrous material as an acoustical enclosure. Considerable reductions in the effects of noise have been achieved, showing that the nickel microfibrous material can be used to construct an acoustical enclosure.

As further work to this dissertation, a gyroscope can be designed and fabricated to carry out the differential measurement. It is suggested to design Gyro 1 and Gyro 2 to have the same natural frequency and to fabricate them side by side on the same silicon-on-insulator wafer.

REFERENCES

1. Acar, C., Shkel, A., "MEMS Vibratory Gyroscopes Structural Approaches to Improve Robustness," Springer, 2009.
2. Meriam, J.L., Kraige, L.G., "Engineering Mechanics Dynamics," John Wiley and Sons, 2002.
3. Beeby, S., Ensell, G., Kraft, M., White, N., "MEMS Mechanical Sensors," Artech House Inc., 2004.
4. Mochida, Y., Tamura, M., Ohwada, K., "A micromachined vibrating rate gyroscope with independent beams for the drive and detection modes," Elsevier, Sensors and Acuators 80, 170-178, 2000.
5. Rashed, R., Momeni, H., "System Modeling of MEMS Gyroscopes," Mediterranean Conference on Control and Automation, 2007.
6. Acar, C., Shkel, A., "MEMS Gyroscopes with Structurally Decoupled 2-DOF Drive and Sense Mode Ocillators," Nanotech, Vol. 1, 2003.
7. Yunker, W.N., "Sound Attenuation Using MEMS Fabricated Acoustic Metamaterials," MS Thesis, Auburn University, 2012.
8. Brown, T. G., "Harsh Military Environments and Microelectromechanical (MEMS) Devices," Proceedings of IEEE Sensors, 2, pp. 753-760, 2003.

9. Weinberg, M. S., and Kourepenis, A., "Error Sources in In-plane Silicon Tuning-fork MEMS Gyroscopes," Microelectromechanical Systems, 15(3), pp. 479-491, 2006.

10. Dean, R., Flowers, G., Hodel, S., MacAllister, K., Horvath, R., Matras, A., Robertson, G., and Glover, R., "Vibration Isolation of MEMS Sensors for Aerospace Applications," Proceedings of the IMAPS International Conference and Exhibition on Advanced Packaging and Systems, Reno, NV, pp. 166-170, 2002.

11. Dean, R., Flowers, G., Ahmed, A., Hodel, A., Roth, G., Castro, S., Zhou, R., Rifki, R., Moreira, A., Grantham, B., Bittle, D., Brunsch, J., "On the degradation of MEMS gyroscope performance in the presence of high power acoustic noise," Proc. of ISIE, 1435-1440, 2007.

12. Dean, R., Castro, S., Flowers, G.T., Roth, G., Ahmed, A., Hodel, A.S., Grantham, B.E., Bittle, D. A., Brunsch, J.P., "A Characterization of the Performance of a MEMS Gyroscope in Acoustically Harsh Environments," Industrial Electronic, IEEE Transactions on, Vol 58, Issue 7, 2591-2596, 2011.

13. Yunker, W. N., Soobramaney, P., Black, M., Dean, R. N., Flowers, G. T., Ahmed, A., " The underwater effects of high power, high frequency acoustic noise on MEMS gyroscopes," Proc. of ASME IDETC2011-47180, 2011.

14. Castro, S., Roth, G., Dean, R., Flowers, G.T., Grantham, B., "Influence of acoustic noise on the dynamic performance of MEMS gyroscopes," ASME IMECE2007-42108, 2007.

15. Roth, G., "Simulation of the Effects of Acoustic Noise on MEMS Gyroscope," MS Thesis, Auburn University, 2009.

16. Yunker, W.N., Stevens, C.B., George, T. F., Dean R.N, "Sound attenuation using microelectromechanical systems fabricated acoustic metamaterials," Journal of Applied Physics 113, 024906, 2013.
17. Arenas, J.P., Crocker M.J., "Recent Trends in Porous Sound-Absorbing Materials," Sound and Vibration, 44(7), 12-18, 2010.
18. Harris, C.M., "Handbook of noise control," McGraw-Hill, Inc, 1957.
19. Ashby, M.F., Lu, T., "Metal foams: A survey, Science in China," Series B, Vol. 46, No. 6, 521-532, 2003.
20. Schmidt, M., Schwertfeger, F., "Applications for silica aerogel products," Journal of Non-Crystalline Solids, 225, 364-368, 1998.
21. Crocker M.J., "Handbook of acoustics," John Wiley & Sons, Inc., 1998.
22. Wilson, C.E., "Noise control," Krieger Publishing Company, 2006.
23. Vissamraju, K., "Measurement of Absorption Coefficient of Road Surfaces Using Impedance Tube Method," MS Thesis, Auburn University, 2005.
24. Delany, M.E., Bazley, E.N., "Acoustical properties of fibrous absorbent materials," Applied Acoustics, 3, 105-116, 1970.
25. Komatsu, T., "Improvement of the Delany-Bazely and Miki models for fibrous sound-absorbing materials," Acoustical Science and Technology, 29(2), 121-129, 2008.
26. Dunn, I.P., Davern W.A., "Calculation of Acoustic Impedence of Multi-layer Absorbers," Applied Acoustics 19, 321-334, 1986.
27. Voronina, N., "Acoustic Properties of Fibrous Materials," Applied Acoustics 42, 165-174, 1994.

28. Rivin, E.I., “Passive Vibration Isolation,” ASME Press, New York, 2003.

29. Rao, S.S., “Mechanical Vibrations,” Pearson Prentice Hall, New Jersey, 228-243, 2004.

30. Crede, C.E., “ Vibration and Shock Isolation,” John Wiley and Sons Inc., New York, 176-186, 1951.

31. Inman, D., “Encyclopedia of Vibration,” Volume 1, Academic Press, 2002.

32. Meffert, M. W., “Preparation & characterization of sintered metal microfiber based composite materials for heterogeneous catalyst application,” PhD dissertation, Auburn University, 60-64, (1998).

33. Tatarchuk, B. J., Rose, M. F., Krishnagopalan, A., “Mixed fiber composite structures,” US Patent 5,102,745, April 7, 1992.

34. Tatarchuk, B. J., Rose, M. F., Krishnagopalan, A., Zabasajja, J. N., Kohler, D. “Preparation of mixed fiber composite structures,” US Patent 5,304,330, April 19, 1994.

35. Burch, N. H., Black, M. N., Dean, R. N., Flowers, G. T., “Microfibrous metallic cloth for damping enhancement in printed circuit boards,” Proc. SPIE 7643, 2010.

36. Zhu, W. H., Flanzer, M. E., Tatarchuk, B.J., “Nickel–zinc accordion-fold batteries with microfibrous electrodes using a papermaking process”, Journal of Power Sources, 112, 353-366, 2002.

37. Harris, D. K., Cahela, D. R., Tatarchuk, B.J, “Wet layup and sintering of metal-containing microfibrous composites for chemical processing opportunities,” Composites Part A - Applied Science And Manufacturing, 32(8), 1117-1126, 2001.

38. Dean, R., Burch, N., Black, M., Flowers, G., "Microfibrous metallic cloth for acoustic isolation of a MEMS gyroscope," Proc. SPIE 7979, 2011.

39. Hyatt, N., Black, M., Dean, R., Flowers, G., Grantham, B., Garner, R., "Damping enhancement in printed circuit boards with potting materials or microfibrous metallic cloth," Proc. of IDETC/VIB-87846, 2009.

40. Storm, M. C., "Prediction of sintered fibrous metal liner influence on muffler sound attenuation performance and noise emission for single-cylinder motorcycle engine exhaust," Proc. of NCAD2008-73022, 2008.

41. Datasheet, "ADXRS652 ± 250^{o}/sec Yaw Rate Gyro," Analog Devices, Inc., Rev A.

42. Solberg, V., "Design Guidelines for Surface Mount and Fine-pitch Technology," McGraw-Hill, 1996.

43. Lindsey, D., "Digital Printed Circuit Design and Drafting," Bishop Graphics, Inc., 1986.

44. http://www.mathworks.com/help/simulink/slref/bandlimitedwhitenoise.html

45. http://enterprise.astm.org/filtrexx40.cgi?+REDLINE_PAGES/C522.htm

46. Hatch, M.R., "Vibration simulation using MATLAB and ANSYS," Chapman & Hall/CRC, 2001.

47. Bao, M.H., " Handbook of Sensors and Actuators," Elsevier, 2000.

APPENDIX A

A.1 Maximum Displacement Transmissibility

For a vibration system with base motion, the displacement transmissibility which is the ratio of the output displacement *X* to the input displacement *Y* is given by

$$\left|\frac{X}{Y}\right| = \left[\frac{1+4\zeta^2 r^2}{(1-r^2)^2+4\zeta^2 r^2}\right]^{1/2}, \tag{A.1}$$

where *r* is the frequency ratio and z is the damping ratio.

The frequency ratio r_m at the maximum displacement transmissibility is obtained by solving

$$\frac{d}{dr}\left[\left|\frac{X}{Y}\right|\right] = 0. \tag{A.2}$$

Differentiating the displacement transmissibility with respect to r:

$$\frac{d}{dr}\left\{\left[\frac{1+4\zeta^2 r^2}{(1-r^2)^2+4\zeta^2 r^2}\right]^{1/2}\right\} =$$

$$\frac{1}{2}\left[\frac{1+4\zeta^2 r^2}{(1-r^2)^2+4\zeta^2 r^2}\right]^{-1/2} \times \frac{\left\{\left[(1-r^2)^2+4\zeta^2 r^2\right](8\zeta^2 r)-(1+4\zeta^2 r^2)[-4r(1-r^2)+8\zeta^2 r]\right\}}{[(1-r^2)^2+4\zeta^2 r^2]^2} \quad . \tag{A. 3}$$

Simplifying Eqn. (A.3) and equating to zero give

$$4r - 4r^3 - 8\zeta^2 r^5 = 0. \tag{A.4}$$

or

$$2\zeta^2 r^4 + r^2 - 1 = 0. \tag{A.5}$$

Solving Eqn. (A.5) gives

$$r_m{}^2 = \frac{\sqrt{1+8\zeta^2}-1}{(2\zeta^2)^2}, \tag{A.6}$$

or

$$r_m = \frac{1}{2\zeta}\sqrt{\sqrt{1+8\zeta^2}-1}\ . \tag{A.7}$$

A.2 Damping Ratio as a Function of Maximum Amplitude

The maximum transmissibility amplitude A_m occurs at the frequency ratio r_m given by Eqn. (A.7). Substituting r_m in Eqn. (A.1) gives

$$A_m{}^2 = \left[\frac{1+4\zeta^2 r_m{}^2}{(1-r_m{}^2)^2+4\zeta^2 r_m{}^2}\right]. \tag{A.8}$$

Substituting Eqn. (A.7) in Eqn. (A.8) gives

$$A_m{}^2 = \frac{8\zeta^4\sqrt{1+8\zeta^2}}{\sqrt{1+8\zeta^2}\left(8\zeta^4-4\zeta^2+\sqrt{1+8\zeta^2}-1\right)}$$

$$= \frac{8\zeta^4}{\left(8\zeta^4-4\zeta^2+\sqrt{1+8\zeta^2}-1\right)}. \tag{A.9}$$

Therefore

$$A_m = \left[\frac{8\zeta^4}{8\zeta^4-4\zeta^2+\sqrt{1+8\zeta^2}-1}\right]^{1/2}. \tag{A.10}$$

APPENDIX B

B.1 Solving Equations of Motion

B.1.1 Drive Motion

The equation of motion for the drive direction is

$$m\ddot{x} + c\dot{x} + kx = F \sin wt \, . \tag{B.1}$$

Let

$$x_p = X \cos(wt - \emptyset) = X \cos wt \cos \emptyset + X \sin wt \sin \emptyset. \tag{B.2}$$

$$\therefore \dot{x}_p = -Xw \sin(wt - \emptyset) = -Xw \sin wt \cos \emptyset + Xw \cos wt \sin \emptyset, \tag{B.3}$$

and

$$\ddot{x}_p = -Xw^2 \cos(wt - \emptyset) = -Xw^2 \cos wt \cos \emptyset - Xw^2 \sin wt \sin \emptyset. \tag{B.4}$$

Substituting Eqns. (B.2) – (B.4) in Eqn. (B.1) gives

$$-mXw^2 \cos wt \cos \emptyset - mXw^2 \sin wt \sin \emptyset - cXw \sin wt \cos \emptyset +$$

$$cXw \cos wt \sin \emptyset + KX \cos wt \cos \emptyset + KX \sin wt \sin \emptyset = F \sin wt. \tag{B.5}$$

Separating the coefficients of $\sin wt$ and $\cos wt$ gives

$$-mXw^2 \sin wt \sin \emptyset - cXw \sin wt \cos \emptyset + KX \sin wt \sin \emptyset = F \sin wt, \tag{B.6}$$

and

$$-mXw^2 \cos wt \cos \emptyset + cXw \cos wt \sin \emptyset + KX \cos wt \cos \emptyset = 0. \tag{B.7}$$

Simplifying Eqns. (B.6) and (B.7) gives

$$X[(K - mw^2) \sin \emptyset - cw \cos \emptyset] = F, \tag{B.8}$$

and

$$X[(K - mw^2)\cos\emptyset + cw\sin\emptyset] = 0. \quad \text{(B.9)}$$

Solving Eqns. (B.8) and (B.9) gives

$$X = \frac{F}{[(K-mw^2)^2+(cw)^2]^{1/2}}, \quad \text{(B.10)}$$

and

$$\emptyset = \tan^{-1}\left(\frac{-(K-mw^2)}{cw}\right). \quad \text{(B.11)}$$

At drive force frequency $w = w_n$

$$\emptyset = 0, \quad \text{(B.12)}$$

and

$$x_p = X\cos w_n t. \quad \text{(B.13)}$$

Therefore

$$\dot{x}_p = -Xw_n\sin w_n t. \quad \text{(B.14)}$$

B.1.2 Sense Motion

The equation of motion for the sense direction is

$$m\ddot{y} + c\dot{y} + ky + 2m\Omega\dot{x} = 0. \quad \text{(B.15)}$$

Substituting Eqn. (B.14) in Eqn. (B.15) gives

$$m\ddot{y} + c\dot{y} + ky = 2m\Omega X w_n \sin w_n t. \quad \text{(B.16)}$$

Let

$$y_p = Y\sin(w_n t - \beta) = Y\sin w_n t\cos\beta - Y\cos w_n t\sin\beta. \quad \text{(B.17)}$$

Therefore

$$\dot{y_p} = Y w_n\cos(w_n t - \beta) = Yw_n\cos w_n t\cos\beta + Yw_n\sin w_n t\sin\beta, \quad \text{(B.18)}$$

and

$$\ddot{y}_p = -Y{w_n}^2 \sin(w_n t - \beta) = -Y{w_n}^2 \sin w_n t \cos\beta + Y{w_n}^2 \cos w_n t \sin\beta. \quad \text{(B.19)}$$

Substituting Eqns. (B.17) - (B.19) in Eqn. (B.16) gives

$$-mY{w_n}^2 \sin w_n t \cos\beta + mY{w_n}^2 \cos w_n t \sin\beta + cYw_n \cos w_n t \cos\beta + cYw_n \sin w_n t \sin\beta + KY \sin w_n t \cos\beta - K\,Y \cos w_n t \sin\beta = 2m\Omega X w_n \sin(w_n t). \quad \text{(B.20)}$$

Separating the coefficients of $\sin wt$ and $\cos wt$ gives

$$-mY{w_n}^2 \sin w_n t \cos\beta + cYw_n \sin w_n t \sin\beta + KY \sin w_n t \cos\beta = 2m\Omega X w_n \sin w_n t, \quad \text{(B.21)}$$

and

$$mY{w_n}^2 \cos w_n t \sin\beta + cYw_n \cos w_n t \cos\beta - K\,Y \cos w_n t \sin\beta = 0\ . \quad \text{(B.22)}$$

Simplifying Eqns. (B.21) and (B.22) gives

$$Y[(K - m{w_n}^2)\cos\beta + cw_n \sin\beta] = 2m\Omega X w_n\ , \quad \text{(B.23)}$$

and

$$Y[-(K - m{w_n}^2)\sin\beta + cw_n \cos\beta] = 0\ . \quad \text{(B.24)}$$

Solving Eqns. (B.23) and (B.24) gives

$$\beta = \tan^{-1}\frac{cw_n}{(K - m{w_n}^2)}\ , \quad \text{(B.25)}$$

and

$$Y = \frac{2m\Omega X w_n}{[(K - mw^2)^2 + (cw)^2]^{1/2}}\ . \quad \text{(B.26)}$$

At $w=w_n$

$$\beta = \frac{\pi}{2}\ , \quad \text{(B.27)}$$

and

$$y_p = Y \sin(w_n t - \frac{\pi}{2}) = -Y \cos w_n t\ . \quad \text{(B.28)}$$

$$\therefore y_p = \frac{-2m\Omega F}{c^2 w_n} \cos w_n t \ . \tag{B.29}$$

B.2 Natural Frequency Computation

B.2.1 Basic Vibratory Gyroscope

The equations of motion for the gyroscope of section 2.1.1 are reproduced below:

$$\ddot{x} + \frac{c_x}{m}\dot{x} + \left(\frac{k_x}{m} - \Omega^2\right)x - \ 2\Omega\dot{y} = \ \frac{F_D}{m}\sin \omega t \ , \tag{B.30}$$

and

$$\ddot{y} + \frac{c_y}{m}\dot{y} + \left(\frac{k_y}{m} - \Omega^2\right)y + \ 2\Omega\dot{x} = \ 0. \tag{B.31}$$

The equations of motion were converted to state space form

$$\dot{z} = Az + B, \tag{B.32}$$

where

$$z = \begin{bmatrix} z_1 \\ z_2 \\ z_3 \\ z_4 \end{bmatrix} = \begin{bmatrix} x \\ y \\ \dot{x} \\ \dot{y} \end{bmatrix}, \tag{B.34}$$

$$B = \begin{bmatrix} 0 \\ 0 \\ \frac{F_D}{m}\sin \omega t \\ 0 \end{bmatrix}, \tag{B.35}$$

and

$$A = \begin{bmatrix} 0 & 0 & 1 & 0 \\ 0 & 0 & 0 & 1 \\ \left(-\frac{k_x}{m} + \Omega^2\right) & 0 & -\frac{c_x}{m} & 2\Omega \\ 0 & \left(-\frac{k_y}{m} + \Omega^2\right) & -2\Omega & -\frac{c_y}{m} \end{bmatrix}. \tag{B.36}$$

The eigenvalues of matrix *A* were numerically computed in Matlab using the following parameters: m=1.0 x 10^{-8} kg, $k_x = k_y$ = 77.38 N/m, $c_x = c_y$ = 5 x 10^{-7} N.s/m and Ω = 1 rad/s. The computed eigenvalues were -25 ± 87967i and -25 ± 87965i. The damped

natural frequencies were obtained from the imaginary part of the eigenvalues [46] and were equal to 14000 Hz.

B.2.2 Gyroscope for Noise Simulation

The equations of motion of the gyroscope model of section 2.2.1 are reproduced below:

$$m_f\ddot{x}_f + c_x(\dot{x}_f - \dot{x}_p) + c_z\dot{x}_f + k_x(x_f - x_p) + k_z x_f - 2m_f\Omega\dot{y}_f - m_f\Omega^2 x_f = F_N \sin\omega t - F_D \sin\omega_n t, \quad \text{(B.37)}$$

$$m_p\ddot{x}_p + c_x(\dot{x}_p - \dot{x}_f) + k_x(x_p - x_f) - 2m_p\Omega\dot{y}_p - m_p\Omega^2 x_p = F_D \sin\omega_n t, \quad \text{(B.38)}$$

$$m_f\ddot{y}_f + c_y(\dot{y}_f - \dot{y}_p) + c_z\dot{y}_f + k_y(y_f - y_p) + k_z y_f + 2m_f\Omega\dot{x}_f - m_f\Omega^2 y_f = F_N \sin\omega t, \quad \text{(B.39)}$$

and

$$m_p\ddot{y}_p + c_y(\dot{y}_p - \dot{y}_f) + k_y(y_p - y_f) + 2m_p\Omega\dot{x}_p - m_p\Omega^2 y_p = 0. \quad \text{(B.40)}$$

The equations of motion were converted to state space form

$$\dot{z} = Az + B \quad \text{(B.41)}$$

where

$$z = \begin{bmatrix} z_1 \\ z_2 \\ z_3 \\ z_4 \\ z_5 \\ z_6 \\ z_7 \\ z_8 \end{bmatrix} = \begin{bmatrix} x_f \\ x_p \\ y_f \\ y_p \\ \dot{x}_f \\ \dot{x}_p \\ \dot{y}_f \\ \dot{y}_p \end{bmatrix}, \quad \text{(B.42)}$$

$$B = \begin{bmatrix} 0 \\ 0 \\ 0 \\ 0 \\ \frac{F_N}{m_f}\sin\omega t - \frac{F_D}{m_f}\sin\omega_n t \\ \frac{F_D}{m_p}\sin\omega_n t \\ \frac{F_N}{m_f}\sin\omega t \\ 0 \end{bmatrix} \quad \text{(B.43)}$$

and

$$A = \begin{bmatrix} 0 & 0 & 0 & 0 & 1 & 0 & 0 & 0 \\ 0 & 0 & 0 & 0 & 0 & 1 & 0 & 0 \\ 0 & 0 & 0 & 0 & 0 & 0 & 1 & 0 \\ 0 & 0 & 0 & 0 & 0 & 0 & 0 & 1 \\ -\frac{k_x}{m_f} - \frac{k_z}{m_f} + \Omega^2 & \frac{k_x}{m_f} & 0 & 0 & -\frac{c_x}{m_f} - \frac{c_z}{m_f} & \frac{c_x}{m_f} & 2\Omega & 0 \\ \frac{k_x}{m_p} & -\frac{k_x}{m_p} + \Omega^2 & 0 & 0 & \frac{c_x}{m_p} & -\frac{c_x}{m_p} & 0 & 2\Omega \\ 0 & 0 & -\frac{k_y}{m_f} - \frac{k_z}{m_f} + \Omega^2 & \frac{k_y}{m_f} & -2\Omega & 0 & -\frac{c_y}{m_f} - \frac{c_z}{m_f} & \frac{c_y}{m_f} \\ 0 & 0 & \frac{k_y}{m_p} & -\frac{k_y}{m_p} + \Omega^2 & 0 & -2\Omega & \frac{c_y}{m_p} & -\frac{c_y}{m_p} \end{bmatrix}. \quad \text{(B.44)}$$

The eigenvalues of matrix A were numerically computed in Matlab using the following parameters: m_f=3.8 x 10^{-4} kg, m_p =1.0 x 10^{-8} kg, k_x =k_y = 77.38 N/m, c_x = c_y = 5 x 10^{-7} N.s/m, k_z = 200 N/m, c_z = 5 x 10^{-3} N.s/m, and Ω = 1 rad/s.

The computed eigenvalues were: -25.001 ± 87968i, -25.001 ± 87966i, -6.5697 ± 724.44i, and -6.5878 ± 726.44i. The damped natural frequencies were obtained from the imaginary part of the eigenvalues and were equal to 14001 Hz, 14000 Hz, 115.3 Hz and 115.62 respectively.

B.3 Force Approximation from Sound Pressure Level

The sound pressure level L_P is given by

$$L_P = 10 \lg \left(\frac{{p^2}_{rms}}{{p^2}_{ref}} \right), \tag{B.45}$$

where ${p^2}_{rms}$ is the mean square sound pressure and p_{ref} is the hearing threshold pressure [22].

For a sound pressure level of 126 dB

$$10 \lg \left(\frac{{p^2}_{rms}}{{p^2}_{ref}} \right) = 126 \; dB. \tag{B.46}$$

Therefore

$$\begin{aligned} {p^2}_{rms} &= 10^{126/10} \times {p^2}_{ref} \\ &= 10^{126/10} \times (20 \times 10^{-6})^2 = 1592.4 \;\; \text{Pa}^2. \end{aligned} \tag{B.47}$$

The peak pressure for a pure tone is given by [22]

$$P = \sqrt{2 \times {p^2}_{rms}} \, . \tag{B.48}$$

Therefore

$$P = \sqrt{2 * 1592.4} = 56.43 \text{ Pa}$$

The force due to the sound pressure, *F*, was approximated by

$$F = P \times A \, , \tag{B.49}$$

where *A* is the surface area of one side of a gyroscope.

Therefore the approximated force was obtained:

$$F = 56.43 \times (7.2 \times 10^{-3}) \times (3.1 \times 10^{-3})$$

$$= 1.26 \text{ x } 10^{-3} \text{ N.}$$

APPENDIX C

C.1 Matlab Codes for Solving the Basic Vibratory Gyroscope Model

```
% Basic Vibratory Gyroscope
% 2 DOF

clc;
clear all;
close all;
format compact;
format short g;
diary off;

global B fd w mp kx ky cx cy;

% mass 'mp' of proof mass
mp = 1e-8;
%'fd' frequency of driving force
fd=14003;
% 'kx' stiffness in x direction
kx=77.38;
% 'ky' stiffness in y direction
ky=77.38;
% 'cx' damping in y direction
cx=5e-7;
% 'cy' damping in y direction
cy=5e-7;


% 'B' input amplitude of drive force signal
B=1e-6;

%'w' angular velocity of gyroscopic frame
w=1;

 init = [0,0,0,0];
[t,z] = ode45(@newgyro2dof, (0:0.000001:.6),init);

z1 = z(:,1);
z2 = z(:,2);
z3 = z(:,3);
z4 = z(:,4);
```

```
Q=[z1(3.90023e5:3.91023e5) z2(3.90023e5:3.91023e5)];
j=(1:1001)*0.000001;
figure(1)
subplot (2,1,1)
plot(j,Q(:,1),'LineWidth',1.5);
grid on
title('Drive Mode Response','FontSize',14);
xlabel ('Time, s','FontSize',12);
ylabel ('Displacement (x),  m','FontSize',12);
axis([0,1e-3,-3e-5,3e-5])

subplot (2,1,2)
plot(j,Q(:,2),'LineWidth',1.5);
grid on
title('Sense Mode Response','FontSize',14);
xlabel ('Time, s','FontSize',12);
ylabel ('Displacement (y),  m','FontSize',12);
axis([0,1e-3,-1.2e-6,1.2e-6])
```

```
% Basic Vibratory Gyroscope function
% 2 DOF

function zprime = newgyro2dof(t,z)

global B fd w mp kx ky cx cy;

zprime = zeros(4,1);

Fd=B*sin(2*pi*fd*t);

zprime(1)= z(3);
zprime(2)= z(4);
zprime(3)= -1/mp*(cx*z(3)+ kx*z(1))+ 2*w*z(4)+ w^2*z(1)+ Fd/mp;
zprime(4)= -1/mp*(cy*z(4)+ ky*z(2))- 2*w*z(3)+ w^2*z(2);

return;
```

C.2 Matlab Codes for Solving the Four-degree-of-freedom Gyroscope Model

```
% Simulation of the effects of noise on a gyrosocpe
% 4 DOF

clc;
clear all;
close all;
format compact;
```

```
format short g;
diary off;

global B C fd w mp mf fn kx ky kz cx cy cz;

% mass 'mp' of proof mass
mp = 1e-8;
% mass 'mf' of frame
mf = 3.8e-4;
%'fn' frequency of noise
fn=14003;
%'fd' frequency of driving force
fd=14003;
% 'kx' stiffness in x direction
kx=77.38;
% 'ky' stiffness in y direction
ky=77.38;
% 'kz' stiffness between gyro and pcb
kz=200;
% 'cx' damping in y direction
cx=5e-7;
% 'cy' damping in y direction
cy=5e-7;
% 'cz' damping between gyro and pcb
cz=5e-3;

% 'B' input amplitude of drive force signal
B=1e-6;
% 'C' input amplitude of disturbance force
C=1.26e-3;

%'w' angular velocity of gyroscopic frame
w=1;


init = [0,0,0,0,0,0,0,0];
[t,z] = ode45(@newgyro4dof, (0:0.000001:1.2),init);

z1 = z(:,1);
z2 = z(:,2);
z3 = z(:,3);
z4 = z(:,4);
z5 = z(:,5);
z6 = z(:,6);
z7 = z(:,7);
z8 = z(:,8);
z9=B*sin(2*pi*fd*t);

figure(1)
plot(t,z1,'b');
grid on
xlabel ('Time');
ylabel ('Displacement(Xf)');

figure(2)
```

```
plot(t,z2);
grid on
xlabel ('Time');
ylabel ('Displacement(xp)');


figure(3)
plot(t,z3);
grid on
xlabel ('Time');
ylabel ('Displacement(Yf)');

figure(4)
plot(t,z4);
grid on
xlabel ('Time');
ylabel ('Displacement(Yp)');

figure(5)
Youtput = z4-z3;
plot (t,Youtput);
grid on
xlabel ('Time');
ylabel ('Displacement(Youtpout)');




% Function for simulating noise on gyroscope
% 4 DOF

function zprime = newgyro4dof(t,z)

global B C fd w mp mf fn kx ky kz cx cy cz;

zprime = zeros(8,1);

Fd=B*sin(2*pi*fd*t);
FN=C*sin(2*pi*fn*t);

zprime(1)= z(5);
zprime(2)= z(6);
zprime(3)= z(7);
zprime(4)= z(8);
zprime(5)= -1/mf*(cx*(z(5)-z(6))+ cz*z(5)+ kx*(z(1)-z(2))+ kz*z(1))+
2*w*z(7)+ w^2*z(1)+ FN/mf - Fd/mf;
zprime(6)= -1/mp*(cx*(z(6)-z(5))+ kx*(z(2)-z(1)))+ 2*w*z(8)+ w^2*z(2)+
Fd/mp;
zprime(7)= -1/mf*(cy*(z(7)-z(8))+ cz*z(7)+ky*(z(3)-z(4))+ kz*z(3))-
2*w*z(5)+ w^2*z(3)+ FN/mf;
zprime(8)= -1/mp*(cy*(z(8)-z(7))+ ky*(z(4)-z(3)))- 2*w*z(6)+ w^2*z(4);

return;
```

APPENDIX D

The engineering drawings for the design and manufacture of the text fixtures are shown in the first section of this appendix. The second section contains a series of plots for the vibration experiments performed to characterize the nickel microfibrous materials. Each plot contains five transfer functions based on the source amplitudes used during the tests. The total number of plots for all the tests performed is 170 but only 40 plots are shown for brevity. As such there are two plots for each number of layers (1-5) for each of the four different material types used.

From each plot the natural frequencies and the maximum amplitudes of the transfer functions were recorded in tabular form. The third section of this appendix contains the tables for all the experiments performed (that is the 170 plots).

D.1 Mechanical Drawings for Fixture Parts

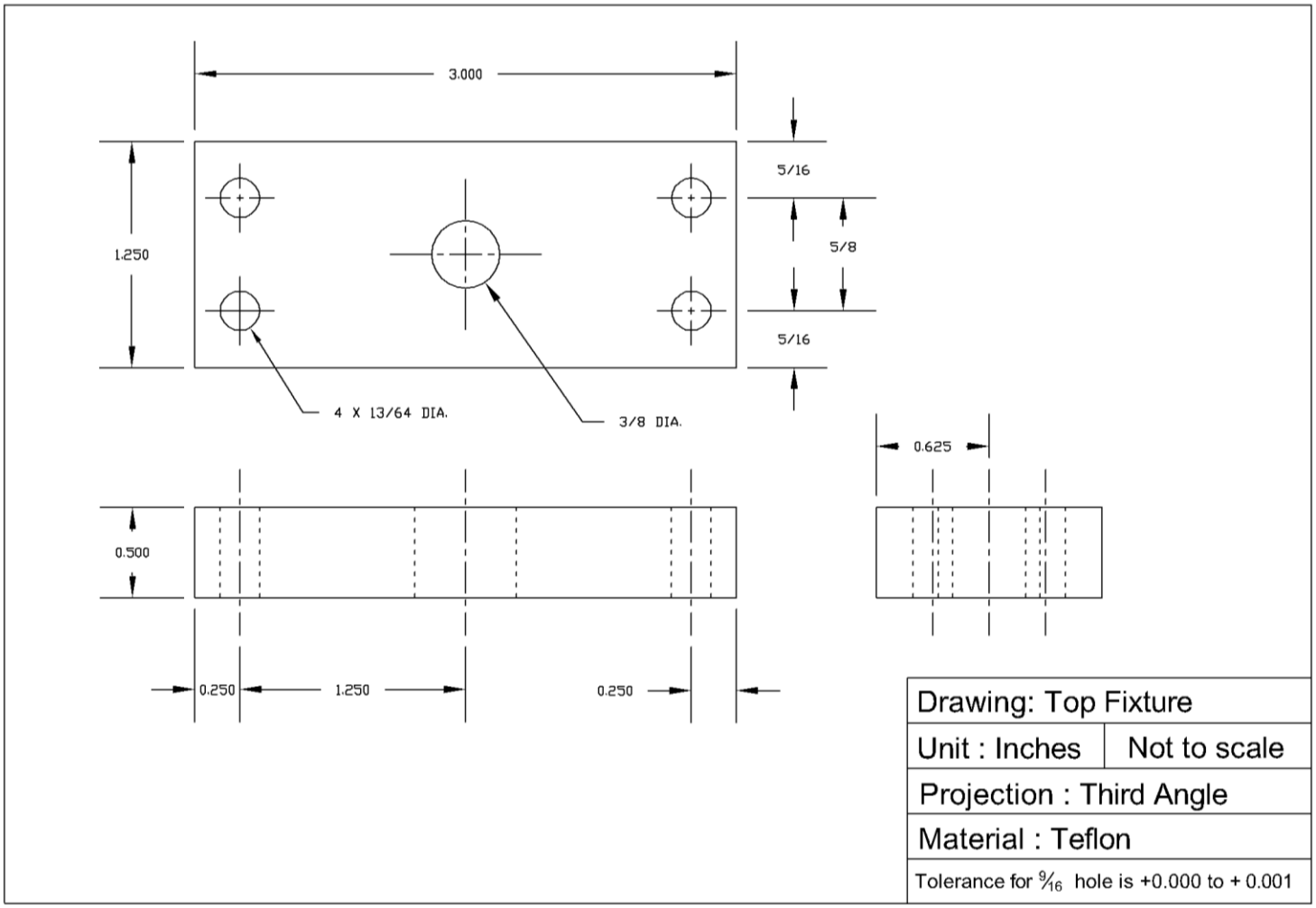

Figure D.1 Mechanical drawing of top fixture.

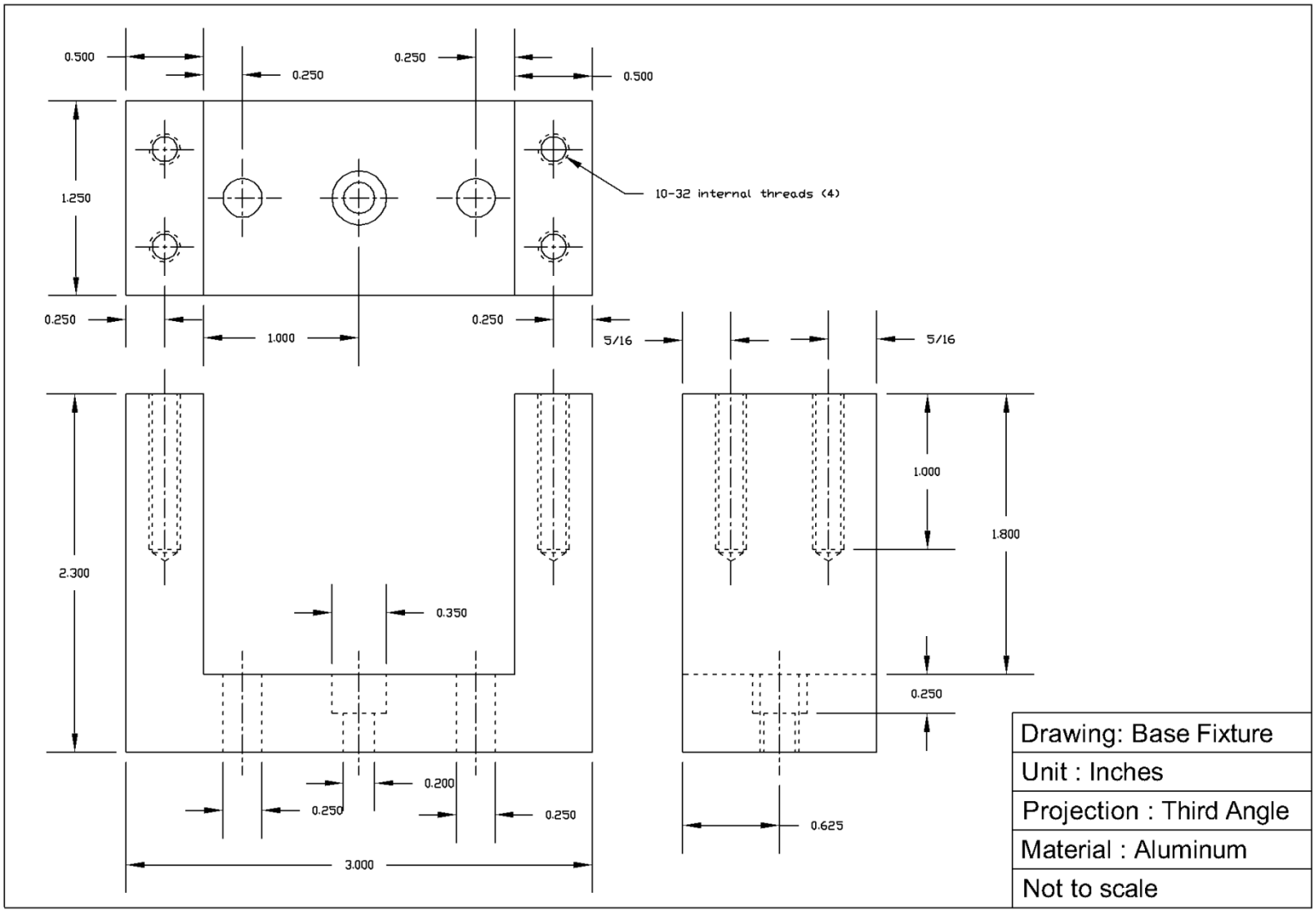

Figure D.2 Mechanical drawing of bottom fixture.

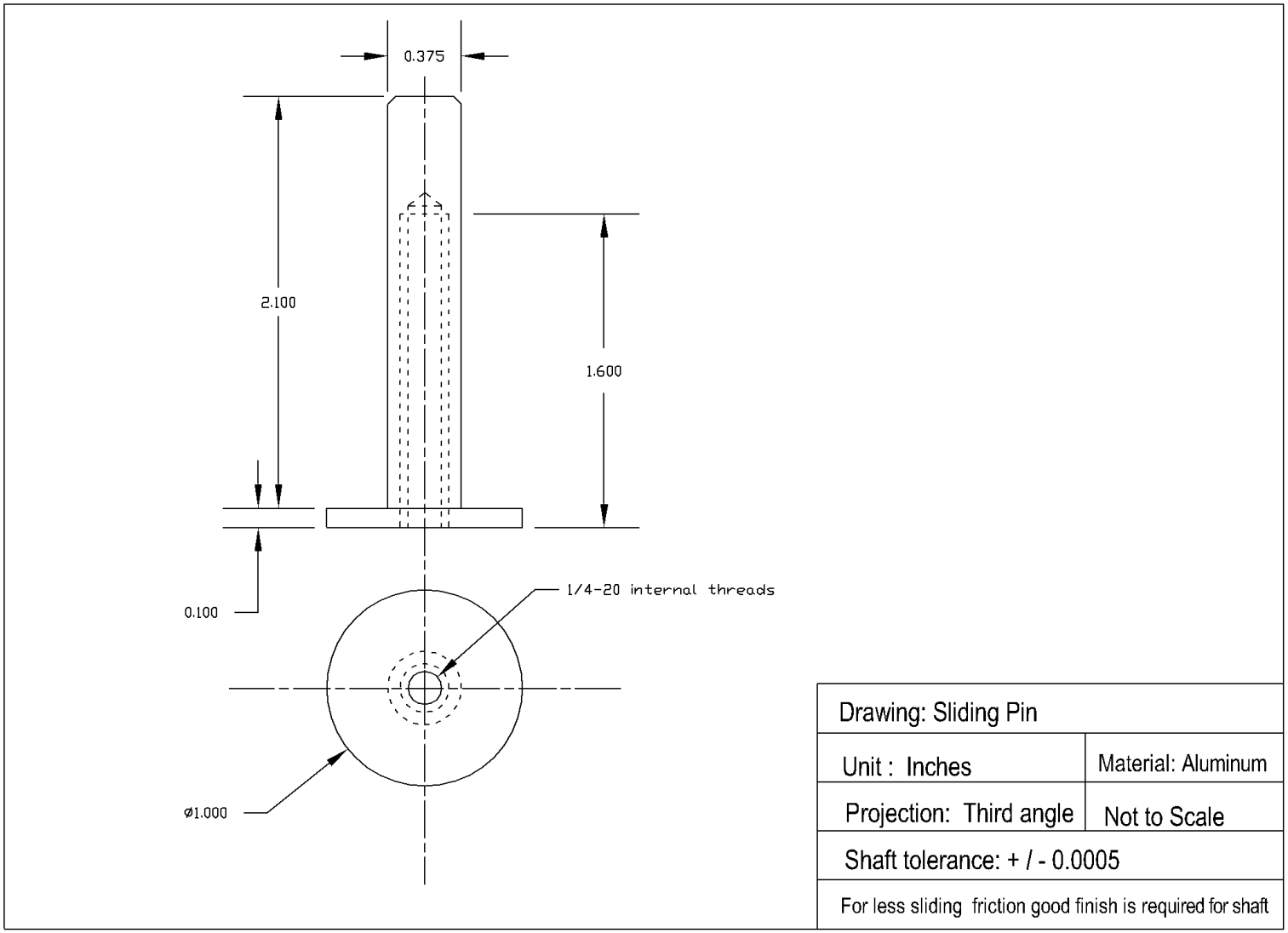

Figure D.3 Mechanical drawing of sliding pin.

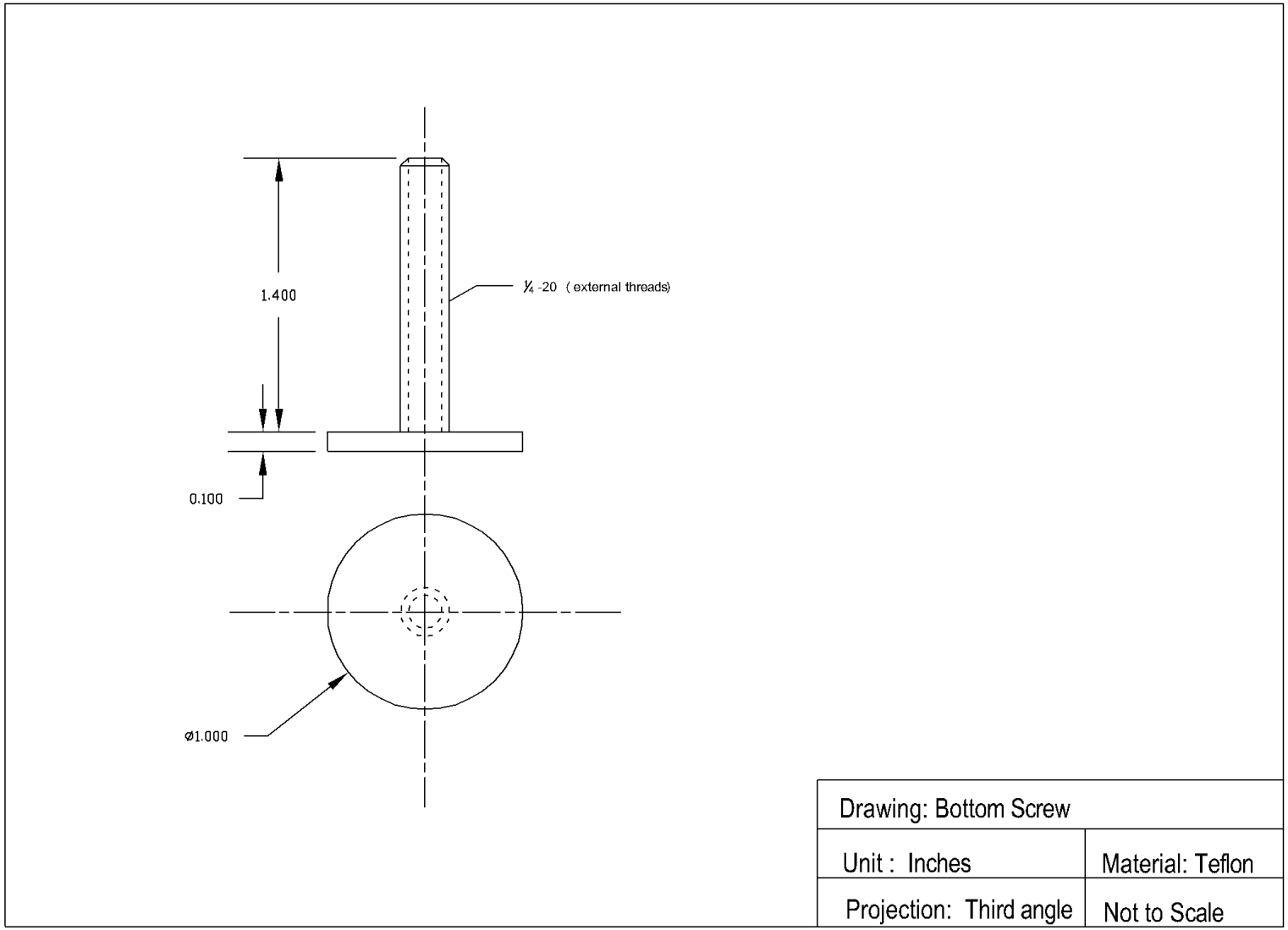

Figure D.4 Mechanical drawing of lower screw.

D.2 Plots of Vibration Tests

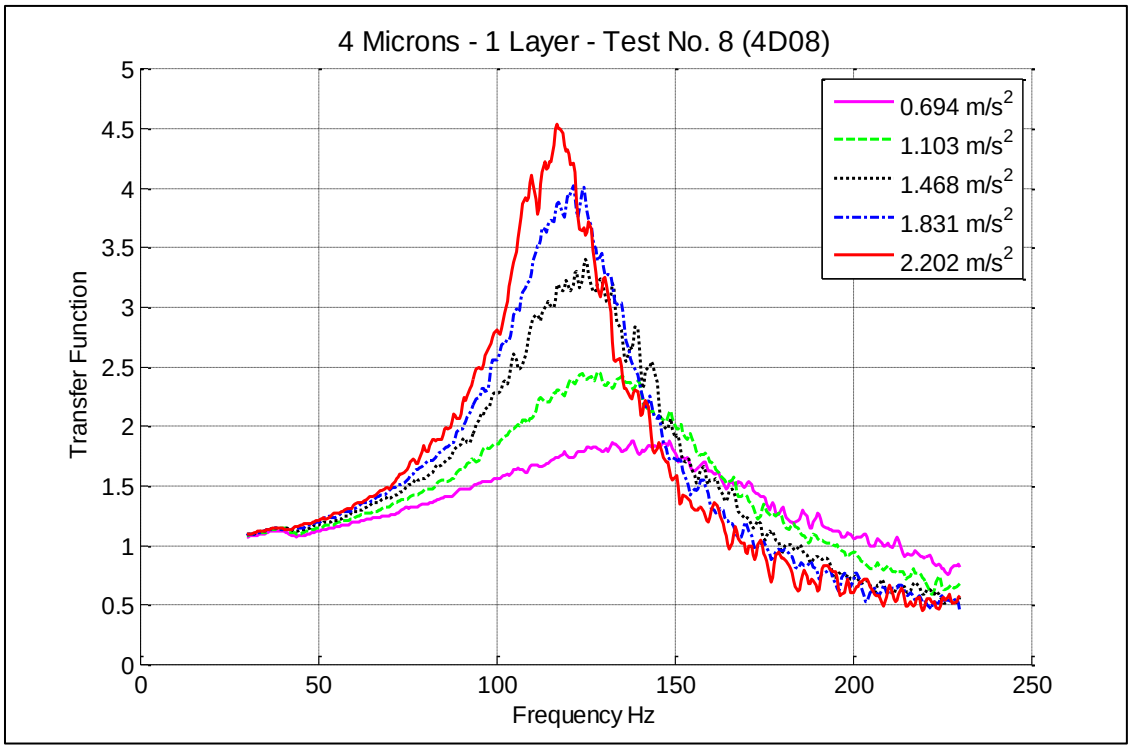

Figure D.5 Transfer functions for 1 layer (sample 08) of 4 microns media.

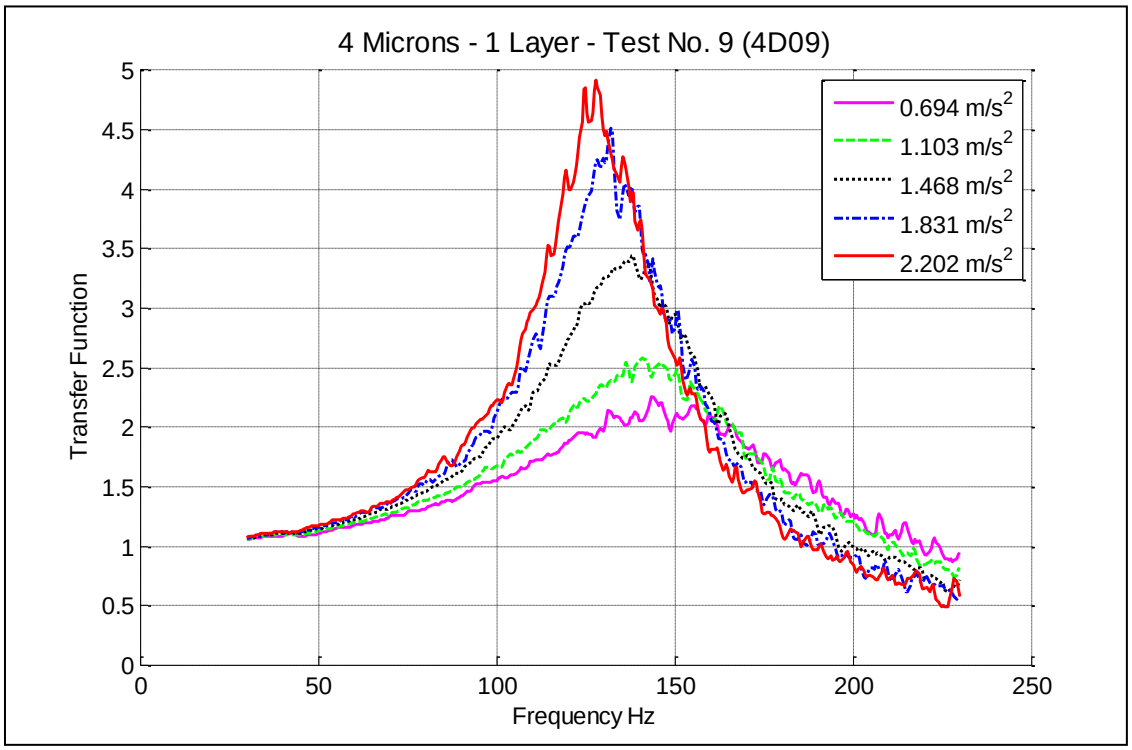

Figure D.6 Transfer functions for 1 layer (sample 09) of 4 microns media.

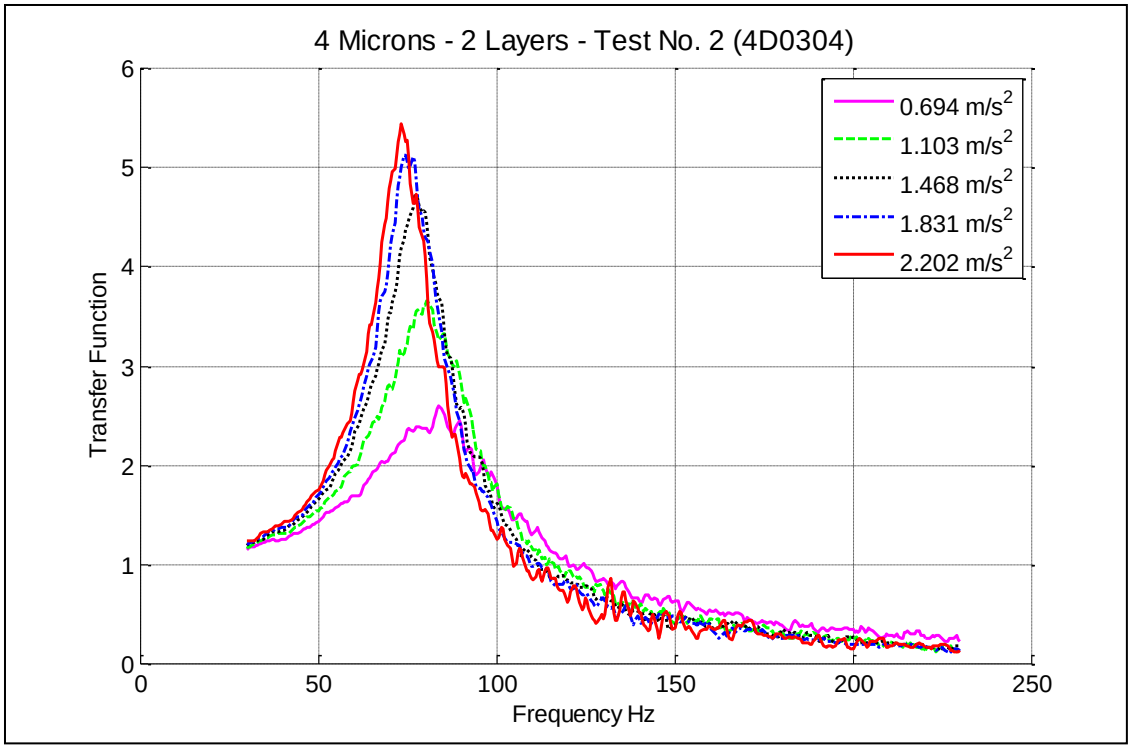

Figure D.7 Transfer functions for 2 layers (samples 03/04) of 4 microns media.

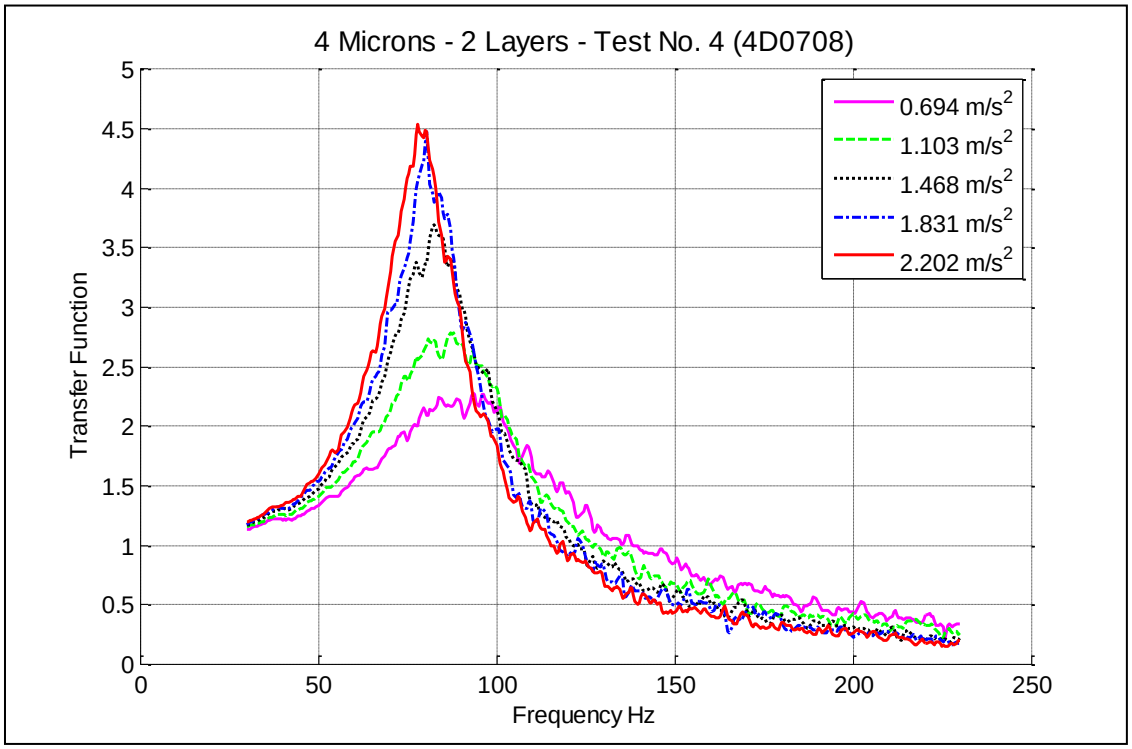

Figure D.8 Transfer functions for 2 layers (samples 07/08) of 4 microns media.

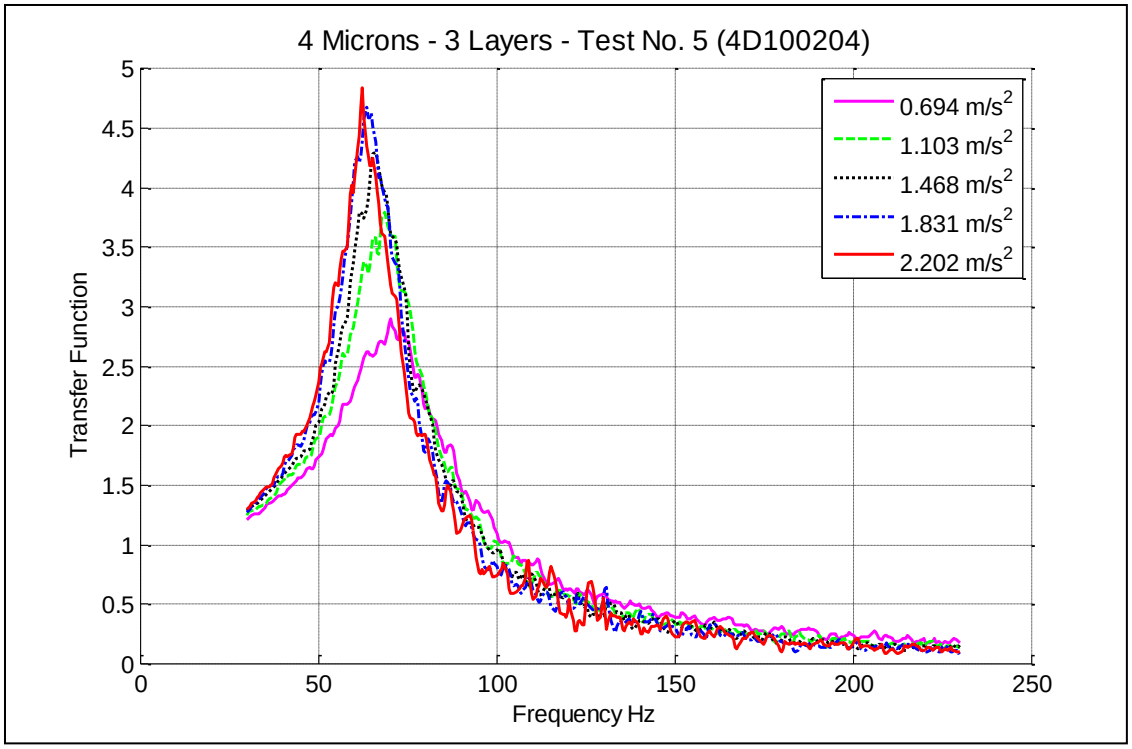

Figure D.9 Transfer functions for 3 layers (samples 10/02/04) of 4 microns media.

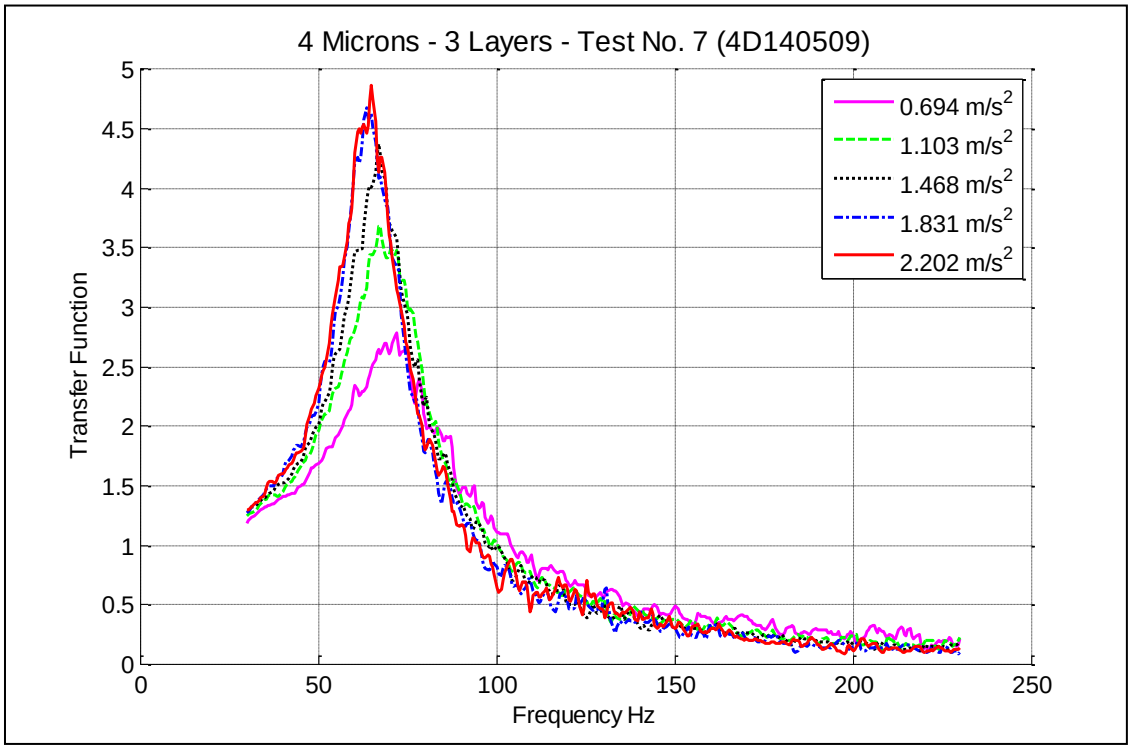

Figure D.10 Transfer functions for 3 layers (samples 14/05/09) of 4 microns media.

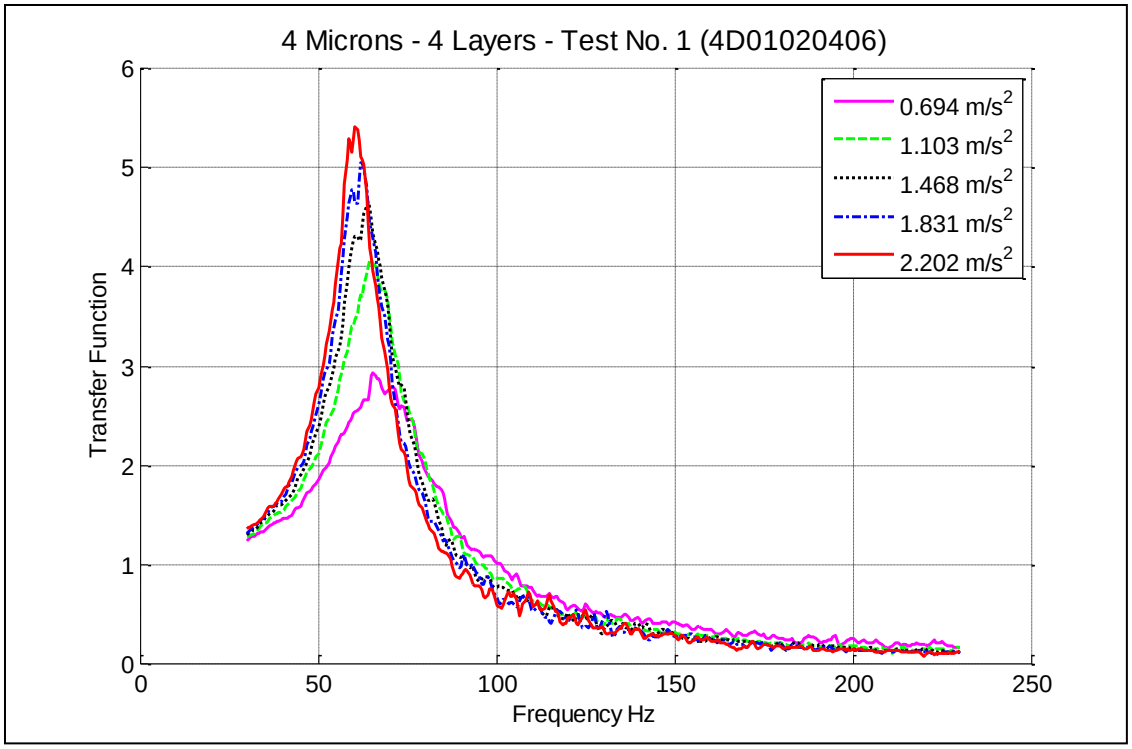

Figure D.11 Transfer functions for 4 layers (samples 01/02/04/06) of 4 microns media.

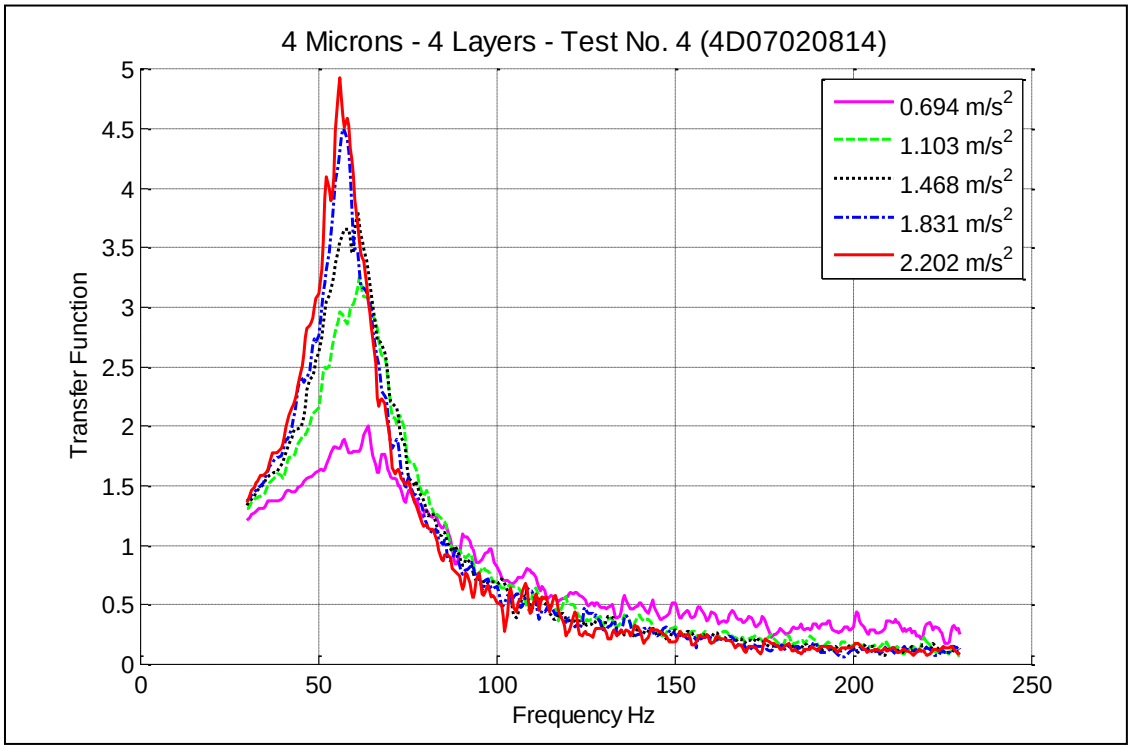

Figure D.12 Transfer functions for 4 layers (samples 07/02/08/14) of 4 microns media.

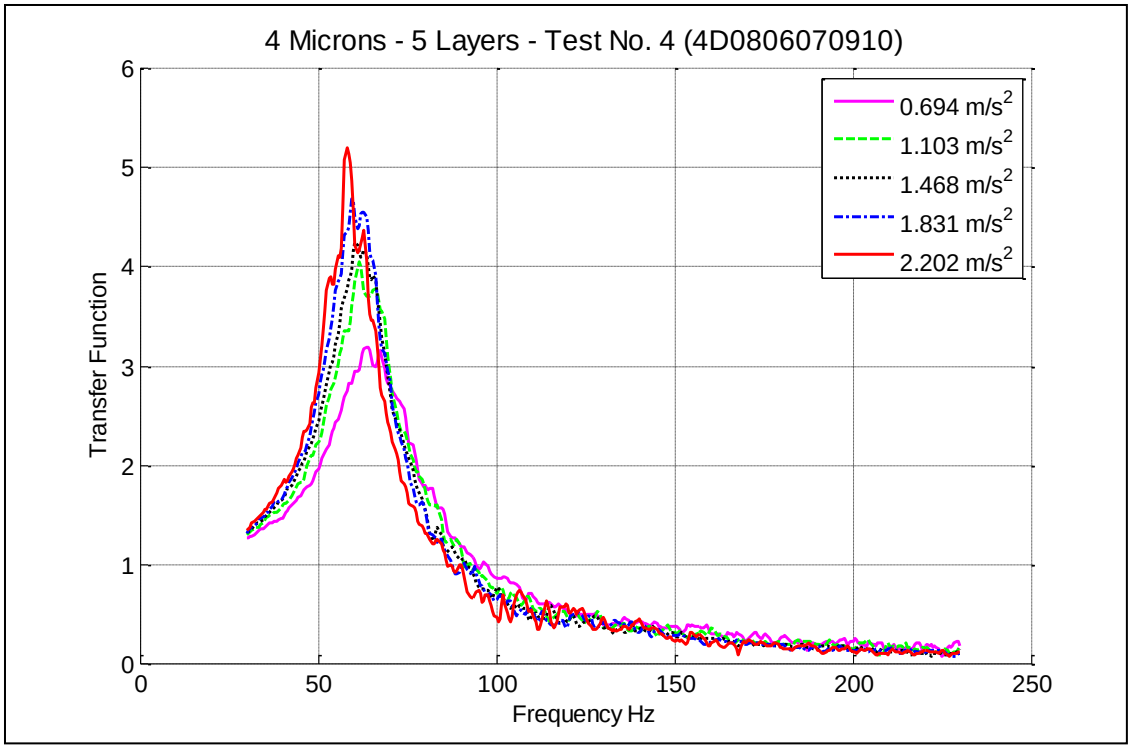

Figure D.13 Transfer functions for 5 layers (samples 08/06/07/09/10) of 4 microns media.

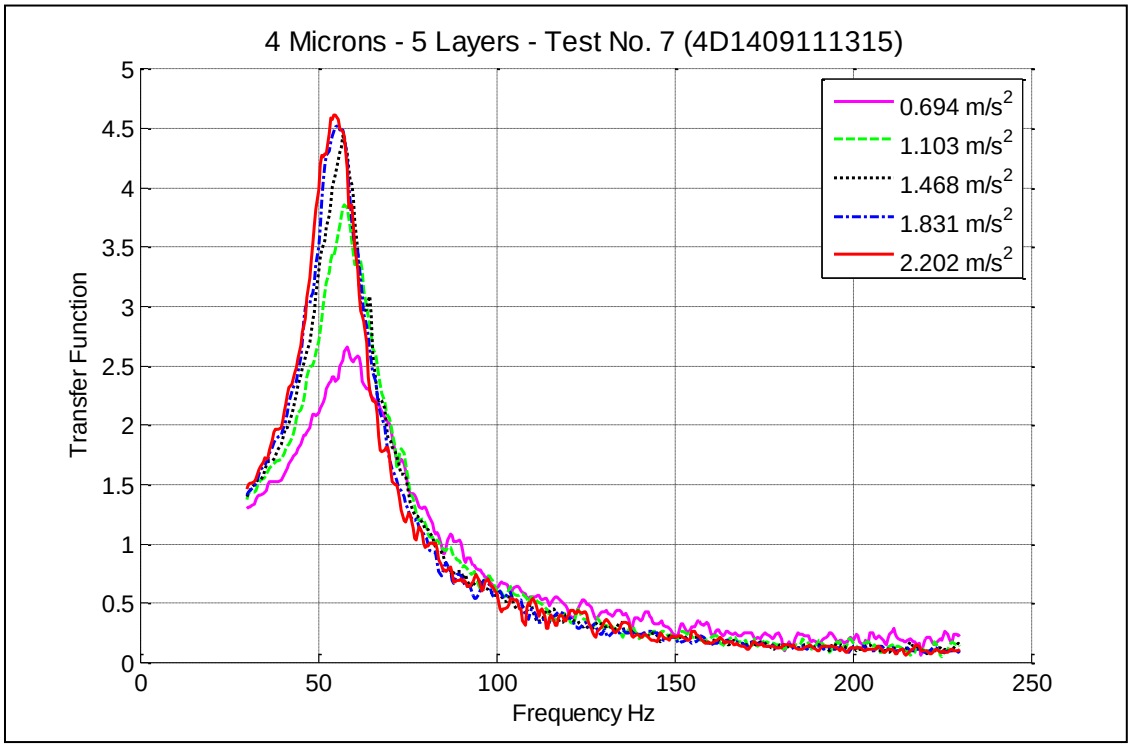

Figure D.14 Transfer functions for 5 layers (samples 14/09/11/13/15) of 4 microns media.

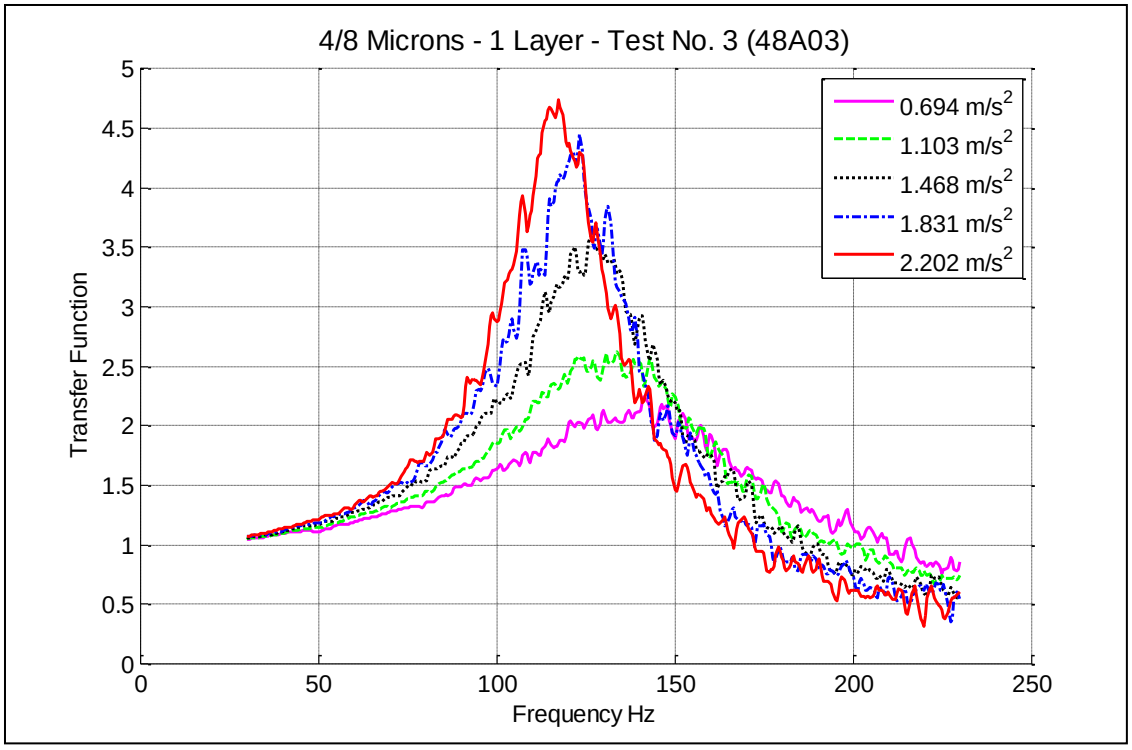

Figure D.15 Transfer functions for 1 layer (sample 03) of 4/8 microns media.

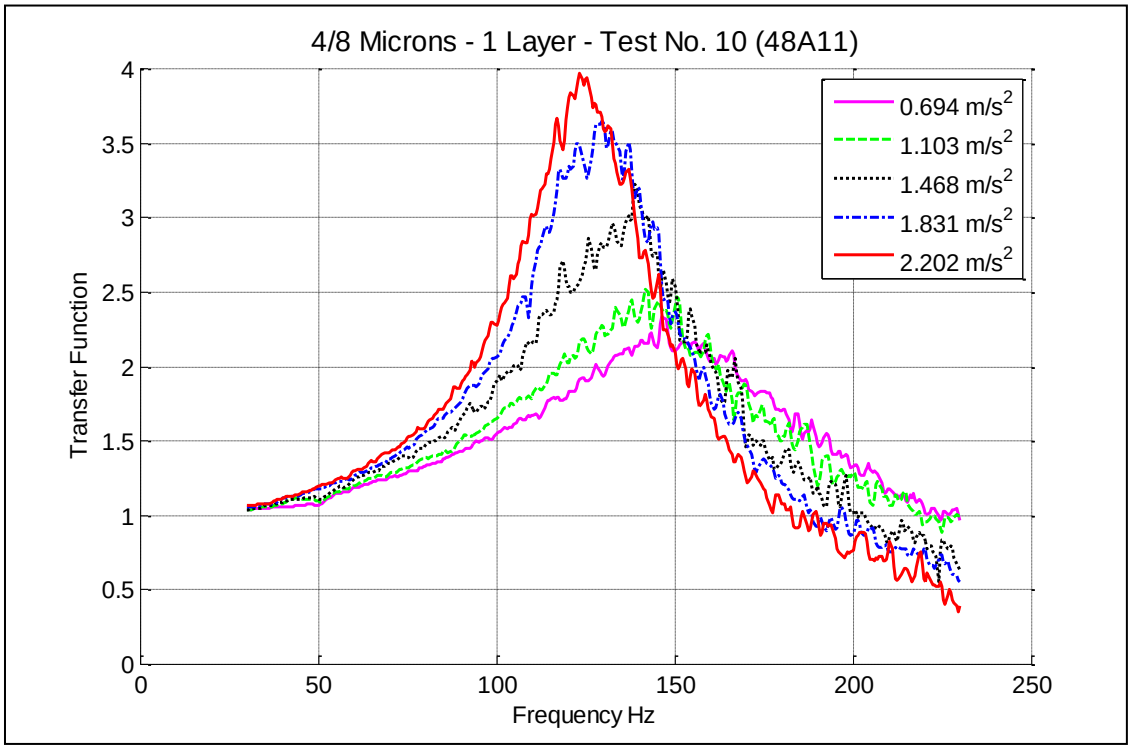

Figure D.16 Transfer functions for 1 layer (sample 11) of 4/8 microns media.

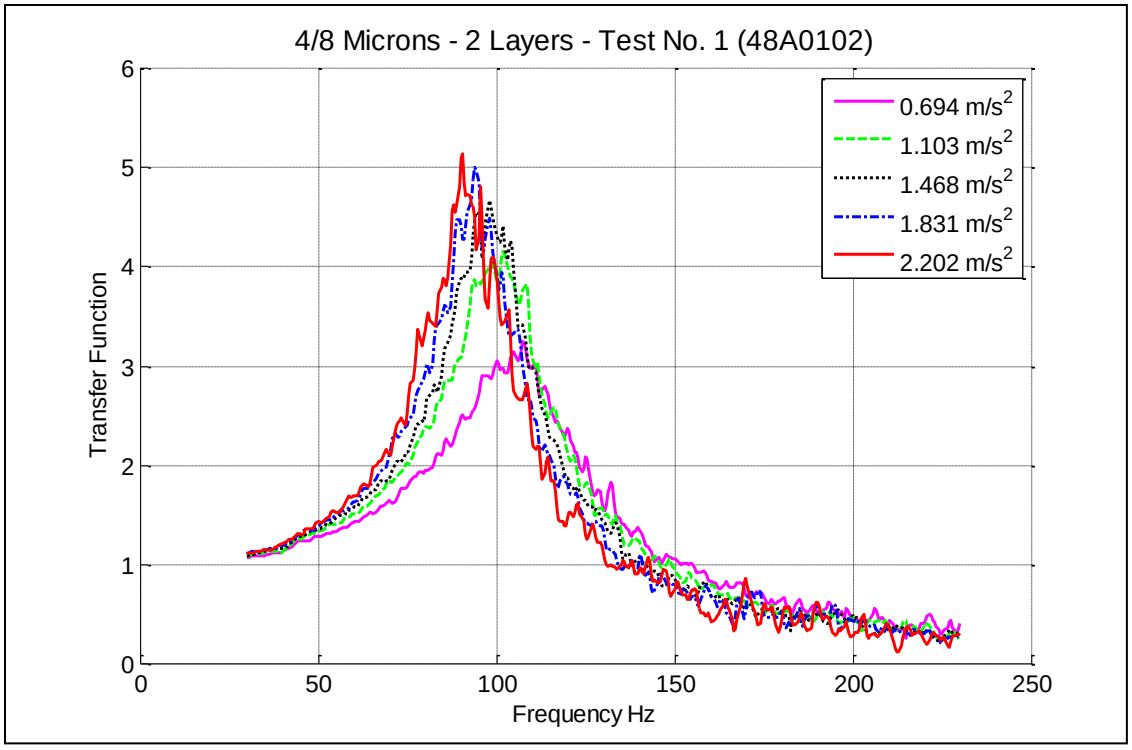

Figure D.17 Transfer functions for 2 layers (samples 01/02) of 4/8 microns media.

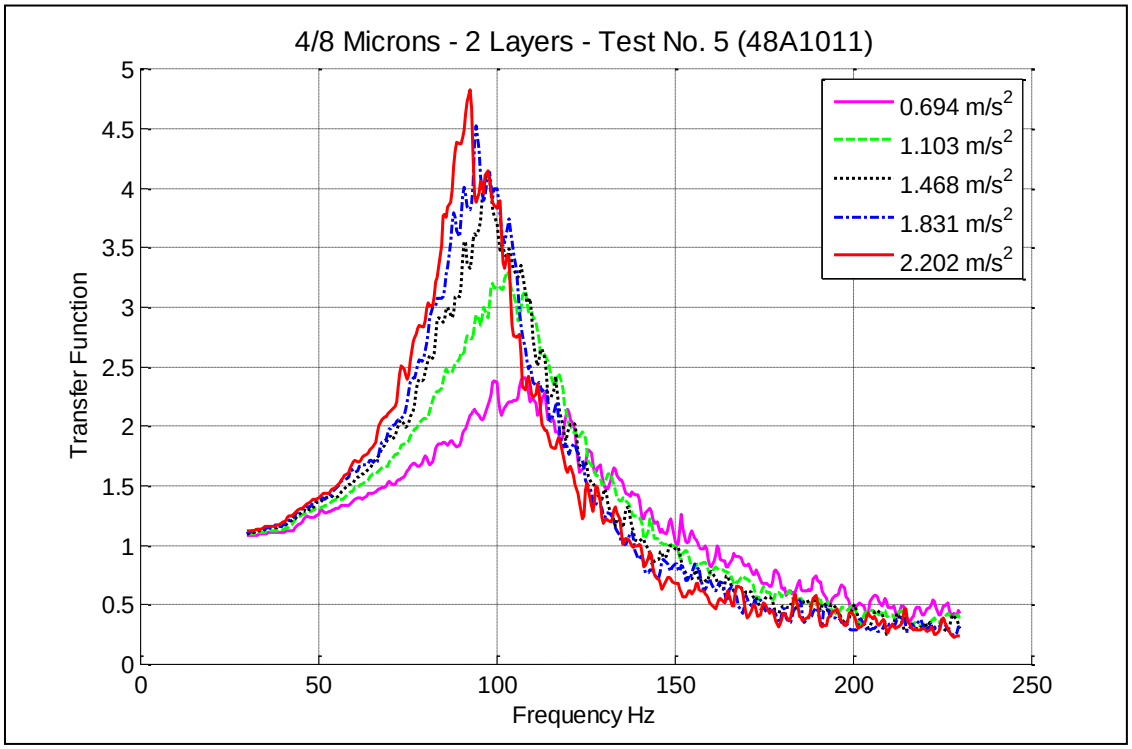

Figure D.18 Transfer functions for 2 layers (samples 10/11) of 4/8 microns media.

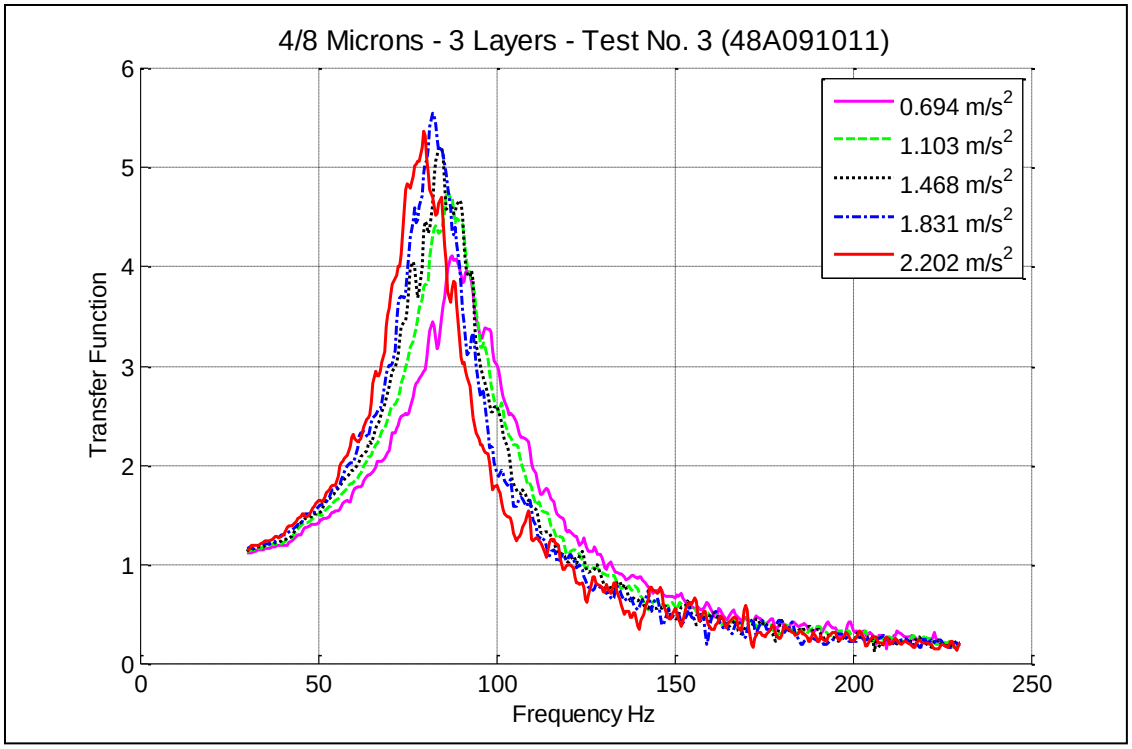

Figure D.19 Transfer functions for 3 layers (samples 09/10/11) of 4/8 microns media.

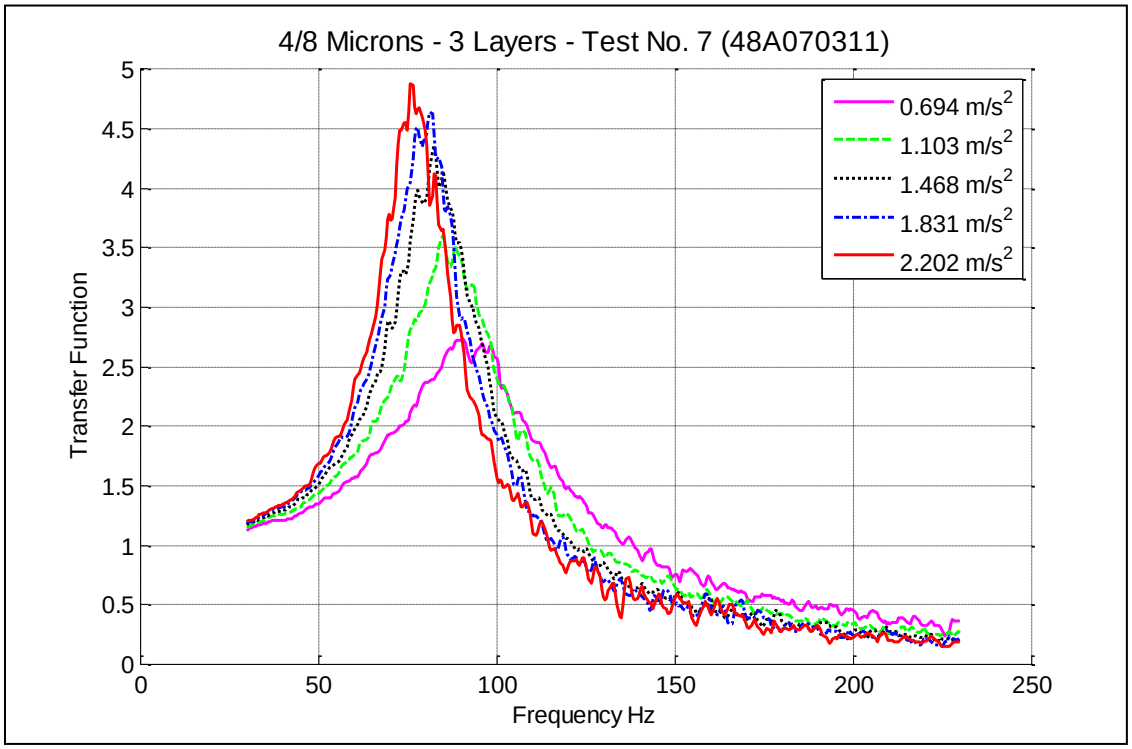

Figure D.20 Transfer functions for 3 layers (samples 07/03/11) of 4/8 microns media.

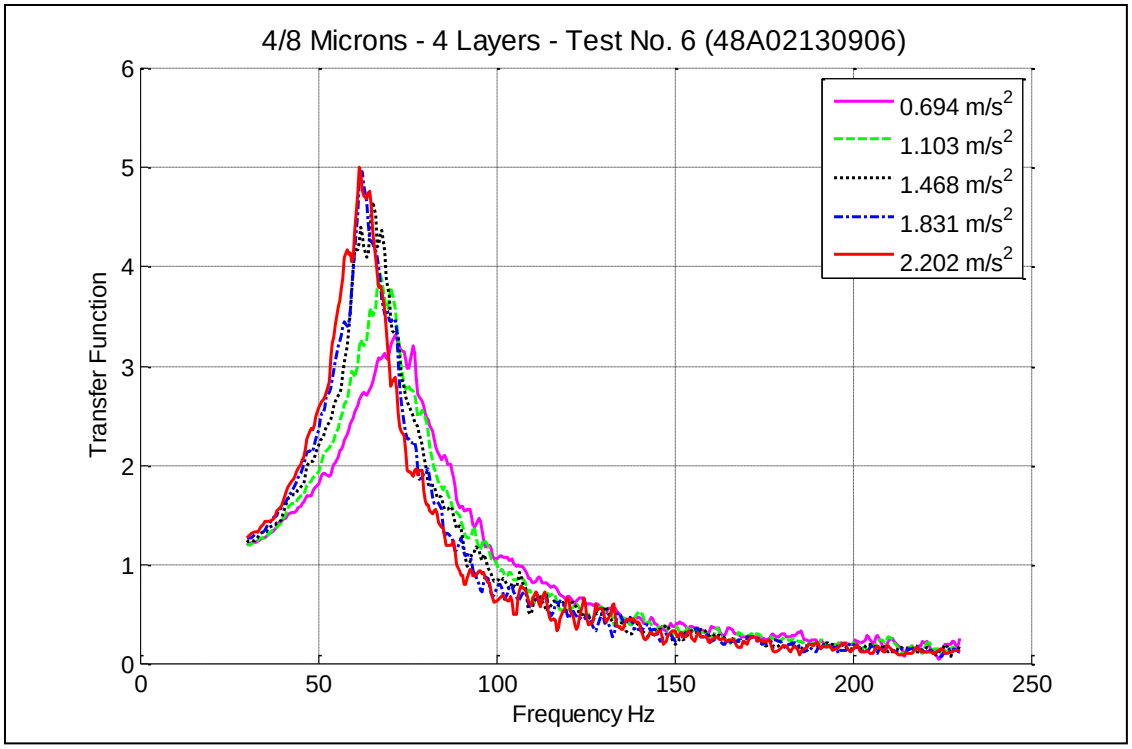

Figure D.21 Transfer functions for 4 layers (samples 02/13/09/06) of 4/8 microns media.

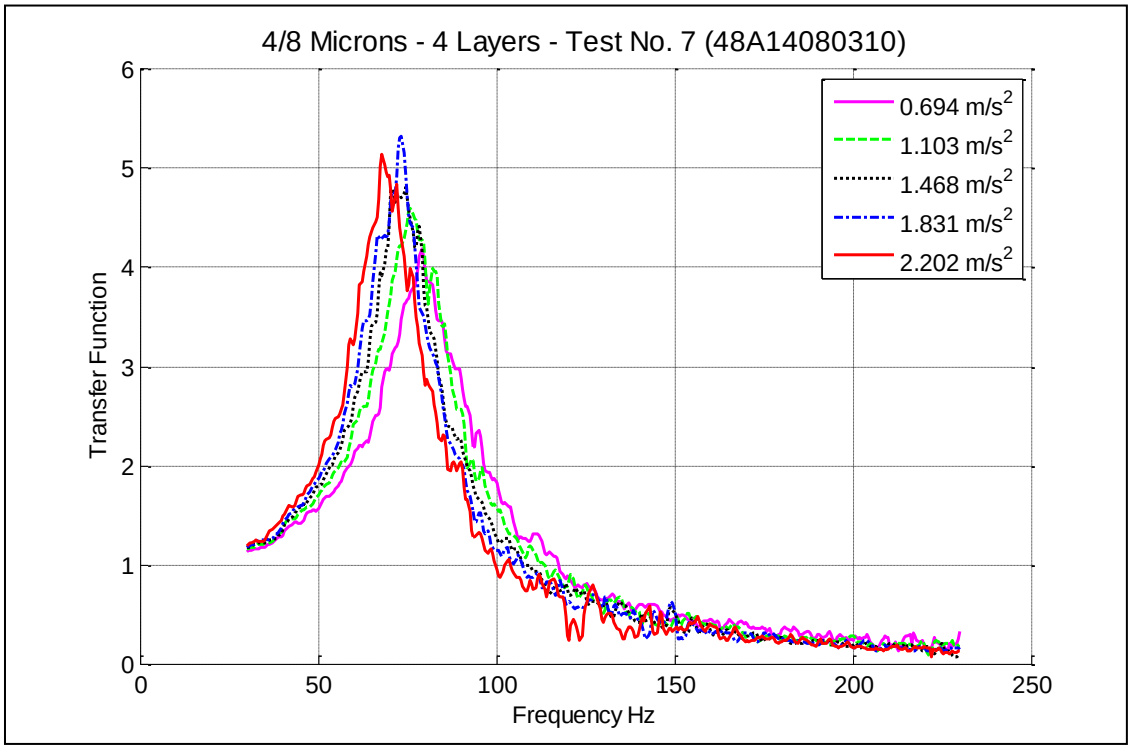

Figure D.22 Transfer functions for 4 layers (samples 14/08/03/10) of 4/8 microns media.

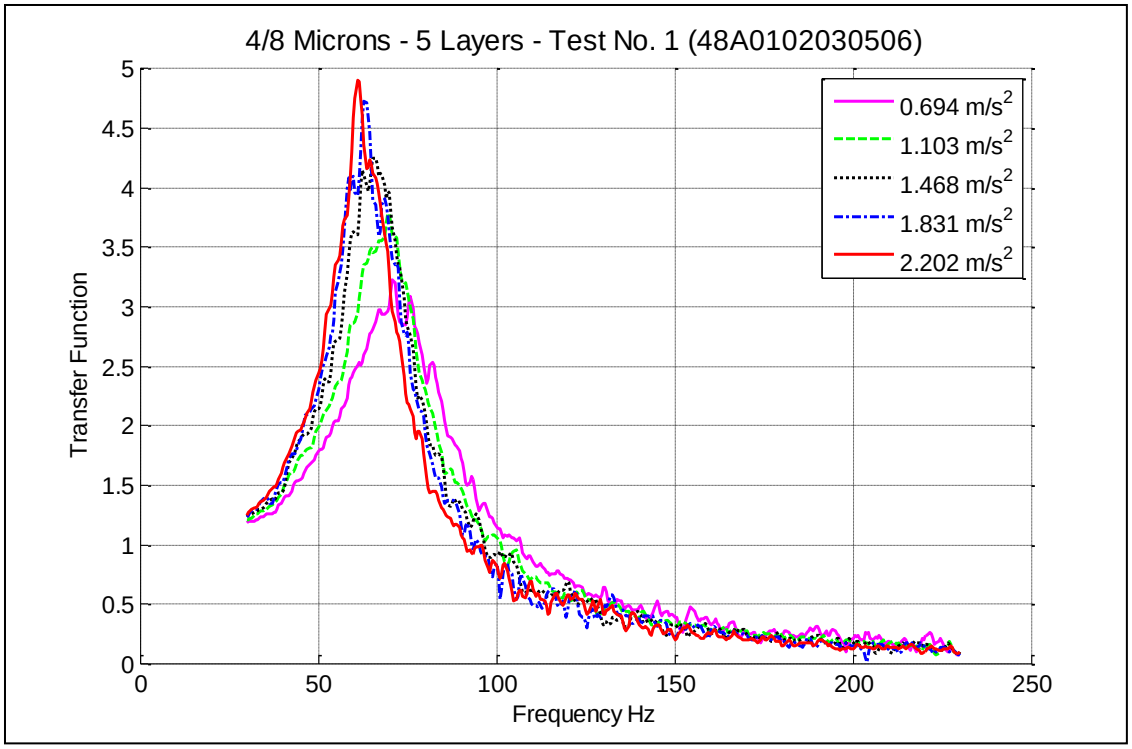

Figure D.23 Transfer functions for 5 layers (samples 01/02/03/05/06) of 4/8 microns media.

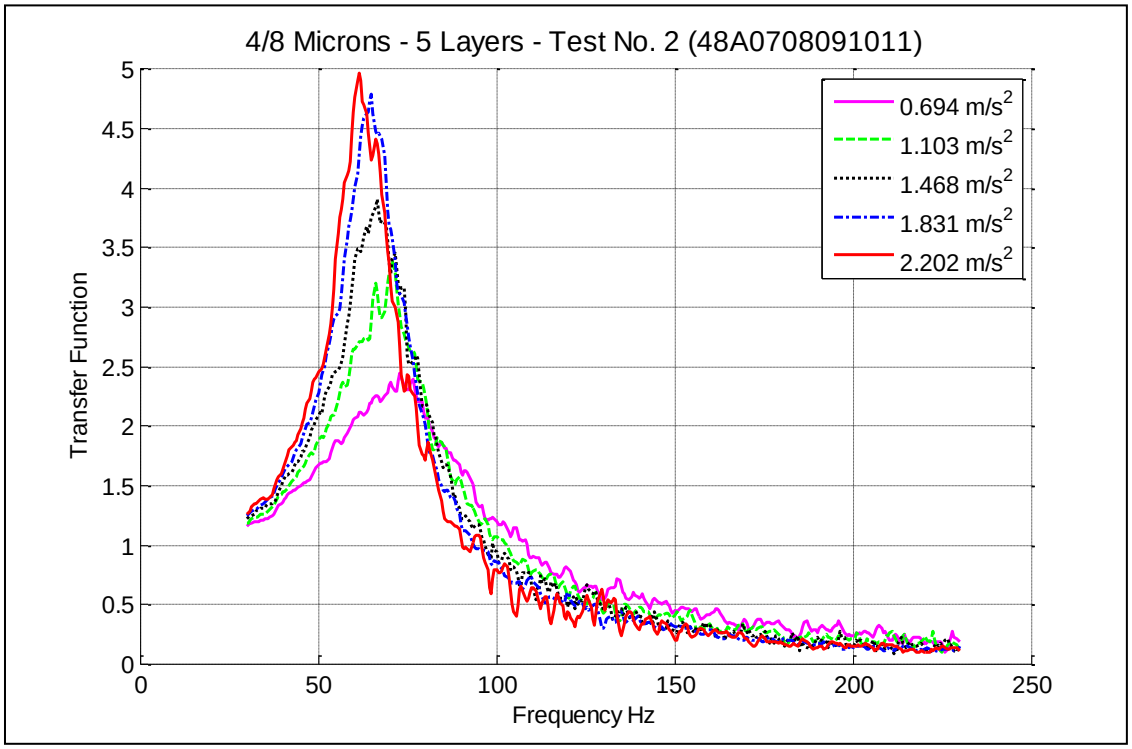

Figure D.24 Transfer functions for 5 layers (samples 07/08/09/10/11) of 4/8 microns media.

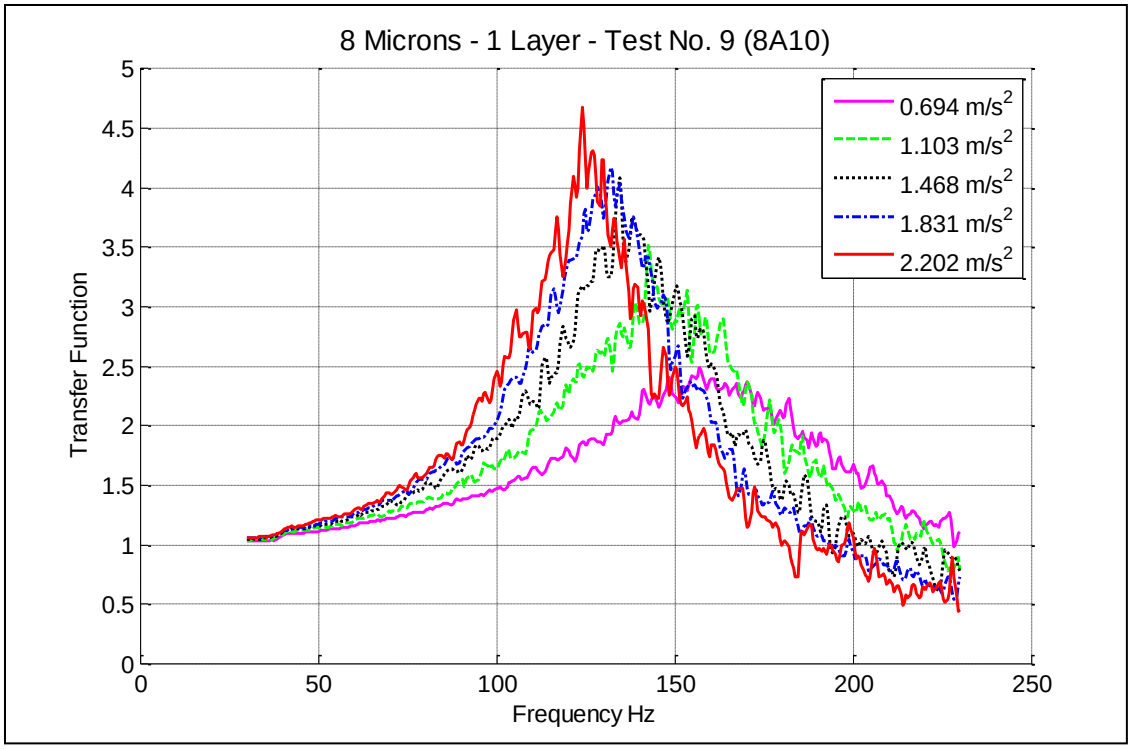

Figure D.25 Transfer functions for 1 layer (sample 10) of 8 microns media.

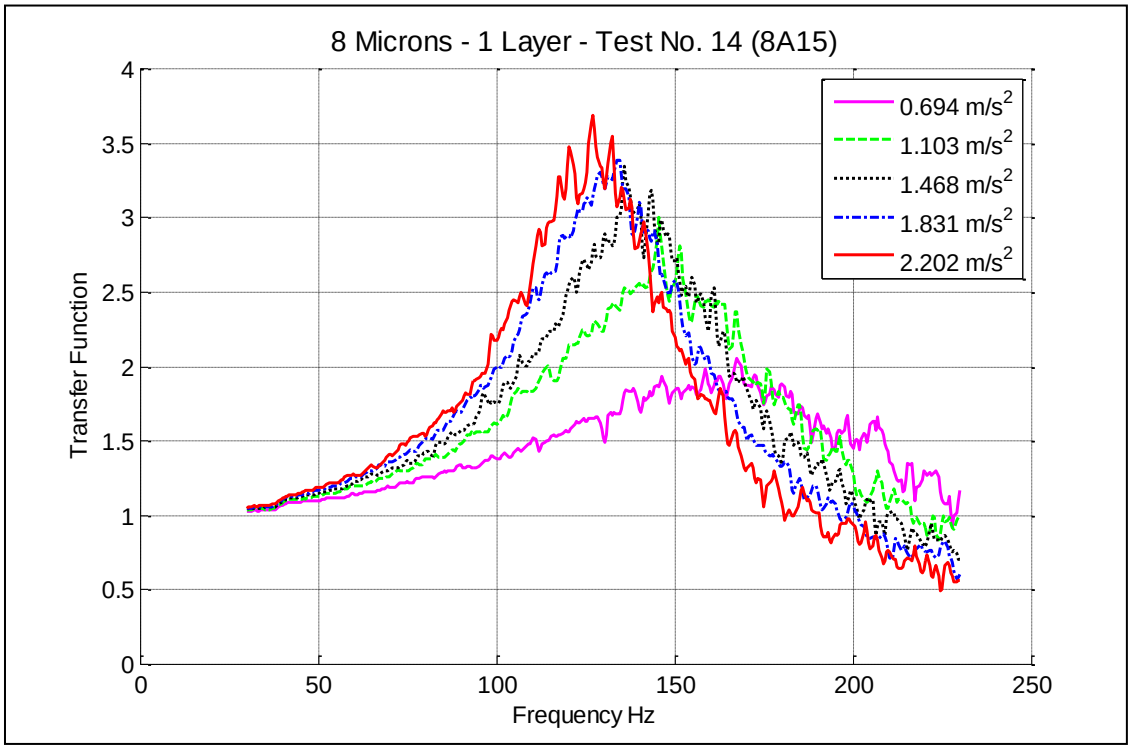

Figure D.26 Transfer functions for 1 layer (sample 15) of 8 microns media.

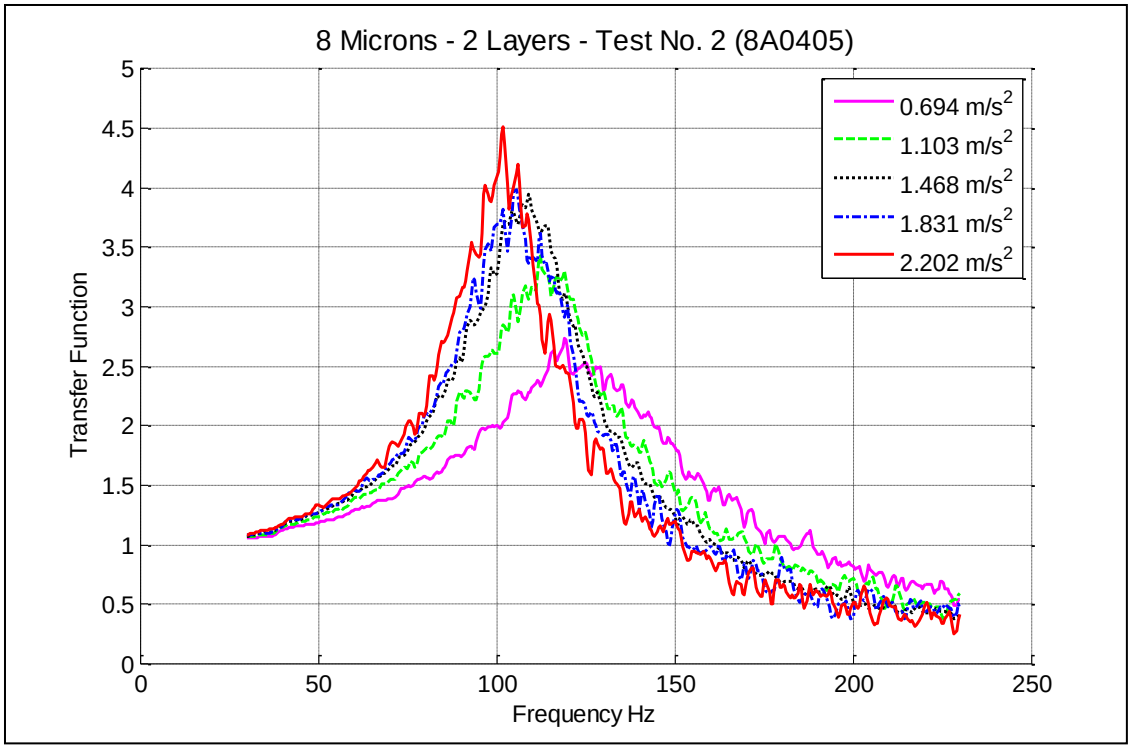

Figure D.27 Transfer functions for 2 layers (samples 04/05) of 8 microns media.

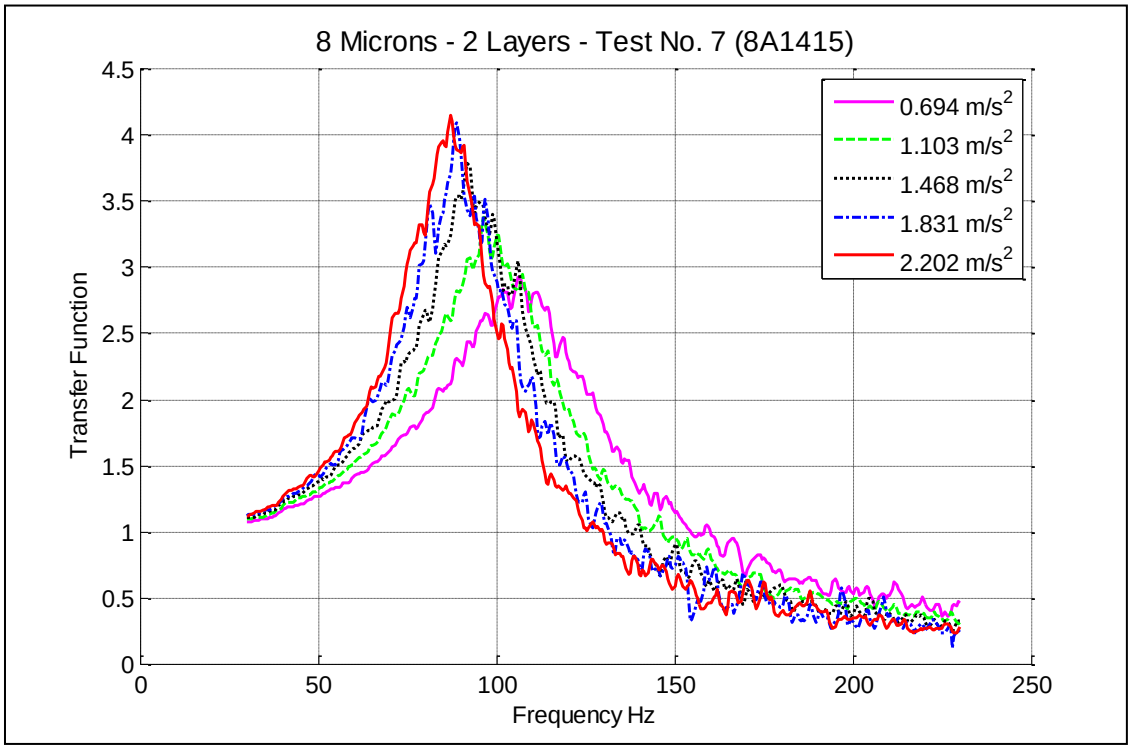

Figure D.28 Transfer functions for 2 layers (samples 14/15) of 8 microns media.

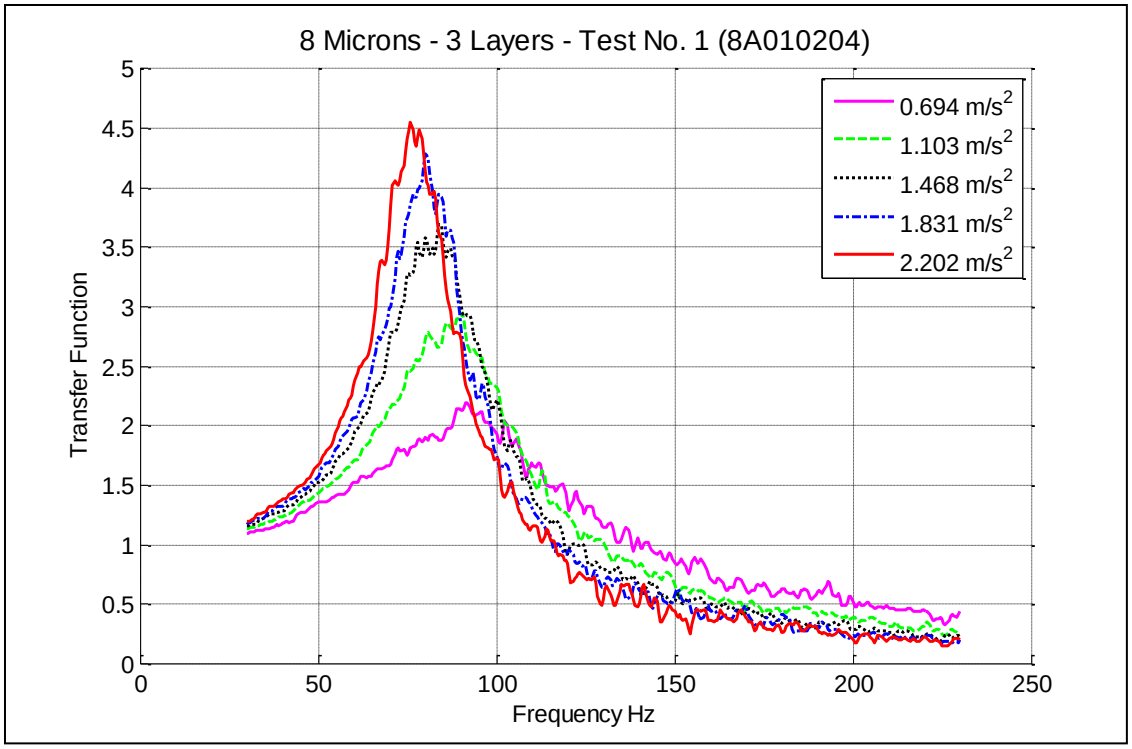

Figure D.29 Transfer functions for 3 layers (samples 01/02/04) of 8 microns media.

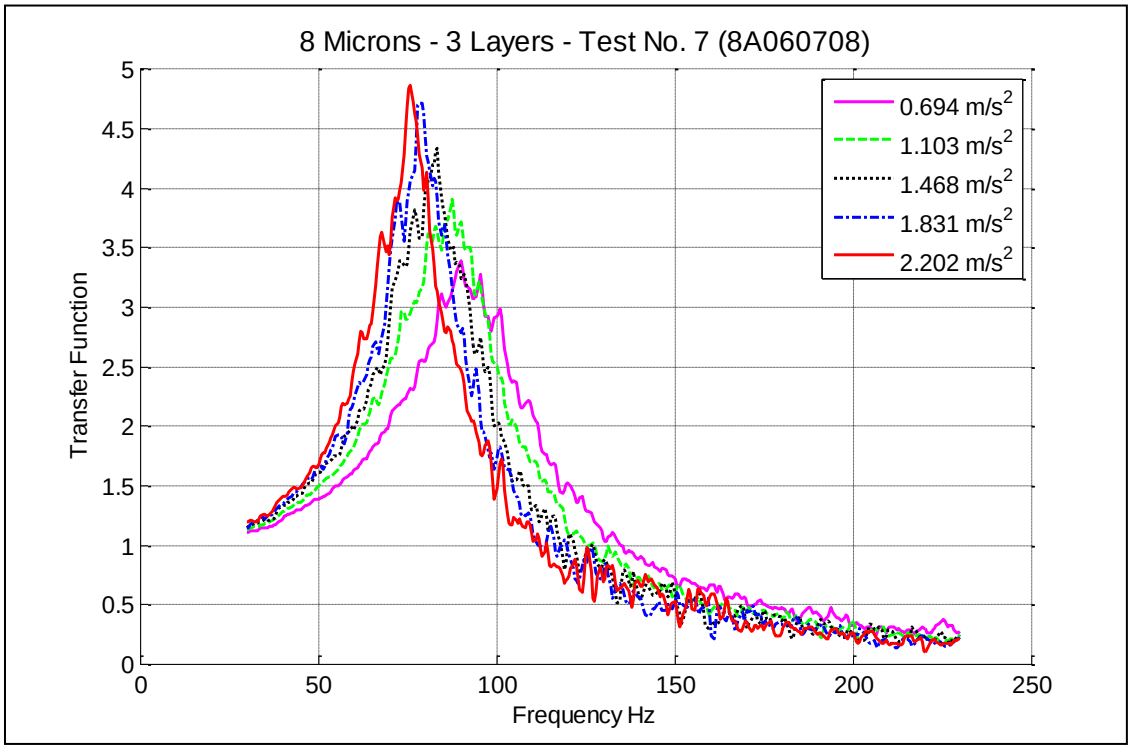

Figure D.30 Transfer functions for 3 layers (samples 06/07/08) of 8 microns media.

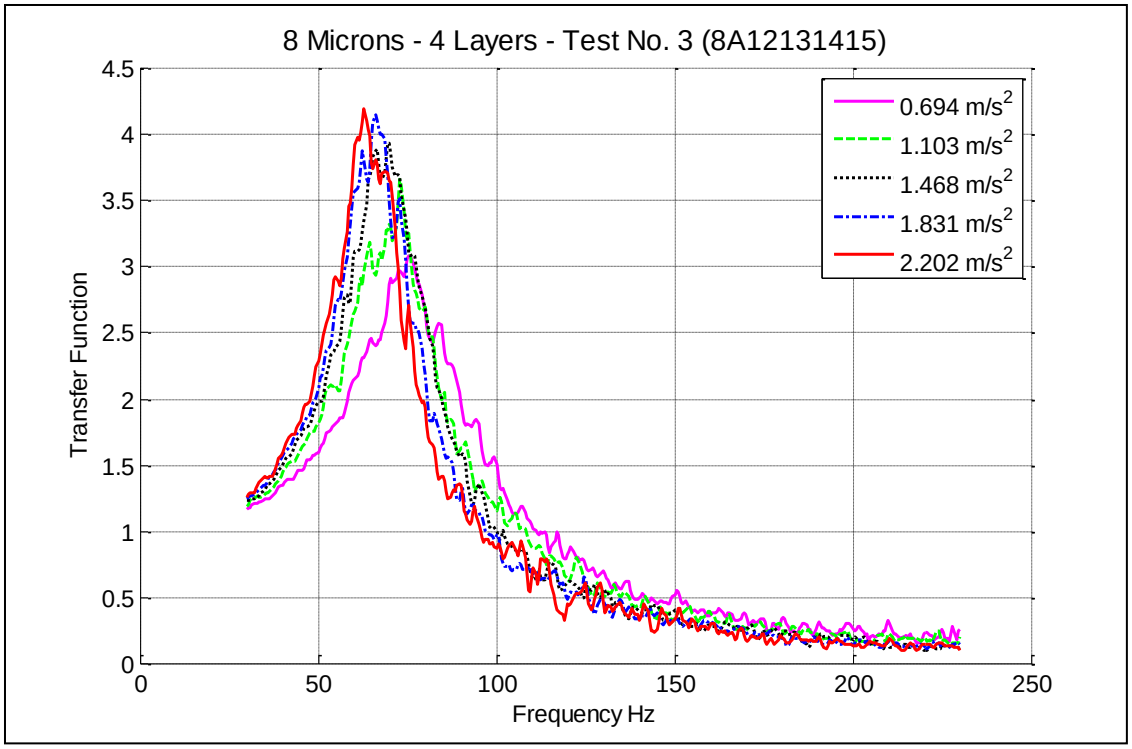

Figure D.31 Transfer functions for 4 layers (samples 12/13/14/15) of 8 microns media.

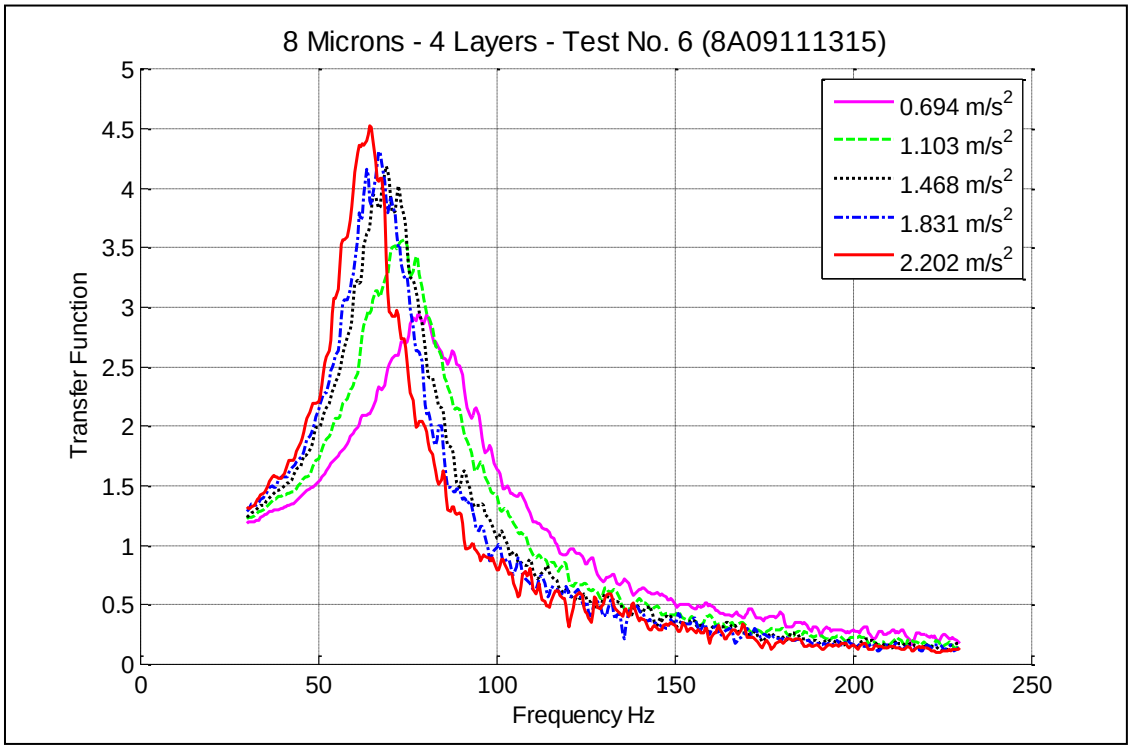

Figure D.32 Transfer functions for 4 layers (samples 09/11/13/15) of 8 microns media.

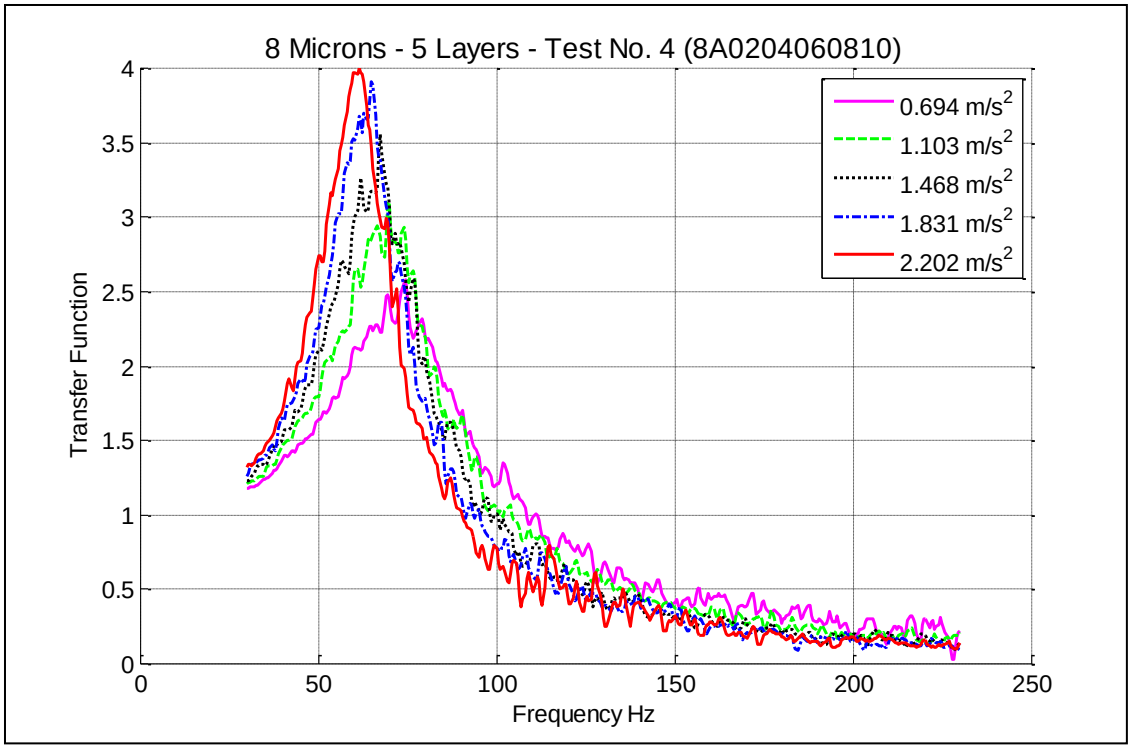

Figure D.33 Transfer functions for 5 layers (samples 02/04/06/08/10) of 8 microns media.

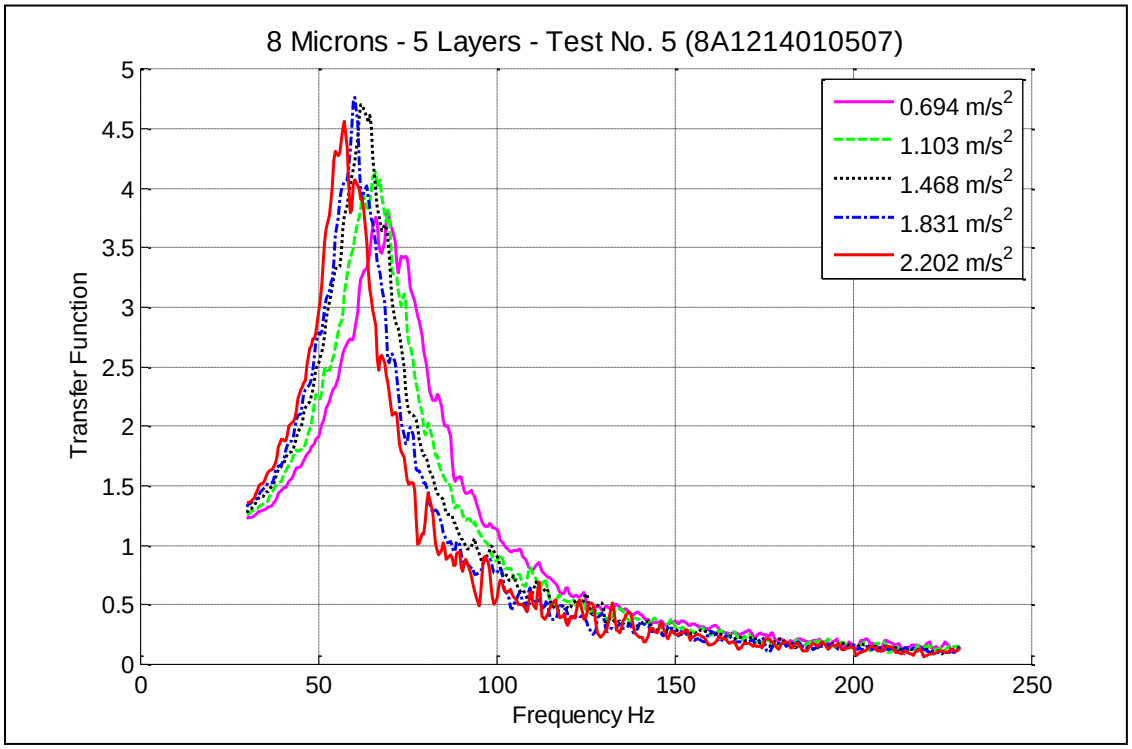

Figure D.34 Transfer functions for 5 layers (samples 12/14/01/05/07) of 8 microns media.

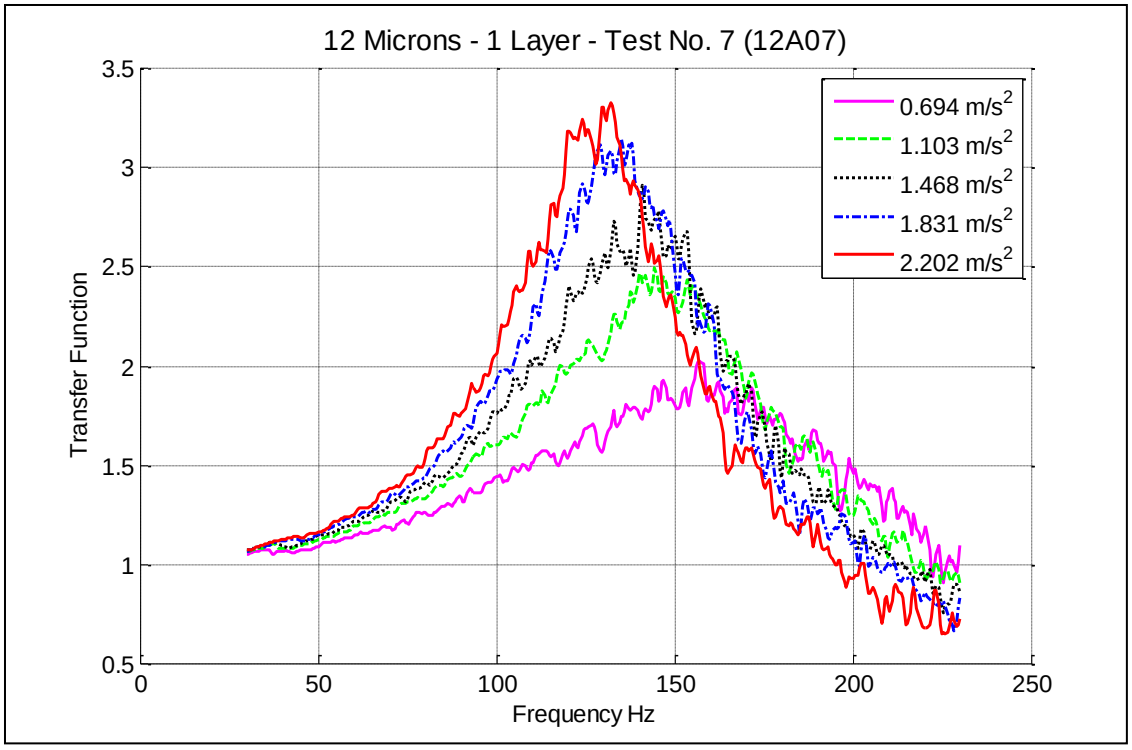

Figure D.35 Transfer functions for 1 layer (sample 07) of 12 microns media.

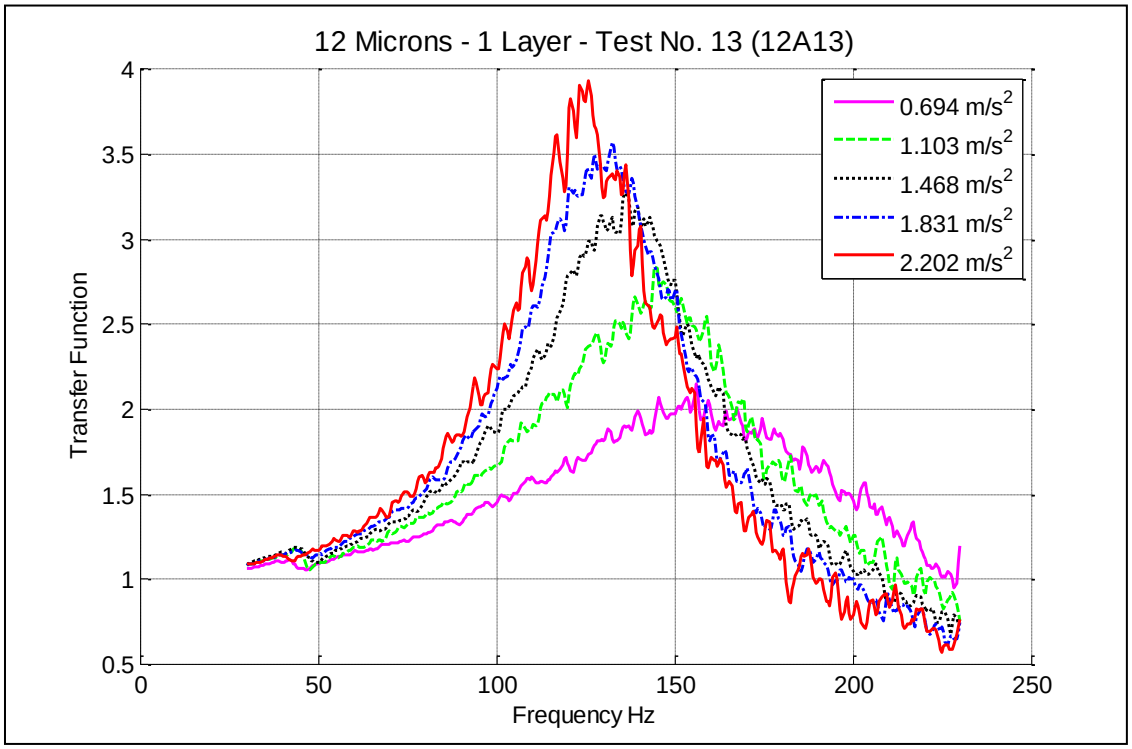

Figure D.36 Transfer functions for 1 layer (sample 13) of 12 microns media.

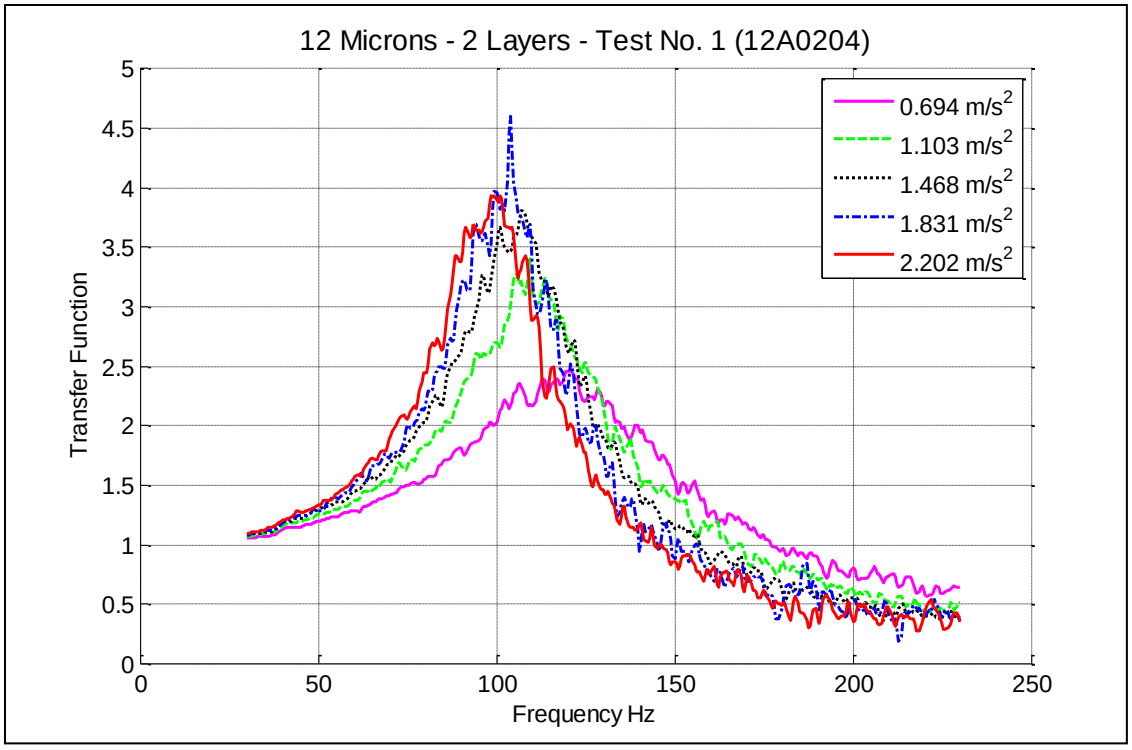

Figure D.37 Transfer functions for 2 layers (samples 02/04) of 12 microns media.

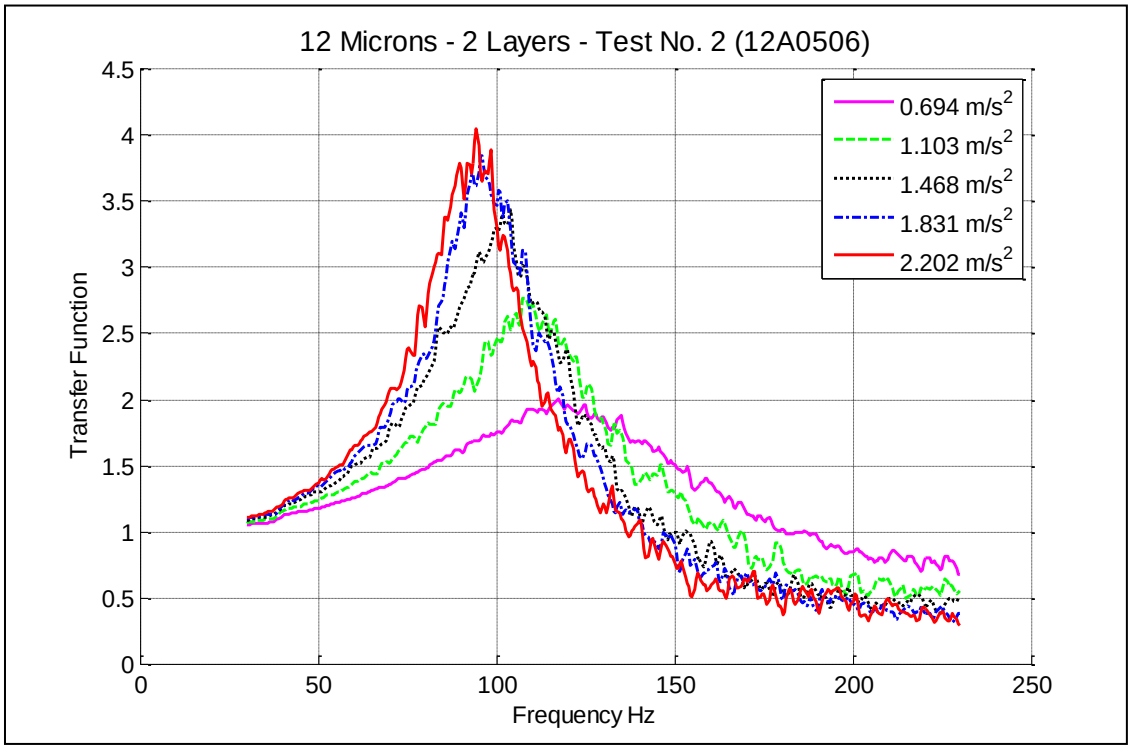

Figure D.38 Transfer functions for 2 layers (samples 05/06) of 12 microns media.

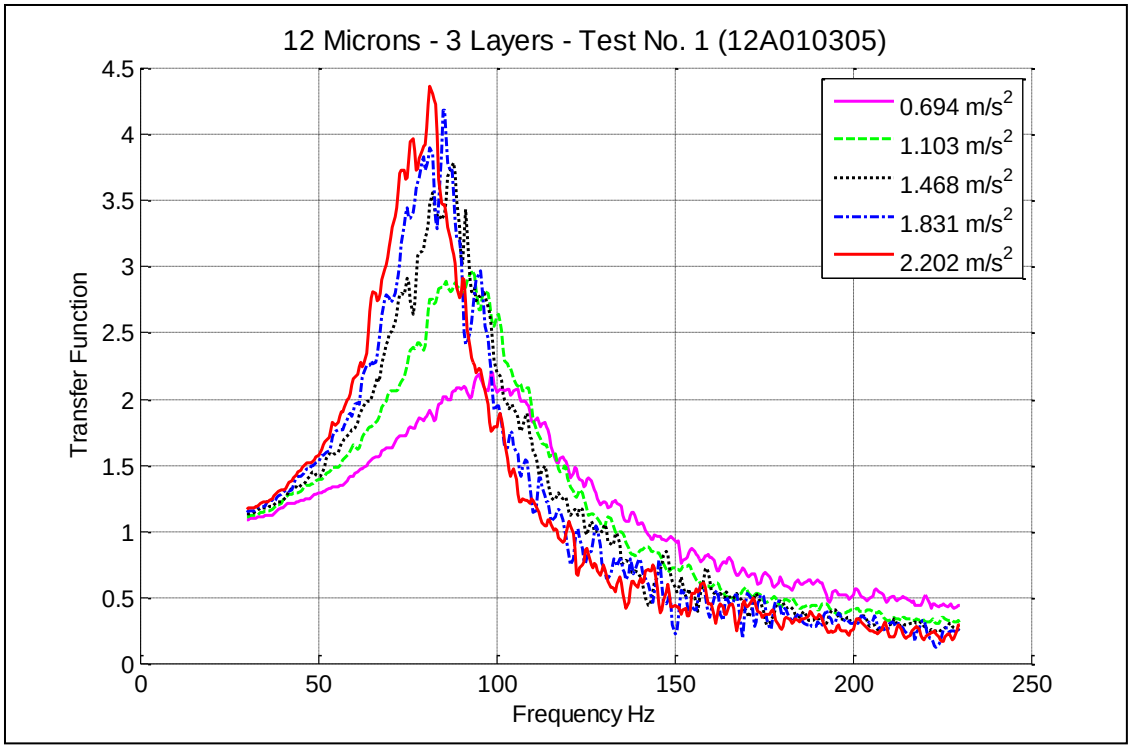

Figure D.39 Transfer functions for 3 layers (samples 01/03/05) of 12 microns media.

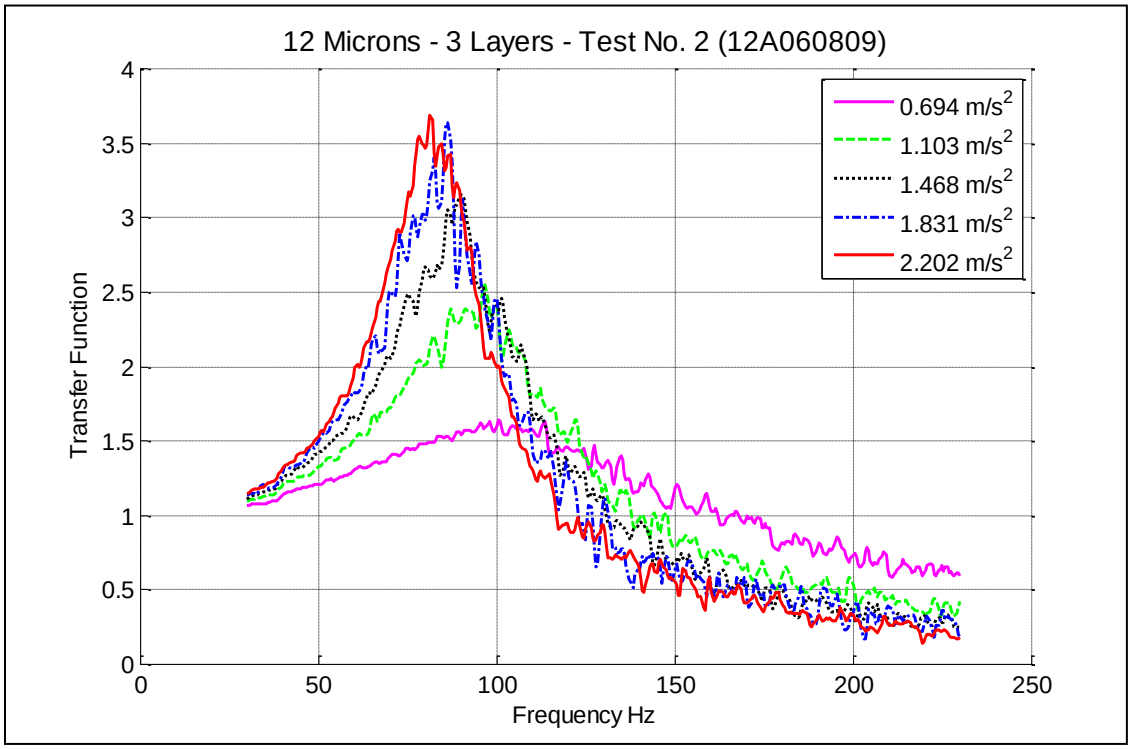

Figure D.40 Transfer functions for 3 layers (samples 06/08/09) of 12 microns media.

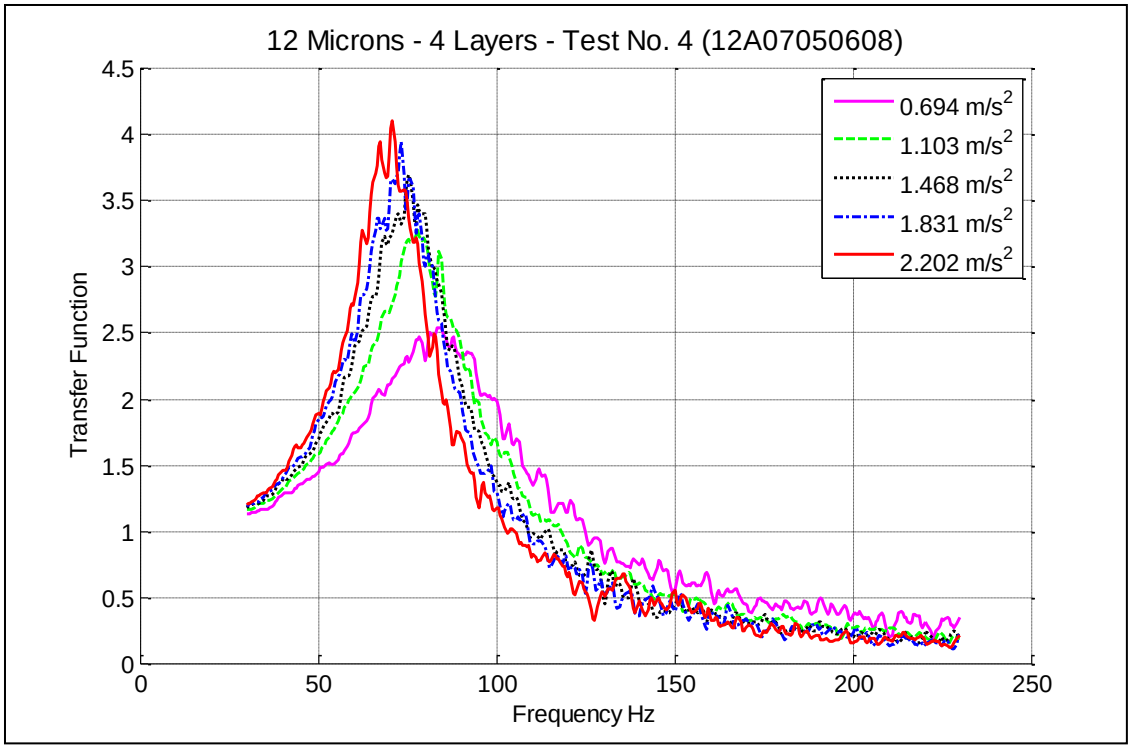

Figure D.41 Transfer functions for 4 layers (samples 07/05/06/08) of 12 microns media.

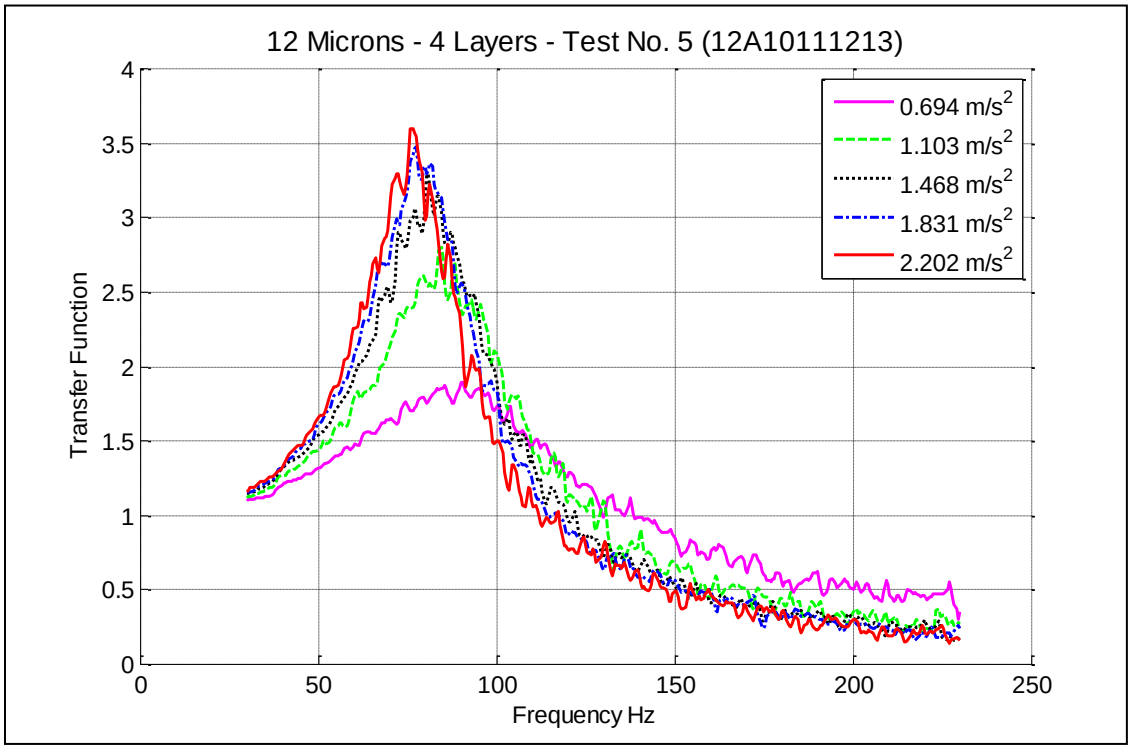

Figure D.42 Transfer functions for 4 layers (samples 10/11/12/13) of 12 microns media.

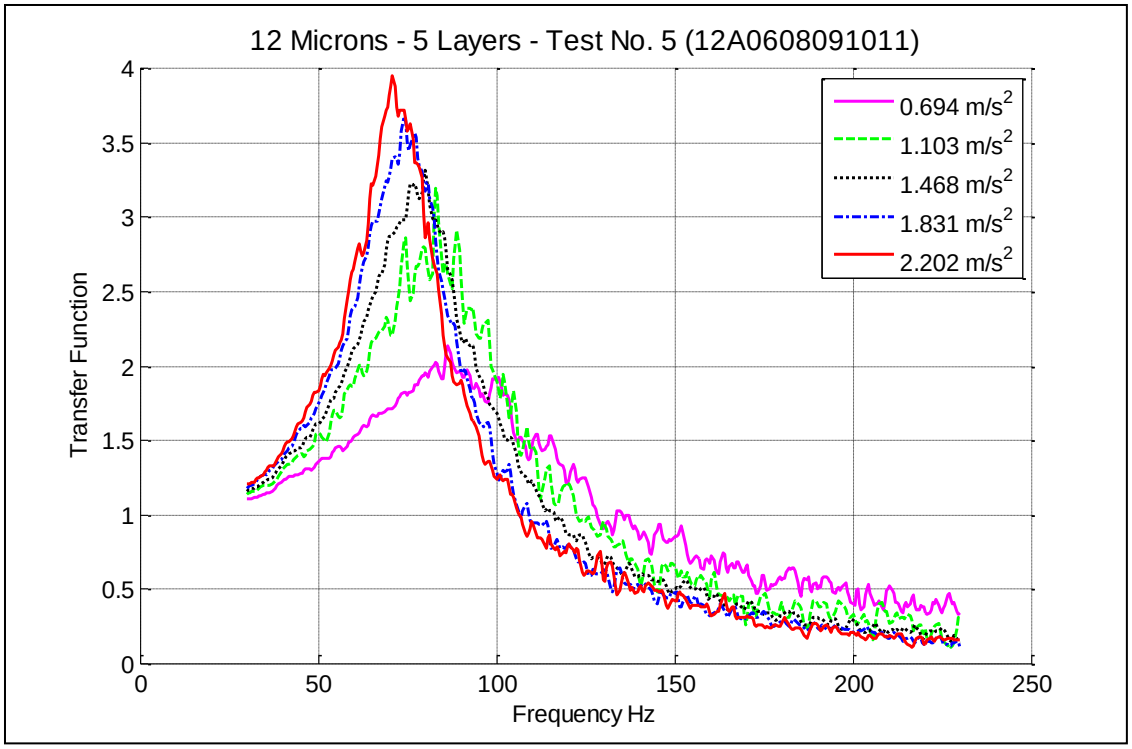

Figure D.43 Transfer functions for 5 layers (samples 06/08/09/10/11) of 12 microns media.

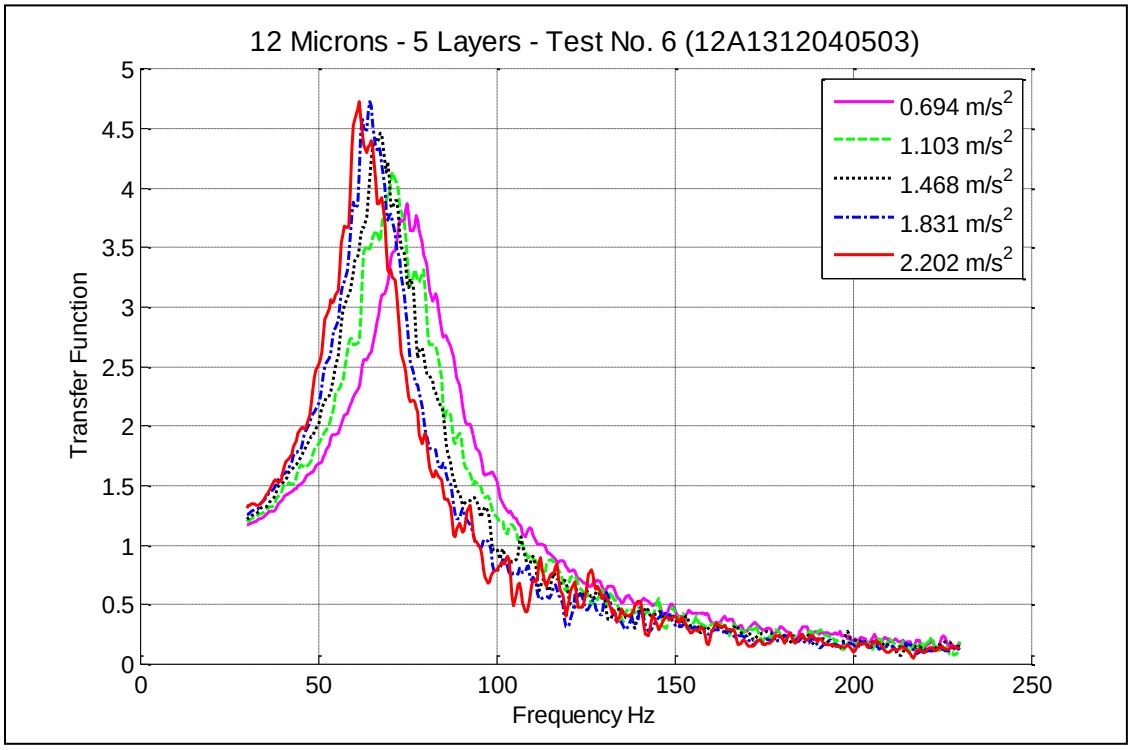

Figure D.44 Transfer functions for 5 layers (samples 13/12/04/05/03) of 12 microns media.

D.3 Experimental Data for the Natural Frequencies of 4 Microns Media

		Microfibrous Sample – 4 Microns - 1 Layer - (Natural Frequency / Hz)							
		4D01	**4D02**	**4D03**	**4D04**	**4D05**	**4D06**	**4D07**	**4D08**
Input Vibration Amplitude (m/s^2)	**0.694**	119	135.5	120.5	126.5	133.5	153	133.5	138.5
	1.103	115.5	124.5	117.5	119	128	141	129	128.5
	1.468	114	122.5	113	113.5	125.5	137	126.5	125
	1.831	113.5	118.5	108.5	107	124.5	134.5	122.5	121.5
	2.202	111	117.5	105.5	104	123	132	118.5	117

Table D.1a Natural frequencies of 1 layer of 4 microns media.

		Microfibrous Sample – 4 Microns - 1 Layer - (Natural Frequency / Hz)							
		4D09	**4D10**	**4D11**	**4D12**	**4D13**	**4D14**	**4D15**	**AV**
Input Vibration Amplitude (m/s^2)	**0.694**	144	123.5	128.5	134	134	131.5	108	**130.90**
	1.103	141	118	124.5	127	126	123	104.5	**124.47**
	1.468	138.5	114	123	120.5	122	122	101	**121.20**
	1.831	132	108.5	120	117.5	120.5	118.5	96.5	**117.60**
	2.202	128	107	117	114	117.5	116.5	96	**114.97**

Table D.1b Natural frequencies of 1 layer of 4 microns media.

		Microfibrous Sample – 4 Microns - 2 Layers - (Natural Frequency / Hz)							
		4D0102	**4D0304**	**4D0506**	**4D0708**	**4D0910**	**4D1112**	**4D1314**	**AV**
Input Vibration Amplitude (m/s^2)	**0.694**	80.5	84	95	93.5	103	87.5	86.5	**90.00**
	1.103	78.5	80.5	91.5	88	98.5	81.5	84	**86.07**
	1.468	78	77	90.5	82.5	94	79.5	82.5	**83.43**
	1.831	76	74.5	89	80.5	92	77	81.5	**81.50**
	2.202	75.5	73.5	87	78	89	76.5	80	**79.93**

Table D.2 Natural frequencies of 2 layers of 4 microns media.

		Microfibrous Sample – 4 Microns - 3 Layers - (Natural Frequency / Hz)							
		4D020103	**4D040507**	**4D060911**	**4D081315**	**4D100204**	**4D120810**	**4D140509**	**AV**
Input Vibration Amplitude (m/s^2)	**0.694**	70.5	74	84	71	70.5	72	72	**73.43**
	1.103	68	73	79	68	68.5	69.5	67.5	**70.50**
	1.468	66	68.5	75.5	63.5	66	65.5	67	**67.43**
	1.831	63.5	64.5	73.5	63	63.5	63.5	65.5	**65.29**
	2.202	63	64	70.5	60.5	62.5	62	65	**63.93**

Table D.3 Natural frequencies of 3 layers of 4 microns media.

		Microfibrous Sample – 4 Microns - 4 Layers - (Natural Frequency / Hz)							
		4D01020406	**4D03081012**	**4D05141501**	**4D07020814**	**4D09041015**	**4D11061203**	**4D13050709**	**AV**
Input Vibration Amplitude (m/s^2)	**0.694**	65.5	64.5	66	64	68	59.5	68	**65.07**
	1.103	64.5	60.5	64.5	61.5	65.5	56.5	66.5	**62.79**
	1.468	64	57.5	62	61	63.5	55	65	**61.14**
	1.831	62.5	56.5	61	57	63	54.5	63	**59.64**
	2.202	60.5	56	58.5	56	61.5	53	61.5	**58.14**

Table D.4 Natural frequencies of 4 layers of 4 microns media.

		Microfibrous Sample – 4 Microns - 5 Layers - (Natural Frequency / Hz)							
		4D0203050709	**4D0411131501**	**4D0602030405**	**4D0806070910**	**4D1008111213**	**4D1214150107**	**4D1409111315**	**AV**
Input Vibration Amplitude (m/s^2)	**0.694**	59.5	58	51	63.5	54.5	58	58	**57.50**
	1.103	58	57	50.5	61.5	53.5	56	57.5	**56.29**
	1.468	57	55	48.5	60.5	53	54.5	57	**55.07**
	1.831	56.5	53	47.5	59.5	50.5	53	55.5	**53.64**
	2.202	55.5	53	46.5	58	50	52	54.5	**52.79**

Table D.5 Natural frequencies of 5 layers of 4 microns media.

D.4 Experimental Data for the Maximum Amplitude of the Transfer Functions of 4 Microns Media

		Microfibrous Sample – 4 Microns - 1 Layer - (Amplitude)							
		4D01	**4D02**	**4D03**	**4D04**	**4D05**	**4D06**	**4D07**	**4D08**
Input Vibration Amplitude (m/s^2)	**0.694**	3.0906	3.7144	1.9611	1.6786	2.3325	2.2602	2.1566	1.8801
	1.103	4.3385	4.2733	2.4696	2.6624	2.8484	2.5716	2.3079	2.4526
	1.468	6.1616	4.6092	3.5353	3.5892	3.8969	3.3723	3.0277	3.4060
	1.831	7.4348	4.8140	4.4414	4.2806	4.3210	3.7910	3.6251	4.0203
	2.202	7.6475	5.4012	4.7919	5.0536	4.8450	4.3823	4.3592	4.5349

Table D. 6a Maximum amplitude of the transfer functions of 1 layer of 4 microns media.

		Microfibrous Sample – 4 Microns - 1 Layer - (Amplitude)							
		4D09	**4D10**	**4D11**	**4D12**	**4D13**	**4D14**	**4D15**	**AV**
Input Vibration Amplitude (m/s^2)	**0.694**	2.2526	1.9761	3.0345	1.9479	1.9378	2.1205	2.5095	**2.3235**
	1.103	2.5783	3.1093	4.3659	2.5410	2.5373	2.8789	2.9664	**2.9934**
	1.468	3.4371	4.6848	4.4764	3.3434	3.2398	3.4154	4.1609	**3.8904**
	1.831	4.5057	5.1291	5.3373	4.3205	4.1470	3.8866	4.6509	**4.5804**
	2.202	4.9089	5.5017	5.8304	5.0538	4.4711	4.5283	4.9279	**5.0825**

Table D.6b Maximum amplitude of the transfer functions of 1 layer of 4 microns media.

		Microfibrous Sample – 4 Microns - 2 Layers - (Amplitude)							
		4D0102	**4D0304**	**4D0506**	**4D0708**	**4D0910**	**4D1112**	**4D1314**	**AV**
Input Vibration Amplitude (m/s^2)	**0.694**	2.0815	2.5941	2.8776	2.2791	2.7100	2.7707	3.4040	**2.6739**
	1.103	3.0537	3.6641	4.2323	2.7880	3.1256	3.8479	4.7485	**3.6372**
	1.468	4.0552	4.7214	4.9805	3.6915	3.5776	4.3763	5.0449	**4.3496**
	1.831	4.3658	5.1260	5.4391	4.4754	4.2920	4.9676	5.4514	**4.8739**
	2.202	5.1141	5.4461	5.7392	4.5309	4.3824	4.7233	5.5318	**5.0668**

Table D.7 Maximum amplitude of the transfer functions of 2 layers of 4 microns media.

		Microfibrous Sample – 4 Microns - 3 Layers - (Amplitude)							
		4D020103	**4D040507**	**4D060911**	**4D081315**	**4D100204**	**4D120810**	**4D140509**	**AV**
Input Vibration Amplitude (m/s^2)	**0.694**	2.7648	2.1660	3.2985	4.3174	2.8953	1.6257	2.7888	**2.8366**
	1.103	3.7801	3.1807	3.9217	5.0933	3.7945	2.5380	3.6814	**3.7128**
	1.468	4.4609	3.6866	4.6750	5.2577	4.2903	3.0294	4.3715	**4.2531**
	1.831	4.8002	4.2225	4.7711	5.4083	4.6736	3.5481	4.5896	**4.5733**
	2.202	5.2976	4.5409	4.9636	5.6972	4.8398	3.9298	4.8574	**4.8752**

Table D.8 Maximum amplitude of the transfer functions of 3 layers of 4 microns media.

		Microfibrous Sample – 4 Microns - 4 Layers - (Amplitude)							
		4D01020406	**4D03081012**	**4D05141501**	**4D07020814**	**4D09041015**	**4D11061203**	**4D13050709**	**AV**
Input Vibration Amplitude (m/s^2)	**0.694**	2.9355	1.7069	4.5592	2.0036	3.4572	3.3105	1.8302	**2.8290**
	1.103	4.0726	3.0210	4.8421	3.2552	4.4678	4.0032	2.8356	**3.7854**
	1.468	4.6526	3.5525	5.3350	3.8075	4.9897	4.4782	3.0747	**4.2700**
	1.831	5.0513	3.9273	5.4117	4.5031	5.2796	4.7799	3.2839	**4.6053**
	2.202	5.4084	4.1802	5.6864	4.9223	5.9215	4.8345	3.8058	**4.9656**

Table D.9 Maximum amplitude of the transfer functions of 4 layers of 4 microns media.

		Microfibrous Sample – 4 Microns - 5 Layers - (Amplitude)							
		4D0203050709	**4D0411131501**	**4D0602030405**	**4D0806070910**	**4D1008111213**	**4D1214150107**	**4D1409111315**	**AV**
Input Vibration Amplitude (m/s^2)	**0.694**	1.9444	3.7801	1.7548	3.1909	2.4954	3.6432	2.6633	**2.7817**
	1.103	2.1140	4.7523	3.0103	4.0512	3.1741	4.4452	3.8501	**3.6282**
	1.468	3.1812	5.2947	3.8618	4.2500	3.6832	4.8266	4.4288	**4.2180**
	1.831	3.7390	5.3362	4.2704	4.6847	4.0178	5.0223	4.5247	**4.5136**
	2.202	4.4816	5.4410	4.6572	5.2049	4.3602	5.0625	4.6173	**4.8321**

Table D.10 Maximum amplitude of the transfer functions of 5 layers of 4 microns media.

D.5 Experimental Data for the Natural Frequencies of 4/8 Microns Media

		Microfibrous Sample – 4/8 Microns - 1 Layer - (Natural Frequency / Hz)						
		48A01	***48A02***	***48A03***	***48A05***	***48A06***	***48A07***	***48A08***
Input Vibration Amplitude (m/s^2)	**0.694**	*144.5*	*135*	*141.5*	*149*	*142.5*	*150.5*	*141.5*
	1.103	*140*	*131.5*	*134*	*142*	*138.5*	*145*	*138.5*
	1.468	*132*	*128.5*	*126.5*	*133*	*130.5*	*143*	*130*
	1.831	*129.5*	*121*	*123.5*	*130.5*	*126.5*	*137.5*	*128.5*
	2.202	*121*	*116*	*117.5*	*126.5*	*123.5*	*131*	*122*

Table D.11a Natural frequencies of 1 layer of 4/8 microns media.

		Microfibrous Sample – 4/8 Microns - 1 Layer - (Natural Frequency / Hz)							
		48A09	**48A10**	**48A11**	**48A12**	**48A13**	**48A14**	**48A15**	**AV**
Input Vibration Amplitude (m/s^2)	**0.694**	158	135.5	146.5	155	157.5	140	164	**147.21**
	1.103	146	128.5	142	144.5	145.5	131.5	149.5	**139.79**
	1.468	141	124.5	139	141.5	136.5	127	147.5	**134.32**
	1.831	137.5	119	129.5	131	130.5	124	139	**129.11**
	2.202	134	112	123.5	127	126	119.5	134	**123.82**

Table D.11b Natural frequencies of 1 layer of 4/8 microns media.

		Microfibrous Sample – 4/8 Microns - 2 Layers - (Natural Frequency / Hz)							
		48A0102	**48A0305**	**48A0607**	**48A0809**	**48A1011**	**48A1213**	**48A1415**	**AV**
Input Vibration Amplitude (m/s^2)	**0.694**	107.5	102	107	113	108	115	104	**108.07**
	1.103	102	95	101	108	103	103.5	97.5	**101.43**
	1.468	98	91.5	98	106	97.5	100	92.5	**97.64**
	1.831	94	91	95.5	97	94.5	97.5	91.5	**94.43**
	2.202	90.5	89	90.5	95	92.5	95	91	**91.93**

Table D.12 Natural frequencies of 2 layers of 4/8 microns media.

		Microfibrous Sample – 4/8 Microns - 3 Layers - (Natural Frequency / Hz)							
		48A010203	48A050607	48A091011	48A131415	48A150612	48A020913	8A070311	AV
Input Vibration Amplitude (m/s^2)	**0.694**	84	88	87.5	88	85.5	89.5	90.5	**87.57**
	1.103	80	82	86.5	86	83	83	85	**83.64**
	1.468	78	78.5	84	82.5	81	80	82.5	**80.93**
	1.831	74.5	75.5	82	78.5	78	78.5	81.5	**78.36**
	2.202	73	74	79.5	73.5	74	76	76	**75.14**

Table D.13 Natural frequencies of 3 layers of 4/8 microns media.

		Microfibrous Sample – 4/8 Microns - 4 Layers - (Natural Frequency / Hz)							
		48A03050607	48A08091011	48A12131415	48A01020305	48A06071215	48A02130906	48A14080310	AV
Input Vibration Amplitude (m/s^2)	**0.694**	72	78.5	78	77.5	79	71.5	79	**76.50**
	1.103	68.5	73.5	74.5	74	77	67.5	76	**73.00**
	1.468	64.5	72	69	72.5	74	65.5	74.5	**70.29**
	1.831	63	71	66	71.5	72	62.5	73.5	**68.50**
	2.202	63	68.5	65	69	70	61.5	68	**66.43**

Table D.14 Natural frequencies of 4 layers of 4/8 microns media.

		Microfibrous Sample – 4/8 Microns - 5 Layers - (Natural Frequency / Hz)							
		48A0102030506	48A0708091011	48A1213141501	48A1103060912	48A1405071013	48A0502080115	48A0308091013	AV
Input Vibration Amplitude (m/s^2)	**0.694**	71	73	69	75	67.5	70.5	71	**71.00**
	1.103	69.5	71	67.5	73.5	64	67.5	68	**68.71**
	1.468	66	66.5	64.5	65.5	64	65.5	66	**65.43**
	1.831	63	65	62.5	66.5	60	62	62	**63.00**
	2.202	61	61.5	61.5	65	58	58.5	61	**60.93**

Table D.15 Natural frequencies of 5 layers of 4/8 microns media.

D.6 Experimental Data for the Maximum Amplitude of the Transfer Functions of 4/8 Microns Media

		Microfibrous Sample – 4/8 Microns - 1 Layer - (Amplitude)						
		48A01	**48A02**	**48A03**	**48A05**	**48A06**	**48A07**	**48A08**
Input Vibration Amplitude (m/s^2)	**0.694**	1.6613	3.4781	2.2435	3.1152	2.8738	3.5628	3.5206
	1.103	2.3955	4.2372	2.6155	3.9464	4.1916	4.1830	3.9786
	1.468	3.1147	4.8284	3.5998	4.4392	4.6276	4.7799	4.4578
	1.831	3.7156	5.2507	4.4419	4.7320	5.7542	4.7245	4.8737
	2.202	3.8593	5.4351	4.7403	5.0436	5.6432	5.2181	4.8286

Table D.16a Maximum amplitude of the transfer functions of 1 layer of 4/8 microns media.

		Microfibrous Sample – 4/8 Microns - 1 Layer - (Amplitude)							
		48A09	**48A10**	**48A11**	**48A12**	**48A13**	**48A14**	**48A15**	**AV**
Input Vibration Amplitude (m/s^2)	**0.694**	2.6779	2.9903	2.3377	2.6119	3.4014	2.8155	3.3337	**2.9017**
	1.103	4.3481	3.1136	2.5181	3.5739	3.8092	3.4930	3.4610	**3.5618**
	1.468	4.9753	3.8357	3.2300	4.1377	4.3383	4.0583	3.9381	**4.1686**
	1.831	4.9391	3.9191	3.6537	4.3239	4.4676	4.1574	4.4773	**4.5308**
	2.202	4.9882	3.9600	3.9758	4.4971	4.6768	4.4570	4.5066	**4.7021**

Table D.16b Maximum amplitude of the transfer functions of 1 layer of 4/8 microns media.

		Microfibrous Sample – 4/8 Microns - 2 Layers - (Amplitude)							
		48A0102	**48A0305**	**48A0607**	**48A0809**	**48A1011**	**48A1213**	**48A1415**	**AV**
Input Vibration Amplitude (m/s^2)	**0.694**	3.2453	3.8604	3.6616	3.0982	2.4096	3.6172	3.2725	**3.3093**
	1.103	4.1549	4.6097	4.1393	3.2795	3.2959	4.3511	3.9587	**3.9699**
	1.468	4.6644	4.5466	4.6298	4.0313	4.1377	4.9050	4.4207	**4.4765**
	1.831	5.0011	5.1756	5.1710	4.4038	4.5209	5.3878	4.6146	**4.8964**
	2.202	5.1344	5.2836	5.2302	4.7311	4.8224	5.4290	4.5187	**5.0213**

Table D.17 Maximum amplitude of the transfer functions of 2 layers of 4/8 microns media.

		Microfibrous Sample – 4/8 Microns - 3 Layers - (Amplitude)							
		48A010203	**48A050607**	**48A091011**	**48A131415**	**48A150612**	**48A020913**	**48A070311**	**AV**
Input Vibration Amplitude (m/s^2)	**0.694**	2.6602	2.9076	4.1094	4.7700	2.2000	4.2550	2.7300	**3.3760**
	1.103	3.4137	3.8229	4.7599	5.1100	3.3035	5.1145	3.6005	**4.1607**
	1.468	3.9472	4.6222	5.2012	5.1700	4.0169	5.2669	4.3534	**4.6540**
	1.831	4.6195	4.7330	5.5483	5.4500	4.3129	5.4008	4.6354	**4.9571**
	2.202	4.7154	5.3048	5.3627	5.4600	4.6653	5.0933	4.8769	**5.0683**

Table D.18 Maximum amplitude of the transfer functions of 3 layers of 4/8 microns media.

		Microfibrous Sample – 4/8 Microns - 4 Layers - (Amplitude)							
		48A03050607	**48A08091011**	**48A12131415**	**48A01020305**	**48A06071215**	**48A02130906**	**48A14080310**	**AV**
Input Vibration Amplitude (m/s^2)	**0.694**	3.5834	2.3592	4.2788	3.5343	3.4349	3.3051	4.1830	**3.5255**
	1.103	4.0868	2.9278	4.5903	4.1240	3.8919	3.9258	4.5892	**4.0194**
	1.468	4.4825	3.0668	5.1826	4.2942	3.8511	4.6616	4.8064	**4.3350**
	1.831	4.6117	3.6929	5.4189	4.7259	4.0847	4.9581	5.3214	**4.6877**
	2.202	4.7357	3.8145	5.3496	5.1054	4.4250	5.0020	5.1387	**4.7958**

Table D.19 Maximum amplitude of the transfer functions of 4 layers of 4/8 microns media.

		Microfibrous Sample – 4/8 Microns - 5 Layers - (Amplitude)							
		48A0102030506	**48A0708091011**	**48A1213141501**	**48A1103060912**	**48A1405071013**	**48A0502080115**	**48A0308091013**	**AV**
Input Vibration Amplitude (m/s^2)	**0.694**	3.2265	2.4380	3.8941	3.6943	4.0077	3.3721	3.2358	**3.4098**
	1.103	3.7736	3.3857	4.2278	4.0336	4.5383	4.4692	3.8920	**4.0457**
	1.468	4.2505	3.9116	4.5580	4.3469	4.9806	4.8435	4.4542	**4.4779**
	1.831	4.7230	4.7868	4.8022	4.5705	5.1187	4.9807	5.2069	**4.8841**
	2.202	4.8974	4.9661	4.7773	4.6399	5.5292	5.1828	5.4256	**5.0598**

Table D.20 Maximum amplitude of the transfer functions of 5 layers of 4/8 microns media.

D.7 Experimental Data for the Natural Frequencies of 8 Microns Media

		Microfibrous Sample – 8 Microns - 1 Layer - (Natural Frequency / Hz)						
		8A01	**8A02**	**8A04**	**8A05**	**8A06**	**8A07**	**8A08**
Input Vibration Amplitude (m/s^2)	**0.694**	160.5	155	163	171.5	143.5	142.5	150.5
	1.103	140.5	126.5	153	165.5	135.5	132	141
	1.468	133.5	120	146.5	151	124.5	127.5	129.5
	1.831	128.5	116	137.5	146	116	122	126
	2.202	124	114.5	129	137.5	113	118	122

Table D.21a Natural frequencies of 1 layer of 8 microns media.

		Microfibrous Sample – 8 Microns - 1 Layer - (Natural Frequency / Hz)							
		8A09	**8A10**	**8A11**	**8A12**	**8A13**	**8A14**	**8A15**	**AV**
Input Vibration Amplitude (m/s^2)	**0.694**	170	157	155.5	169.5	169	165	167.5	**160.00**
	1.103	154	142.5	143	152	149	153.5	145.5	**145.25**
	1.468	141	134.5	133	141.5	145	147.5	136	**136.50**
	1.831	137.5	132	131	135.5	136.5	138	134	**131.18**
	2.202	127.5	124	124.5	132	129.5	134.5	127	**125.50**

Table D.21b Natural frequencies of 1 layer of 8 microns media.

		Microfibrous Sample – 8 Microns - 2 Layers - (Natural Frequency / Hz)							
		8A0102	**8A0405**	**8A0607**	**8A0809**	**8A1011**	**8A1213**	**8A1415**	**AV**
Input Vibration Amplitude (m/s^2)	**0.694**	103.5	119	126.5	110	110	116	106	**113.00**
	1.103	99	112.5	116	103	101.5	108.5	96.5	**105.29**
	1.468	93.5	109	109	96	99	103.5	92	**100.29**
	1.831	89	105.5	106	94.5	93	97.5	89	**96.36**
	2.202	88	102	101	89	89	93	87	**92.71**

Table D.22 Natural frequencies of 2 layers of 8 microns media.

		Microfibrous Sample – 8 Microns - 3 Layers - (Natural Frequency / Hz)							
		8A010204	**8A050607**	**8A080910**	**8A111213**	**8A141501**	**8A020405**	**8A060708**	**AV**
Input Vibration Amplitude (m/s^2)	**0.694**	91.5	96.5	88	94.5	89.5	88.5	90	**91.21**
	1.103	90.5	90.5	81	91	83	85.5	87.5	**87.00**
	1.468	84	86	79.5	86.5	80	83	83.5	**83.21**
	1.831	80	84.5	76	83	77.5	78.5	78.5	**79.71**
	2.202	76	80.5	72.5	78	75	76	76	**76.29**

Table D.23 Natural frequencies of 3 layers of 8 microns media.

		Microfibrous Sample – 8 Microns - 4 Layers - (Natural Frequency / Hz)							
		8A04050607	**8A08091011**	**8A12131415**	**8A01020405**	**8A06081012**	**8A09111315**	**8A14020406**	**AV**
Input Vibration Amplitude (m/s^2)	**0.694**	83.5	87	75.5	76	77.5	78.5	81.5	**79.93**
	1.103	78.5	76.5	73	72.5	75.5	74	77	**75.29**
	1.468	73.5	71.5	70	71	63.5	69	71.5	**70.00**
	1.831	71	69.5	66	67.5	64	67	68	**67.57**
	2.202	68.5	68	63	66	62.5	64.5	67	**65.64**

Table D.24 Natural frequencies of 4 layers of 8 microns media.

		Microfibrous Sample – 8 Microns - 5 Layers - (Natural Frequency / Hz)							
		8A0102040506	**8A0708091011**	**8A1213141501**	**8A0204060810**	**8A1214010507**	**8A0507111315**	**8A0204051011**	**AV**
Input Vibration Amplitude (m/s^2)	**0.694**	73.5	73	74.5	74.5	69.5	71.5	71	**72.50**
	1.103	70.5	66.5	71.5	70	66	65	66.5	**68.00**
	1.468	67	64.5	65.5	67.5	62.5	63	65	**65.00**
	1.831	65	62	64	65	60.5	61.5	62.5	**62.93**
	2.202	63.5	61	62.5	61.5	57.5	59.5	59.5	**60.71**

Table D.25 Natural frequencies of 5 layers of 8 microns media.

D.8 Experimental Data for the Maximum Amplitude of the Transfer Functions of 8 Microns Media

		Microfibrous Sample – 8 Microns - 1 Layer - (Amplitude)						
		8A01	**8A02**	**8A04**	**8A05**	**8A06**	**8A07**	**8A08**
Input Vibration Amplitude (m/s^2)	**0.694**	1.8168	1.6219	3.3471	3.2278	3.9138	4.2153	3.1339
	1.103	2.2542	2.4243	4.0314	3.3063	4.1937	4.4444	4.0060
	1.468	3.0421	2.9171	3.9951	3.5789	4.3535	4.7416	4.2988
	1.831	3.3491	3.2706	4.1762	3.8211	4.6407	4.6500	4.6000
	2.202	3.8528	3.4241	4.2373	3.9089	5.2687	4.6285	4.7512

Table D.26a Maximum amplitude of the transfer functions of 1 layer of 8 microns media.

		Microfibrous Sample – 8 Microns - 1 Layer - (Amplitude)							
		8A09	**8A10**	**8A11**	**8A12**	**8A13**	**8A14**	**8A15**	**AV**
Input Vibration Amplitude (m/s^2)	**0.694**	1.9406	2.4912	3.5257	3.0915	2.2652	2.0777	2.0587	**2.7662**
	1.103	3.1367	3.5144	4.0523	3.5985	3.3695	3.1814	2.9999	**3.4652**
	1.468	3.4426	4.0848	4.3206	4.0393	3.9416	3.9266	3.3456	**3.8592**
	1.831	3.6016	4.1717	4.6399	4.0919	4.2404	4.1419	3.3844	**4.0557**
	2.202	3.5798	4.6697	4.6325	4.1879	4.1721	4.4500	3.6842	**4.2463**

Table D.26b Maximum amplitude of the transfer functions of 1 layer of 8 microns media.

		Microfibrous Sample – 8 Microns - 2 Layers - (Amplitude)							
		8A0102	**8A0405**	**8A0607**	**8A0809**	**8A1011**	**8A1213**	**8A1415**	**AV**
Input Vibration Amplitude (m/s^2)	**0.694**	2.9575	2.7311	1.8776	3.7443	3.8738	3.9258	2.9248	**3.1478**
	1.103	3.7938	3.4278	2.4706	4.1830	4.6410	5.0249	3.3829	**3.8463**
	1.468	4.4058	3.9415	3.0344	4.3811	4.5737	4.8113	3.7915	**4.1342**
	1.831	4.8427	3.9822	3.5844	4.4137	5.0025	5.0946	4.0975	**4.4311**
	2.202	4.5757	4.5109	3.7535	4.5991	4.7505	5.0733	4.1536	**4.4881**

Table D.27 Maximum amplitude of the transfer functions of 2 layers of 8 microns media.

		Microfibrous Sample – 8 Microns - 3 Layers - (Amplitude)							
		8A010204	8A050607	8A080910	8A111213	8A141501	8A020405	8A060708	AV
Input Vibration Amplitude (m/s^2)	**0.694**	2.1912	2.9269	4.6532	3.7737	3.5800	3.6534	3.3942	**3.4532**
	1.103	2.9501	3.7109	4.8094	3.9606	3.9300	4.3992	3.9002	**3.9515**
	1.468	3.6906	3.9511	4.8496	4.4242	4.1800	4.1128	4.3319	**4.2200**
	1.831	4.2793	4.5487	5.0698	4.8015	4.3400	4.3191	4.7141	**4.5818**
	2.202	4.5501	4.6063	5.1036	5.1478	4.3500	4.6244	4.8655	**4.7497**

Table D.28 Maximum amplitude of the transfer functions of 3 layers of 8 microns media.

		Microfibrous Sample – 8 Microns - 4 Layers - (Amplitude)							
		8A04050607	8A08091011	8A12131415	8A01020405	8A06081012	8A09111315	8A14020406	AV
Input Vibration Amplitude (m/s^2)	**0.694**	3.7871	3.1168	3.0890	4.1101	3.0679	2.9321	3.6528	**3.3937**
	1.103	4.3980	3.4022	3.6572	4.9104	3.6384	3.5695	4.2914	**3.9810**
	1.468	4.8257	3.7233	3.9397	4.5674	3.8267	4.1864	4.6423	**4.2445**
	1.831	4.6936	3.9159	4.1460	4.7589	4.2299	4.3069	4.9550	**4.4295**
	2.202	4.5746	4.1216	4.1911	5.1976	4.5468	4.5207	4.2780	**4.4901**

Table D.29 Maximum amplitude of the transfer functions of 4 layers of 8 microns media.

		Microfibrous Sample – 8 Microns - 5 Layers - (Amplitude)							
		8A0102040506	8A0708091011	8A1213141501	8A0204060810	8A1214010507	8A0507111315	8A0204051011	AV
Input Vibration Amplitude (m/s^2)	**0.694**	3.8538	4.0165	2.4793	2.5761	3.7959	2.3961	3.4571	**3.2250**
	1.103	3.9913	4.3262	3.2929	3.1001	4.1278	2.8647	3.8997	**3.6575**
	1.468	4.1220	4.4464	3.8178	3.5607	4.7041	3.3761	4.0842	**4.0159**
	1.831	4.2514	4.6672	4.0882	3.9097	4.7613	2.9225	4.5009	**4.1573**
	2.202	4.2210	4.5710	4.4387	3.9983	4.5597	3.5791	4.3146	**4.2403**

Table D.30 Maximum amplitude of the transfer functions of 5 layers of 8 microns media.

D.9 Experimental Data for the Natural Frequencies of 12 Microns Media

		Microfibrous Sample – 12 Microns-1 Layer- (Natural Frequency / Hz)						
		12A01	**12A02**	**12A03**	**12A04**	**12A05**	**12A06**	**12A07**
Input Vibration Amplitude (m/s^2)	**0.694**	178.5	159.5	174	163.5	162.5	159	157
	1.103	158.5	153	150.5	154	144	148.5	144.5
	1.468	155	142.5	140.5	144	136.5	139.5	141
	1.831	146.5	136.5	136	135.5	131.5	137	135
	2.202	140.5	131	131.5	133	126.5	133.5	132

Table D.31a Natural frequencies of 1 layer of 12 microns media.

		Microfibrous Sample – 12 Microns - 1 Layer- (Natural Frequency / Hz)						
		12A08	**12A09**	**12A10**	**12A11**	**12A12**	**12A13**	**AV**
Input Vibration Amplitude (m/s^2)	**0.694**	160	175.5	160.5	162	158.5	156	**163.58**
	1.103	144.5	163	146.5	144	148.5	144.5	**149.54**
	1.468	137.5	147.5	138.5	132	139	136	**140.73**
	1.831	133.5	140.5	134	125.5	129	132.5	**134.85**
	2.202	126.5	130.5	126	124	124	126	**129.62**

Table D.31b Natural frequencies of 1 layer of 12 microns media.

		Microfibrous Sample – 12 Microns - 2 Layers- (Natural Frequency / Hz)							
		12A0204	**12A0506**	**12A0809**	**12A1011**	**12A1213**	**12A0507**	**12A0103**	**AV**
Input Vibration Amplitude (m/s^2)	**0.694**	121	117.5	118	119.5	125	125	125.5	**121.64**
	1.103	109.5	108	105.5	114.5	117	113	112.5	**111.43**
	1.468	107.5	104	101	106	113	108.5	109	**107.00**
	1.831	104	96	97.5	103	107.5	103	105	**102.29**
	2.202	101	94.5	93.5	98	105	101	101.5	**99.21**

Table D.32 Natural frequencies of 2 layers of 12 microns media.

		Microfibrous Sample – 12 Microns - 3 Layers- (Natural Frequency / Hz)							
		12A010305	**12A060809**	**12A101112**	**12A130204**	**12A050607**	**12A091011**	**12A121302**	**AV**
Input Vibration Amplitude (m/s^2)	**0.694**	98.5	100.5	111	96.5	102	103	98	**101.36**
	1.103	93.5	97	103.5	82	96.5	98.5	91	**94.57**
	1.468	88	90.5	98	79	82	94.5	86	**88.29**
	1.831	85.5	86	92.5	76.5	79.5	90.5	81.5	**84.57**
	2.202	81.5	81.5	91	71	76	87.5	80	**81.21**

Table D.33 Natural frequencies of 3 layers of 12 microns media.

		Microfibrous Sample – 12 Microns - 4 Layers- (Natural Frequency / Hz)							
		12A02040506	**12A08091011**	**12A12130103**	**12A07050608**	**12A10111213**	**12A05060712**	**12A01020308**	**AV**
Input Vibration Amplitude (m/s^2)	**0.694**	82.5	96	81.5	83.5	90	87.5	86	**86.71**
	1.103	74.5	87.5	78	78	84.5	84.5	80	**81.00**
	1.468	68.5	85.5	76	75.5	81	82	75	**77.64**
	1.831	65	80.5	71.5	73.5	77.5	76	74	**74.00**
	2.202	63.5	79.5	70	71	76	74.5	67.5	**71.71**

Table D.34 Natural frequencies of 4 layers of 12 microns media.

		Microfibrous Sample – 12 Microns - 5 Layers - (Natural Frequency / Hz)							
		12A0204050608	**12A0910111213**	**12A0103071011**	**12A0506081213**	**12A0608091011**	**12A1312040503**	**12A0203010704**	**AV**
Input Vibration Amplitude (m/s^2)	**0.694**	74.5	81	82	76	86.5	75	82.5	**79.64**
	1.103	68.5	76	75.5	71.5	83	71	75	**74.36**
	1.468	67	71.5	72.5	67.5	80	67.5	73	**71.29**
	1.831	65.5	69	71	65.5	74	64.5	72.5	**68.86**
	2.202	62	67.5	70	62	71	61.5	69	**66.14**

Table D.35 Natural frequencies of 5 layers of 12 microns media.

D.10 Experimental Data for the Maximum Amplitude of the Transfer Functions of 12 Microns Media

		Microfibrous Sample – 12 Microns - 1 Layer - (Amplitude)						
		12A01	**12A02**	**12A03**	**12A04**	**12A05**	**12A06**	**12A07**
Input Vibration Amplitude (m/s^2)	**0.694**	2.0495	3.5800	1.9042	3.9558	1.9443	3.9160	2.0292
	1.103	2.3504	4.1300	2.4677	3.9896	2.8385	4.6428	2.4926
	1.468	2.7667	4.6900	3.1181	4.3923	3.4916	5.4440	2.9100
	1.831	3.4957	4.7800	3.5546	4.5018	3.9971	5.3383	3.1437
	2.202	3.9384	5.0300	3.9243	4.4972	4.1019	5.3424	3.3277

Table D.36a Maximum amplitude of the transfer functions of 1 layer of 12 microns media.

		Microfibrous Sample – 12 Microns - 1 Layer - (Amplitude)						
		12A08	**12A09**	**12A10**	**12A11**	**12A12**	**12A13**	**AV**
Input Vibration Amplitude (m/s^2)	**0.694**	3.2300	1.6850	2.8016	2.7820	2.0847	2.1445	**2.6236**
	1.103	3.9290	2.0005	3.3023	3.8014	2.3553	2.8409	**3.1647**
	1.468	4.1230	2.7859	3.9767	4.2652	3.4505	3.2726	**3.7451**
	1.831	4.8763	3.4645	4.2305	4.7040	3.7589	3.5710	**4.1090**
	2.202	4.4379	3.8150	4.2957	4.5952	4.5733	3.9318	**4.2931**

Table D.36b Maximum amplitude of the transfer functions of 1 layer of 12 microns media.

		Microfibrous Sample – 12 Microns - 2 Layers - (Amplitude)							
		12A0204	**12A0506**	**12A0809**	**12A1011**	**12A1213**	**12A0507**	**12A0103**	**AV**
Input Vibration Amplitude (m/s^2)	**0.694**	2.4696	2.0014	2.0588	1.7499	3.5661	3.5371	2.8589	**2.6060**
	1.103	3.4051	2.7616	2.5380	2.8302	4.2177	2.7608	3.6513	**3.1664**
	1.468	3.8047	3.4303	3.3585	3.4927	4.4662	3.5798	3.8722	**3.7149**
	1.831	4.5932	3.8478	3.6706	3.7436	5.0211	4.3420	4.1913	**4.2014**
	2.202	3.9369	4.0533	4.1108	4.1881	4.8551	4.3703	4.5110	**4.2894**

Table D.37 Maximum amplitude of the transfer functions of 2 layers of 12 microns media.

		Microfibrous Sample – 12 Microns - 3 Layers - (Amplitude)							
		12A010305	**12A060809**	**12A101112**	**12A130204**	**12A050607**	**12A091011**	**12A121302**	**AV**
Input Vibration Amplitude (m/s^2)	**0.694**	2.1974	1.6436	3.9253	1.7999	2.1174	3.1394	3.4919	**2.6164**
	1.103	2.9582	2.5480	4.4592	2.9087	2.9242	3.9868	4.6102	**3.4850**
	1.468	3.7821	3.1592	4.6922	3.3311	2.9575	4.2257	4.3424	**3.7843**
	1.831	4.1892	3.6381	4.9063	3.8118	3.5322	4.6353	4.8278	**4.2201**
	2.202	4.3654	3.6886	4.9060	3.8524	3.6567	4.5360	5.2855	**4.3272**

Table D.38 Maximum amplitude of the transfer functions of 3 layers of 12 microns media.

		Microfibrous Sample – 12 Microns - 4 Layers - (Amplitude)							
		12A02040506	**12A08091011**	**12A12130103**	**12A07050608**	**12A10111213**	**12A05060712**	**12A01020308**	**AV**
Input Vibration Amplitude (m/s^2)	**0.694**	2.7904	2.0298	3.4514	2.5435	1.8958	2.4594	3.1469	**2.6167**
	1.103	3.7587	3.8872	4.0485	3.2821	2.8058	3.2303	3.5271	**3.5057**
	1.468	3.8798	3.5610	4.2641	3.7016	3.2963	3.8428	4.5457	**3.8702**
	1.831	4.4711	3.9846	4.5062	3.9430	3.4764	4.3841	4.4863	**4.1788**
	2.202	4.2047	4.0148	4.7552	4.1076	3.5986	4.5082	4.6791	**4.2669**

Table D.39 Maximum amplitude of the transfer functions of 4 layers of 12 microns media.

		Microfibrous Sample – 12 Microns - 5 Layers - (Amplitude)							
		12A0204050608	**12A0910111213**	**12A0103071011**	**12A0506081213**	**12A0608091011**	**12A1312040503**	**12A0203010704**	**AV**
Input Vibration Amplitude (m/s^2)	**0.694**	1.9417	3.1633	2.1100	2.1272	2.1405	3.8677	3.1737	**2.6463**
	1.103	2.6882	4.1413	3.1470	3.1239	3.1925	4.1280	4.3927	**3.5448**
	1.468	3.4718	4.5964	3.4724	3.6476	3.3152	4.4652	4.5538	**3.9318**
	1.831	3.5811	4.9393	4.0801	3.9558	3.6838	4.7228	4.6759	**4.2341**
	2.202	3.9811	4.8485	4.0821	3.8749	3.9487	4.7198	5.0201	**4.3536**

Table D.40 Maximum amplitude of the transfer functions of 5 layers of 12 microns media.

APPENDIX E

E.1 Matlab Codes for Stiffness and Damping Calculations

```
%% Computation of stiffness and Damping
%4 MICRONS

% Enter mass 'm' kg
m = 35.34e-3;


% Enter Frequencies of Maximum Transmissibility
% Example Wx1: Maximum frequency for 1 layer and with increasing
amplitude
% Fibre size x microns
W41 = [130.90 124.47   121.20   117.60  114.97]*2*pi;
W42 = [90.00  86.07    83.43    81.50   79.93]*2*pi;
W43 = [73.43  70.50    67.43    65.29   63.93]*2*pi;
W44 = [65.07  62.79    61.14    59.64   58.14]*2*pi;
W45 = [57.50  56.29    55.07    53.64   52.79]*2*pi;

% Enter Maximum Amplitudes of Transmissibility
% Example, Ax1 = Maximum Amplitudes for 1 layer and with increasing
% amplitude. Fibre size x microns
A41 = [2.3235   2.9934  3.8904  4.5804  5.0825];
A42 = [2.6739   3.6372  4.3496  4.8739  5.0668];
A43 = [2.8366   3.7128  4.2531  4.5733  4.8752];
A44 = [2.8290   3.7854  4.2700  4.6053  4.9656];
A45 = [2.7817   3.6282  4.2180  4.5136  4.8321];

% Calculating Damping Ratio Zeta
A4 = [A41 A42 A43 A44 A45];
Z4 = zeros;

for r=1:25
   A = A4(r);
   n=0;
   x=7;

   while (x-A) >= 0.0001
       n = n+1;
       z = 0.1 + (n*0.0001);
       x = sqrt ((8*z^4)/(8*z^4 - 4*z^2 + sqrt(1+8*z^2)-1));

   end
   Z4(r) = z;
end
```

```
Z41 = [Z4(1) Z4(2) Z4(3) Z4(4) Z4(5)];
Z42 = [Z4(6) Z4(7) Z4(8) Z4(9) Z4(10)];
Z43 = [Z4(11) Z4(12) Z4(13) Z4(14) Z4(15)];
Z44 = [Z4(16) Z4(17) Z4(18) Z4(19) Z4(20)];
Z45 = [Z4(21) Z4(22) Z4(23) Z4(24) Z4(25)];

%Calculating Natural frequency Wn
Wn41 = W41./(sqrt((sqrt(1 + 8*Z41.^2)-1)/(4*Z41.^2)));
Wn42 = W42./(sqrt((sqrt(1 + 8*Z42.^2)-1)/(4*Z42.^2)));
Wn43 = W43./(sqrt((sqrt(1 + 8*Z43.^2)-1)/(4*Z43.^2)));
Wn44 = W44./(sqrt((sqrt(1 + 8*Z44.^2)-1)/(4*Z44.^2)));
Wn45 = W45./(sqrt((sqrt(1 + 8*Z45.^2)-1)/(4*Z45.^2)));


%Calculating Stiffness
K41 = (Wn41.^2)*m;
K42 = (Wn42.^2)*m;
K43 = (Wn43.^2)*m;
K44 = (Wn44.^2)*m;
K45 = (Wn45.^2)*m;

%Plotting figures
N = [1 2 3 4 5];

%Rearranging Stiffness with respect to amplitude for plotting
K420 = [K41(1) K42(1) K43(1) K44(1) K45(1)];
K430 = [K41(2) K42(2) K43(2) K44(2) K45(2)];
K440 = [K41(3) K42(3) K43(3) K44(3) K45(3)];
K450 = [K41(4) K42(4) K43(4) K44(4) K45(4)];
K460 = [K41(5) K42(5) K43(5) K44(5) K45(5)];

%Rearranging Damping with respect to amplitude for plotting
Z420 = [Z41(1) Z42(1) Z43(1) Z44(1) Z45(1)];
Z430 = [Z41(2) Z42(2) Z43(2) Z44(2) Z45(2)];
Z440 = [Z41(3) Z42(3) Z43(3) Z44(3) Z45(3)];
Z450 = [Z41(4) Z42(4) Z43(4) Z44(4) Z45(4)];
Z460 = [Z41(5) Z42(5) Z43(5) Z44(5) Z45(5)];


figure(1)
plot (N,K420,'-oK','LineWidth',2.5);
%pbaspect([1.6;1;1])
grid on
set(gca,'XTick',[0 1 2 3 4 5]);
xlabel ('Number of layers','FontSize',12);
ylabel ('Stiffness K, N/m','FontSize',12);
title('4 Microns - Stiffness against Number of Layers','FontSize',14)
hold on
plot (N,K430,'--^R','LineWidth',2.5);
hold on
plot (N,K440,':sG','LineWidth',2.5);
hold on
plot (N,K450,'-.dB','LineWidth',2.5);
hold on
```

```
plot (N,K460,'-vC','LineWidth',2.5);
hold on
h = legend('0.694 m/s^2','1.103 m/s^2','1.468 m/s^2','1.831
m/s^2','2.202 m/s^2');

figure(2)
plot (N,Z420,'-oK','LineWidth',2.5);
%pbaspect([1.6;1;1])
grid on
set(gca,'XTick',[0 1 2 3 4 5]);
xlabel ('Number of layers','FontSize',12);
ylabel ('Damping Ratio','FontSize',12);
title('4 Microns - Damping Ratio against Number of
Layers','FontSize',14)
hold on
plot (N,Z430,'--^R','LineWidth',2.5);
hold on
plot (N,Z440,':sG','LineWidth',2.5);
hold on
plot (N,Z450,'-.dB','LineWidth',2.5);
hold on
plot (N,Z460,'-vC','LineWidth',2.5);
hold on
h = legend('0.694 m/s^2','1.103 m/s^2','1.468 m/s^2','1.831
m/s^2','2.202 m/s^2');

Z4 = [Z41;Z42;Z43;Z44;Z45]


%% Computation of stiffness and Damping
%48 MICRONS

% Enter mass 'm' kg
m = 35.34e-3;


% Enter Frequencies of Maximum Transmissibility
% Example Wx1: Maximum frequency for 1 layer and with increasing
amplitude
% Fibre size x microns
W481 = [147.21  139.79  134.32  129.11  123.82]*2*pi;
W482 = [108.07  101.43  97.64   94.43   91.93]*2*pi;
W483 = [87.57   83.64   80.93   78.36   75.14]*2*pi;
W484 = [76.50   73.00   70.29   68.50   66.43]*2*pi;
W485 = [71.00   68.71   65.43   63.00   60.93]*2*pi;

% Enter Maximum Amplitudes of Transmissibility
% Example, Ax1 = Maximum Amplitudes for 1 layer and with increasing
% amplitude. Fibre size x microns
A481 = [2.9017  3.5618  4.1686  4.5308  4.7021];
A482 = [3.3093  3.9699  4.4765  4.8964  5.0213];
A483 = [3.3760  4.1607  4.6540  4.9571  5.0683];
A484 = [3.5255  4.0194  4.3350  4.6877  4.7958];
A485 = [3.4098  4.0457  4.4779  4.8841  5.0598];
```

```
% Calculating Damping Ratio Zeta
A48 = [A481 A482 A483 A484 A485];
Z48 = zeros;

for r=1:25
   A = A48(r);
   n=0;
   x=7;

   while (x-A) >= 0.0001
       n = n+1;
       z = 0.1 + (n*0.0001);
       x = sqrt ((8*z^4)/(8*z^4 - 4*z^2 + sqrt(1+8*z^2)-1));

   end
   Z48(r) = z;
end

Z481 = [Z48(1) Z48(2) Z48(3) Z48(4) Z48(5)];
Z482 = [Z48(6) Z48(7) Z48(8) Z48(9) Z48(10)];
Z483 = [Z48(11) Z48(12) Z48(13) Z48(14) Z48(15)];
Z484 = [Z48(16) Z48(17) Z48(18) Z48(19) Z48(20)];
Z485 = [Z48(21) Z48(22) Z48(23) Z48(24) Z48(25)];

%Calculating Natural frequency Wn
Wn481 = W481./(sqrt((sqrt(1 + 8*Z481.^2)-1)/(4*Z481.^2)));
Wn482 = W482./(sqrt((sqrt(1 + 8*Z482.^2)-1)/(4*Z482.^2)));
Wn483 = W483./(sqrt((sqrt(1 + 8*Z483.^2)-1)/(4*Z483.^2)));
Wn484 = W484./(sqrt((sqrt(1 + 8*Z484.^2)-1)/(4*Z484.^2)));
Wn485 = W485./(sqrt((sqrt(1 + 8*Z485.^2)-1)/(4*Z485.^2)));



%Calculating Stiffness
K481 = (Wn481.^2)*m;
K482 = (Wn482.^2)*m;
K483 = (Wn483.^2)*m;
K484 = (Wn484.^2)*m;
K485 = (Wn485.^2)*m;

%Plotting figures
N = [1 2 3 4 5];

%Rearranging Stiffness with respect to amplitude for plotting
K4820 = [K481(1) K482(1) K483(1) K484(1) K485(1)];
K4830 = [K481(2) K482(2) K483(2) K484(2) K485(2)];
K4840 = [K481(3) K482(3) K483(3) K484(3) K485(3)];
K4850 = [K481(4) K482(4) K483(4) K484(4) K485(4)];
K4860 = [K481(5) K482(5) K483(5) K484(5) K485(5)];

%Rearranging Damping with respect to amplitude for plotting
Z4820 = [Z481(1) Z482(1) Z483(1) Z484(1) Z485(1)];
Z4830 = [Z481(2) Z482(2) Z483(2) Z484(2) Z485(2)];
Z4840 = [Z481(3) Z482(3) Z483(3) Z484(3) Z485(3)];
Z4850 = [Z481(4) Z482(4) Z483(4) Z484(4) Z485(4)];
```

```
Z4860 = [Z481(5) Z482(5) Z483(5) Z484(5) Z485(5)];


figure(3)
plot (N,K4820,'-oK','LineWidth',2.5);
%pbaspect([1.6;1;1])
grid on
set(gca,'XTick',[0 1 2 3 4 5]);
xlabel ('Number of layers','FontSize',12);
ylabel ('Stiffness K, N/m','FontSize',12);
title('4/8 Microns - Stiffness against Number of Layers','FontSize',14)
hold on
plot (N,K4830,'--^R','LineWidth',2.5);
hold on
plot (N,K4840,':sG','LineWidth',2.5);
hold on
plot (N,K4850,'-.dB','LineWidth',2.5);
hold on
plot (N,K4860,'-vC','LineWidth',2.5);
hold on
h = legend('0.694 m/s^2','1.103 m/s^2','1.468 m/s^2','1.831
m/s^2','2.202 m/s^2');

figure(4)
plot (N,Z4820,'-oK','LineWidth',2.5);
%pbaspect([1.6;1;1])
grid on
set(gca,'XTick',[0 1 2 3 4 5]);
xlabel ('Number of layers','FontSize',12);
ylabel ('Damping Ratio','FontSize',12);
title('4/8 Microns - Damping Ratio against Number of
Layers','FontSize',14)
hold on
plot (N,Z4830,'--^R','LineWidth',2.5);
hold on
plot (N,Z4840,':sG','LineWidth',2.5);
hold on
plot (N,Z4850,'-.dB','LineWidth',2.5);
hold on
plot (N,Z4860,'-vC','LineWidth',2.5);
hold on
h = legend('0.694 m/s^2','1.103 m/s^2','1.468 m/s^2','1.831
m/s^2','2.202 m/s^2');

Z48 = [Z481;Z482;Z483;Z484;Z485]



%% Computation of stiffness and Damping
%8 MICRONS

% Enter mass 'm' kg
m = 35.34e-3;
```

```
% Enter Frequencies of Maximum Transmissibility
% Example Wx1: Maximum frequency for 1 layer and with increasing
amplitude
% Fibre size x microns
W81 = [160.00   145.25  136.50  131.18  125.50]*2*pi;
W82 = [113.00   105.29  100.29  96.36   92.71]*2*pi;
W83 = [91.21    87.00   83.21   79.71   76.29]*2*pi;
W84 = [79.93    75.29   70.00   67.57   65.64]*2*pi;
W85 = [72.50    68.00   65.00   62.93   60.71]*2*pi;

% Enter Maximum Amplitudes of Transmissibility
% Example, Ax1 = Maximum Amplitudes for 1 layer and with increasing
% amplitude. Fibre size x microns
A81 = [2.7662   3.4652  3.8592  4.0557  4.2463];
A82 = [3.1478   3.8463  4.1342  4.4311  4.4881];
A83 = [3.4532   3.9515  4.2200  4.5818  4.7497];
A84 = [3.3937   3.9810  4.2445  4.4295  4.4901];
A85 = [3.2250   3.6575  4.0159  4.1573  4.2403];

% Calculating Damping Ratio Zeta
A8 = [A81 A82 A83 A84 A85];
Z8 = zeros;

for r=1:25
   A = A8(r);
   n=0;
   x=7;

   while (x-A) >= 0.0001
       n = n+1;
       z = 0.1 + (n*0.0001);
       x = sqrt ((8*z^4)/(8*z^4 - 4*z^2 + sqrt(1+8*z^2)-1));

   end
   Z8(r) = z;
end

Z81 = [Z8(1) Z8(2) Z8(3) Z8(4) Z8(5)];
Z82 = [Z8(6) Z8(7) Z8(8) Z8(9) Z8(10)];
Z83 = [Z8(11) Z8(12) Z8(13) Z8(14) Z8(15)];
Z84 = [Z8(16) Z8(17) Z8(18) Z8(19) Z8(20)];
Z85 = [Z8(21) Z8(22) Z8(23) Z8(24) Z8(25)];

%Calculating Natural frequency Wn
Wn81 = W81./(sqrt((sqrt(1 + 8*Z81.^2)-1)/(4*Z81.^2)));
Wn82 = W82./(sqrt((sqrt(1 + 8*Z82.^2)-1)/(4*Z82.^2)));
Wn83 = W83./(sqrt((sqrt(1 + 8*Z83.^2)-1)/(4*Z83.^2)));
Wn84 = W84./(sqrt((sqrt(1 + 8*Z84.^2)-1)/(4*Z84.^2)));
Wn85 = W85./(sqrt((sqrt(1 + 8*Z85.^2)-1)/(4*Z85.^2)));

%Calculating Stiffness
K81 = (Wn81.^2)*m;
K82 = (Wn82.^2)*m;
K83 = (Wn83.^2)*m;
K84 = (Wn84.^2)*m;
```

```
K85 = (Wn85.^2)*m;

%Plotting figures
N = [1 2 3 4 5];

%Rearranging Stiffness with respect to amplitude for plotting
K820 = [K81(1) K82(1) K83(1) K84(1) K85(1)];
K830 = [K81(2) K82(2) K83(2) K84(2) K85(2)];
K840 = [K81(3) K82(3) K83(3) K84(3) K85(3)];
K850 = [K81(4) K82(4) K83(4) K84(4) K85(4)];
K860 = [K81(5) K82(5) K83(5) K84(5) K85(5)];

%Rearranging Damping with respect to amplitude for plotting
Z820 = [Z81(1) Z82(1) Z83(1) Z84(1) Z85(1)];
Z830 = [Z81(2) Z82(2) Z83(2) Z84(2) Z85(2)];
Z840 = [Z81(3) Z82(3) Z83(3) Z84(3) Z85(3)];
Z850 = [Z81(4) Z82(4) Z83(4) Z84(4) Z85(4)];
Z860 = [Z81(5) Z82(5) Z83(5) Z84(5) Z85(5)];


figure(5)
plot (N,K820,'-oK','LineWidth',2.5);
%pbaspect([1.6;1;1])
grid on
set(gca,'XTick',[0 1 2 3 4 5]);
xlabel ('Number of layers','FontSize',12);
ylabel ('Stiffness K, N/m','FontSize',12);
title('8 Microns - Stiffness against Number of Layers','FontSize',14)
hold on
plot (N,K830,'--^R','LineWidth',2.5);
hold on
plot (N,K840,':sG','LineWidth',2.5);
hold on
plot (N,K850,'-.dB','LineWidth',2.5);
hold on
plot (N,K860,'-vC','LineWidth',2.5);
hold on
h = legend('0.694 m/s^2','1.103 m/s^2','1.468 m/s^2','1.831
m/s^2','2.202 m/s^2');

figure(6)
plot (N,Z820,'-oK','LineWidth',2.5);
%pbaspect([1.6;1;1])
grid on
set(gca,'XTick',[0 1 2 3 4 5]);
xlabel ('Number of layers','FontSize',12);
ylabel ('Damping Ratio','FontSize',12);
title('8 Microns - Damping Ratio against Number of
Layers','FontSize',14)
hold on
plot (N,Z830,'--^R','LineWidth',2.5);
hold on
plot (N,Z840,':sG','LineWidth',2.5);
hold on
plot (N,Z850,'-.dB','LineWidth',2.5);
hold on
```

```
plot (N,Z860,'-vC','LineWidth',2.5);
hold on
h = legend('0.694 m/s^2','1.103 m/s^2','1.468 m/s^2','1.831
m/s^2','2.202 m/s^2');

Z8 = [Z81;Z82;Z83;Z84;Z85]



%% Computation of stiffness and Damping
%12 MICRONS

% Enter mass 'm' kg
m = 35.34e-3;


% Enter Frequencies of Maximum Transmissibility
% Example Wx1: Maximum frequency for 1 layer and with increasing
amplitude
% Fibre size x microns
W121 = [163.54  149.54  140.73  134.85  129.62]*2*pi;
W122 = [121.64  111.43  107.00  102.29  99.21]*2*pi;
W123 = [101.36  94.57   88.29   84.57   81.21]*2*pi;
W124 = [86.71   81.00   77.64   74.00   71.71]*2*pi;
W125 = [79.64   74.36   71.29   68.86   66.14]*2*pi;

% Enter Maximum Amplitudes of Transmissibility
% Example, Ax1 = Maximum Amplitudes for 1 layer and with increasing
% amplitude. Fibre size x microns
A121 = [2.6236  3.1647  3.7451  4.1090  4.2931];
A122 = [2.6060  3.1664  3.7149  4.2014  4.2894];
A123 = [2.6164  3.4850  3.7843  4.2201  4.3272];
A124 = [2.6167  3.5057  3.8702  4.1788  4.2669];
A125 = [2.6463  3.5448  3.9318  4.2341  4.3536];

% Calculating Damping Ratio Zeta
A12 = [A121 A122 A123 A124 A125];
Z12 = zeros;

for r=1:25
   A = A12(r);
   n=0;
   x=7;

   while (x-A) >= 0.0001
       n = n+1;
       z = 0.1 + (n*0.0001);
       x = sqrt ((8*z^4)/(8*z^4 - 4*z^2 + sqrt(1+8*z^2)-1));

   end
   Z12(r) = z;
end

Z121 = [Z12(1) Z12(2) Z12(3) Z12(4) Z12(5)];
```

```
Z122 = [Z12(6) Z12(7) Z12(8) Z12(9) Z12(10)];
Z123 = [Z12(11) Z12(12) Z12(13) Z12(14) Z12(15)];
Z124 = [Z12(16) Z12(17) Z12(18) Z12(19) Z12(20)];
Z125 = [Z12(21) Z12(22) Z12(23) Z12(24) Z12(25)];

%Calculating Natural frequency Wn
Wn121 = W121./(sqrt((sqrt(1 + 8*Z121.^2)-1)/(4*Z121.^2)));
Wn122 = W122./(sqrt((sqrt(1 + 8*Z122.^2)-1)/(4*Z122.^2)));
Wn123 = W123./(sqrt((sqrt(1 + 8*Z123.^2)-1)/(4*Z123.^2)));
Wn124 = W124./(sqrt((sqrt(1 + 8*Z124.^2)-1)/(4*Z124.^2)));
Wn125 = W125./(sqrt((sqrt(1 + 8*Z125.^2)-1)/(4*Z125.^2)));

%Calculating Stiffness
K121 = (Wn121.^2)*m;
K122 = (Wn122.^2)*m;
K123 = (Wn123.^2)*m;
K124 = (Wn124.^2)*m;
K125 = (Wn125.^2)*m;

%Plotting figures
N = [1 2 3 4 5];

%Rearranging Stiffness with respect to amplitude for plotting
K1220 = [K121(1) K122(1) K123(1) K124(1) K125(1)];
K1230 = [K121(2) K122(2) K123(2) K124(2) K125(2)];
K1240 = [K121(3) K122(3) K123(3) K124(3) K125(3)];
K1250 = [K121(4) K122(4) K123(4) K124(4) K125(4)];
K1260 = [K121(5) K122(5) K123(5) K124(5) K125(5)];

%Rearranging Damping with respect to amplitude for plotting
Z1220 = [Z121(1) Z122(1) Z123(1) Z124(1) Z125(1)];
Z1230 = [Z121(2) Z122(2) Z123(2) Z124(2) Z125(2)];
Z1240 = [Z121(3) Z122(3) Z123(3) Z124(3) Z125(3)];
Z1250 = [Z121(4) Z122(4) Z123(4) Z124(4) Z125(4)];
Z1260 = [Z121(5) Z122(5) Z123(5) Z124(5) Z125(5)];



figure(7)
plot (N,K1220,'-oK','LineWidth',2.5);
%pbaspect([1.6;1;1])
grid on
set(gca,'XTick',[0 1 2 3 4 5]);
xlabel ('Number of layers','FontSize',12);
ylabel ('Stiffness K, N/m','FontSize',12);
title('12 Microns - Stiffness against Number of Layers','FontSize',14)
hold on
plot (N,K1230,'--^R','LineWidth',2.5);
hold on
plot (N,K1240,':sG','LineWidth',2.5);
hold on
plot (N,K1250,'-.dB','LineWidth',2.5);
hold on
plot (N,K1260,'-vC','LineWidth',2.5);
hold on
```

```
h = legend('0.694 m/s^2','1.103 m/s^2','1.468 m/s^2','1.831
m/s^2','2.202 m/s^2');

figure(8)
plot (N,Z1220,'-oK','LineWidth',2.5);
%pbaspect([1.6;1;1])
grid on
set(gca,'XTick',[0 1 2 3 4 5]);
xlabel ('Number of layers','FontSize',12);
ylabel ('Damping Ratio','FontSize',12);
title('12 Microns - Damping Ratio against Number of
Layers','FontSize',14)
hold on
plot (N,Z1230,'--^R','LineWidth',2.5);
hold on
plot (N,Z1240,':sG','LineWidth',2.5);
hold on
plot (N,Z1250,'-.dB','LineWidth',2.5);
hold on
plot (N,Z1260,'-vC','LineWidth',2.5);
hold on
h = legend('0.694 m/s^2','1.103 m/s^2','1.468 m/s^2','1.831
m/s^2','2.202 m/s^2');


Z12 = [Z121;Z122;Z123;Z124;Z125]
```

APPENDIX F

F.1 Acoustical Test Results for Gyroscopes G3-G7

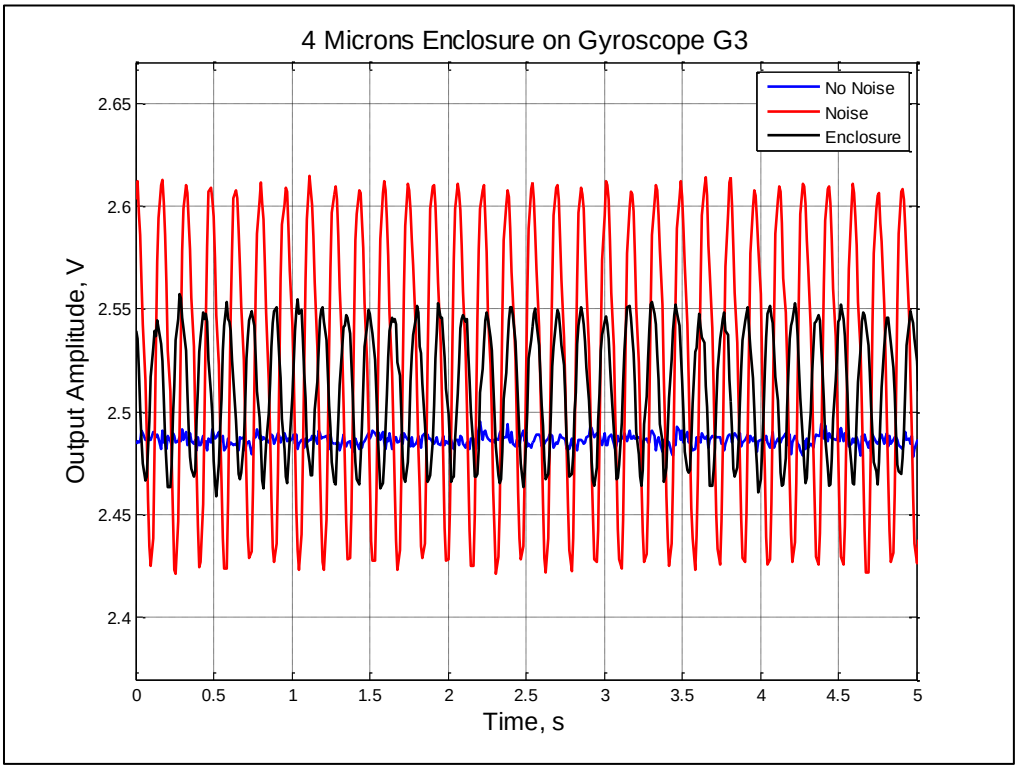

Figure F.1 Experimental results of the 4 microns enclosure on gyroscope G3.

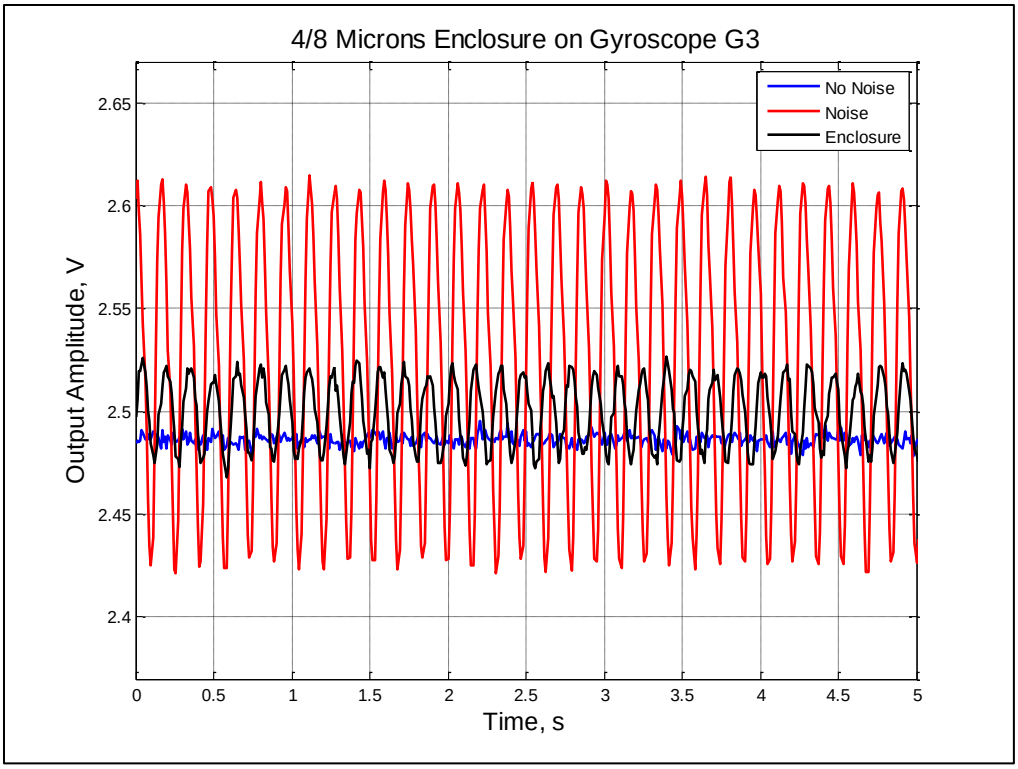

Figure F.2 Experimental results of the 4/8 microns enclosure on gyroscope G3.

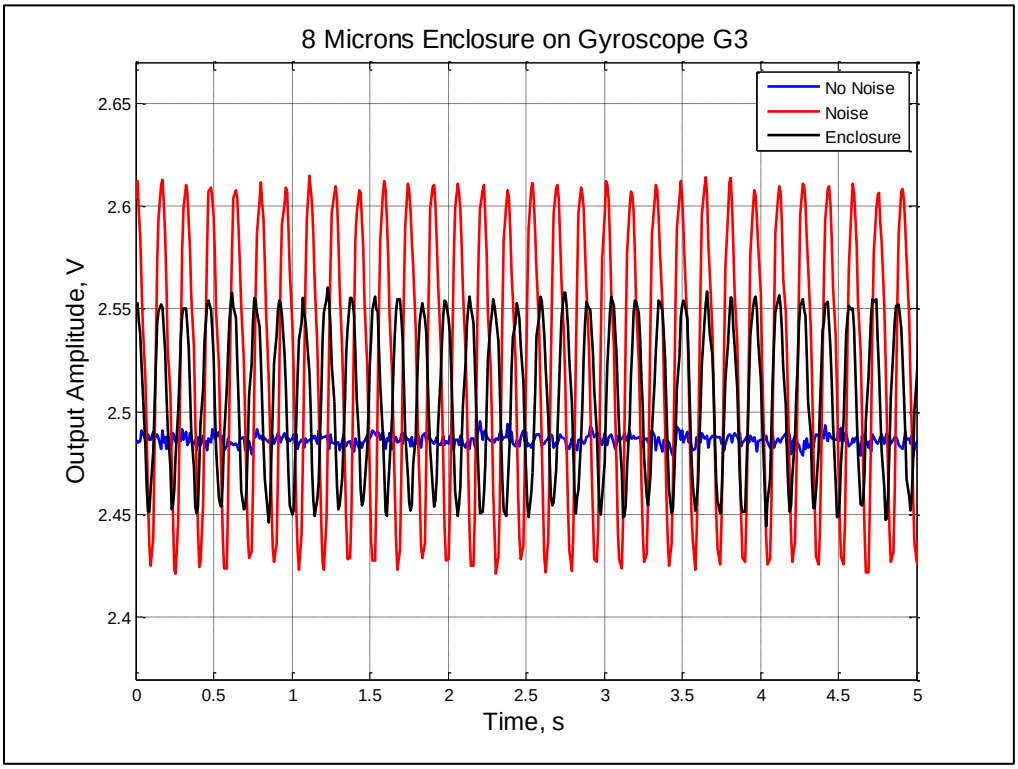

Figure F.3 Experimental results of the 8 microns enclosure on gyroscope G3.

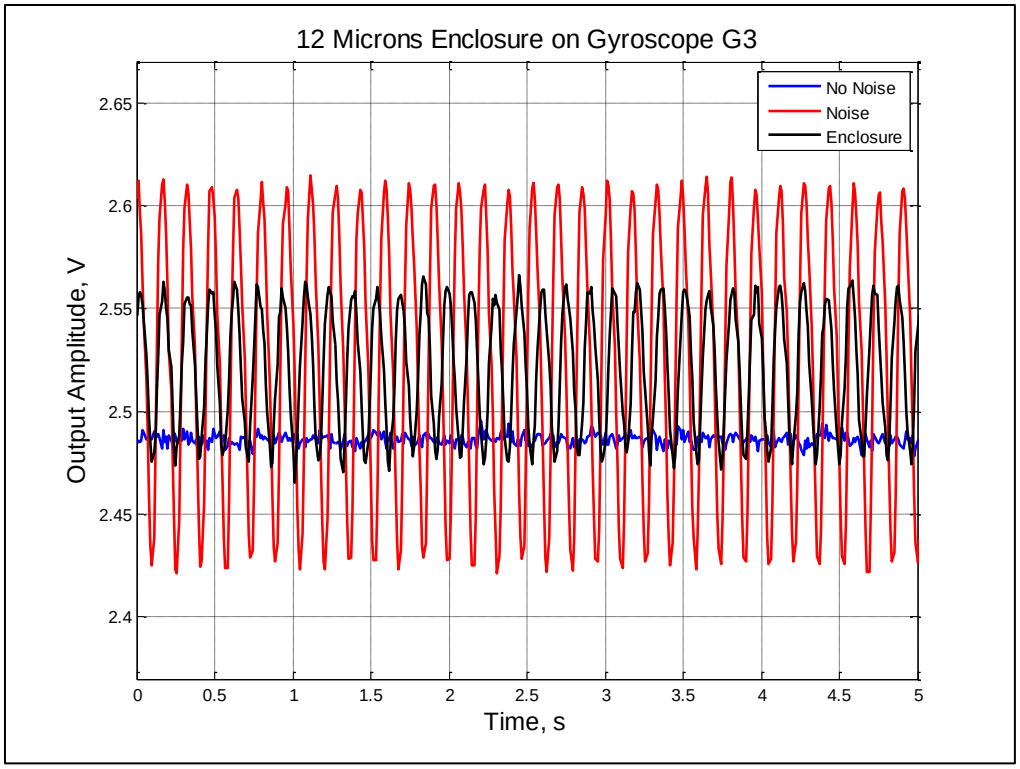

Figure F.4 Experimental results of the 12 microns enclosure on gyroscope G3.

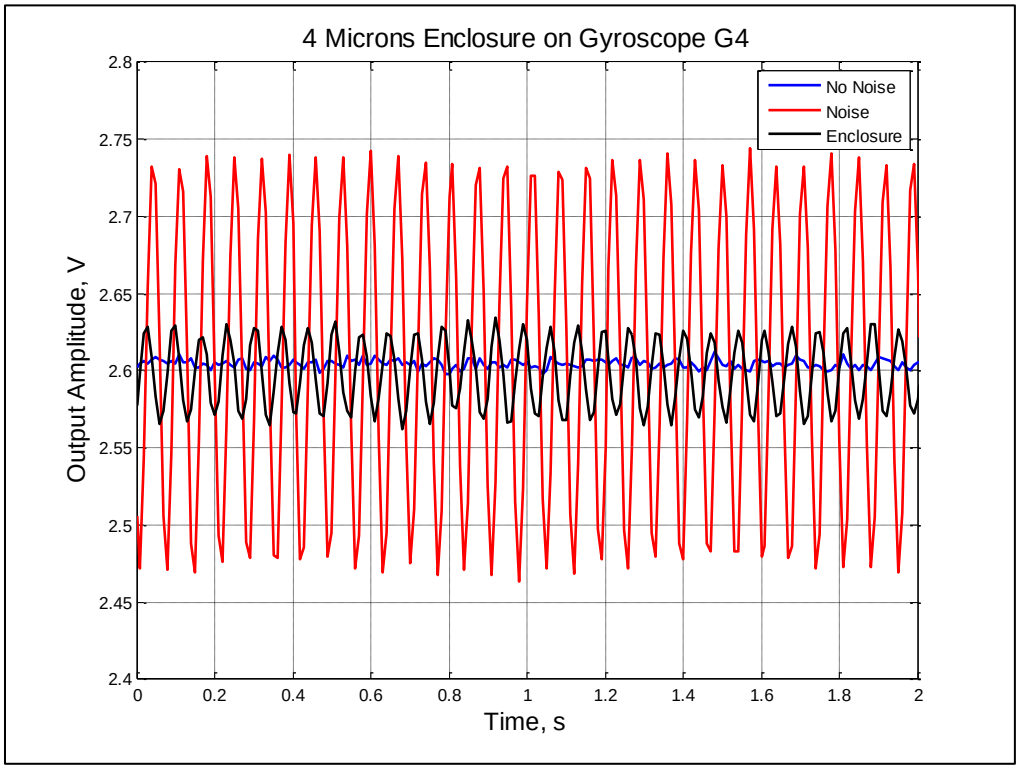

Figure F.5 Experimental results of the 4 microns enclosure on gyroscope G4.

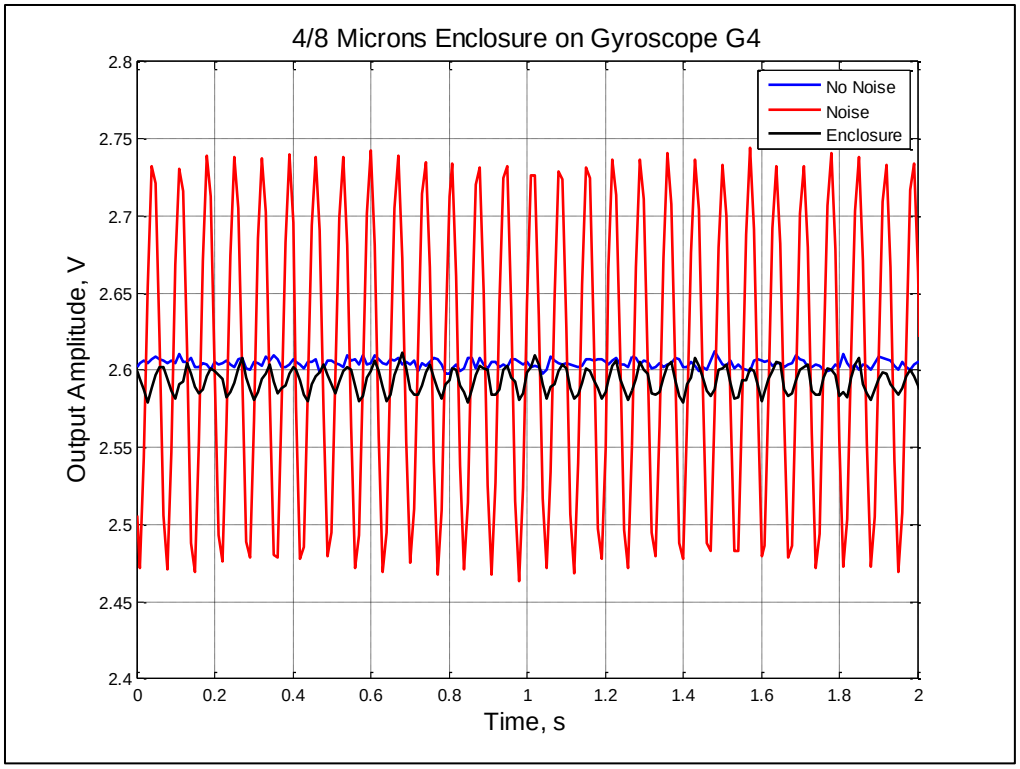

Figure F.6 Experimental results of the 4/8 microns enclosure on gyroscope G4.

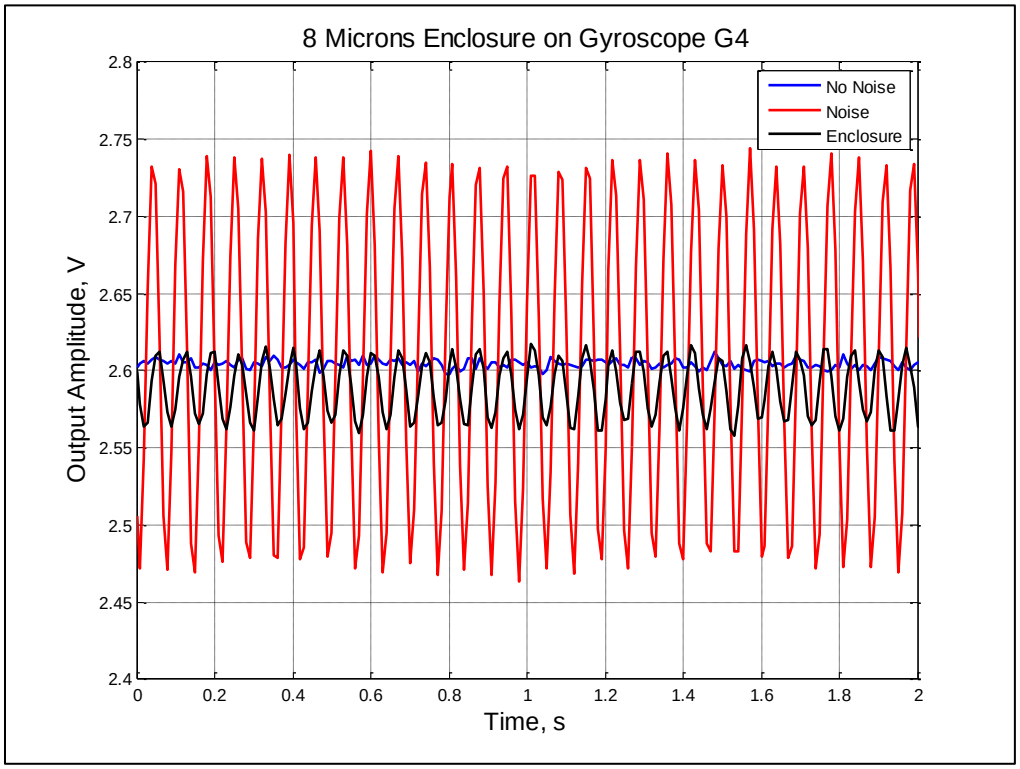

Figure F.7 Experimental results of the 8 microns enclosure on gyroscope G4.

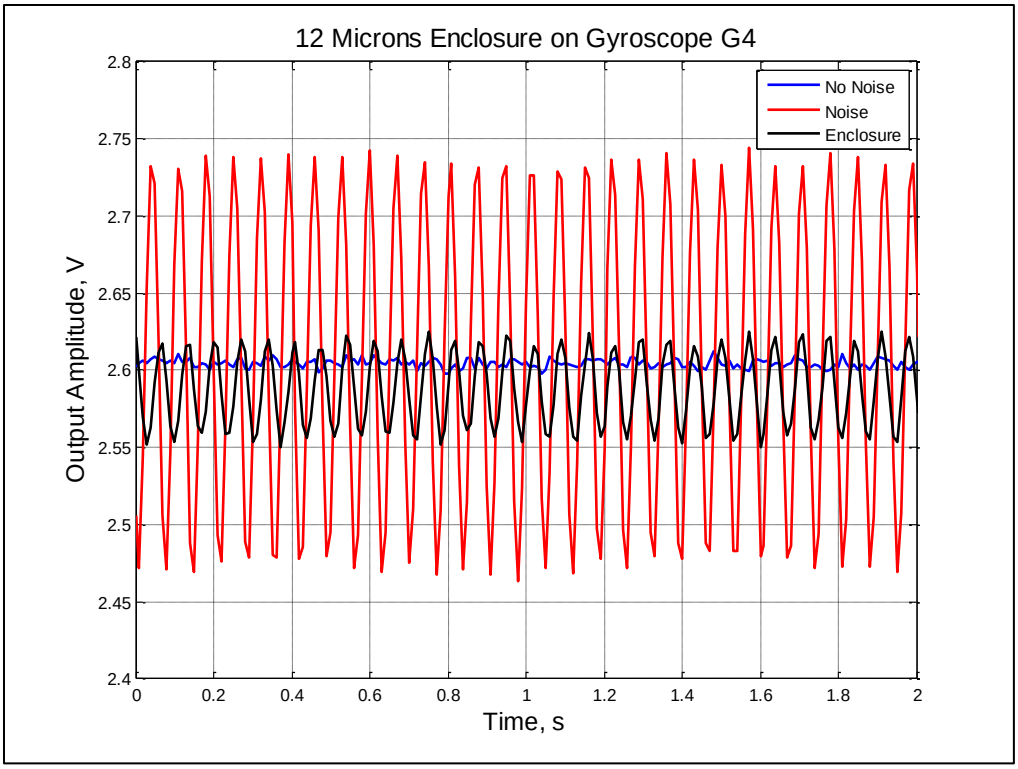

Figure F.8 Experimental results of the 12 microns enclosure on gyroscope G4.

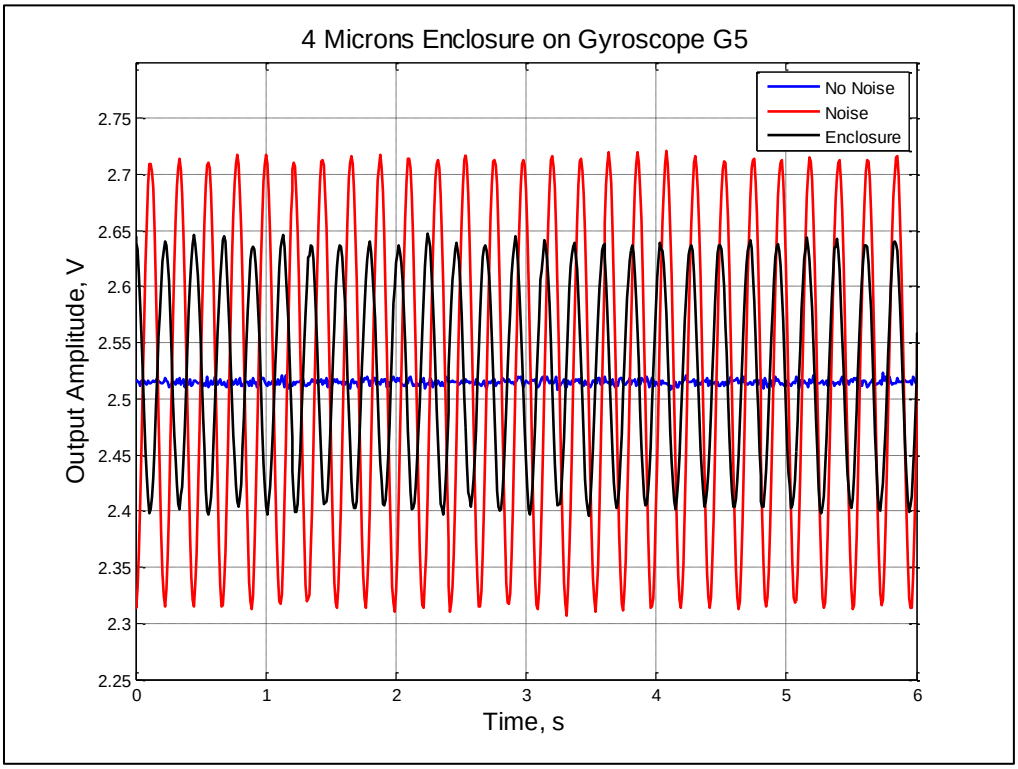

Figure F.9 Experimental results of the 4 microns enclosure on gyroscope G5.

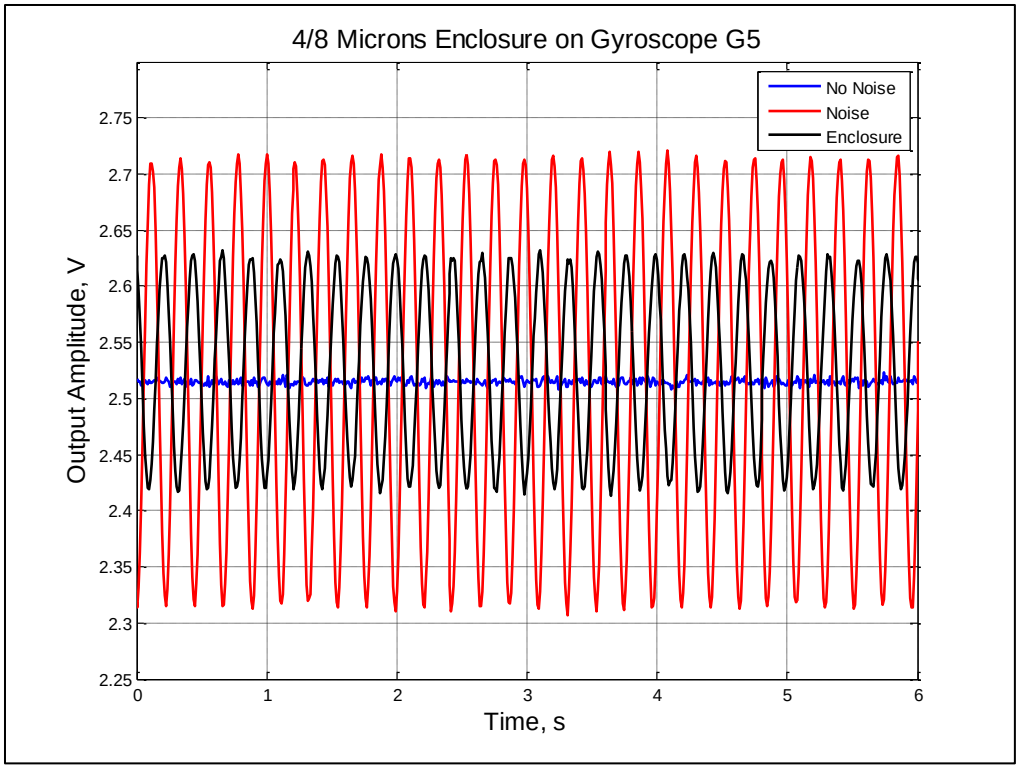

Figure F.10 Experimental results of the 4/8 microns enclosure on gyroscope G5.

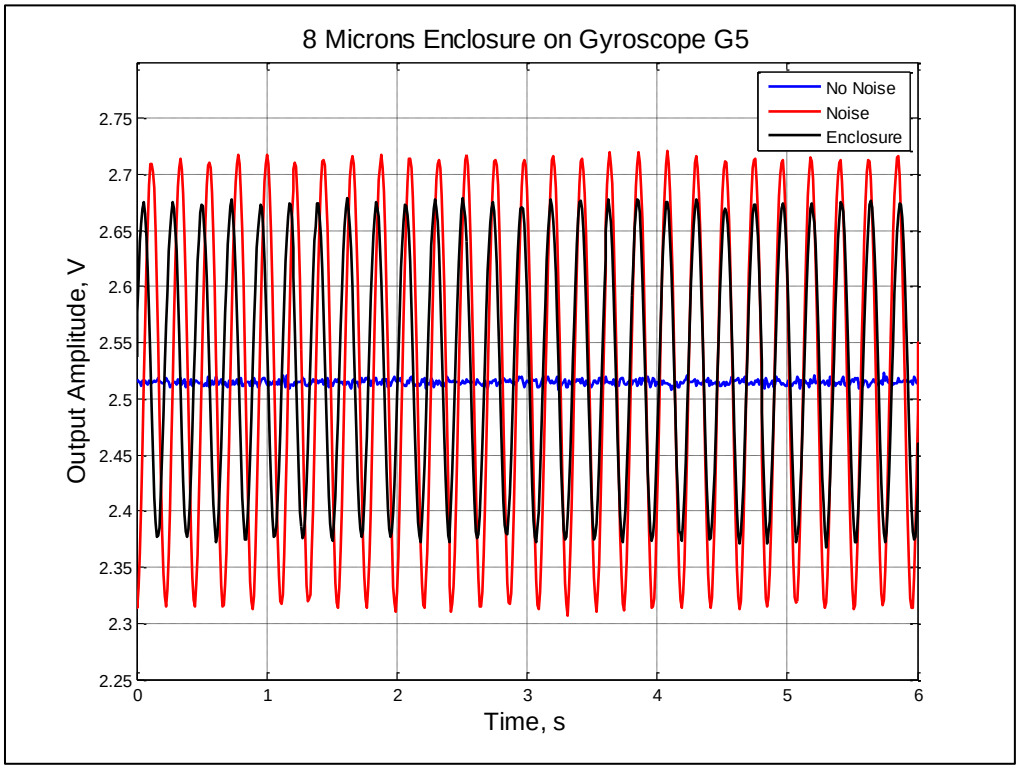

Figure F.11 Experimental results of the 8 microns enclosure on gyroscope G5.

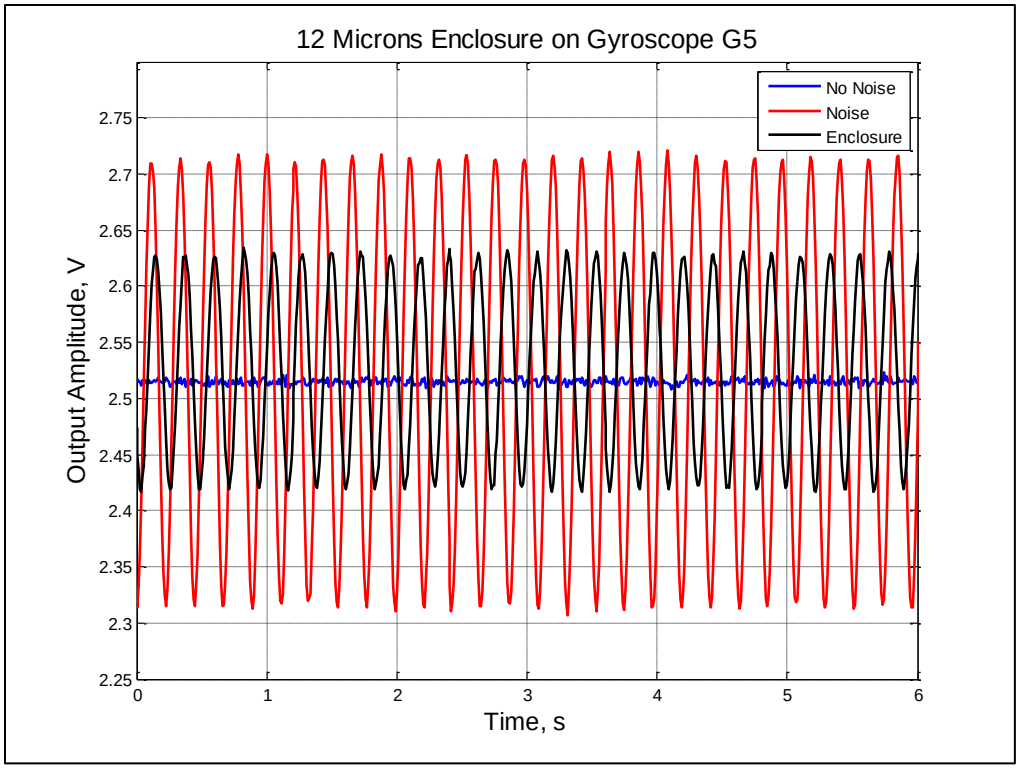

Figure F.12 Experimental results of the 12 microns enclosure on gyroscope G5.

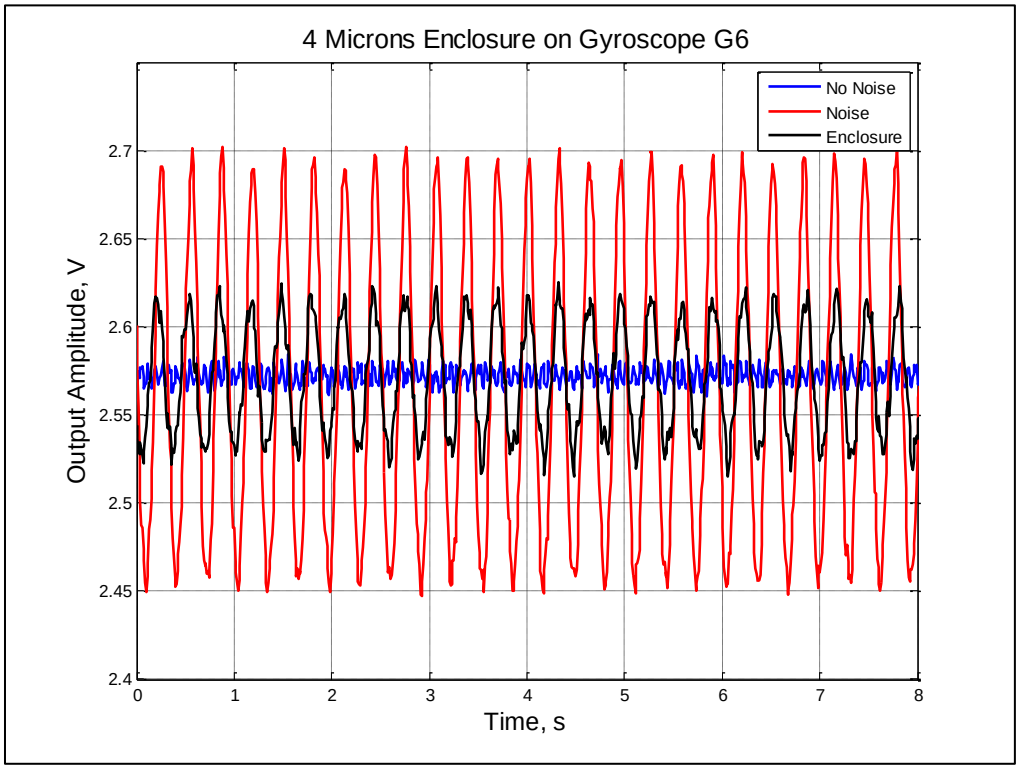

Figure F.13 Experimental results of the 4 microns enclosure on gyroscope G6.

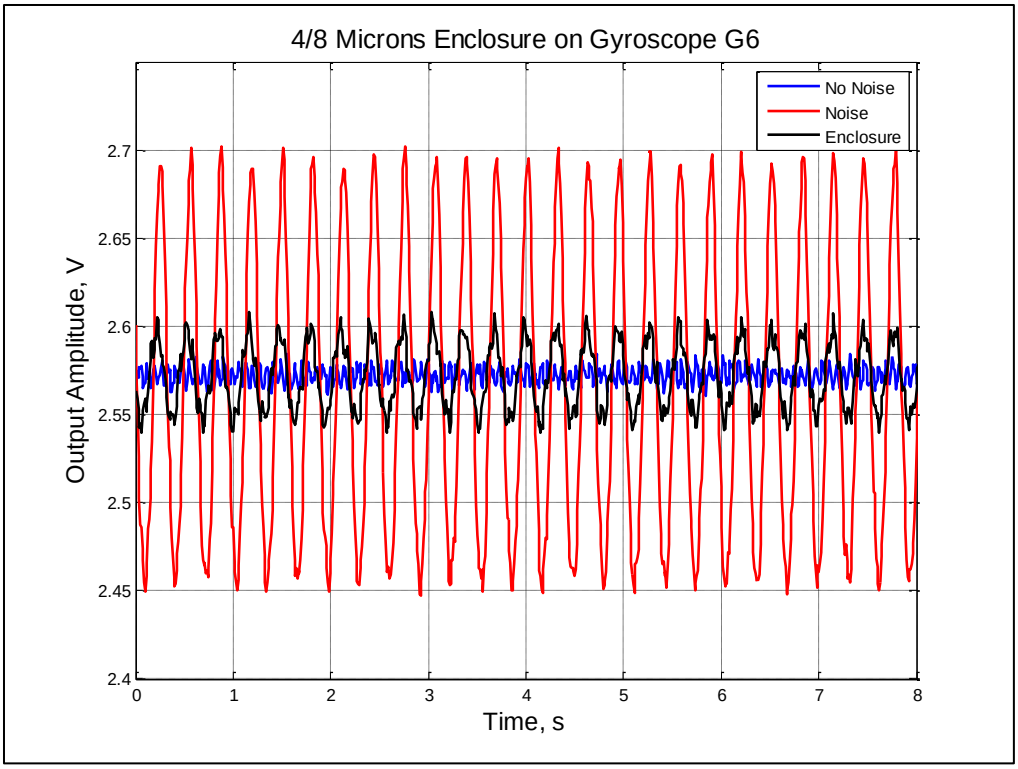

Figure F.14 Experimental results of the 4/8 microns enclosure on gyroscope G6.

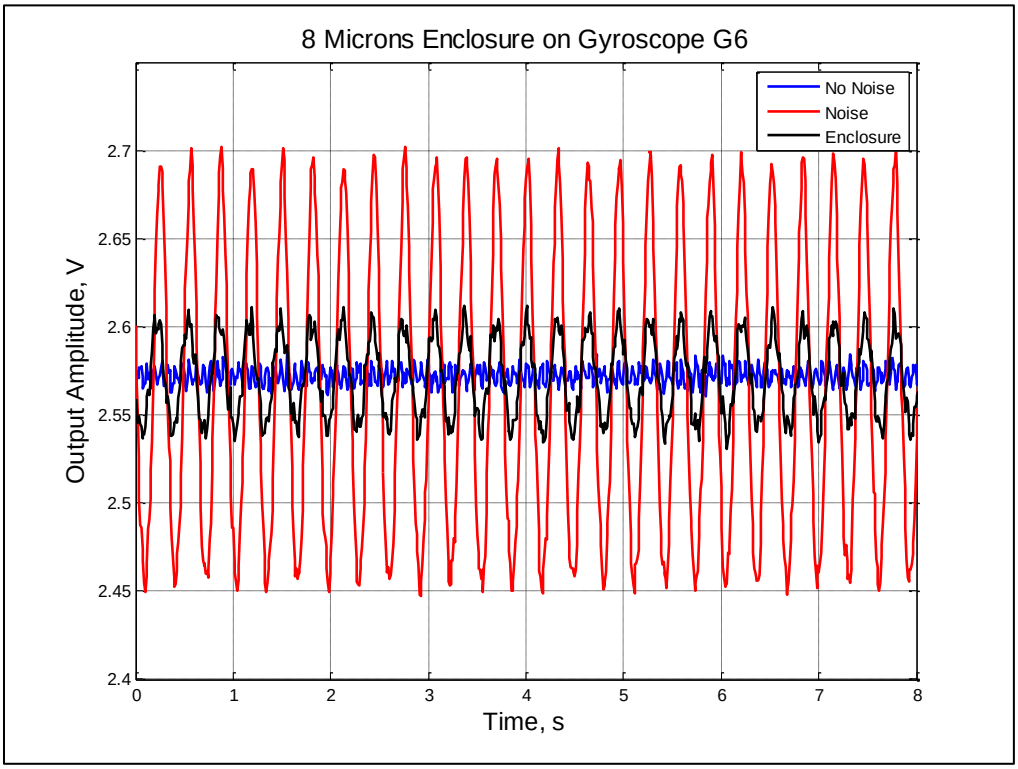

Figure F.15 Experimental results of the 8 microns enclosure on gyroscope G6.

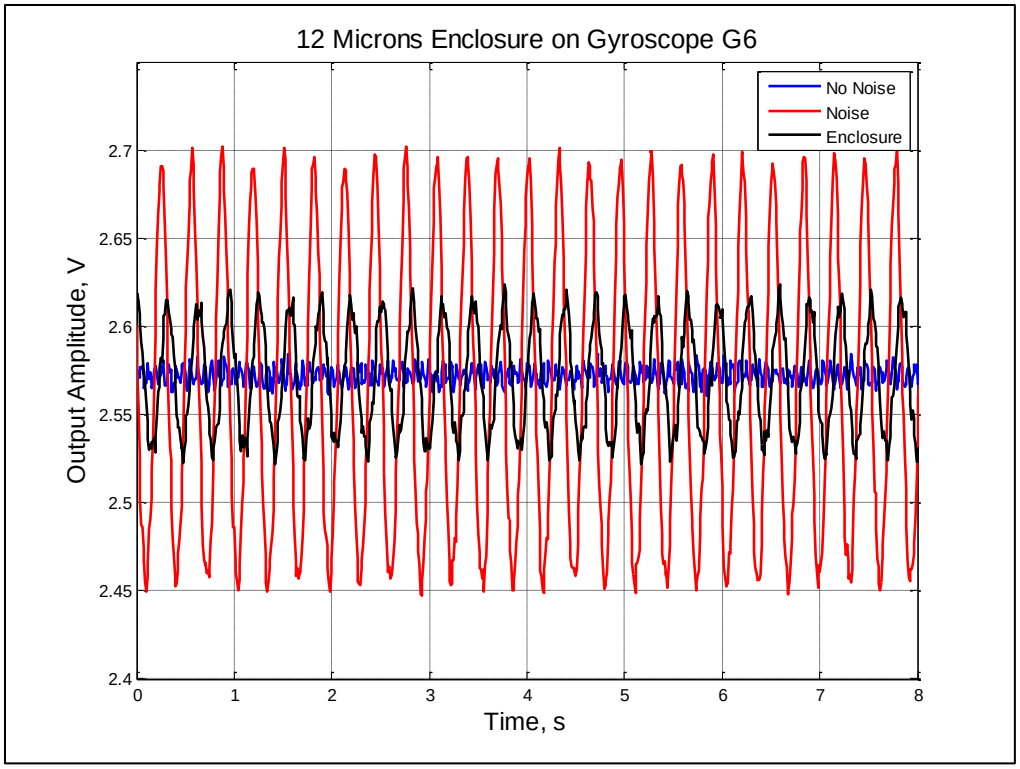

Figure F.16 Experimental results of the 12 microns enclosure on gyroscope G6.

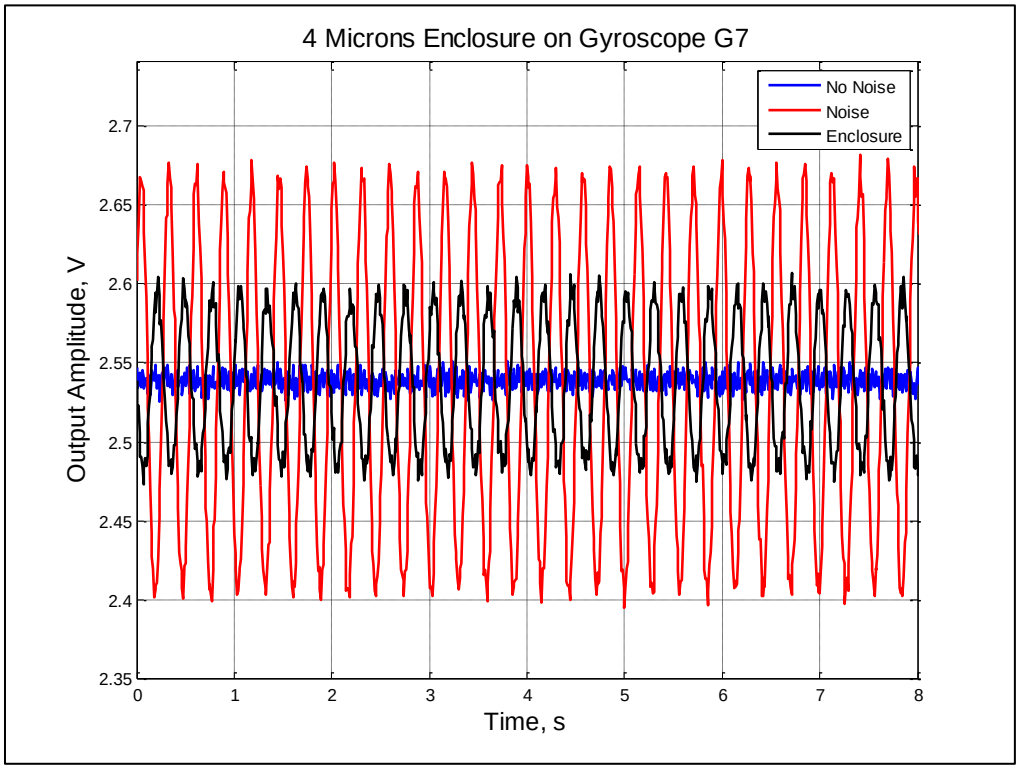

Figure F.17 Experimental results of the 4 microns enclosure on gyroscope G7.

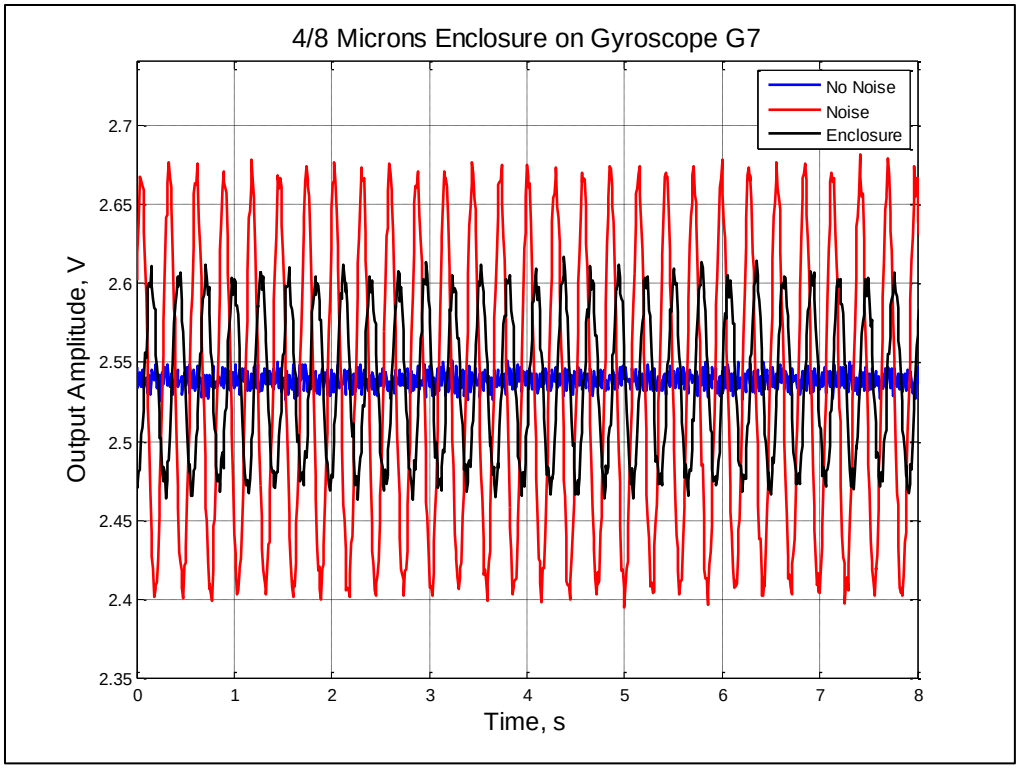

Figure F.18 Experimental results of the 4/8 microns enclosure on gyroscope G7.

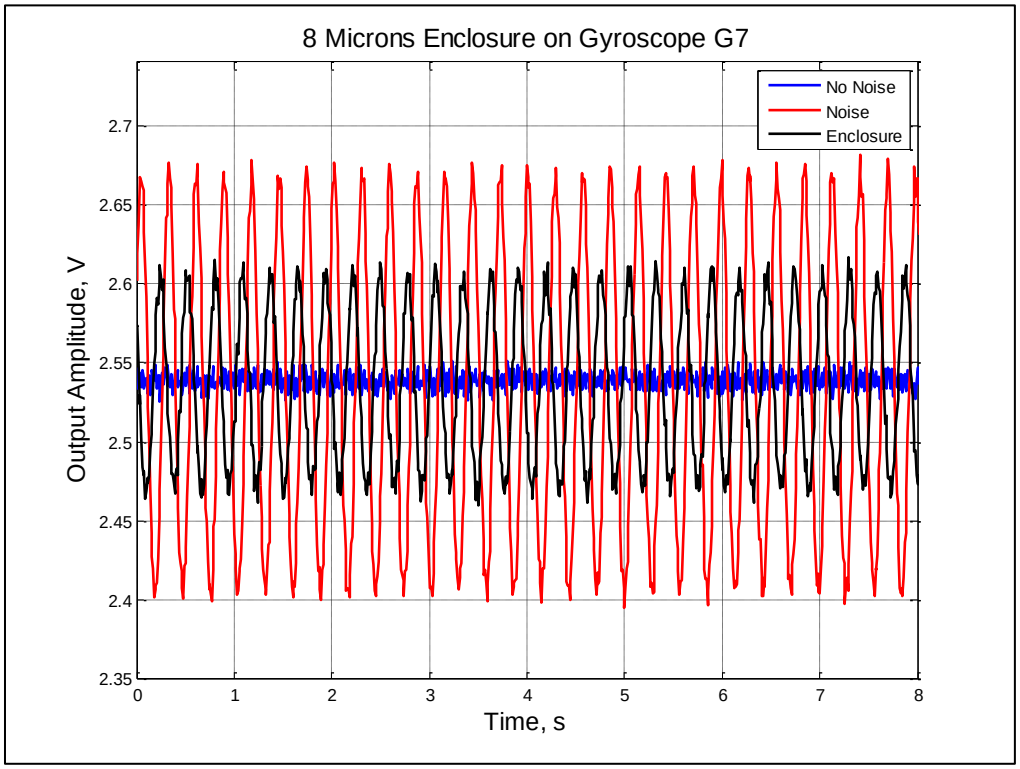

Figure F.19 Experimental results of the 8 microns enclosure on gyroscope G7.

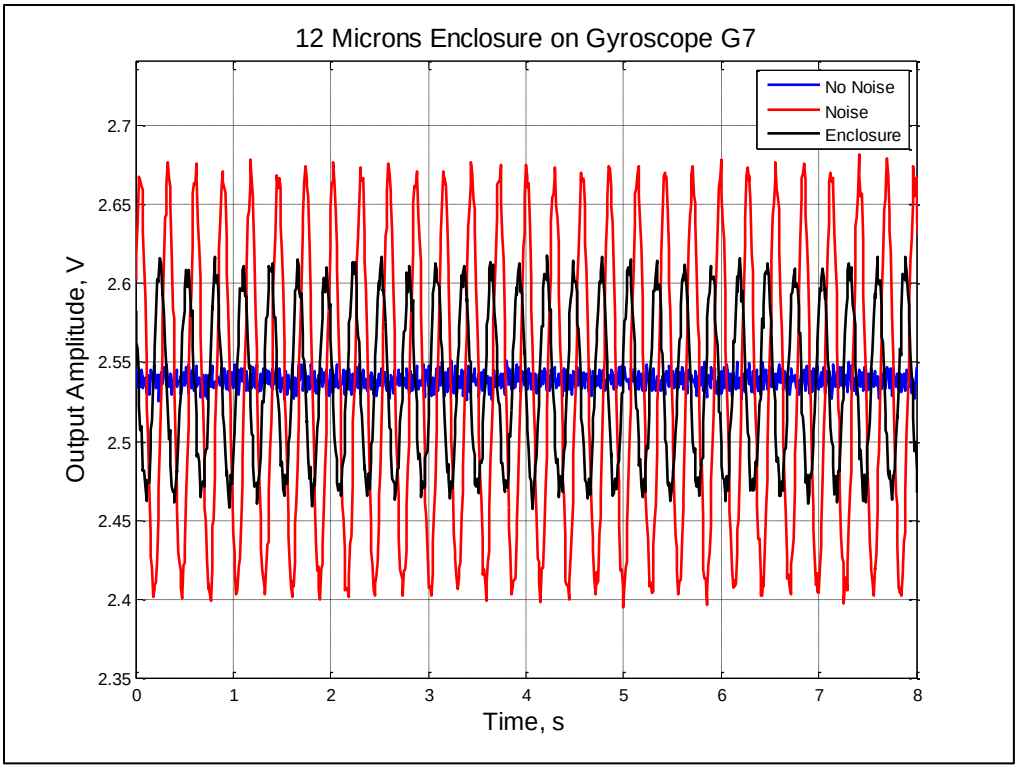

Figure F.20 Experimental results of the 12 microns enclosure on gyroscope G7.